Design of Printed Array Antennas for Wireless Communications

By

Wenting Li

A Thesis Submitted to the University of Kent
For the Degree of Doctor of Philosophy
In Electronic Engineering

August 2018

Abstract

Compared to parabolic reflector antennas, printed array antennas have compact size, light weight and low cost. Many printed array antennas have been reported in the literature, but there are lots of challenges remaining. For example, how to achieve polarization-reconfigurable circularly polarized (CP) array antennas? How to reduce the thickness of folded reflectarray CP antennas? How to increase the bandwidth of reflectarray antennas? How to achieve multi-beam radiation? To tackle these challenges, several novel designs of printed array antennas are proposed in this dissertation.

First, a novel design of a polarization-reconfigurable CP antenna is proposed. It is the first time an electronically polarization-reconfigurable CP antenna with a single-substrate polarizer is reported. The antenna consists of a slot antenna and an electronically polarization-reconfigurable polarizer (EPRP), which could convert the linearly polarized (LP) waves from the slot antenna to CP waves. The polarization of the antenna could be electronically switched to left-hand circular polarization (LHCP) or right-hand circular polarization (RHCP) by changing the states of the positive-intrinsic-negative (PIN) diodes that are loaded on the polarizer. There are several features of applying an EPRP in this design. 1) The DC circuit of PIN diodes is completely isolated from the RF signals. 2) The PIN diodes are not mounted on the RF feed network. 3) In this antenna, 32 PIN diodes are mounted on the EPRP. The average current of each PIN diode is quite small. Therefore, the antenna can radiate more power without damaging the diodes. 4) The gain of antennas is improved as the aperture of the slot antenna is enlarged by the EPRP.

Then, a novel folded CP reflectarray with a significantly-reduced antenna thickness is designed. The antenna consists of a CP feed antenna, a reflecting surface and a circular polarization selective surface (CPSS). The CPSS is transparent for RHCP waves and reflects LHCP waves. By applying the CPSS as the polarization grid for CP waves, the thickness of the CP reflectarray antenna is reduced significantly. It is the first time that the CPSS is applied as the polarization grid in a folded CP reflectarray antenna.

To overcome the problem of narrow bandwidth of reflectarrays, one ultra-wide-band tightly coupled dipole reflectarray (TCDR) antenna is proposed. This is the first report of a reflectarray using the concept of tightly coupled elements, and the reflectarray antenna is shown to achieve much wider working bandwidth compared with all the reflectarray antennas that are reported in the previous literature. The reflectarray consist of a wide-

band feed antenna and a wide-band reflecting surface. The proposed antenna combines the features of tightly coupled arrays and those of reflectarrays. As a result, the TCDR antenna has an ultra-wide bandwidth, and a much simpler feed network compared with tightly coupled arrays and other ultra-wide-band direct radiation array. A novel method to minimize the phase errors of the wideband reflectarray is also proposed. In its operating frequency band, the TCDR antenna has stable main beams and reasonable side lobe levels (SLL). A new method of improving the polarization purity of the TCDR antenna is also proposed. Based on the method, two reflectarray antennas are designed and simulated. The simulated results show that the proposed method could reduce the cross-polarization of the TCDR antenna significantly.

Finally, a novel method of designing a Nolen matrix is proposed, and the derivation of the method is given as well. The method is more concise compared with that reported in the previous literature. Based on this method, a multi-beam antenna fed by a 5×5 Nolen matrix network is proposed. The multi-beam antenna is simulated, fabricated and measured. The simulated and measured results prove the effectiveness of the proposed method of designing a Nolen matrix.

In this thesis, in order to accurately evaluate the performance of the proposed antennas, full-wave electromagnetic simulations are carried out by using commercial tools such as High Frequency Structure Simulator and Computer Simulation Technology Microwave Studio. Prototypes of the antenna designs are fabricated and measured. The simulated and measured results agree well.

Acknowledgement

Firstly, I would like to express my sincere thanks to my supervisor Professor Steven Gao for the help and support in the PhD program. His guidance and encouragement broaden my horizons on electromagnetic field and microwave technology. He gives me a lot of insightful comments and suggestions, which inspire me to research the world.

I also want to thank the academic staff, technicians and colleagues at the School of Engineering and Digital Arts, University of Kent. Without their support, I cannot finish my project.

Finally, I would like to thank my family and friends. Thanks to their understanding, support and encouragement, I can complete my research.

Contents

Abbreviations

3D	Three-Dimensional
5G	Fifth-Generation
AR	Axial Ratio
ARBW	AR Bandwidth
BC	Bias Circuit
BFN	Beam Forming Network
BW	Bandwidth
CP	Circularly Polarized
CPSS	Computer Simulation Technology
CST	Circular Polarization Selective Surface
DC	Direct Current
EPRP	Electronically Polarization-Reconfigurable Polarizer
FAST	Five-hundred-meter Aperture Spherical Telescope
FSS	Frequency Selective Surface
Gbps	Gigabit Per Second
HFSS	High Frequency Structural Simulator
LHCP	Left-hand Circular Polarization
LP	Lineally Polarized
LPDA	Log-Periodic Dipole Array
LTE	Long Term Evolution

MBA	Multi-Beam Antenna
Mbps	Megabit Per Second
MEM	Micro Electro Mechanical
MIMO	Multiple-Input and Multiple-Output
PRS	Partially Reflective Surface
PIN	Positive-Intrinsic-Negative
RF	Radio Frequency
RHCP	Right-hand Circular Polarization
SIW	Substrate Integrated Waveguide
SNR	Signal to Noise Ratio
SLL	Side Lobe Level
TCDR	Tightly Coupled Dipole Reflectarray
TTD	True-Time-Delay

Nomenclature

α	flare angle of the LPDA
Γ_{cp-cp}	S parameter from co-polarization to co-polarization
$\Gamma_{cp-cp}(A)$	S parameters from co-polarization to co-polarization of unit A
$\Gamma_{cp-cp}(B)$	S parameter from co-polarization to co-polarization of unit B
Γ_{cp-xp}	S parameter from cross-polarization to co-polarization
$\Gamma_{cp-xp}(A)$	S parameter from cross-polarization to co-polarization of unit A
$\Gamma_{cp-xp}(B)$	S parameter from cross-polarization to co-polarization of unit B
Γ_{pq}	S parameter from q-axis polarization to p-axis polarization
Γ_{xp-cp}	S parameter from co-polarization to cross-polarization
$\Gamma_{xp-cp}(A)$	S parameter from co-polarization to cross-polarization of unit A
$\Gamma_{xp-cp}(B)$	S parameter from co-polarization to cross-polarization of unit B
Γ_{xp-xp}	S parameter from cross-polarization to cross-polarization
$\Gamma_{xp-xp}(A)$	S parameter from cross-polarization to cross-polarization of unit A
$\Gamma_{xp-xp}(B)$	S parameter from cross-polarization to cross-polarization of unit B
λ_0	wavelength of electromagnetic waves in free space
(φ_b, θ_b)	beam direction of the reflectarray antenna
φ_{mn}	value of a phase shifter
φ'_{mn}	modified value of a phase shifter
$\Phi_i(x_i, y_i)$	phase of the incident waves

$\Phi_r(x_i, y_i)$ phase of the reflection coefficient

$\Phi_t(x_i, y_i)$ phase of the reflected waves

$\vec{\mathbf{a}}$ vector consisting of $a_{11},\ a_{21}, \cdots, a_{M1}$

a_m input port

a_{mn} electric field value at the point connecting two couplers or that on an input port

ac length of the element of the folded CP reflectarray

ap length of the element of the CPSS

B bandwidth

b_n output port

C max capacity of a system

$C_{0\text{-}off}$ capacitance of the PIN diode when it is OFF

C_1 phase of incident waves at the phase center of the feed antenna

D diameter of the hole

$d(l_1)$ average curve of $d_f(l_1)$

$d(x_i, y_i)$ required equivalent distance delay

$d_f(l_1)$ equivalent distance delay versus l_1 at frequency f

$d_f(lsp_1)$ equivalent distance delay versus lsp_1 at frequency f

dsp length of the element based on the stacked patch

dx length of the element of the TCDR antenna dy width of the element of the TCDR antenna

$\overrightarrow{\mathbf{e_m}}$ excitation vector whose elements are the electric field values on output ports with a_m being excited with unit power

E_1 E-field along the diagonal of the bottom ring

E_2 E-field along the diagonal of the top ring

E_{cp}^{inc} incident E-field along co-polarization

E_x^{inc} incident E-field along x axis

E_{xp}^{inc} incident E-field along cross-polarization

E_y^{inc} incident E-field along y axis

E_{cp}^{ref} reflected E-field along co-polarization

E_x^{ref} reflected E-field along x axis

E_{xp}^{ref} reflected E-field along cross-polarization

E_y^{ref} reflected E-field along y axis

f_{mn} electric field value at the point connecting a phase shifter and a coupler or that on an output port

$\mathbf{F_{mn}}$ vector consisting of $f_{m1}, f_{m2}, \cdots, f_{mn}$

fl_1 length of the first arm of the LPDA

fl_2 length of the second arm of the LPDA

fw_1 width of the first arm of the LPDA

fw_2 width of the second arm of the LPDA

h distance between the polarizer and the slot antenna

h_1 distance between the top of the element and the first metal surface

h_2 distance between the first metal surface and the second metal surface

h_n(n=3, 4, 5, 6 and 7) height of the metal ridge in the horn antenna

h_n(n=8) distance between the coaxial cable and the bottom of the horn antenna

hh_n(n=1 and 2) height of the horn antenna

k_0 wave number in free space

l_2 length of the delay line between the dipole and the first metal surface

lf length of the fixed part of the dipole

lp length of metal arm of the element of the CPSS

lpa length of the patch A

lpb length of the patch B

lsp_1 length of the bottom patch

lsp_2 length of the top patch

$p_f(x, y)$ position of the phase center at frequency f

R_i distance between the element and the phase center of the feed antenna

Rb radius of the bottom ring

Rt radius of the top ring

S width of the slot of the diagonal

[S]	S parameter matrix of the coupler
S_{mn}	S parameter from the port n to the port m
$\frac{S}{N}$	the signal to noise ratio
S(p,q)	S parameter from the port p to the port q
S(Port1_L,Port1_L)	S parameter from the LHCP waves of the port 1 to the LHCP waves of the port 1
S(Port1_L,Port1_R)	S parameter from the RHCP waves of the port 1 to the LHCP waves of the port 1
S(Port1_R,Port1_L)	S parameter from the LHCP waves of the port 1 to the RHCP waves of the port 1
S(Port1_R,Port1_R)	S parameter from the RHCP waves of the port 1 to the RHCP waves of the port 1
S(Port2_R,Port2_R)	S parameter from the RHCP waves of the port 2 to the RHCP waves of the port 2
$\sin^2 \theta_{mn}$	coupling value of a coupler
T	period of electromagnetic waves
t_n(n=1 and 2)	thickness of the substrate
tair	thickness of the air gap
ts	thickness of the substrate
tsp	thickness of the substrate of the stacked patch
w_n(n=1 and 2)	width of the horn antenna

w_n(n=3, 4, 5 and 6)	width of the metal ridge in the horn antenna
Wb	width of the bottom ring
Wd	width of the diagonal
wd_n(n=1 and 2)	width of the dipole
wd_3	width of the delay line
wp	width of metal arm of the element of the CPSS
Wt	width of the top ring
(x_i, y_i)	coordinate of the element
Z_1	impedance along the diagonal of the bottom ring
Z_2	impedance along the diagonal of the top ring

List of Figures

List of Tables

Chapter 1. Introduction

In this thesis, several novel designs of printed array antennas are proposed to overcome the challenges in wireless communications. The research background and the motivation of the PhD program are introduced first. Then, the array antennas are reviewed. Following that are the details of each antenna design proposed in the PhD project. The last part concludes the thesis and shows future work.

1.1 Motivation

Due to the rapid development of wireless communication, the number of the users is increasing fast, and services with higher bit rate data are required. It is widely foreseen that an enormous rise in traffic will appear in mobile and personal communications.

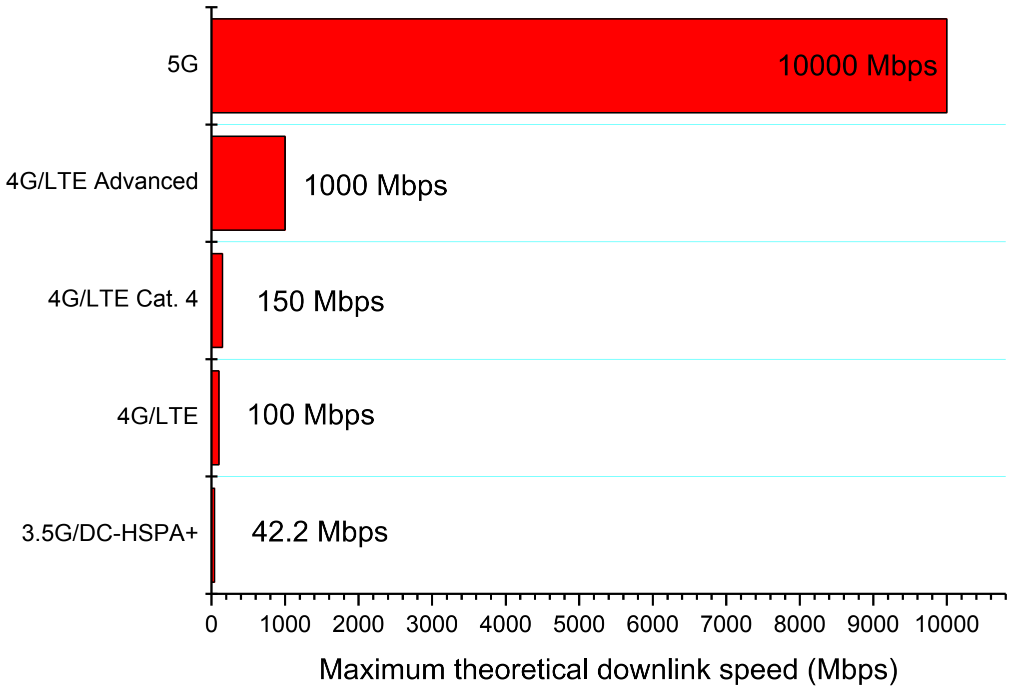

Figure 1-1 Maximum theoretical downlink speed by technology generation [1]

Figure 1-1 shows the maximum theoretical downlink speed by technology generation [1]. It can be seen the theoretical downlink speed of 5G is ten times as that of 4G/Long Term Evolution (LTE) Advanced. It also should be noted 10 Gbps is the minimum theoretical upper limit speed specified for 5G.

To support the rise in traffic, manufacturers and operators have to offer sufficient capacity in the networks. Therefore, the signal to noise ratio (SNR) and the bandwidth of the communication system are needed to be improved.

In 5G, array antennas [2] are usable over greater distances, which is an important part of a system that works at 6GHz or higher frequency. Array antennas have relatively high gains, which could improve SNR and broaden the communication capacity. In this situation, max equivalent isotropic radiated power (EIRP) limits should be considered. When the user device is connected, the beam of the array should direct at the user, and track the user device during the connection. The MIMO antenna is another method to increase the capacity of the communication system which is often discussed. The MIMO antenna makes it possible to establish multiple radio connections between a user device and a station.

Whatever antenna technologies are applied in communication systems, as the forefront of the wireless communication system, the performance of the antennas affects the entire system significantly. Therefore, the performance of antennas is required to be better and better. For some application scenarios, antennas are supposed to have a high gain with low profile, multiple beams, multiple polarizations or a wide working band.

In order to obtain high gain antennas, parabolic reflector antennas are traditional solution. However, the shortcomings of a parabolic reflector antenna limit its application in the communication system. Firstly, parabolic antennas are not easy to manufacture. The reflecting surface of a parabolic antenna is a metal curved surface, not a planar surface. To manufacture the curved surface could cost much time and money. Secondly, the beam of a parabolic reflector antenna is hard to scan electronically, which limits its application in 5G communication. Therefore, printed array antennas [3] with low cost could play a better role in 5G communication. Many printed array antennas have been reported, but there are lots of challenges remaining, which include achieving polarization-reconfigurable CP array antennas, reducing the thickness of folded reflectarray CP antennas, increasing the bandwidth of reflectarray antennas, and realizing multi-beam radiation. In order to solve these problems, several novel designs of printed array antennas are proposed in this thesis, which are listed below.

1.2 Main Contributions

In this PhD research project, several novel techniques of antenna designs are proposed. A brief summary of major contributions from the PhD project work is given below.

a) Polarization-Reconfigurable Circularly Polarized Planar Antenna Using Switchable Polarizer

Circularly polarized antennas are a type of antenna with circular polarization [3]. In this design, the antenna consists of a slot antenna and an electronically polarization-reconfigurable polarizer (EPRP), which could convert the LP waves from the slot antenna to CP waves [4]. The polarization of the CP waves could be electronically switched to LHCP or RHCP by changing the states of the PIN diodes that are loaded on the polarizer.

There are several advantages of applying an EPRP in the design. 1) The DC circuit of PIN diodes is completely isolated from the RF signals. Thus, DC blocking capacitors are not needed in the feed network of the antenna, which simplifies the design of the feed network. 2) The PIN diodes are not mounted on the RF feed network. Thus, the loss of the PIN diodes has less effect on the total radiation efficiency of the antenna. 3) In this antenna, 32 PIN diodes are mounted on the EPRP. The average current of each PIN diode is quite small. Therefore, the antenna can radiate more power without damaging the diodes. 4) The gain of antennas is improved as the aperture of the slot antenna is enlarged by the EPRP.

It is the first time an electronically polarization-reconfigurable CP antenna with a single-substrate polarizer is reported.

b) Folded Circularly Polarized Reflectarray Antenna

This CP reflectarray antenna contains a CP feed antenna, a reflecting surface and a circular polarization selective surface (CPSS). The function of the CPSS is similar with that of the polarization grid used in folded LP reflectarrays. The CPSS is transparent for right-hand circularly polarized (RHCP) waves and reflects left-hand circularly polarized (LHCP) waves. By applying the CPSS as a polarization grid for CP waves, the profile of the CP reflectarray is reduced by almost 87%.

It is the first time that a folded CP reflectarray with a CPSS as the polarization grid is proposed.

c) Ultra-Wide-Band Tightly Coupled Dipole Reflectarray (TCDR) Antenna

In this design, the reflectarray consist of a log-periodic dipole array (LPDA) as the feed antenna and a reflecting surface [5]. In the design of the unit cell on the reflecting surface, the concept of ”tightly coupled element” is proposed. Such elements have wide impedance bandwidth.

The proposed TCDR antenna combines the advantages of tightly coupled arrays and those of reflectarrays. Therefore, the TCDR antenna has a wide bandwidth with a much simpler feed network compared with tightly coupled arrays, connected arrays and other wide-band direct radiation array. In its operating frequency band, the radiation performance of the TCDR antenna is quite stable and the side lobe levels (SLL) is below -10 dB. A method to minimize the phase errors of the wideband reflectarray is also developed.

d) Low Cross-Polarization Wide-band TCDR Antenna

A method to suppress the cross-polarization of the TCDR antenna is proposed. In this method, two types of elements with symmetrical configurations are placed on the reflecting surface. Due to the symmetry, most of the cross-polarization could be cancelled. Thus, the low cross-polarization level is achieved.

In the design, the derivation of the method is given. Based on the method, two different TCDR antennas are proposed, of which the cross-polarization is much lower than that of the original TCDR antenna.

e) A Novel Method of Designing an M×N Nolen Matrix

In the design, a novel method to design an M×N Nolen matrix is proposed. The derivation of the method is shown. Compared with the method reported in the previous literature, this method is more concise and understandable. A 3×3 Nolen matrix is built step by step to show the design process in detail.

Then, a multi-beam antenna fed by a 5×5 Nolen matrix is fabricated and measured. The simulated and measured results prove that the proposed method is effective.

1.3 Publication List

Papers:

1. **Wenting Li**, Steven Gao, Yuanming Cai, Qi Luo, Mohammed Sobhy, Gao Wei, Jiadong Xu, Jianzhou Li, Changying Wu, and Zhiqun Cheng. "Polarization-Reconfigurable Circularly Polarized Planar Antenna Using Switchable Polarizer." *IEEE Transactions on Antennas and Propagation* 65, no. 9 (2017): 4470-4477.

2. **Wenting Li**, Steven Gao, Long Zhang, Qi Luo and Yuanming Cai. "An Ultra-wide-band Tightly Coupled Dipole Reflectarray Antenna" *IEEE Transactions on Antennas and Propagation*66, no. 2 (2018): 533-540.

3. **Wenting Li**, Steven Gao, Long Zhang, Qi Luo, Chao Gu and Yuanming Cai. "Folded Circularly Polarized Reflectarray Antenna Using Circular Polarization Selective Surface," submitted to *IEEE Transactions on Antennas and Propagation*.

4. **Wenting Li**, Steven Gao, Long Zhang. "A Novel Method of Designing an M×N Nolen Matrix," submitted to *IEEE Transactions on Antennas and Propagation*.

5. **Wenting Li**, Steven Gao, Qi Luo."An Ultra-Wide-Band Reflectarray Antenna With Low Cross-Polarization," submitted to *IEEE Transactions on Antennas and Propagation*.

6. Long Zhang, Steven Gao, Qi Luo, **Wenting Li**, Yejun He, and Qingxia Li. "Single-Layer Wideband Circularly Polarized High-Efficiency Reflectarray for Satellite Communications." *IEEE Transactions on Antennas and Propagation* 65, no. 9 (2017): 4529-4538.

7. Yuan-Ming Cai, Steven Gao, Yingzeng Yin, **Wenting Li**, and Qi Luo. "Compact-Size Low-Profile Wideband Circularly Polarized Omnidirectional Patch Antenna With Reconfigurable Polarizations." *IEEE Transactions on Antennas and Propagation* 64, no. 5 (2016).

8. Long Zhang, Steven Gao, Qi Luo, Paul R. Young, **Wenting Li**, and Qingxia Li. "Inverted-S Antenna With Wideband Circular Polarization and Wide Axial Ratio Beamwidth." *IEEE Transactions on Antennas and Propagation* 65, no. 4 (2017): 1740-1748.

9. Chao Gu, Steven Gao, Benito Sanz-Izquierdo, Edward A. Parker, **Wenting Li**, Xuexia Yang, and Zhiqun Cheng. "Frequency-Agile Beam-Switchable Antenna." *IEEE Transactions on Antennas and Propagation* 65, no. 8 (2017): 3819-3826.

10. Long Zhang, Steven Gao, Qi Luo, **Wenting Li**, and Qingxia Li. "Wideband Dual Circularly Polarized Beam-Scanning Array For Ka-Band Satellite Communications." *Microwave and Optical Technology Letters* 59, no. 8 (2017): 1962-1967.

11. Long Zhang, Steven Gao, Qi Luo, and **Wenting Li**. "Wideband Circularly Polarized Wide-Beamwidth Antenna Using S-Shaped Dipole." In *Antenna Technology: Small Antennas, Innovative Structures, and Applications (iWAT), 2017 International Workshop on*, pp. 118-121. IEEE, 2017.

12. Cai, Yuan-Ming, **Wenting Li**, Wei Hu, and Yingzeng Yin. "A Wideband Compact Horizontally Polarized Omnidirectional Antenna for 2G/3G/LTE." *International Journal of RF and Microwave Computer-Aided Engineering* 28, no. 5 (2018): e21256.

1.4 Outline of Thesis

This thesis consists of six chapters and is organized as follows.

Chapter 1 states a brief research background and the motivation of the PhD project. Moreover, the main novelties and contributions of the work are listed.

Chapter 2 describes the research progress on several array antennas. Several antenna techniques including reflectarrays, multi-beam antennas and polarization-reconfigurable CP antennas are reviewed.

Chapter 3 presents the CP array antennas. In this chapter, a polarization-reconfigurable CP antenna and a folded CP reflectarray antenna are introduced. For, the polarization-reconfigurable CP antenna, its polarization can be control by the status of the PIN diodes on the polarizer. And a CPSS is applied in the design of the folded CP reflectarray to reduce the profile of the reflectarray antenna.

Chapter 4 shows an ultra-wide-band tightly coupled dipole reflectarray antenna. By introducing the tightly coupled unit cell, the bandwidth of the reflectarray antenna is increased extremely. Then, a method to suppress the cross-polarization of the wide-band reflectarray antenna is illustrated in this chapter. By arranging the layout of the unit cells on the reflecting surface reasonably, the cross-polarization of the antenna can be reduced significantly.

Chapter 5 introduces a novel method of designing an $M\times N$ Nolen matrix. A 3×3 Nolen matrix is designed step-by-step, to show the method in detail. Then, a 5×5 Nolen matrix is designed, and it is applied to feed a multi-beam antenna with 5 beams. The measured results prove that the method of the designing a Nolen matrix is effective.

Chapter 6 sums up the entire thesis. The research outcomes are highlighted, and the future work is introduced as well.

Chapter 2. Array Antennas

2.1 Introduction

In order to satisfy the increasing demand for the mobile communication services including data services and voice services, the communication system needs more and more capacity. Broadening the bandwidth of the system can increase the capacity of the system. However, the available spectrum for wireless communication is a finite resource. It is impossible to increase the communication capacity by broadening the bandwidth of the system without limitation. So raising the gain of the antennas within max EIRP limits is another important method to increase the communication capacity. Many researchers put forward their ways to realize high gain antennas.

One method of enhancing the gain of an antenna is increasing the aperture of the antenna. Reflector antennas are classic examples of this method. Another way to enlarge the aperture of an antenna is to apply array antennas [6].

The reflector antenna generally includes a feed antenna and a reflector. The reflector could be a plane [7], a corner or a curved surface (i.e. parabolic reflector antennas). Other antennas may contain a primary reflector and a secondary reflector, for example, Cassegrain reflector antenna.

The simplest reflector is a plane reflector. The antenna in [7] includes a metal surface as the reflector and a dipole as the feed antenna. As the dimension of the reflector is finite, the diffraction of waves may introduce perturbations, which can be considered by some special methods [8-10]. To prevent radiation in the back and side directions, a plane reflector could be changed to a corner reflector [11-14]. In [15], a circularly polarized antenna with a corner reflector is realized. Base on the corner reflector, the authors replace the metal reflector with an FSS [16, 17].

To improve the antenna radiation, the reflector then is upgraded to a parabolic reflector. The parabolic reflector antennas are widely used in TV communications, satellite communications [2] and so on. Parabolic reflectors include parabolic cylinders [18-30] and paraboloids [31-40]. For antennas with parabolic cylinder reflectors, the feed antenna is usually a linear dipole, a linear array, or a slotted waveguide. For antennas with paraboloidal reflectors, horn antennas or waveguides could act as the feed antennas. Paraboloidal reflector antennas are widely used as high gain antennas [41]. In [42], the paraboloidal reflector antenna are used in radio telescope systems. In [43], when the antenna is working, the active reflector of the 500-m aperture spherical telescope (FAST) would change to a paraboloidal reflector.

Although paraboloidal reflector antennas are widely used, they have two drawbacks. The first is that the curved surface of the reflector is not easy to manufacture. Especially when the antenna works at high frequency, the fluctuation on the reflector surface would lead to quite large phase distribution errors. The other disadvantage of paraboloidal reflector antennas is that the beam cannot scan electronically.

To realize electronic scanning, the researchers focus on phased arrays. The beam of a phased array is able to scan electronically. However, the feed networks of phased arrays are complex when the number of the elements is very large.

Therefore, researchers proposed reflectarray antennas to achieve electronic beam-scanning ability with a simple feed network. The reflectarray combines the features of reflector antennas and phased arrays.

Apart from increasing the gain of the antenna to improve the SNR, the antennas with multiple beams and multiple polarizations could also broaden the capacity of a communication system. Therefore, the previous works about reflectarrays, multi-beam antennas and polarization-reconfigurable CP antennas are reviewed in this section.

2.2 Reflectarray Antennas

As stated above, the reflectarray antenna combines the advantages of reflector antennas and those of phased array antennas. Reflectarrays feature low mass, low cost, electronic beam scanning and the simple feed network.

Figure 2-1 shows the configuration of a typical reflectarray antenna. It generally consists of two parts. One part is the feed antenna, and the other part is the reflecting surface which contains many reflecting element. Many antennas could be chosen as the feed antenna. A classical one is a horn antenna.

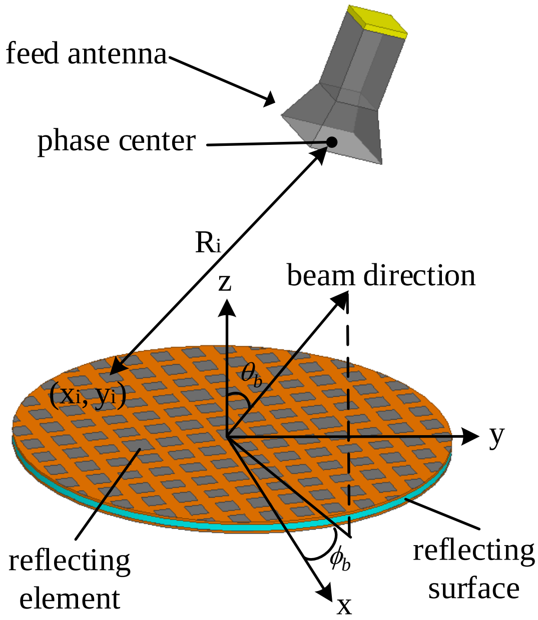

Figure 2-1 Configuration of a reflectarray antenna

When the reflectarray antenna works, the feed antenna illuminates the reflecting surface. The EM waves generated by the feed antenna excite the elements on the reflecting surface. After the elements receive the energy from the feed antenna, they are able to re-radiate and form a beam in the far field.

During the elements reflecting the EM waves generated from the feed antenna, an element can be seen as a one-port network, which is shown in Figure 2-2.

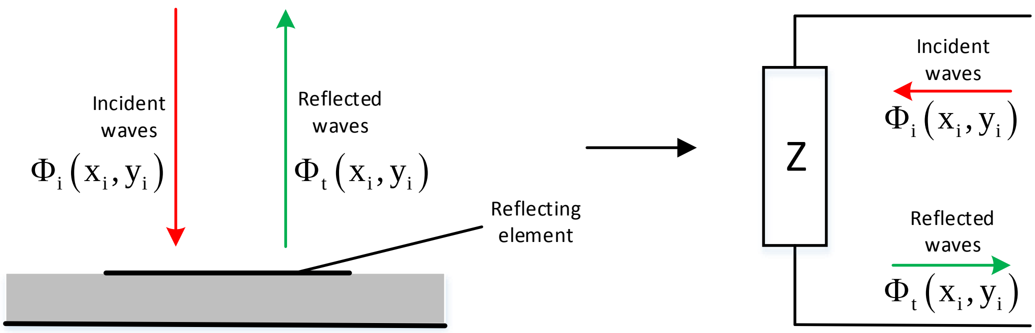

Figure 2-2 An element is equivalent to one port network

The phase of the reflection coefficient of the one-port network is set as $\Phi_r(x_i, y_i)$ where (x_i, y_i) is the coordinate of the element. The phase of the incident waves is set as

$\Phi_i(x_i, y_i)$, and $\Phi_t(x_i, y_i)$ represents the phase of the reflected waves. According to networks theory, equation (2-1) is obtained.

$$\Phi_t(x_i, y_i) = \Phi_i(x_i, y_i) + \Phi_r(x_i, y_i) \tag{2-1}$$

If the distance between the element and the phase center of the feed antenna is set R_i , and the phase of incident waves at the phase center of the feed antenna is C_1, the phase of incident waves $\Phi_i(x_i, y_i)$ is given according to equation (2-2), where k_0 is the wave number in free space. In the following derivation, the phase center of the feed antenna is assumed to be stable, which means R_i is frequency independent.

$$\Phi_i(x_i, y_i) = C_1 - R_i k_0 \tag{2-2}$$

Substituting the equation (2-2) into the equation (2-1) gives equation (2-3).

$$\Phi_t(x_i, y_i) = \Phi_r(x_i, y_i) + C_1 - R_i k_0 \tag{2-3}$$

At this time, the reflectarray antenna can be seen as a conventional array antenna with phase distribution $\Phi_t(x_i, y_i)$. If the beam direction of the reflectarray antenna is (φ_b, θ_b) , $\Phi_t(x_i, y_i)$ meets equation (2-4), according to the array antenna theory, where C_2 is a constant.

$$\Phi_t(x_i, y_i) = -k_0(x_i \sin\theta_b \cos\theta_b + y_i \sin\theta_b \sin\varphi_b) + C_2 \tag{2-4}$$

If $\Phi_t(x_i, y_i)$ in equation (2-4) is replaced with equation (2-3), the equation below is derived.

$$\Phi_r(x_i, y_i) + C_1 - R_i k_0 = -k_0(x_i \sin\theta_b \cos\theta_b + y_i \sin\theta_b \sin\varphi_b) + C_2 \tag{2-5}$$

Equation (2-5) is re-written as

$$\Phi_r(x_i, y_i) = -k_0(x_i \sin\theta_b \cos\theta_b + y_i \sin\theta_b \sin\varphi_b) + R_i k_0 + C_2 - C_1 \tag{2-6}$$

As C_2 can be an arbitrary constant, $C_2 - C_1$ is set zero to make the equation (2-6) concise. So equation (2-7) is obtained.

$$\Phi_r(x_i, y_i) = -k_0(x_i \sin\theta_b \cos\theta_b + y_i \sin\theta_b \sin\varphi_b) + R_i k_0 \qquad (2\text{-}7)$$

It is revealed that if the element on the reflecting surface meets equation (2-7), the reflectarray antenna is able to form a beam in the far field.

Reflectarray antennas are firstly proposed and constructed by the waveguide array in 1963 [44]. With the development of printed circuit board (PCB) technology, many researchers begin to use printed patches, dipoles and slots with different shapes in the design of reflectarray antennas. In [45-50], the authors use printed patches in Figure 2-3 as unit cells to design reflectarray antennas. The phase of the unit cell's reflection coefficient is controlled by adjusting the length of a microstrip line, which is connected to the patch directly. In [51, 52], patches with aperture coupled delay lines are used to build the reflectarray, which is shown Figure 2-4. In [53-55], printed dipoles with variable lengths are used to design reflectarray antennas. The phase of the unit cell's reflection coefficient is controlled by adjusting the length of the dipole. In [56-58], patches with variable sizes are chosen as cell elements to construct reflectarray antennas. In [59], the unit cell is a patch loaded with a slot. In [60], slots with varying lengths on the ground plane are used to design reflectarray antennas. In [61], slot antennas with microstrip delay lines are applied in the reflectarray design. In [62, 63], rings with variable rotation angles are employed to construct reflectarray antennas. In [64, 65], rings with different radius are used to control the phase. In [54], the authors use crossed dipoles as the elements of the reflectarray. In [66], the reflecting surface is divided into several zones. In different zones, different elements are used. The authors claim that this method could obtain a wide phase range. In [67], crossed slots with varying arms are used as the elements of a CP reflectarray.

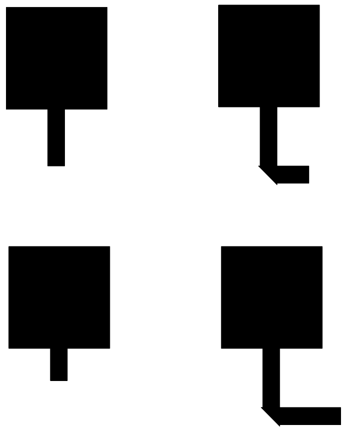

Figure 2-3 Patches connected with delay lines directly

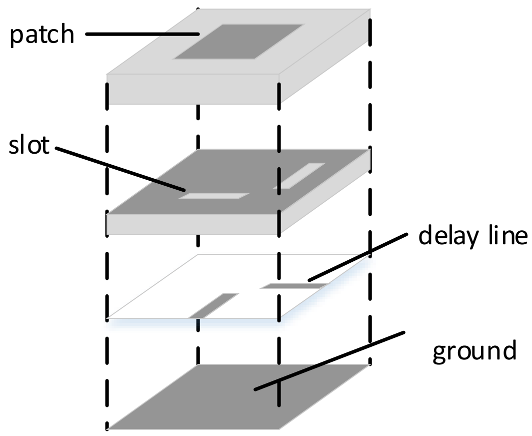

Figure 2-4 Patch with aperture coupled delay lines

To realize beam scanning, the elements can be loaded by PIN diodes [68, 69], phase shifters [70-72] and varactors [73-77]. MEM switches [78, 79], micro-machined motors [80] and photo-induced plasma [81] are also applied to control the phase distribution on the reflecting surface.

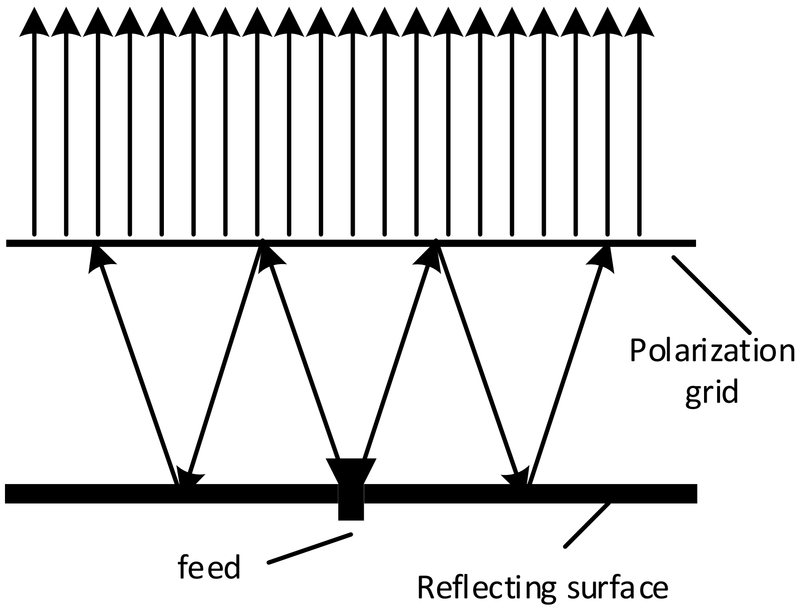

Figure 2-5 Configuration of a folded reflectarray

In order to reduce the profile of a reflectarray antenna, the concept of folded reflectarray is proposed [82-84]. Figure 2-5 shows a basic configuration of a folded reflectarray. Apart from a feed and a reflecting surface, it also contains a polarization grid. When the waves from the feed impinge the polarization grid, they are reflected with polarization unchanged. Then, the waves are reflected by the reflecting surface, in which, the polarization is twisted. After the polarization of the waves is twisted by the reflecting surface, the waves could go through the polarization grid without reflection and form beams in the far field.

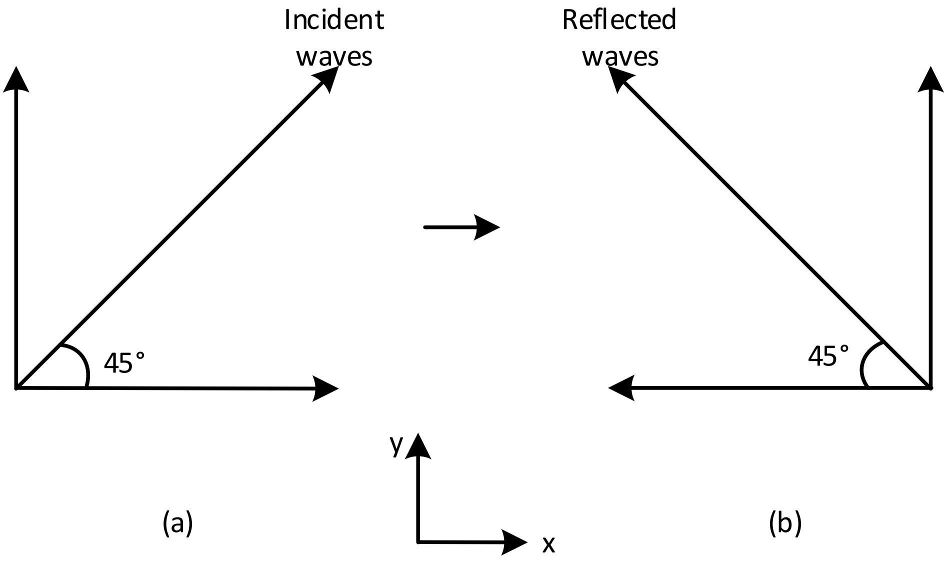

Figure 2-6 Polarizations of (a) incident waves and (b) reflected waves in polarization twist

Figure 2-6 shows the mechanism of the polarization twist on the reflecting surface for linearly polarized waves. The polarization of the incident waves is along $\varphi=45^0$. If the phase differences between reflection coefficients along x and y axis are 180^0, and the amplitudes of reflection coefficients along x and y axis are the same, then, the reflected waves' polarization will be along $\varphi=-45^0$. Thus, the polarization of the incident waves is twisted by 90^0. It can be seen that this method is only effective to linearly polarized waves.

Although reflectarray antennas have many advantages compared with parabolic reflector antennas, reflectarray antennas have the problem of narrow bandwidth. This is mainly caused by two factors: the bandwidth of elements on the reflectarray surface and the differential spatial phase delay [85]. Therefore, many researchers have tried to broaden the bandwidth of reflectarray antennas from these two aspects.

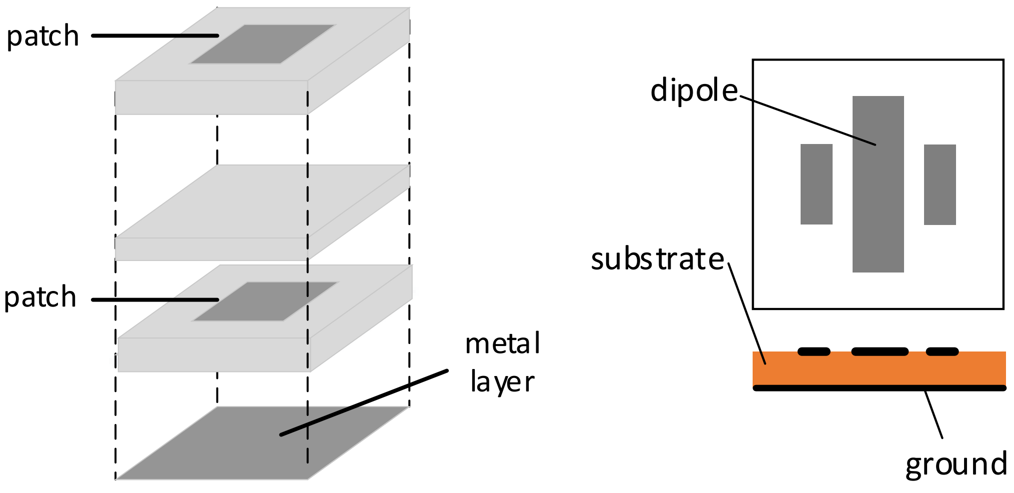

Figure 2-7 Stacked patch element (a) and parallel dipoles element (b)

In [86-89], the authors use stacked patches as the unit cells on the reflectarray surface to broaden the bandwidth of reflectarray antennas, which is shown in Figure 2-7(a). In [90-93], parallel dipoles are employed to enlarge the gain bandwidth of the reflectarray antennas, which is shown in Figure 2-7(b). In [94] the double square rings are used to improve the bandwidth of the reflectarray element. In [95, 96] multiple loops are used as the wideband elements. In [97, 98], patches with true-time-delay lines are chosen as the elements to broaden the bandwidth of reflectarray antennas. The concept based on "artificial impedance surfaces" is used to achieve wide gain bandwidth in [99]. In [100-102], the subwavelength cells are used to design reflectarray antennas. The distance between adjacent unit cells of conventional reflectarray antennas is approximately half of the wavelength of the center frequency while that distance is less than 1/3 wavelength of the center frequency in subwavelength reflectarray antennas. In [103], Bessel filter method is used to design the reflecting surface of the reflectarray antenna. In [104], the authors combine some of the aforementioned wideband reflectarray design approaches.

In [105-108] the elements including rings printed on different substrates are used to realize a dual-band reflectarray. In [58], the stacked patches are used to build the dual-band reflectarray. In [109] two types of elements are printed on one substrate to obtain a dual-band reflectarray. In [110] three types of elements are printed on the same substrate to obtain a tri-band reflectarray. The authors combine the features of antennas reported in [105, 106] and [110] to realize a six-band reflectarray.

2.3 Multi-beam Antennas

The multi-beam antennas are antennas which can form more than one beam in different directions with the same aperture. These antennas usually have two or more ports, and exciting one port can form one beam. This is quite different from the mechanism of phased array antennas [111]. If the ports are connected to a communication system by a multiple-way switch, the multi-beam antennas become beam-switching or beam-steering antennas.

The multi-beam techniques mainly encompass two types. One is the quasi-optic method, which involves a reflector or lens objective and a feed array. The feed array is usually placed near the focal point of the reflector or lens objective. The other method to obtain multiple beams is the circuit beam forming network.

2.3.1 Multi-Beam Parabolic Reflector Antennas

In [112-114], the parabolic reflector antennas are analyzed when the feed antennas are laterally displaced by a few wavelengths. In [115], the authors calculate the radiation patterns of a parabolic reflector antenna with large lateral-feed displacements. In [116], the authors place the multi-feed antennas around the focal point of a reflector to realized a multi-beam reflectarray antenna. In [117], the feed antenna is slid near the focal point to switch the beam of the antenna. In [118], a bifocal lens antenna is designed for multi-beam application by displacing the feed antenna. In [119], an approach of design and optimization of the multi-beam bifocal reflector antennas is presented. In [120], the lens is intended to slide radially and the feed antenna is fixed. In [121], a feed array and a lens are applied to achieve a multi-beam antenna. In [122, 123], the multi-beam antenna is fed by a circular array.

2.3.2 Rotman Lens

Rotman lens is also a quasi-optic method to realize multi-beam networks [124]. Since the Rotman lens is proposed, it receives intensive research as it has advantages of low cost, design simplicity, and wide-angle scanning capabilities. In [125] the original Rotman lens is proposed. Then the microstrip Rotman lens is realized in [126-135]. In [136-142] Rotman lenses based on substrate integrated waveguide (SIW) are reported. Figure 2-8 shows the configuration of a Rotman lens. The parallel plate region is delimited by the port contour. The input ports are placed along a focal arc at one edge of the parallel plate region, while the output ports are located along the other edge. The different distances between a certain input port and all output ports lead to linear progressive phase shifts on the output ports. As the distances differences could achieve true time delay, the Rotman lens is able to work in a wide band. Since a Rotman lens is built without phase shifters, it offers a low-cost, low-profile multi-beam antenna network.

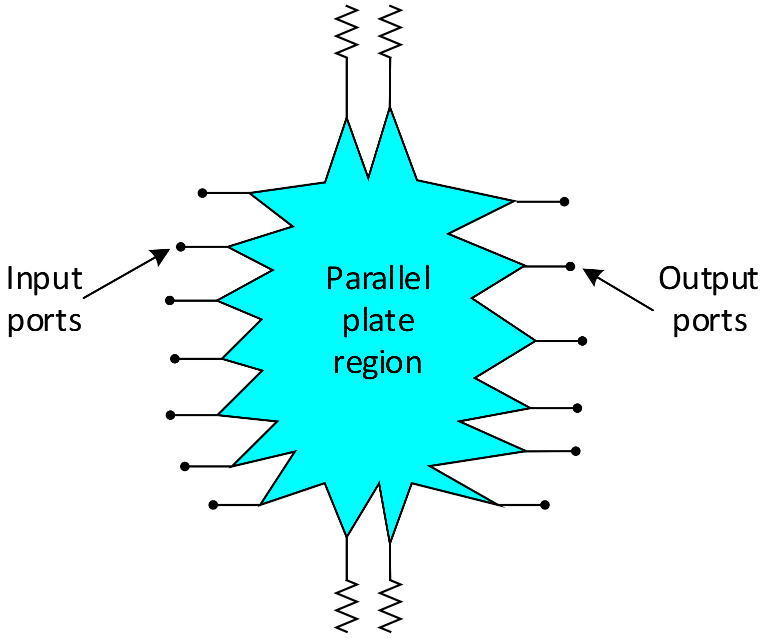

Figure 2-8 Configuration of Rotman lens

2.3.3 Beam Norming Networks

Another method of realizing multiple beams is the circuit beam forming networks, which mainly include Blass matrix [143], Butler matrix [144] and Nolen matrix [145] beam forming networks (BFN).

2.3.3.1 Blass matrix

Blass matrix networks contain phase shifters, directional couplers and resistive terminations, which is shown in Figure 2-9. Besides transferring energy, the feed lines in Figure 2-9 also act as phase shifters. If directional couplers and feed lines are assumed to be ideal, their insertion losses are zero. As the terminations absorb the energy from the input ports, Blass matrix networks are lossy, which is an important characteristic of the Blass matrix.

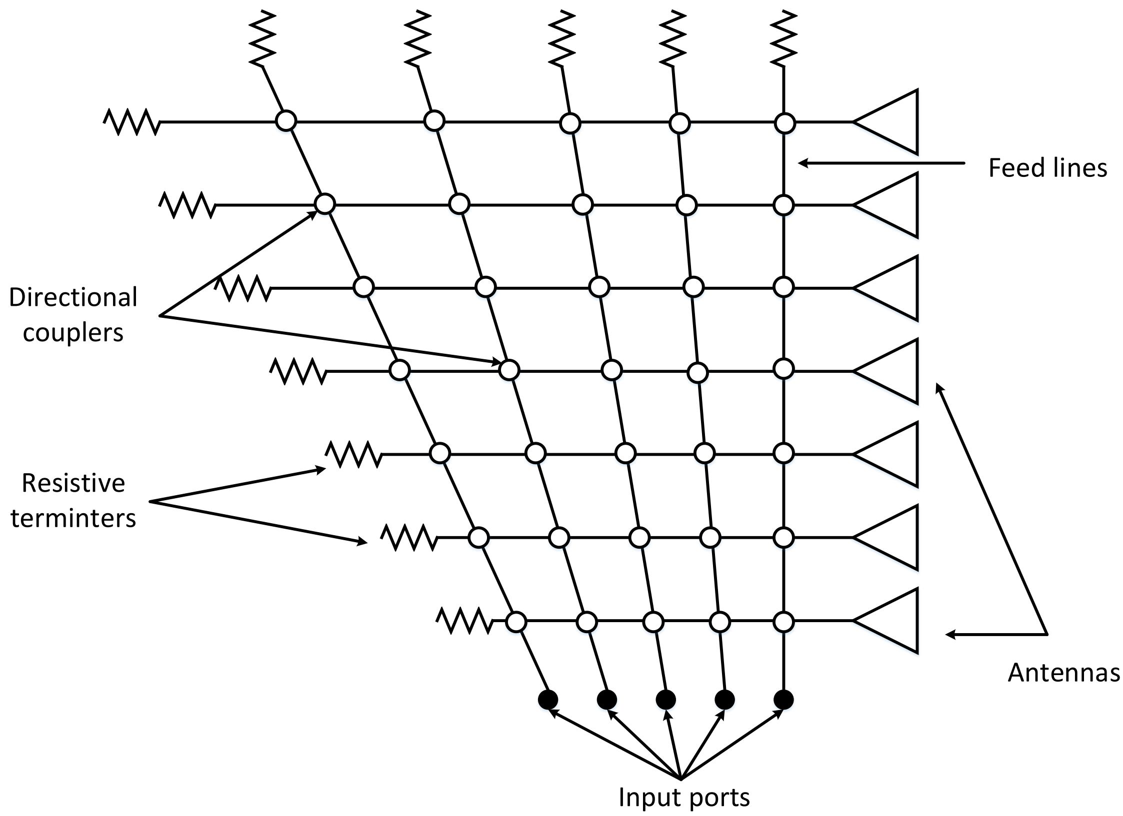

Figure 2-9 Configuration of Blass Matrix [143]

For a Blass matrix, the number of input ports is arbitrary. So is the number of output ports. When an input port is fed, the energy propagates along the feed lines. A part of the energy through directional couplers and feed lines with different lengths excites the antennas connected with output ports. The lengths of feed lines control the phases of antennas, and the antennas form beams in the far field. Except for the energy received by antennas, the rest energy is absorbed by the terminations. If too much energy is absorbed by terminations, the efficiency of Blass matrix beam forming networks could be low.

In [146], a synthesis method for ladder networks and Blass matrices is presented. The authors state that the method leads to less loss than that reported in [147]. In [148], a novel design method for Blass matrix is proposed.

In [149, 150], a multi-beam microstrip patch array fed by a Blass matrix is demonstrated. An antenna with two beams fed by a modified Blass matrix is introduced in [151]. In [152], a Blass matrix based on SIW is reported. A waveguide slotted array fed by a Blass matrix is shown in [153].

2.3.3.2 Butler Matrix

Butler matrix and Nolen matrix networks consist of hybrid couplers and phase shifters. As no terminations exit in these networks, they both are lossless networks, which is a major difference compared with the Blass matrix. However, there are also distinctions between the Butler matrix and the Nolen matrix.

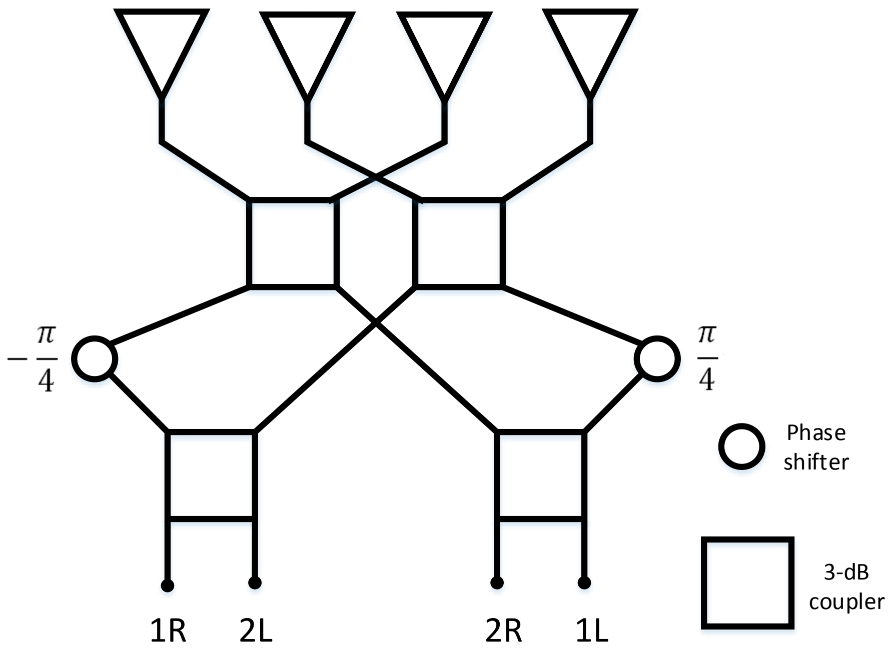

Figure 2-10 A schematic diagram of a 4×4 Butler matrix [154]

Standard Butler matrix networks usually have N input ports and N output ports. And N must be 2 to the power of an integer. That is $N=2^n$ (n>1 and n is an integer). This condition implies that the number of the input ports and output ports is not arbitrary. For an N×N Butler matrix, $(\mathrm{N}/2) \times \log_2 N$ 3dB hybrid couplers and $(N/2) \times (\log_2 N - 1)$ phase shifters are required. Figure 2-10 shows a schematic diagram of a 4×4 Butler matrix. This Butler matrix needs 4 couplers and 2 phase shifters. Although some specific Butler matrix networks break the design rule above, these networks are not standard Butler matrix networks [155, 156]. And these networks usually are oversized and use complicated couplers instead of 3dB couplers.

In [157], a wideband millimeter-wave Butler matrix network is realized. In [158-160], the authors build a wideband Butler matrix network based on SIW. A waveguide slot array fed by a Butler matrix with side lobe control is reported in [161]. In [162, 163], the authors realize the multi-beam antenna with low side lobe by introducing attenuators. The authors use a similar method to suppress the side lobe without attenuators in [164-166]. In [156], a design approach for wideband Butler matrices is proposed. In [167, 168], a 4×4 Butler matrix network is used to feed the antenna. In [169], the Butler matrix is used to feed a 2-D beam-switching array antenna. In [170], a CP beam-switching antenna is fed by a Butler matrix network.

2.3.3.3 Nolen Matrix

A Nolen matrix can be seen as a modified Blass matrix. It removes the terminations from a Blass matrix and needs fewer couplers. Figure 2-11 shows the structure of a Nolen matrix. In a Nolen matrix, every cross point is a node, which encompasses a phase shifter and a coupler. It should be noted that the lines outside nodes in Figure 2-11 are not feed lines. Those lines just describe the topology structure of Nolen matrix. This means every node is connected directly without extra feed lines. All the required feed lines are considered as parts of phase shifters and couplers when designing a Nolen matrix network.

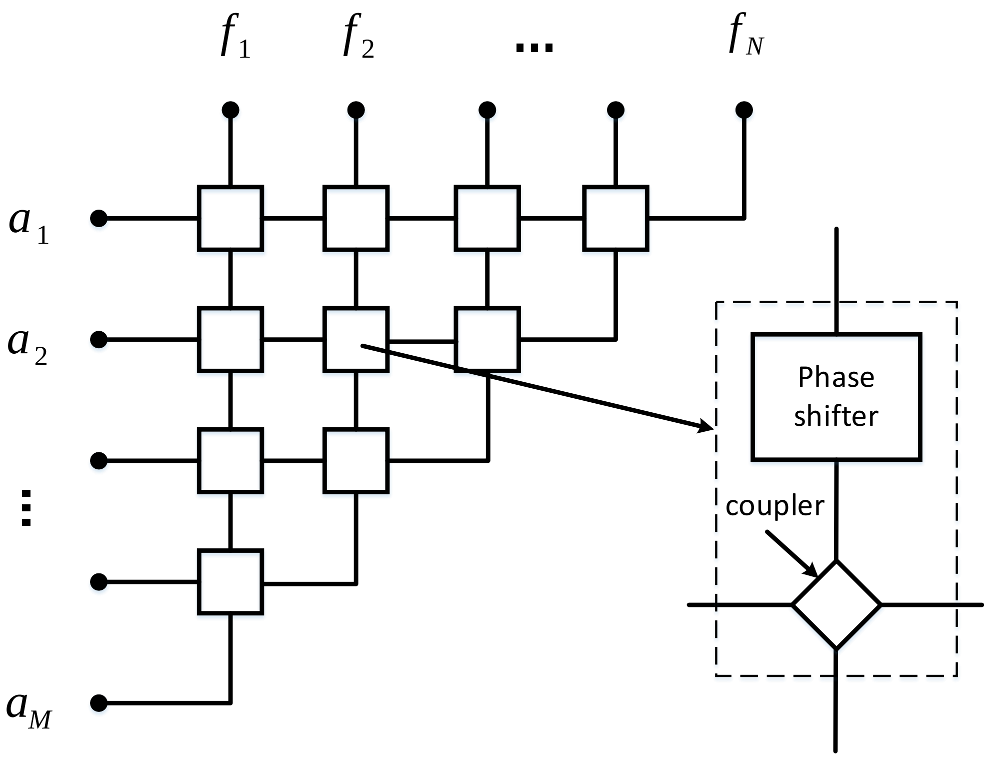

Figure 2-11 A schematic diagram of a Nolen matrix

An M×N Nolen matrix network is characterized by the arbitrary number of input and output ports if M≤N, which makes Nolen matrix networks more flexible than Butler matrix networks because the number of input and output ports of Butler matrix networks must be equal and it needs to be 2 to the power of an integer [154]. Nolen matrix networks are lossless networks as well if phase shifters and couplers are assumed to be ideal.

2.3.3.4 Comparison Between Blass, Butler and Nolen Matrix Networks

Table 2-1 Comparison Between Blass, Butler and Nolen Matrix Networks

Matrix type	If lossless	Limitation on the number of input and output ports
M×N Blass matrix	lossy	None
M×N Butler matrix	lossless	$M=N=2^n$ (n is an integer and larger than 1)
M×N Nolen matrix	lossless	M≤N

Table 2-1 compares the three networks mentioned above in terms of inherent losses and the limitation on input and output ports. It can be seen the limitation on Butler Matrix networks is the strictest, and Blass matrix networks are lossy. Nolen matrix networks combine the advantages of the Butler matrix and Blass matrix networks. On one hand, Nolen matrix networks are lossless. On the other hand, the limitation on Nolen matrix networks is not as strict as that on Butler matrix networks. It only requires that the number of input ports is not larger than that of outputs ports. As a result, Nolen matrix networks are more flexible than Butler matrix networks. For example, the Nolen matrix could realize 5×5 network easily while the standard Butler matrix could not.

2.4 Polarization-Reconfigurable CP antenna

Polarization-reconfigurable CP antennas have the advantages of both circular polarization and polarization reconfigurability. Thus they attracted lots of research interests. Such antennas can enable more reliable wireless connections in dynamic communication environment conditions [171].

CP planar antennas can be realized by a microstrip patch [172] or a printed slot [173] using multiple feeds or one single feed. Alternatively, CP antennas can be implemented by using crossed-dipoles [174]. The helix antennas [175] and spiral antennas [176] are classical examples of broadband CP antennas. Apart from the antennas mentioned above, CP antennas can also be achieved by using a polarizer to convert LP waves to CP waves [177-179]. One main advantage of utilizing a polarizer is that it can enhance the gain of a CP antenna without resorting to an array antenna, which requires a complicated feed network. In [177], using meander lines to design a polarizer consisting of four substrates is reported. In [178] and [179], metasurfaces are used to convert LP waves to CP waves. Compared to the conventional CP antenna array, using a polarizer to generate CP waves does not need a complex, lossy feed network. Thus, a CP antenna with a polarizer has the potential of achieving higher efficiency, in particular at higher frequencies when the loss in feed networks becomes significant. It is also possible to achieve high gain CP antennas using a partially reflective surface (PRS) [180]. However, the PRS CP antenna typically requires about 1/2 wavelength distance between the PRS and the ground plane while the distance between the polarizer and the source antenna can be reduced to approximately 1/17 wavelength [178]. Thus, a CP antenna using a polarizer can have a very low profile.

Polarization-reconfigurable CP antennas have been studied by many researchers [181]. The polarization reconfiguration can be obtained by introducing PIN diodes or varactors to the feed networks of antennas [182-185], using multiport networks to switch antennas' polarizations [186, 187] and modifying the antennas' geometry to alter their polarizations [188-193]. For example, in [185], the corresponding feed probe of a corners-truncated patch antenna is switched to realize different polarizations by adding PIN diodes to the feed network. In [187], the authors use a 90^0 hybrid coupler to feed the antenna, and the polarizations are switched by feeding different input ports. In [189], two perpendicular slots are introduced on a patch antenna. Each slot is loaded by one PIN diode. By controlling the states of the PIN diodes, the polarization could be altered. However, disadvantages of using these techniques are that the antennas have a complicated DC controlling circuitry, and it is rather difficult to extend them to a large-scale array antenna for high gain CP antenna applications.

2.5 Summary

Although the reflectarrays, multi-beam antennas and polarization-reconfigurable CP antennas have been developed for many years, there are still some problems need to be solved. Some of them are listed as follows:

- The polarization-reconfigurable CP antennas reported are hard to be extended to an array antenna.
- The profile of CP reflectarrays is quite high. Although folded reflectarrays have been proposed to reduce the profile of the reflectarrays, the antennas reported in the literature are LP reflectarrays.
- The bandwidth still is the most significant limitation on reflectarray antennas. Although many researchers have tried to broaden the bandwidth of reflectarrays, the bandwidth of reflectarray is still not as wide as other wide-band antennas.
- The method of designing a Nolen matrix has been proposed. However, the method is not concise enough.

Then, the author of this thesis proposes some solutions, trying to solve the problems mentioned above.

- A polarization-reconfigurable CP antenna is proposed, which is easy to be extended to an array antenna
- A folded CP reflectarray is designed to reduce the profile of the reflectarray.
- Tightly coupled reflectarray is presented to improve the bandwidth of the reflectarray.
- A novel method is proposed to design a Nolen matrix, which is more concise compared with the method reported in the previous literature.

Chapter 3. Circularly Polarized Array Antennas

Circularly polarized (CP) antennas are important for wireless systems (mobile satellite communications, Global Navigation Satellite Systems, wireless local area networks, etc.), because no strict alignment between transmitting and receiving antennas is needed, and CP antennas can reduce the 'Faraday rotation' effect of the ionosphere [3, 194].

In this section, two types of CP antennas are introduced. One is a polarization-reconfigurable CP antenna. The other is a folded CP reflectarray antenna.

3.1 Polarization-Reconfigurable CP Antenna

In this subsection, a polarization-reconfigurable CP antenna consisting of a switchable polarizer loaded by PIN diodes and a slot antenna is presented. Instead of modifying the feed networks, switching the input ports of feed networks, or changing the geometry of antennas to realize reconfigurable polarization, an electronically polarization-reconfigurable polarizer (EPRP) is used in the proposed antenna. There are four advantages of using an EPRP: 1) The DC circuit of PIN diodes is completely isolated from the RF signals. Thus, DC blocking capacitors are not needed in the feed network of the antenna, which simplifies the design of the feed network. 2) The PIN diodes are not mounted on the RF feed network. Thus, the loss of the PIN diodes has less effect on the total radiation efficiency of the antenna. 3) It increases the power handling of the antenna compared with the designs reported in [182-193]. In the presented design, 32 PIN diodes are mounted on the polarizer. The average current of each PIN diode is much smaller than that of PIN diodes used in [182-193]. Therefore, the antenna can radiate more power without damaging the diodes. 4) The gain of antennas is improved by the EPRP.

Although one polarization-reconfigurable antenna with a polarizer is reported in [179], it is obtained by mechanically rotating the polarizer, which has the disadvantage of slow switching. Besides the advantages mentioned above, it is demonstrated that the proposed antenna can be easily extended to a larger size array if higher gain is needed, and only minor modifications to the DC bias circuit are needed.

3.1.1 Design of the Polarization-reconfigurable Antenna Using EPRP

Figure 3-1 shows the configuration of the polarization-reconfigurable CP antenna. The antenna consists of a polarizer and a feed antenna, and the polarizer is placed above the feed antenna. The polarizer is the critical component to achieve the reconfigurable CP radiation. A slot antenna is employed as the feed antenna due to its simple structure. In principle other types of antennas such as a patch antenna can also be used as the feed antenna.

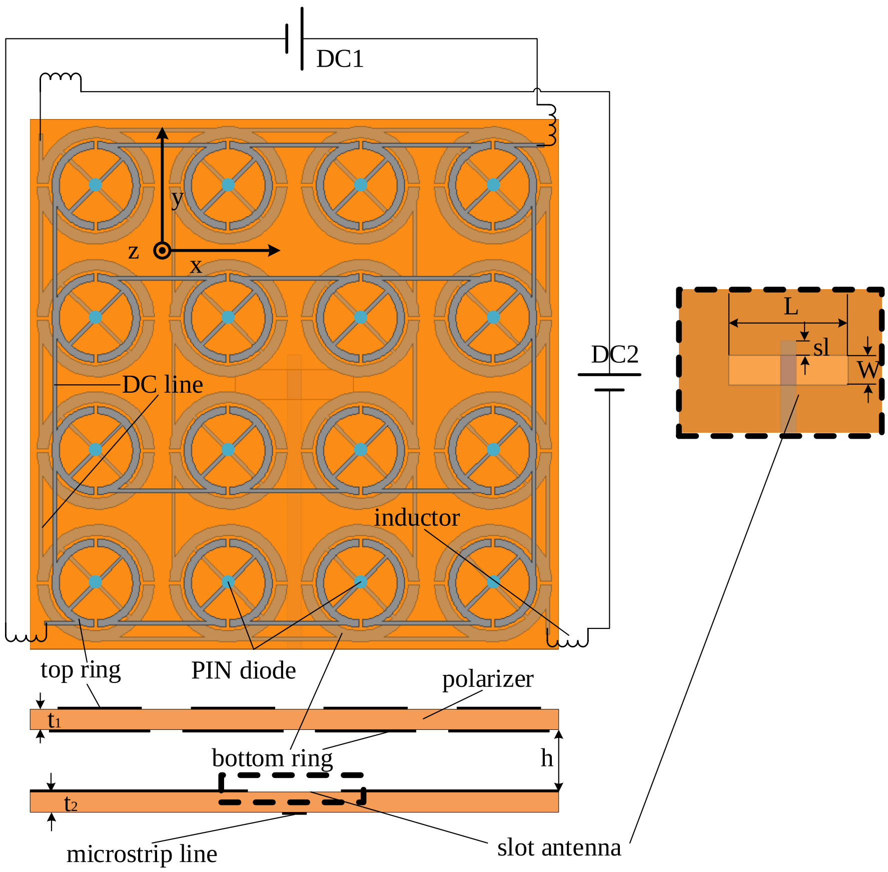

Figure 3-1 Configuration of the polarization-reconfigurable antenna

The polarizer contains 16 unit cells, which are placed as a 4×4 array. The unit cell has two rings with diagonals printed on the substrate (Rogers RO4003C). The top view of the unit cell is shown in Figure 3-2(b). It should be noted that the sizes of top rings and bottom rings are approximately the same. The differences between them in Figure 3-2(b) are enlarged to clarify the structure of the unit cell. This also applies to Figure 3-3. The perimeter of the ring is approximately equal to one effective wavelength in the substrate. Diagonals are introduced to the ring to generate circular polarization. The diagonal of the top ring is perpendicular to that of the bottom ring. PIN diodes (SMP1345-079LF) are loaded in the middle of all diagonals. Both the top ring and the bottom ring are divided into two parts by slots so that PIN diodes are biased by DC power. The slots on the top ring are aligned vertically while the slots on the bottom ring are aligned horizontally. Simulated results show that adding these slots slightly shifts the center frequency of the axial ratio (AR) bandwidth to a higher frequency. The width of the slot is 0.2mm. The widths of diagonals *Wd* are identical for all rings. Except for the different sizes, the bottom ring can be seen as the top ring being rotated by 90^0 counterclockwise.

PIN diodes are controlled by two pairs of DC lines, which determine the bias voltage on the PIN diodes of top rings and bottom rings respectively. The structure of these two pairs of DC lines is identical, which is demonstrated in Figure 3-2(a). For the top rings in Figure 3-1, the four PIN diodes in the same row form a series circuit. As there are 4 rows, the PIN diodes form 4 series circuits, which are biased by DC power in parallel. The DC network of the bottom rings can be seen as that of the top rings being rotated by 90^0 counterclockwise. The radiation from the DC lines (caused by the induced current) on the polarizer can affect the axial ratio of the antenna. To reduce this effect, the layout of the DC network of the top rings is perpendicular to that of the bottom rings so that the DC network can have more rotational symmetry; thus, those unwanted radiations from the induced currents of DC lines can be canceled as much as possible. When the PIN diodes of top rings are OFF and those of bottom rings are ON, the antenna works as an RHCP antenna. When the PIN diodes of top ring are ON and those of bottom rings are OFF, the antenna operates as an LHCP antenna.

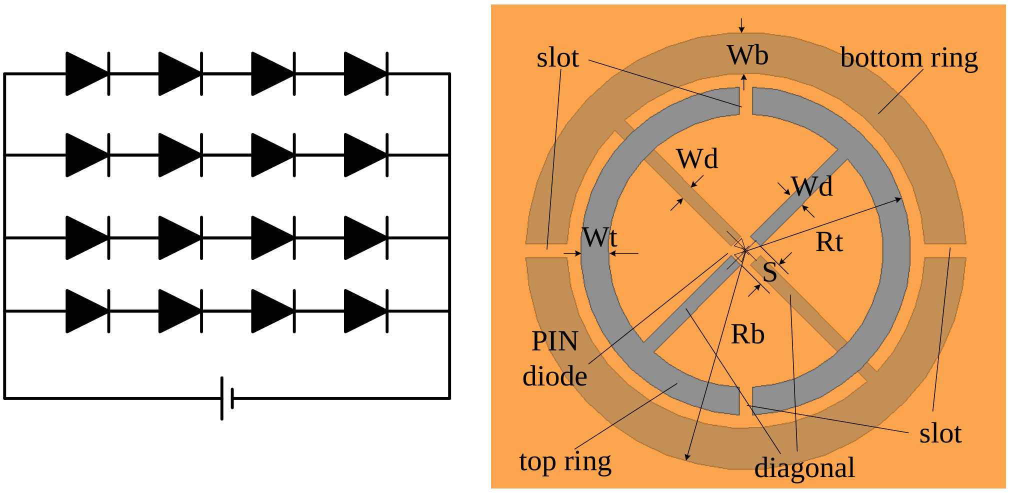

(a) (b)

Figure 3-2 (a) DC circuit diagram of PIN diodes and (b) unit cell of the polarizer

To verify the design concept, an antenna prototype working at 2.5 GHz is designed. The thickness of the polarizer t_1 is 0.813 mm. The distance between the polarizer and the feed antenna *h* is initially set 1/17 wavelength according to [178]. Then, the value of *h* is chosen to be 8.2 mm ($0.07\lambda_0$) after performing optimizations in EM simulator, to shift the center frequency of the AR bandwidth (ARBW) to 2.5 GHz. The dimension of the whole antenna is 120×120 mm^2. To achieve the compact size, the distance between adjacent unit cells of the polarizer is 27 mm, which is only larger than the diameter of bottom rings by 0.6 mm. Other parameters are given in TABLE I. In order to increase the overlapped AR bandwidth between LHCP and RHCP, the radius and width of the bottom ring are slightly larger than those of the top ring.

Table 3-1 Parameters of the Unit Cell (unit: mm)

Wd	*Rb*	*Rt*	*Wb*	*Wt*	*S*
0.8	13.2	13	1.7	1.05	1.1

3.1.2 Simulations and Analysis

The LP waves from the slot antenna can excite the rings of the polarizer to radiate. Then the LP waves are converted to LHCP waves or RHCP waves by the polarizer when the states of PIN diodes of top rings are different from those of bottoms rings.

3.1.2.1 Physical Mechanism of Generating CP Waves

The slot antenna is placed along the x-axis, and the polarization of LP waves generated by the slot antenna is along the y-axis. The E-field is decomposed into two orthogonal components, E_2 and E_1. E_2 is along the diagonal of the top ring while E_1 is along that of the bottom ring. E_2 and E_1 are in phase. Both of them are shown in Figure 3-3. Along E_2 and E_1, the impedance of the unit cell on the polarizer is represented by Z_2 and Z_1, respectively.

When the state of the PIN diode of the top ring is different with that of the bottom ring, the phase of Z_2 and that of Z_1 are different as well. As a result, the phase of the induced current on the diagonal of the top ring is different compared to the bottom ring. As the phase difference exists, when the induced currents on the diagonals of the polarizer could have 90^0 degree at some frequency point, the polarizer could generate CP wave in the far field.

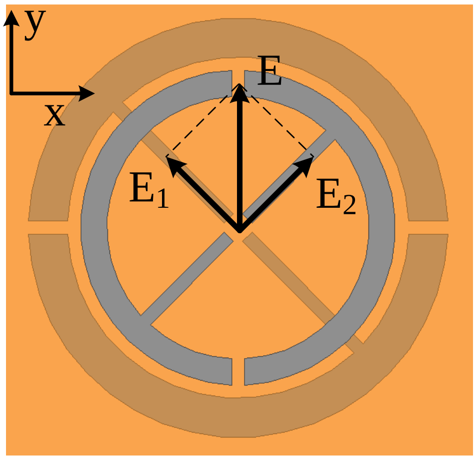

Figure 3-3 E-field and its components E_1 and E_2

Figure 3-4 shows the current distributions on diagonals of the polarizer when the presented antenna works as an LHCP or RHCP antenna. In the case of LHCP radiation, it can be seen that the amplitude of the current on the diagonal of the bottom ring reaches maximum while the current on diagonal of the top ring reaches minimum when t=0. When t=T/4, the maximum current amplitude is observed on diagonal of the top ring. It indicates that there is a 90^0 phase difference between current on top ring diagonal and that on bottom ring diagonal.

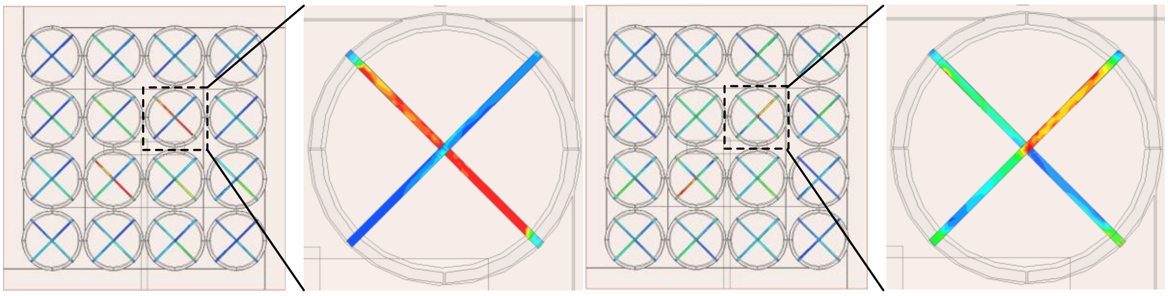

(a) t=0, LHCP (b) t=T/4 , LHCP

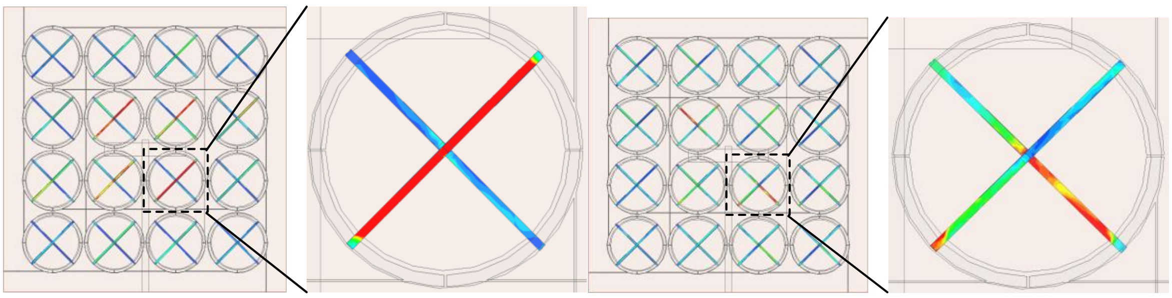

(c) t=0, RHCP (d) t=T/4, RHCP

Figure 3-4 Current on diagonals of the polarizer for LHCP and RHCP

3.1.2.2 Gain enhancement

One of the advantages of using EPRP is that it can improve the gain of the antenna. The reason is that the current distribution is more average after introducing EPRP. Figure 3-5 shows the current distributions of a slot antenna and the proposed antenna when it works as an RHCP antenna. For the slot antenna in Figure 3-5(b), it can be observed that the current mainly distributes around the slot. For the proposed antenna in Figure 3-5(a), the current covers the whole aperture of the antenna. So the EPRP enlarges the effective aperture of the antenna, thus enhancing the gain.

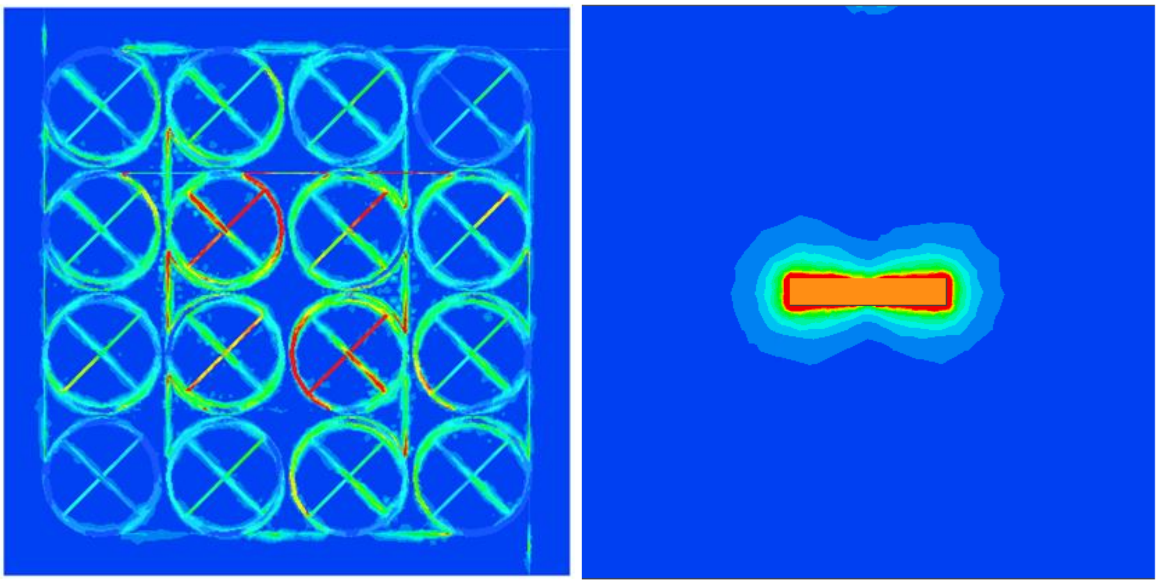

(a) (b)

Figure 3-5 Current distributions of (a) the proposed antenna and (b) a slot antenna

3.1.2.3 Parametric Study

In this subsection, some important parameters of the proposed antenna are discussed. The following parameters are studied when the antenna works as an RHCP antenna. Figure 3-6(a) shows the effect of *h* on the AR of the antenna. When *h* increases from 6.7 mm

(0.056λ$_0$) to 9.7 mm (0.081λ$_0$), the center frequency of the ARBW (AR≤3dB) decreases from 2.55 GHz to 2.4 GHz, which makes it convenient to adjust the center frequency of ARBW. However, with *h* increasing, the AR deteriorates, and the ARBW becomes narrower.

The effect of $C_{0\text{-}off}$ of the PIN diode is also studied. $C_{0\text{-}off}$ is the capacitance of the PIN diode when it is OFF. Figure 3-6(b) shows that the ARBW (AR≤3 dB) of the antenna becomes narrower (from about 150 MHz to 100 MHz) when the value of $C_{0\text{-}off}$ varies from 0.16uF to 0.20uF. The AR also deteriorates when $C_{0\text{-}off}$ goes up. It indicates that it is better to choose PIN diodes with smaller $C_{0\text{-}off}$ to design the presented antenna.

The AR with different values of the radius of the top ring *Rt* is demonstrated in Figure 3-6(c), and that of the bottom ring *Rb* is given in Figure 3-6(d). It can be seen the effect of *Rt* and *Rb* is similar to that of *h*. When *Rt* increases from 13mm to 13.15mm, the center frequency of the ARBW decreases from 2.55 GHz to 2.45 GHz. When *Rb* increases from 13mm to 13.15mm, the center frequency of the ARBW decreases from 2.55 GHz to 2.475 GHz. Moreover, the increase of *Rt* and *Rb* does not lead to the AR deteriorating. Therefore, *Rt* and *Rb* are used to adjust the working frequency of the antenna in the designing.

The effects of the parameters of the antenna operating as an LHCP antenna are similar to those of the antenna operating as an RHCP antenna.

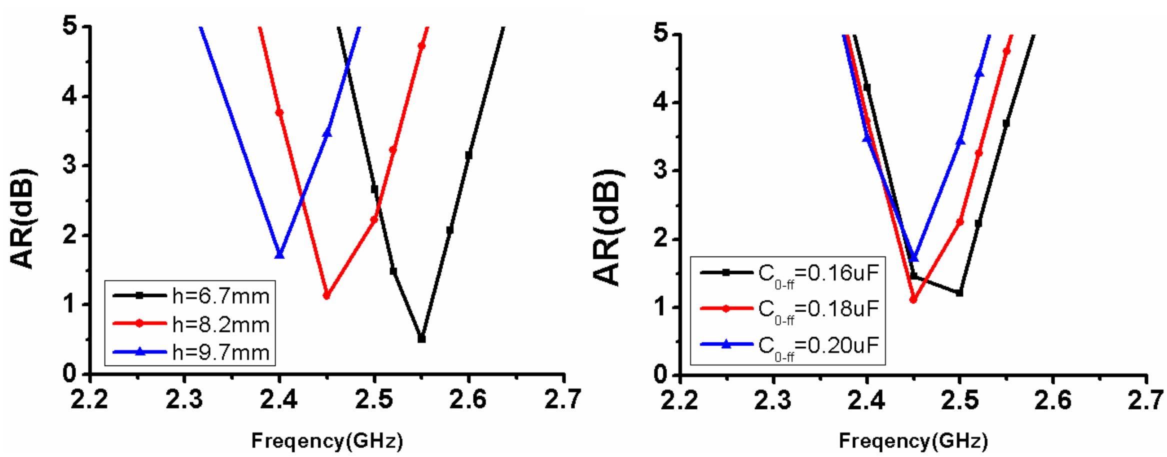

(a) (b)

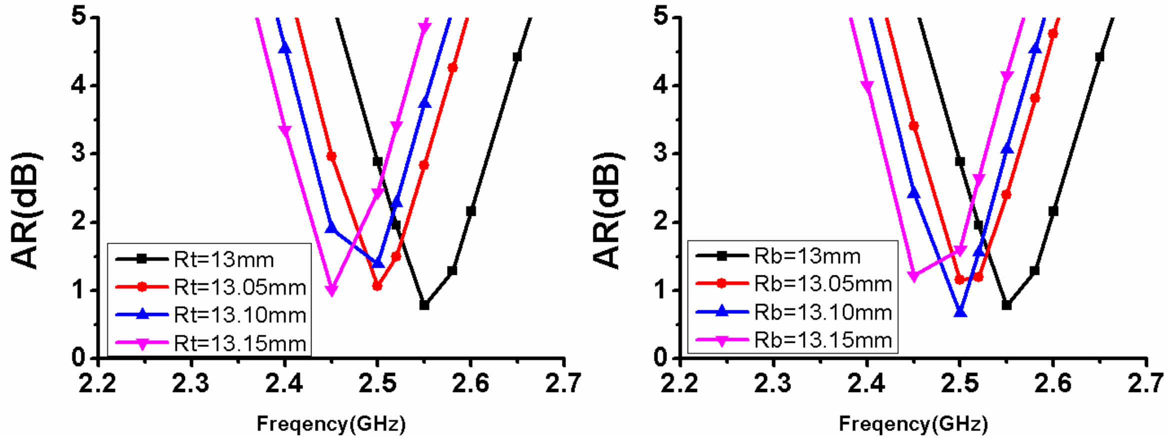

(c) (d)

Figure 3-6 Simulated AR with different (a)*h*, (b)$C_{0\text{-}off}$, (c)*Rt*, (d)*Rb*

3.1.3 Simulated and Measured Results

The polarization-reconfigurable CP antenna is simulated Computer Simulation Technology Microwave Studio. It is optimized by sweeping parameters in the simulation. Then a prototype of the antenna is fabricated, and it is measured. The photos of the fabricated antenna are shown in Figure 3-7.

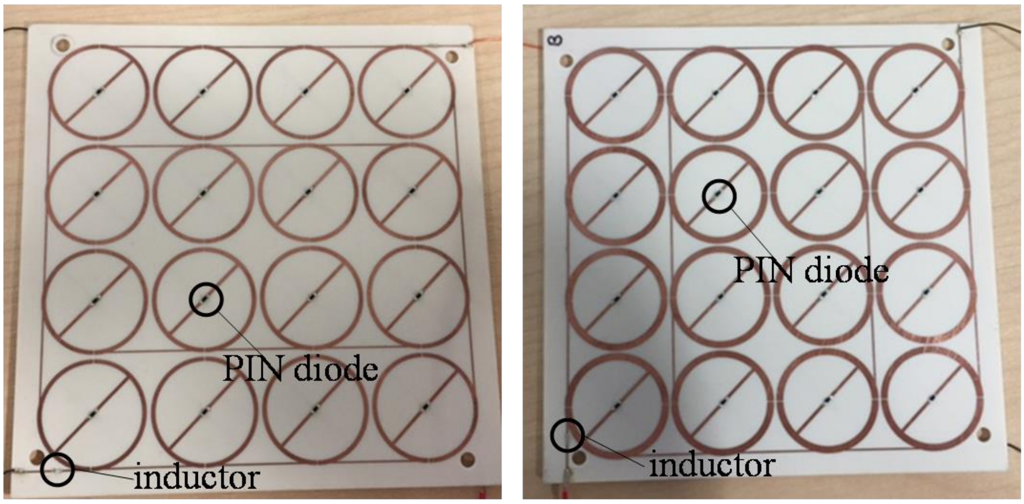

(a) (b)

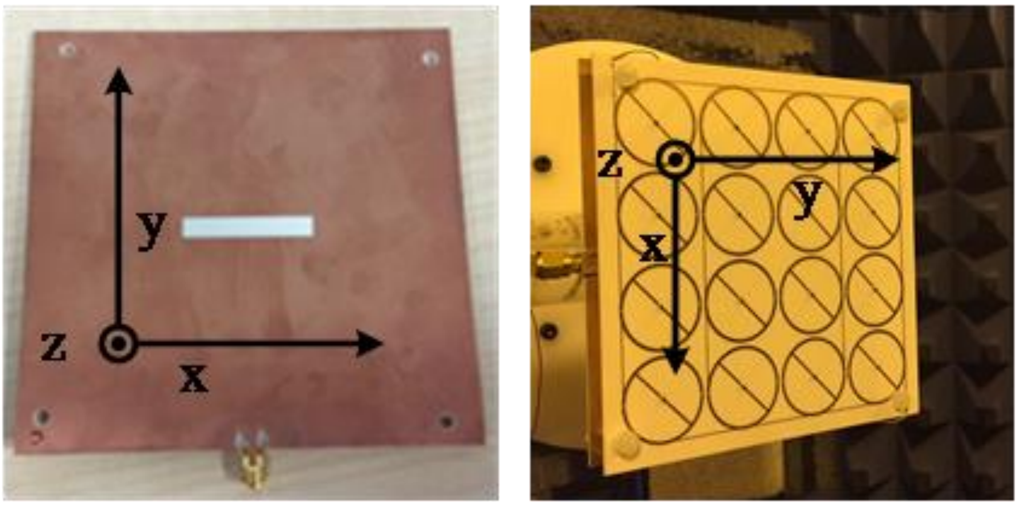

(c) (d)

Figure 3-7 (a)Top side of the polarizer, (b)bottom side of the polarizer, (c)the slot antenna and (d)side view of the polarization-reconfigurable CP antenna

3.1.3.1 Simulated and Measured Results of the polarization-reconfigurable CP Antenna

The simulated and measured $|S_{11}|$ are shown in Figure 3-8 for both RHCP and LHCP. It can be observed that the simulated and measured results agree well. For LHCP, the resonant frequency is 2.5 GHz. The measured $|S_{11}|$ band ($|S_{11}|\leqslant$-10 dB) is from 2.3 GHz to 2.63 GHz, which is slightly narrower than the simulated result, from 2.27 GHz to 2.69 GHz. For RHCP, the resonant frequency is 2.475 GHz, 25 MHz lower than that of LHCP. The measured $|S_{11}|$ band ($|S_{11}|\leqslant$-10 dB) is from 2.27 GHz to 2.65 GHz, which is also narrower than the simulated result. The overlapped impedance bandwidth for both polarizations is from 2.3 GHz to 2.63 GHz. The difference between simulated and measured results is mainly caused by the tolerance of fabrication accuracy.

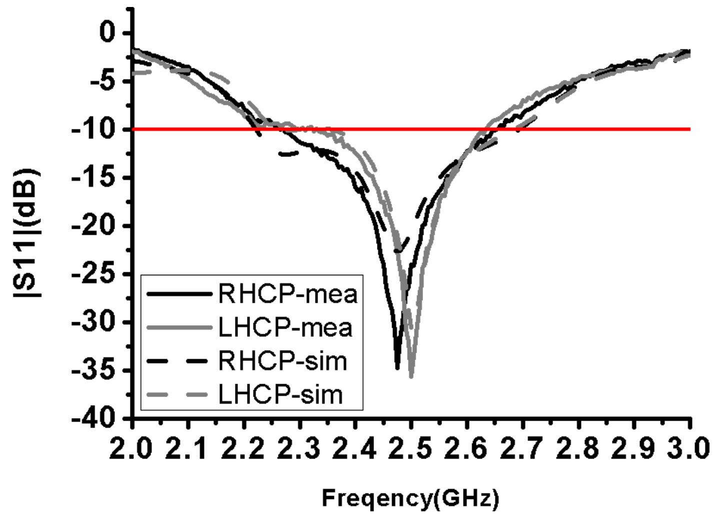

Figure 3-8 Simulated and measured $|S_{11}|$ for RHCP and LHCP

Figure 3-9 shows the simulated and measured AR of the antenna at broadside. In the simulation, the ARBW (AR≤3dB) is from 2.42 GHz to 2.52 GHz for RHCP and from 2.45 GHz to 2.56 GHz for LHCP. The measured ARBW (AR≤3dB) of the RHCP antenna is 90MHz (3.6%), from 2.48 GHz to 2.57 GHz while that of the LHCP antenna is 110MHz (4.3%), from 2.53 GHz to 2.64 GHz. Therefore, the overlapped ARBW of the antenna is from 2.53 GHz to 2.57 GHz (1.6%). It can be seen that the measured ARBW shifts to a higher frequency for both the RHCP antenna and the LHCP antenna. As the ARBW of the proposed antenna is narrow, it can only be used in some narrow band applications, for example, fixed (point-to-point) communications. The narrow bandwidth is mainly limited by the EPRP. Using multi-layer substrates to design the EPRP may increase the band-width, but it also increases the complexity of the antenna.

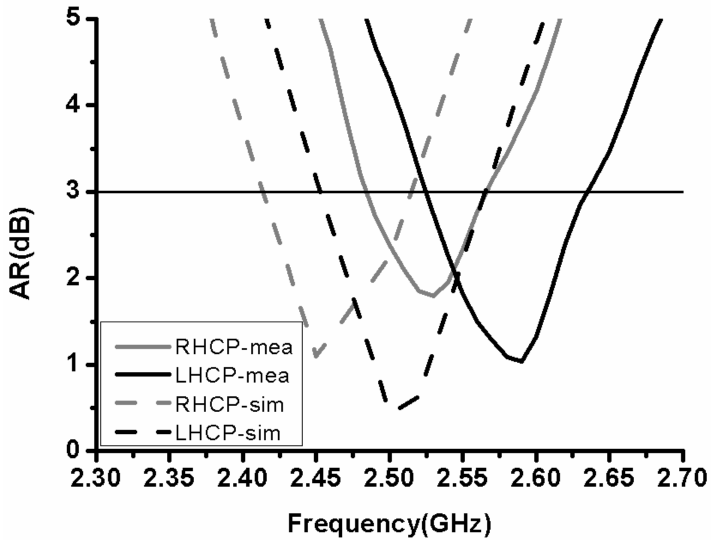

Figure 3-9 Simulated and measured AR of the antenna

As discussed above, the center frequency of the ARBW can be tuned to lower frequency by increasing *h*. The effect of *h* on AR is also investigated during the measurement. Figure 3-10 shows the measured AR with different values of *h*. For the LHCP antenna, when *h* increases from 6.5mm to 8.2mm, the center frequency of the ARBW decreases from 2.65 GHz to 2.59 GHz, and the AR does not deteriorate. However, if *h* increases from 8.2mm to 9.5mm, the AR deteriorates and the minimum value of the AR increases from below 1dB to above 2dB. The effect of *h* on the AR of the RHCP antenna is similar to that of the LHCP antenna. It reveals that *h* cannot be too large although it can adjust the center frequency of the ARBW.

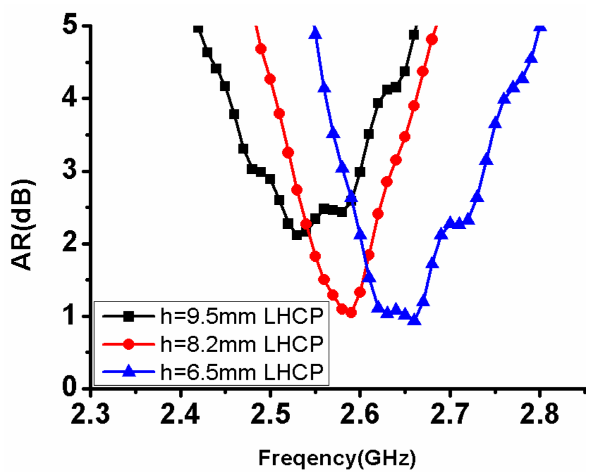

(a) LHCP

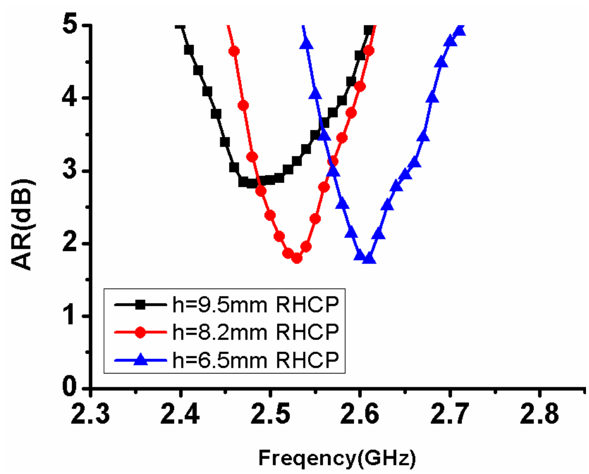

(b) RHCP

Figure 3-10 Measured AR with different values of *h*

Figure 3-11 shows the normalized radiation patterns of the RHCP antenna and the LHCP antenna in YOZ plane. As the center frequency shifts to a higher frequency in the measurement, the simulated patterns in Figure 3-11 are at 2.5 GHz, and the measured patterns are at 2.55 GHz. It can be seen that there is a good agreement between the simulated and measured results.

Figure 3-12 shows the simulated and measured gains from 2.45 GHz to 2.6 GHz. The gain of the slot antenna without EPRP is also shown in Figure 3-12. It can be seen the gain of the slot antenna is enhanced significantly by the EPRP. The fluctuation of the measured gain with frequency comes from the measurement tolerance and the fabrication inaccuracy. For both RHCP and LHCP, the measured gain is higher than 8.6 dBic from 2.45 GHz to 2.6 GHz. The maximum gain achieves 9.6 dBic from 2.53 GHz to 2.57 GHz where the antenna can work either as an RHCP antenna or an LHCP antenna. Some comparisons between the presented antenna and other reported polarization-reconfigurable CP antennas are given in Table 3-2. The overlapped bandwidth in Table 3-2 means that in this band, the antenna could work both in LHCP and RHCP. Compared with the antennas reported in [179, 182-193], which are not easily extended to an array antenna, the presented antenna achieves the highest aperture efficiency. When the antenna works at 2.53 GHz, the gain is higher than 9.5 dBic, and the aperture efficiency is 70%.

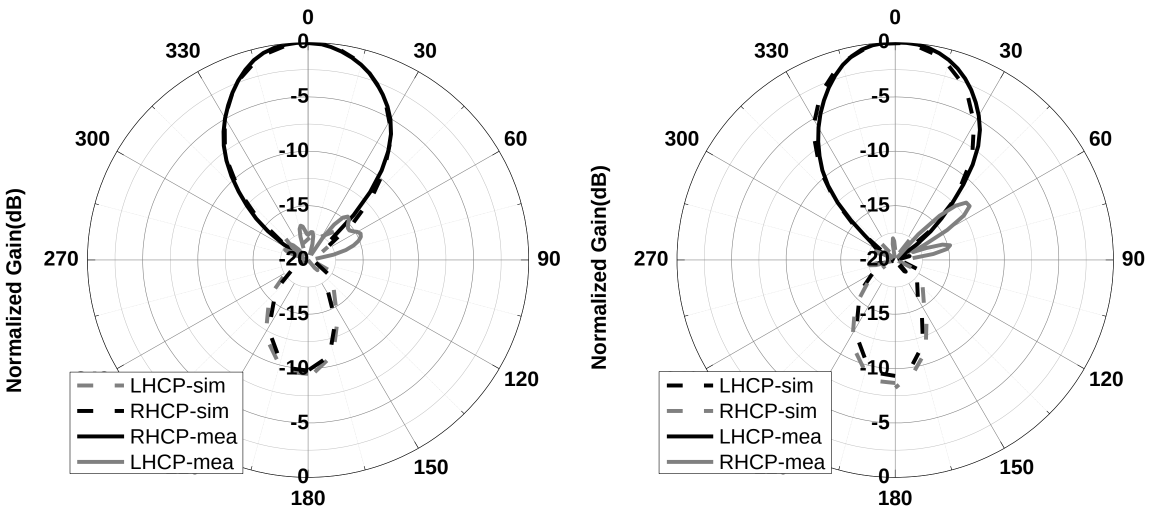

(a) RHCP (b) LHCP

Figure 3-11 Simulated and measured radiation patterns of the antenna in YOZ plane

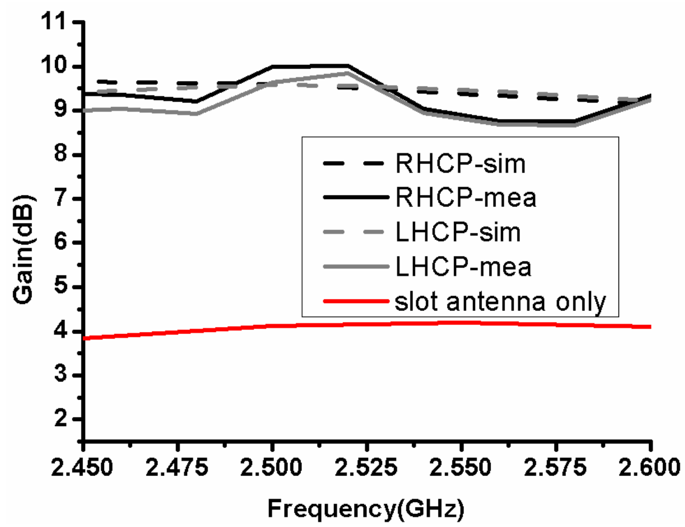

Figure 3-12 Gain of the slot antenna with and without EPRP.

Table 3-2 Comparison with Other Antennas

Ref. No.	Method to realize polarization reconfiguration	Center frequency (GHz)	Overlapped bandwidth	Dimension(mm)	Max gain (dBic)	Aperture efficiency	Electronically controlled	Extend to an array
[180]	Adding PIN diodes to feed slot	5	4%	13.5×18×3.8	5.5	-	Yes	hard
[181]	Controlling the structure of feed networks based on CPW	5.8	0.7%	Not given	6.02	-	Yes	hard
[182]	Using PIN diodes to change the structure of feed networks	2.45	Not given	42.5×42.5×2.6	5	-	Yes	hard
[183]	Adding PIN diodes to feed networks of corners truncated patch antenna	2	8.6%	150×150×16.6	7	-	Yes	hard
[184]	Exciting antenna with different input port	2.68	1.3%	80×60×3.6	8	-	No	hard
[187]	Changing input port	4.02	Not given	140×140×3	8.68	-	No	hard
[188]	Adding PIN diodes to slot on patch antenna	4.55 &4.20	0%	60×60×3.18	Not given	-	Yes	hard
[189]	Same with [187]	4.64	2.7%	40×40×3.18	Not given	-	Yes	hard
[190]	Using PIN diodes to change geometry of ring slot antenna	2.38	3.4%	Not given	4	-	Yes	hard
[191]	Using PIN diodes to change geometry of corners truncated patch antenna	1.6	1.5%	225×225×1.6	5.3	-	Yes	hard
[192]	Changing distance	5.82	0.7%	Not	5.4	-	Yes	hard

	between antenna and dielectric perturbers			given				
[193]	Using PIN diodes to change the slot distribution on ground	2.49	1.2%	Not given	2.97	-	Yes	hard
[179]	rotating the metasurface above the source antenna	3.5	11.4%	π×39×39×not given	7	61%	No	hard
Proposed antenna	Using polarizer loaded by PIN diodes	2.55	1.6%	120×120×10.5	9.6	70%	Yes	easy

3.1.3.2 Array Antenna Study

As mentioned in Section I, this polarization-reconfigurable CP antenna can be easily extended to a large-scale array antenna. Considering the size of the proposed antenna and avoiding grating lobes, the proposed antenna can only be extended to broadside radiating arrays and arrays with small scanning angle. To prove this, a 2×2 array antenna is designed and simulated in this section. Figure 3-13 shows the structure of the EPRP of the array antenna. It can be seen that the positions of DC feed points do not change when the antenna is extended to a 2x2 array antenna. Thus, a $2^n \times 2^n$ array antenna can be obtained by scaling from the 2x2 array antenna in the same way. Here, the 2×2 array antenna is shown to demonstrate the scalability of the presented design. When the presented antenna is used as the unit cell to design an array antenna, only minor modifications to the DC bias circuit are required, which is one of the main advantages of the presented design.

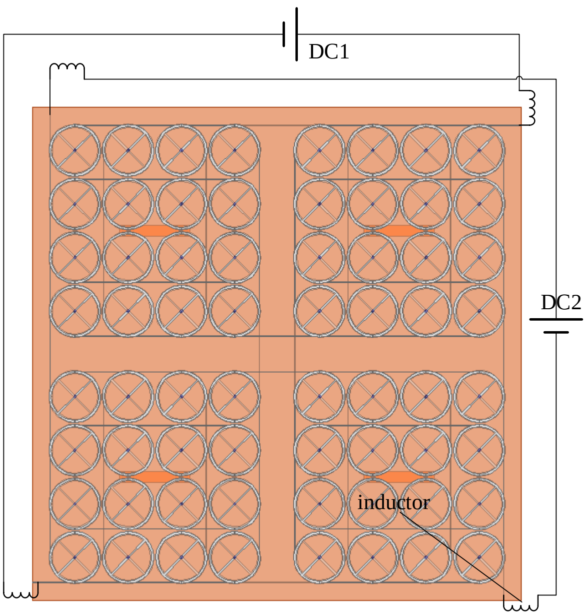

Figure 3-13 Structure of EPRP of array antenna.

All the DC circuits have been considered during the EM simulation. The polarization is still controlled by two pairs of DC lines. When the PIN diodes of the top rings are ON, the array antenna works as an LHCP antenna; when the PIN diodes of the bottom rings are ON, the array antenna works as an RHCP antenna.

Figure 3-14 shows the simulated AR of the 2×2 array antenna at broadside. It is shown in Figure 3-15 that the gain of the array antenna is about 6 dB higher than that of the proposed antenna, which agrees well with the theoretical results. Figure 3-16 shows the simulated and calculated radiation patterns of the array antenna at 2.5 GHz. The calculated patterns are from pattern multiplication for an array antenna. The simulated and calculated patterns agree well, indicating that the minor modifications to bias circuit have little effect on the radiation patterns of the array antenna.

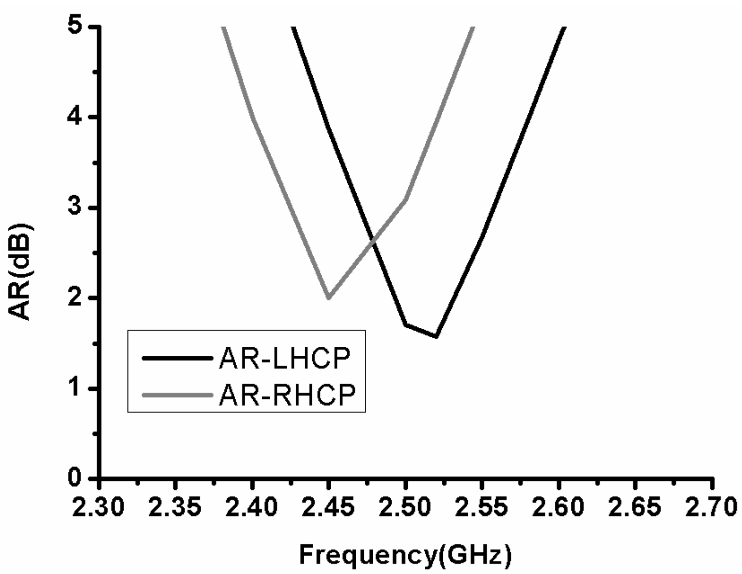

Figure 3-14 Simulated AR of the array antenna

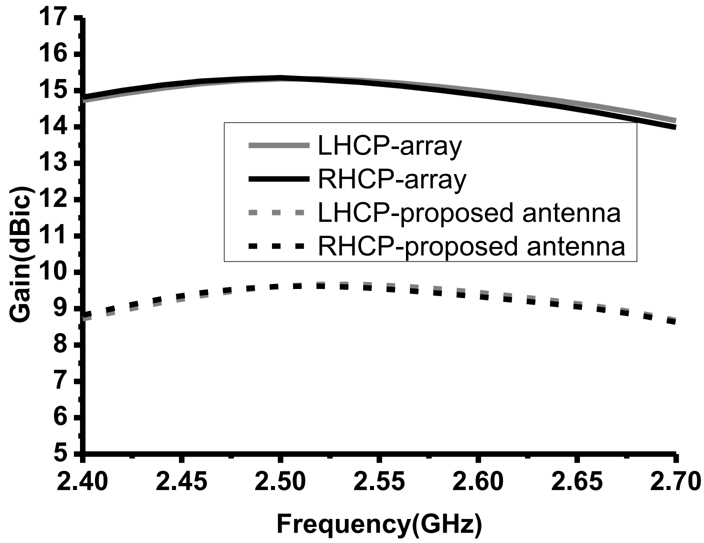

Figure 3-15 Simulated gain of the proposed antenna and array antenna

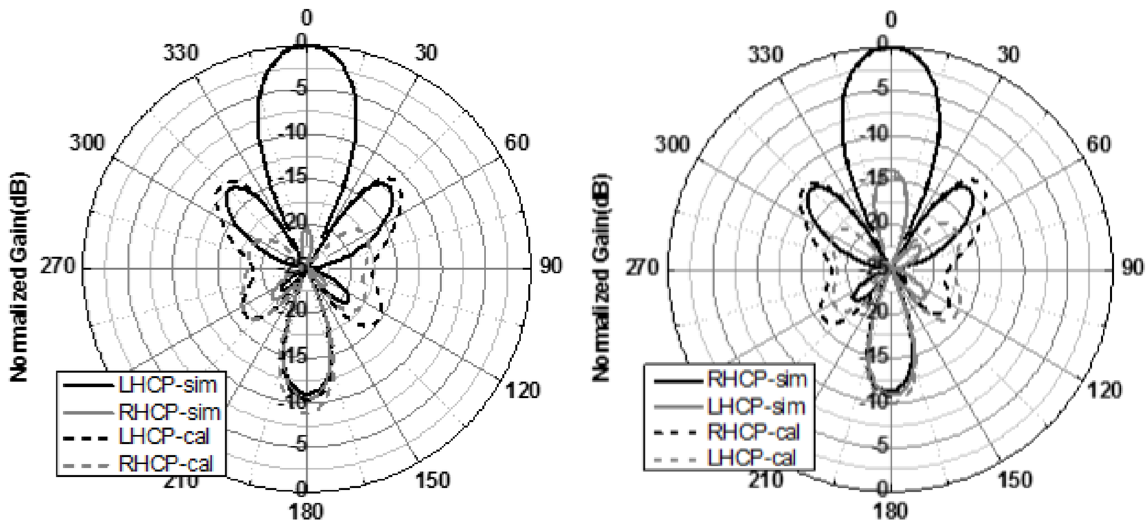

(a) LHCP (b) RHCP

Figure 3-16 Radiation patterns of the array antenna in XOZ plane

3.1.4 Summary

A novel polarization-reconfigurable CP antenna consisting of a polarizer and a slot antenna is presented. The polarization of the antenna can be electronically switched to LHCP or RHCP by changing the states of PIN diodes on the polarizer. Moreover, it is demonstrated that the design is scalable to large-scale array antennas with minor modifications to the DC bias circuit. To prove the design concept, a prototype at 2.5 GHz is fabricated and measured. The measured results and simulated results agree well. The measurement results show that the ARBW of the LHCP antenna is from 2.48 GHz to 2.57 GHz (3.6%) while that of the RHCP antenna is from 2.53 GHz to 2.64 GHz (4.3%). The overlapped ARBW is from 2.53 GHz to 2.57 GHz (1.6%). The gain of the antenna is above 8.5 dBic for both polarizations in the working band, and the highest aperture efficiency of 70% is obtained. As the ARBW of the proposed antenna is narrow, it can be used in some narrow band applications, for example, point-to-point communications. If the ARBW of the proposed antenna becomes wider, it can be applied in more applications, for instance, satellite applications. So broadening the ARBW without making the antenna more complex can be a research target in the future.

3.2 Folded Circularly Polarized Reflectarray Antenna

Circularly polarized reflectarray antennas are widely used in wireless communication systems. Many CP reflectarray have been reported in [195-200].

For linearly polarized reflectarray antennas, folded reflectarray antennas are proposed to reduce the profile of reflectarray antennas. However, no such techniques are applied in circularly polarized reflectarray antennas to decrease the profile. Although the authors in [198] try to reduce the profile of a CP reflectarray, the results are not perfect. The author placed a polarizer above a folded LP reflectarray to obtain a CP reflectarray. But the thickness of the polarizer is larger than $0.8\lambda_0$, which leads to that the profile reduction of the entire antenna is limited.

In this section, a folded CP reflectarray antenna using a circular polarization selective surface (CPSS) is proposed. By introducing the CPSS, the profile of the CP reflectarray could be reduced by about 87%.

3.2.1 Antenna Working Mechanism

The folded CP reflectarray antenna consists of a feed antenna, a CPSS and a reflecting surface. The CPSS would reflect left-hand circularly polarized (LHCP) EM waves completely and allow right-hand circularly polarized (RHCP) EM waves to pass without loss. When the LHCP waves are reflected by the CPSS, the polarization does not change, which is different from LHCP waves impinging a metal surface.

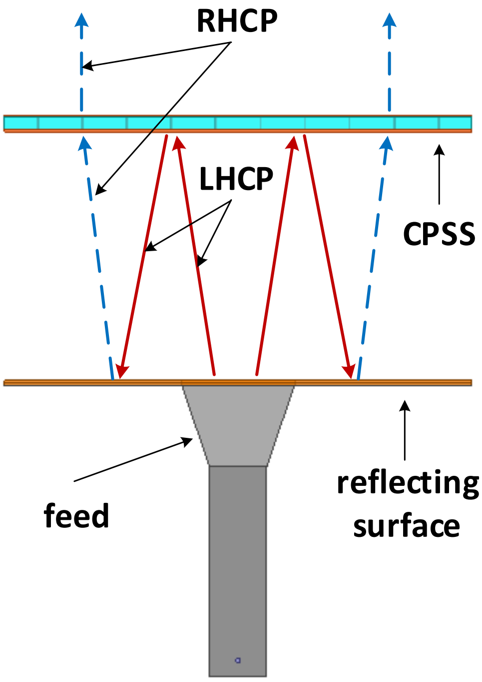

Figure 3-17 Configuration of the folded CP reflectarray antenna

Figure 3-17 shows the configuration of the folded CP reflectarray antenna. The LHCP waves generated by the feed antenna impinge the CPSS. Then, the waves are reflected by the CPSS and keep the polarization unchanged, which results from the feature of the CPSS. This means the reflected waves are still LHCP waves. After being reflected by the CPSS, the waves are reflected by the reflecting surface again. As the reflecting surface is composed of stacked square patches, the reflection from the reflecting surface converts the LHCP waves to RHCP waves. Finally, the RHCP waves can go through the CPSS directly and form beams in free space. The simulated results below will show the characters of the CPSS and the reflecting surface.

3.2.2 Design of the Element of CPSS

The element of the CPSS is the Pierrot structure, which is shown in Figure 3-18. The element contains two substrates (Rogers RO4003C) and an air gap. One rectangular metal arm is printed on the top surface of the substrate A while the other metal arm is printed on the bottom surface of the substrate B. The two arms are placed perpendicularly. The two metal arms are connected by a metal cylinder of which the radius is 0.4 mm. Other parameters are swept in simulation, which are shown in Table 3-3. Table 3-3 is obtained by sweeping parameters in simulation.

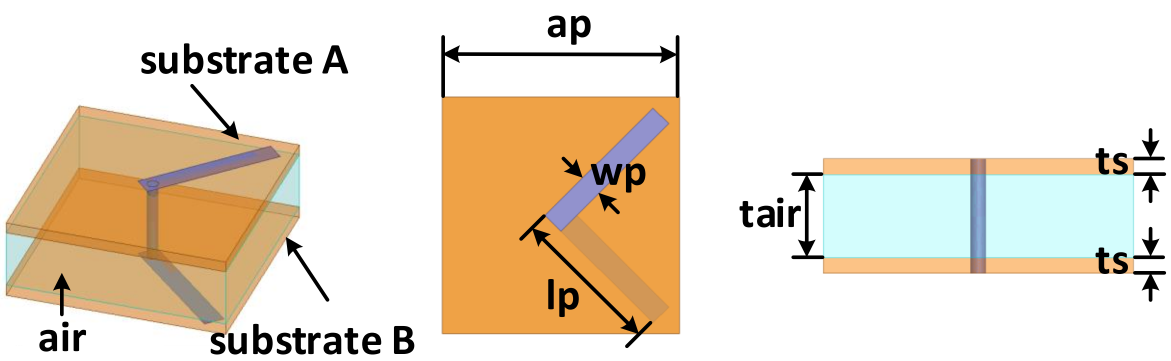

Figure 3-18 Side, top and right views of the elements of the CPSS

Table 3-3 Parameters of the Element of the CPSS (unit: mm)

ap	*lp*	*wp*	*ts*	*tair*
16	10.25	1.5	0.813	4.3

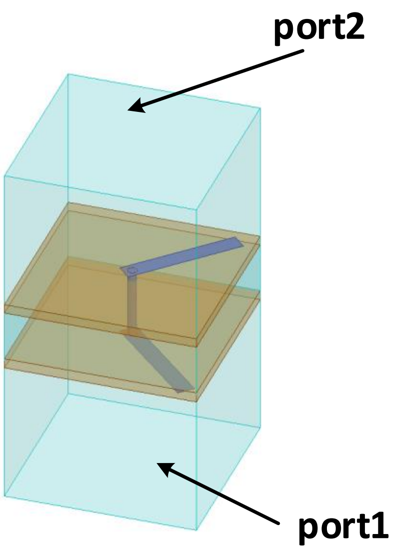

Figure 3-19 Model of elements of CPSS in simulation under periodic boundary condition

Figure 3-19 shows the model of element in the simulation.

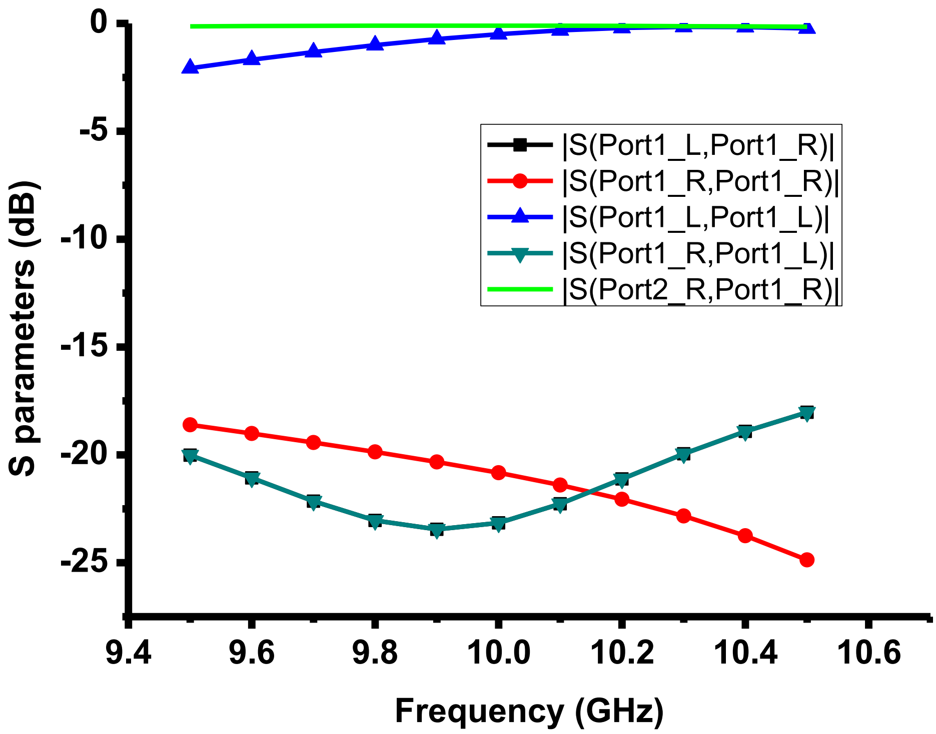

Figure 3-20 Simulated S parameters of the element of CPSS

Simulated scattering parameters of the element of the CPSS are shown in Figure 3-20, which are calculated according to the results in HFSS. |S(Port1_L,Port1_L)|, which is above -0.5 dB at 10 GHz, shows that the LHCP waves from port 1 are reflected by the element of the CPSSS at 10 GHz. |S(Port1_R,Port1_R)| is below -17 dB, and |S(Port2_R,Port1_R)| is above -0.1 dB, which means that the element of the CPSS is nearly transparent to RHCP waves. |S(Port1_L,Port1_R)| and |S(Port1_R,Port1_L)| are both below -20 dB at 10 GHz, which reveals that LHCP and RHCP waves are isolated well. Figure 3-21 shows |S(Port1_L,Port1_L)| when the incident angle of LHCP waves changes.

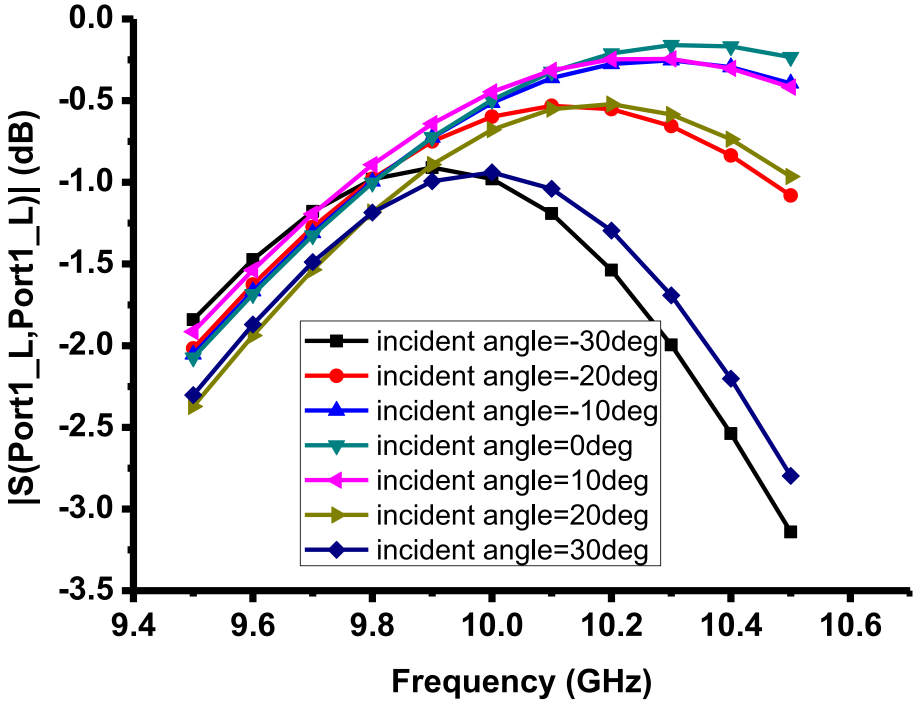

Figure 3-21 |S(Port1_L,Port1_L)| with different incident angles

3.2.3 Design of Reflectarray Element

The stacked square patch is used as the element of the reflectarray antenna. The configuration of the element is shown in Figure 3-22.

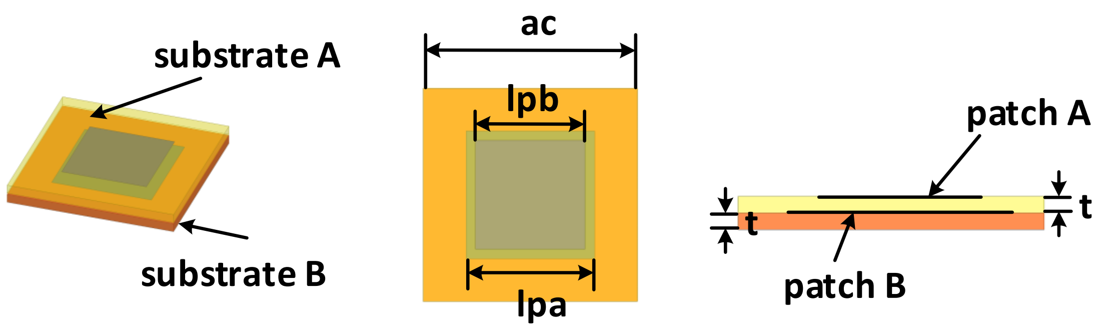

Figure 3-22 Side, top and right views of the elements of the reflectarray

The element consists of two square patches. The smaller patch is printed on the top surface of the substrate A, and the patch with the larger size is printed on the top surface of substrate B. Substrate A and Substrate B are both Rogers RO4003C. The parameters of the element of the reflectarray element are swept in simulations and shown in Table 3-4.

Table 3-4 Parameters of the Element of the Reflectarray (unit: mm)

ac	lpb	ts
10.5	lpa×0.8	0.813

The phase of the reflection coefficient of the element is controlled by the length of the sides of the patch B. The simulated phase shift of the element is shown in Figure 3-23. The phase shift range is from 150 to -217 degree. As the stacked patch is applied in the design of the element, the phase shift range of the element is over 360 degree, which can satisfy the requirement of the reflectarray.

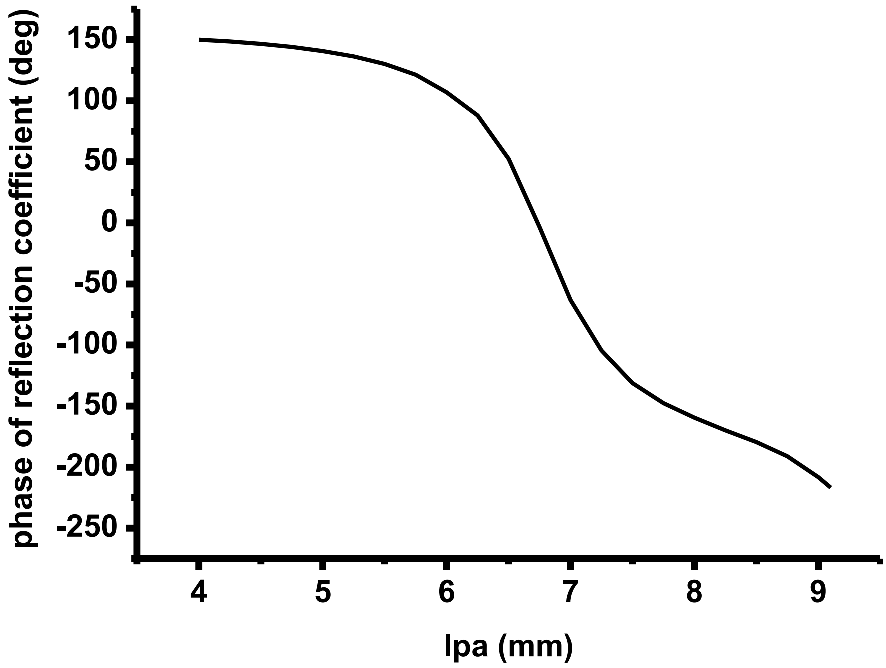

Figure 3-23 Phase of the reflection coefficient of the reflectarray element

3.2.4 Design of Feed Antenna

The feed antenna of the reflectarray is a horn antenna with left-hand circular polarization. The horn antenna is fed by a coaxial cable. The inner conductor of the coaxial cable inserts the horn by 6.55 mm. Other parameters of the horn antenna are shown in Table 3-5. The parameters of the horn are swept in simulations to get better AR.

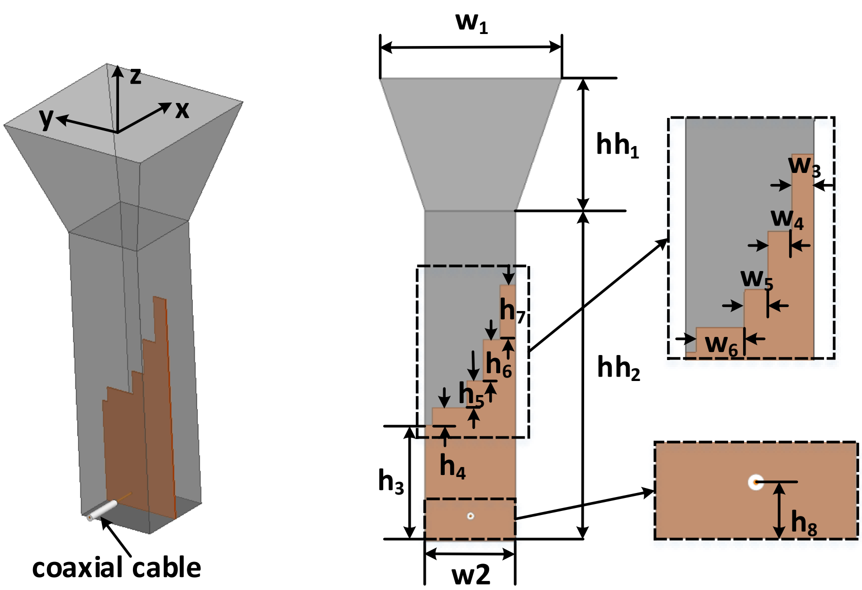

Figure 3-24 Configuration of the feed antenna

Table 3-5 Parameters of the Feed Antenna (unit: mm)

w_1	w_2	w_3	w_4	w_5
41	20.5	3.6	3.8	3.7
w_6	hh_1	hh_2	h_3	h_4
7.8	30	75	26.4	3.9
h_5	h_6	h_7		
6.2	9.3	12.3		

The simulated |S11| of the horn antenna is shown in Figure 3-25. It can be seen the |S11| is below -14 dB from 9.7 to 10.3 GHz. A metal ridge is added in the horn antenna to generated CP waves. As the ridge is zigzag, it may lead to that the horn has multiple resonant frequencies, which include 10.1 GHz. That's why there is a sharp fall in Figure 3-25. Figure 3-26 shows the axial ratio (AR) of the feed antenna at φ=0 and θ=0. The AR (φ=0, θ=0) is below 1.1 dB from 9.7 to 10.3 GHz. Figure 3-27 demonstrates the AR of feed antenna in the working band. It can be seen the AR 3 dB beam width is from 50 to 60 degree.

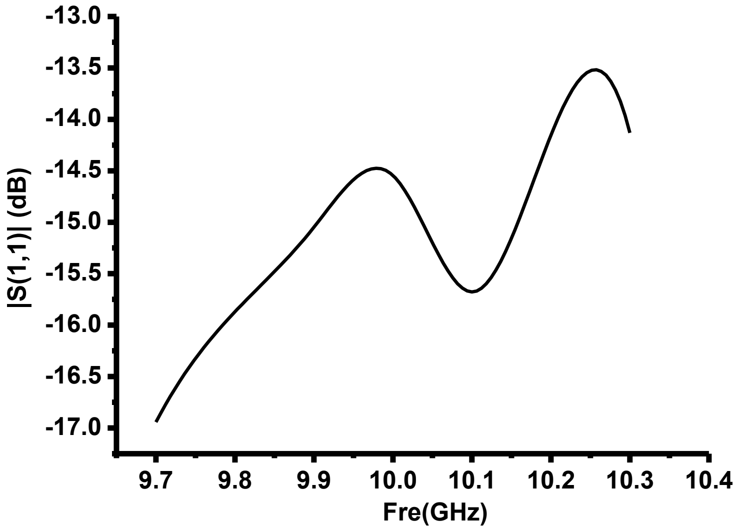

Figure 3-25 Simulated |S11|of the feed antenna

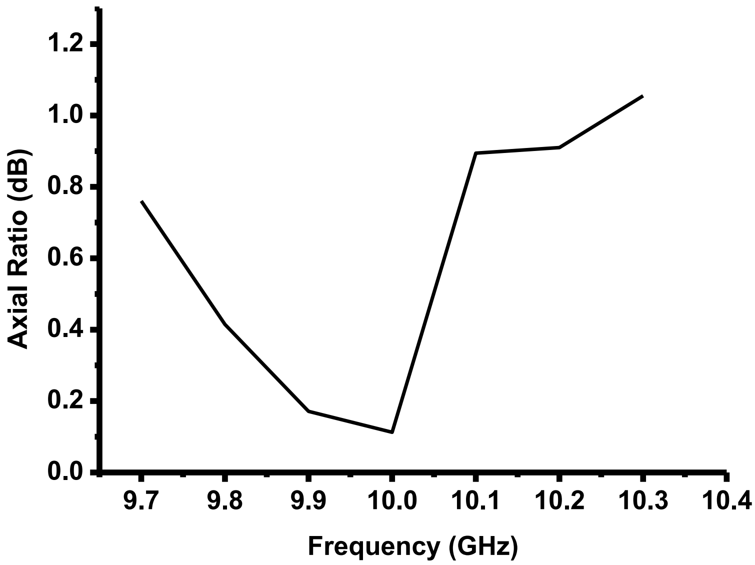

Figure 3-26 Axial ratio (φ=0, θ=0) of the feed antenna

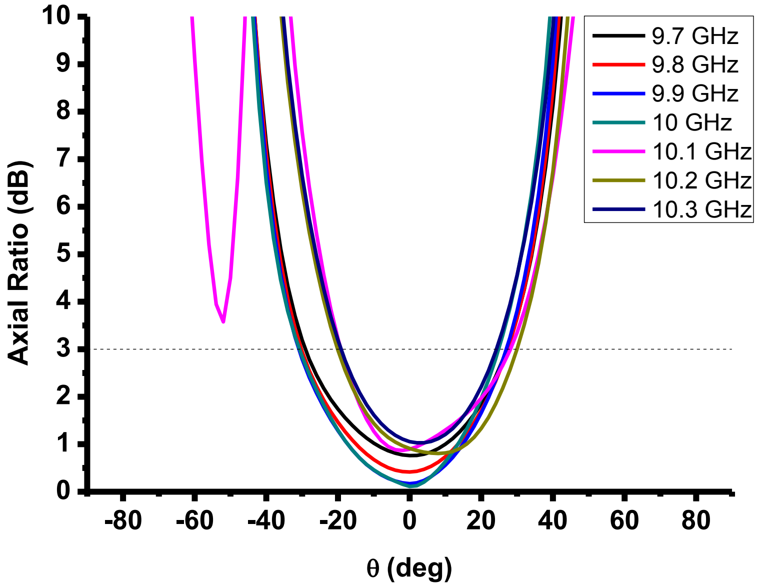

Figure 3-27 Axial ratio of the feed antenna from 9.7 to 10.3 GHz

3.2.5 Design of Reflectarray Antenna with CPSS

Based on the elements of the CPSS and the reflectarray, a folded CP reflectarray antenna working at 10 GHz is proposed. The CPSS of the reflectarray consists of 10×10 elements. The reflecting surface contains 16×16 cells. The feed antenna is an LHCP horn antenna. The distance between CPSS and reflecting surface *h* is 89.1 mm.

The required phase shift for every element on the reflecting surface is demonstrated in Figure 3-28. It should be noted that the results in Figure 3-28 are calculated according to the field results from the simulation of the feed antenna, not from the geometrical optics method of (2-7). According to Figure 3-28, the required *lpa* for every stacked patch on the reflecting surface is calculated via Figure 3-23. Figure 3-29 exhibits the calculated *lpa*. The white square in Figure 3-28 and Figure 3-29 represents the aperture of the feed antenna.

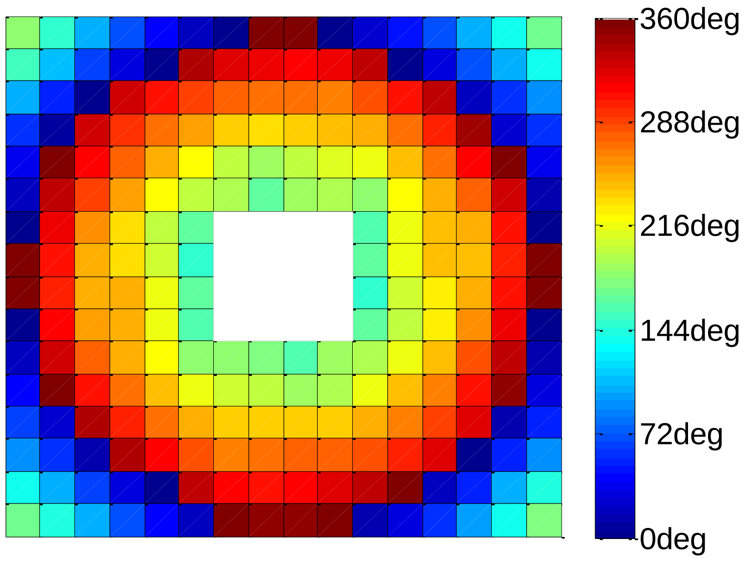

Figure 3-28 Required phase shift for every element on the reflecting surface

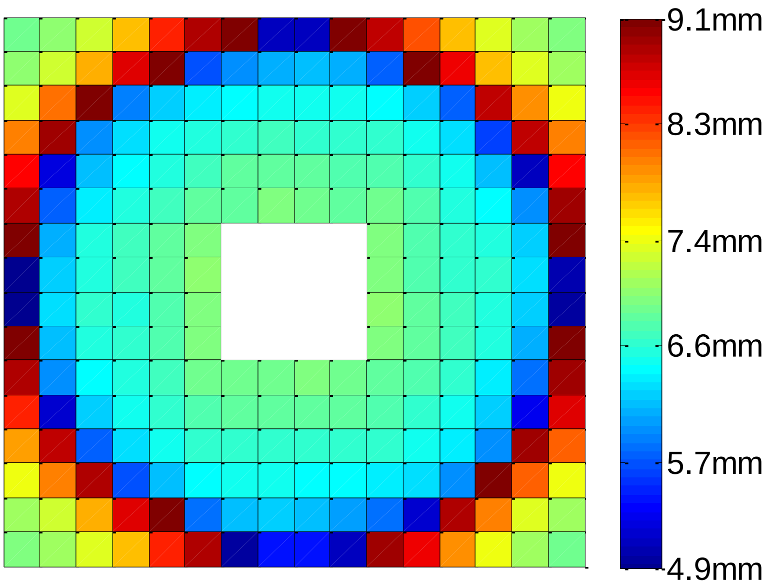

Figure 3-29 Required *lpa* for every element on the reflecting surface

3.2.6 Simulated and Measured Results

The folded CP reflectarray antenna using CPSS is simulated in High Frequency Structure Simulator (HFSS). Then, the prototype is fabricated. Then, the prototype is measured by vector network analyzer. After that, the prototype is placed in an anechoic chamber, and the radiation patterns and gains are measured. Figure 3-30 shows the photograph of the folded CP reflectarray antenna. The simulated and measured results are demonstrated in this subsection as well.

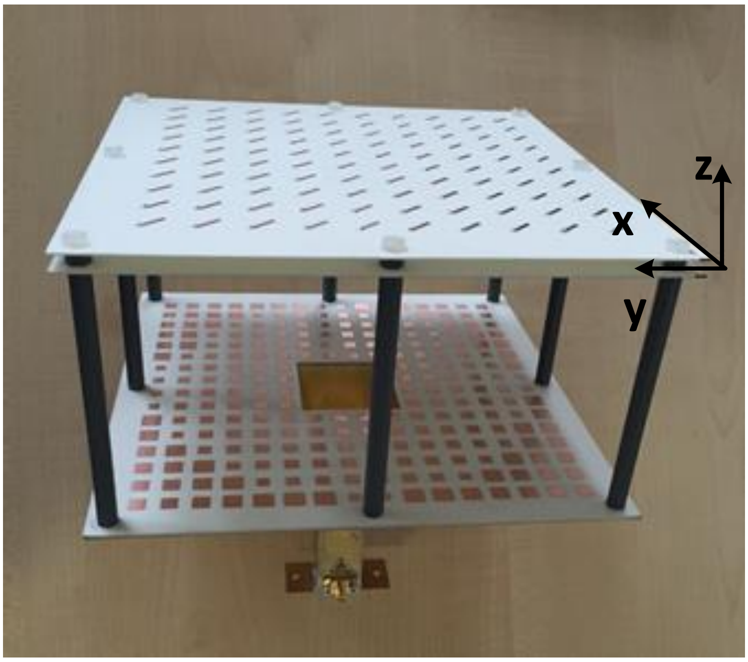

Figure 3-30 Photo of folded CP reflectarray antenna with CPSS

Figure 3-31 shows the simulated and measured reflection coefficient of the folded CP reflectarray. Compared with the |S11| of the horn antenna, the |S11| of the folded CP reflectarray changes a lot due to the existence of CPSS. It can be seen the reflection coefficient is still below -10 dB at 10 GHz.

Figure 3-32 shows the AR of the folded CP reflectarray at broadside in simulation and measurement. It can be seen the measured AR shifts to a lower frequency and deteriorates compared to simulated results. The simulated AR bandwidth (AR≤3 dB) is from 10 to 10.8 GHz, while the measured AR is below 3 dB from 9.8 to 10.6 GHz. The tolerance of fabrication and measurement error may lead to the differences between measured and simulated results.

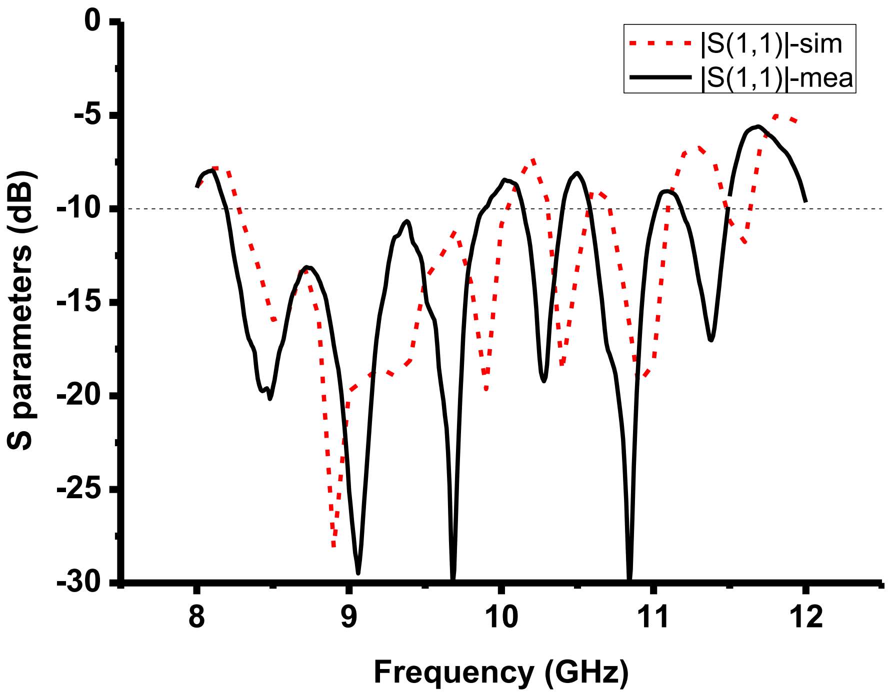

Figure 3-31 Simulated and measured |S11|of the folded CP reflectarray

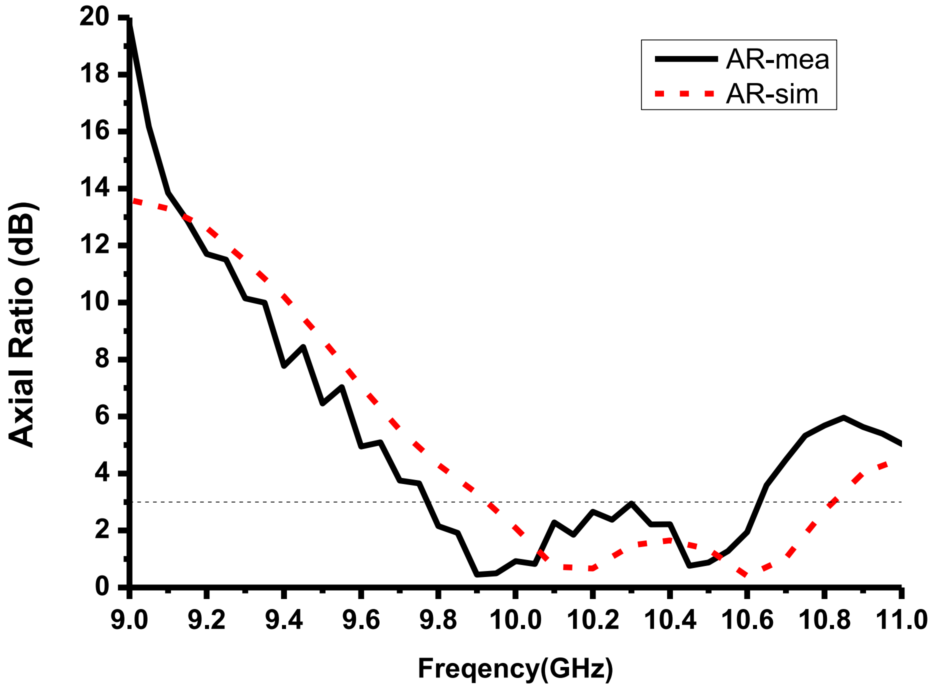

Figure 3-32 Simulated and measured axial ratio at broadside

In Figure 3-32, it is known that the AR of the proposed CP reflectarray is below 3 dB at 10 GHz. Figure 3-33 shows the simulated and measured radiation patterns of the CP reflectarray antenna at 10 GHz. As the measured AR is smaller than the simulated one when the antenna works at 10 GHz, the level of measured LHCP waves is lower than that of simulated LHCP waves. For RHCP waves, the measured side lobe level (SLL) is below -10.8 dB and simulated SLL is below -13.5 dB at 10 GHz. Figure 3-34 and Figure 3-35 show the radiation patterns at 9.9 GHz and 10.1 GHz in $\varphi=0^0$ plane.

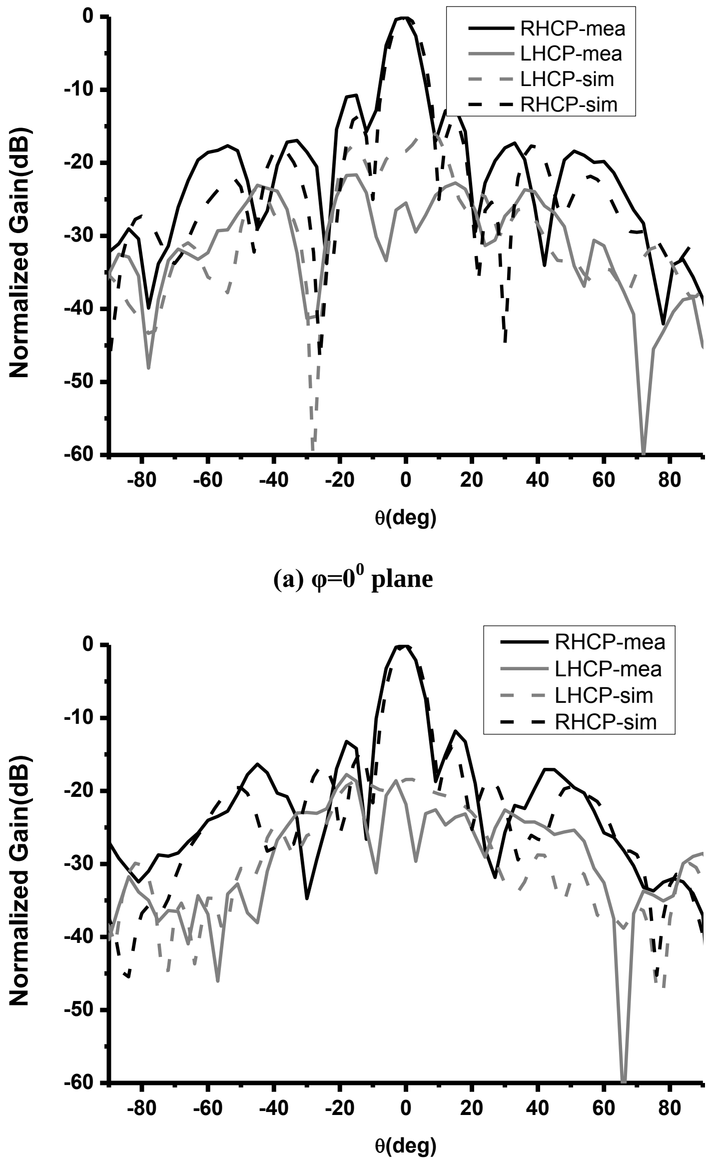

(a) $\varphi=0^0$ plane

(b) $\varphi=90^0$ plane

Figure 3-33 Simulated and measured radiation patterns at 10 GHz

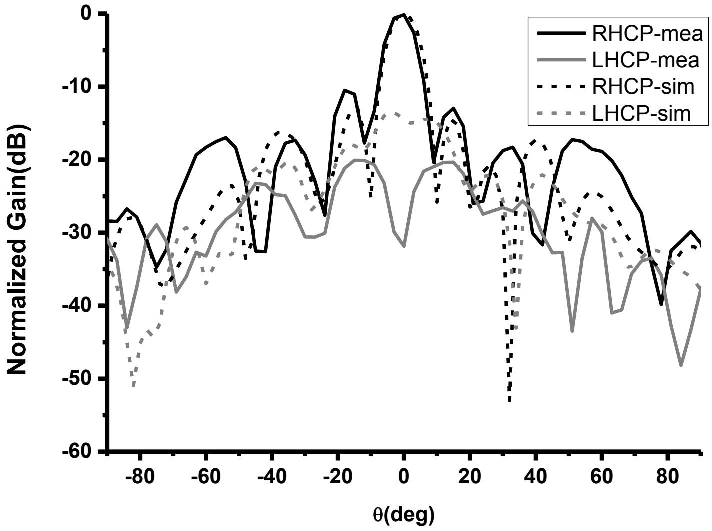

Figure 3-34 Simulated and measured radiation patterns at 9.9 GHz (φ=0^0)

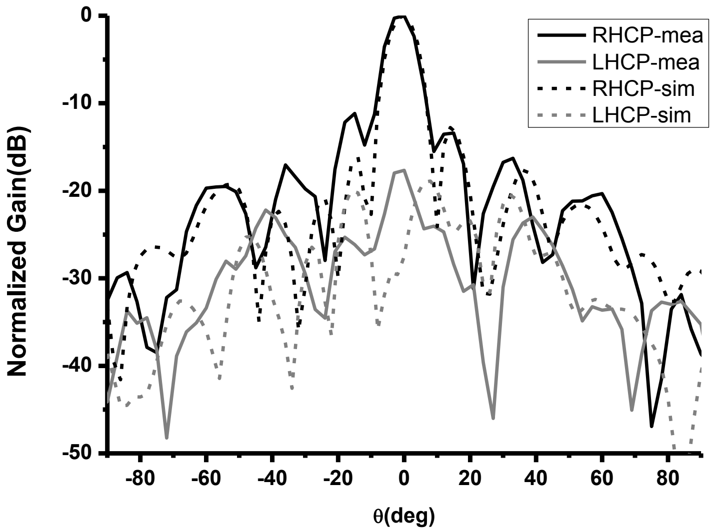

Figure 3-35 Simulated and measured radiation patterns at 10.1 GHz (φ=0^0)

Figure 3-36, Figure 3-37 and Figure 3-38 show the radiation patterns at 9.8, 10.6 and 10.8 GHz. For RHCP waves, it can be seen the main beam is stable and the SLL is below -10 dB at these frequency points.

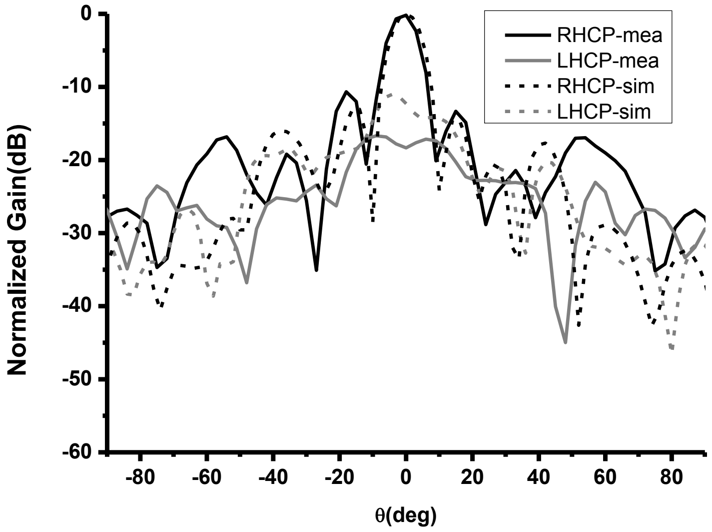

(a) φ=0^0 plane

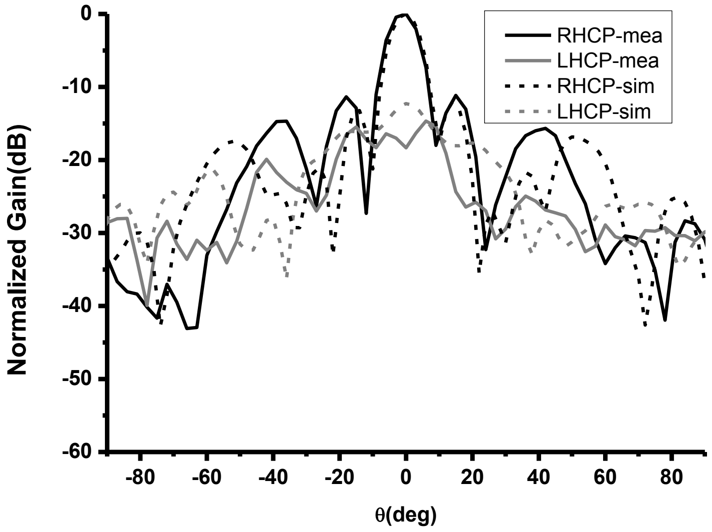

(b) φ=90^0 plane

Figure 3-36 Simulated and measured radiation patterns at 9.8 GHz

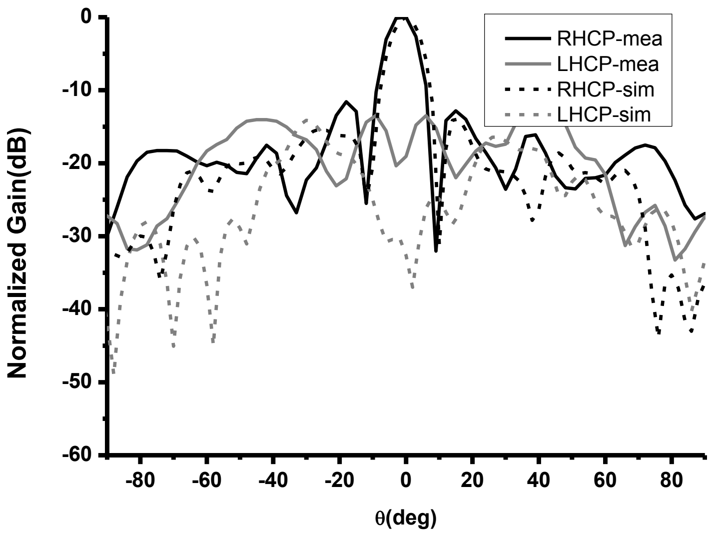

(a) φ=0⁰ plane

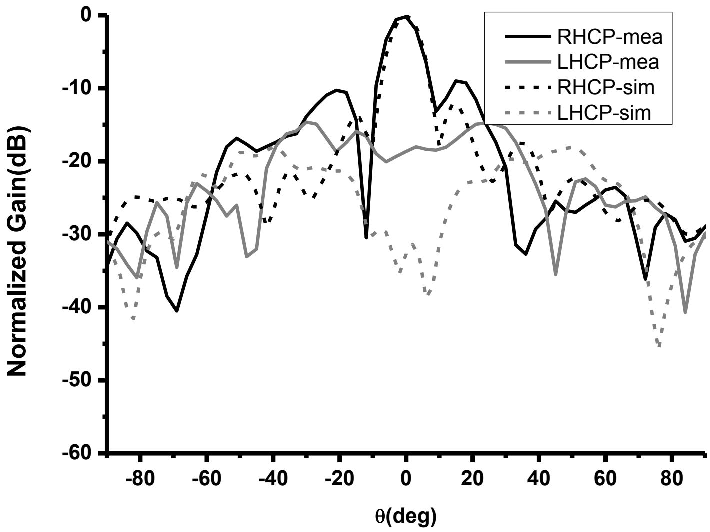

(b) φ=90⁰ plane

Figure 3-37 Simulated and measured radiation patterns at 10.6 GHz

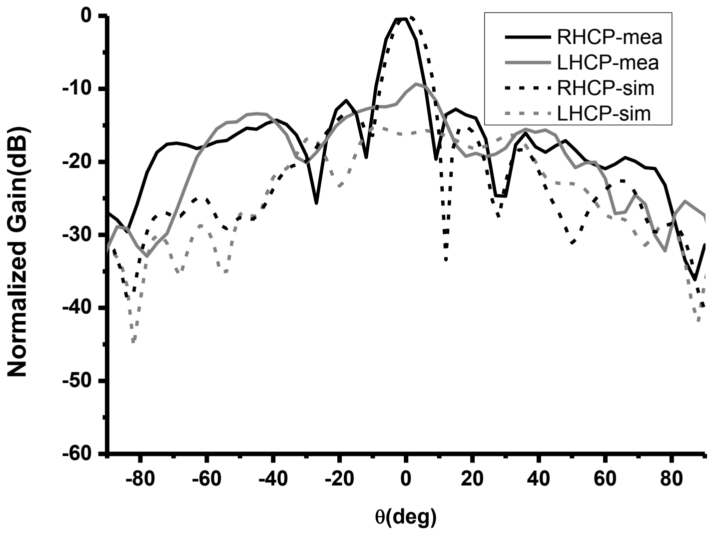

(a) φ=0⁰ plane

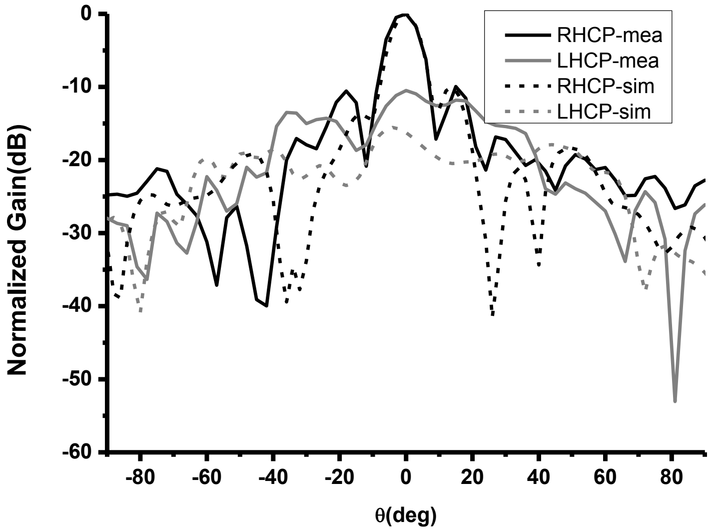

(b) φ=90^0 plane

Figure 3-38 Simulated and measured radiation patterns at 10.8 GHz

Figure 3-39 shows the simulated and measured gains of the folded CP reflectarray antenna. From 10 to 10.8 GHz, the simulated gain varies from 23.2 to 20.9 dBic, and peaks at 10 GHz with 23.2 dBic. The measured gain varies from 22.8 to 20.7 dBic from 9.8 to 10.6 GHz. The highest gain appears at 10.1 GHz. Figure 3-40 shows the simulated and measured aperture efficiency (AE) of the proposed antenna. The simulated AE is over 26% from 10 to 10.8 GHz, and the max AE is 53.5% at 10 GHz. The measured AE is over 27% from 9.8 to 10.6 GHz, and peaks at 10.1 GHz, with the highest AE of 46.9%.

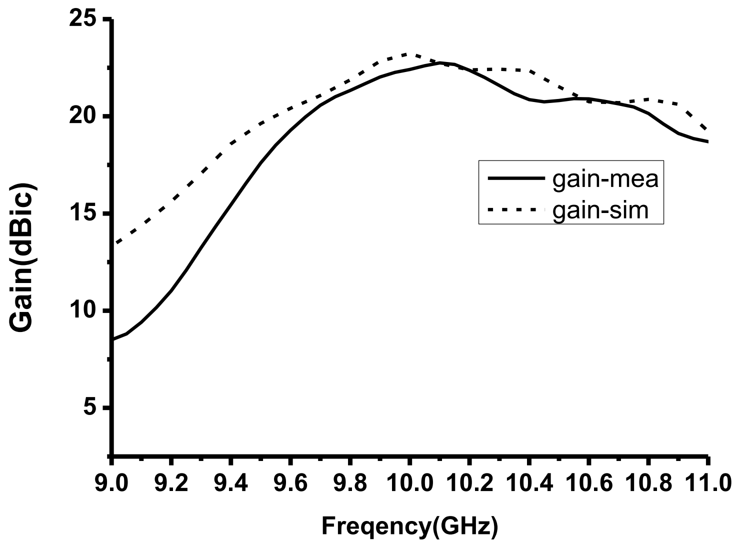

Figure 3-39 Simulated and measured gains

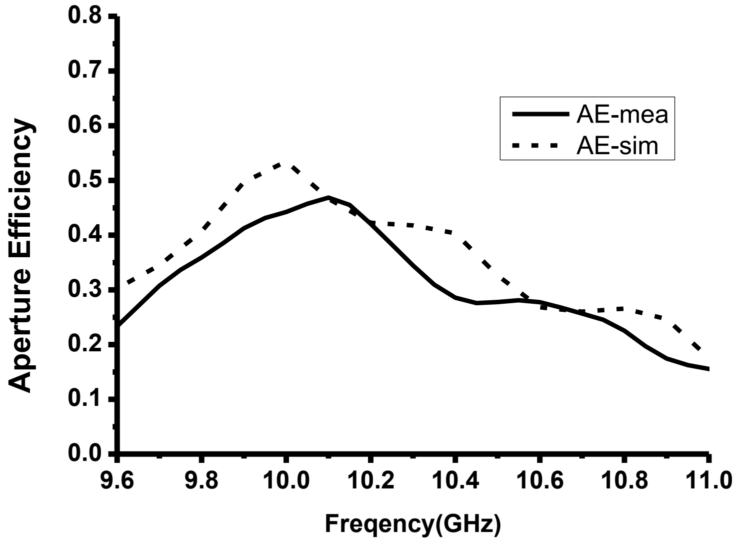

Figure 3-40 Simulated and measured aperture efficiency

3.2.7 Summary

A novel folded CP reflectarray antenna with a CPSS is presented. By introducing the CPSS, the profile of the antenna is decreased by 87% compared with traditional CP reflectarrays. To prove the concept, a prototype working at 10 GHz is designed. Then it is fabricated and measured. The measured results agree with the simulated results. The antenna is designed to operate at 10 GHz. The simulated AR is 2.1 dB, while the measured AR is 1.4 dB at 10 GHz. In simulation and measurement, the SLL is below -10 dB at 10 GHz for RHCP waves. It should be noted that the bandwidth of the antenna is narrow in terms of AR and reflection coefficient. Therefore, broadening the AR and impedance bandwidth can be a research target in the future work.

Chapter 4. Wide-Band Linearly Polarized Reflectarray Antenna

4.1 Introduction

Antenna bandwidth is critical to a wireless communication system. According to Shannon's Theorem, the max capacity of a system is determined by the equation (4-1).

$$C = B \cdot \log_2(1 + \frac{S}{N}) \tag{4-1}$$

In this equation, C represents the maximum possible carrying capacity through a given communication system. B is the bandwidth, and $\frac{S}{N}$ is the signal to noise ratio (SNR). It can be seen that the bandwidth and SNR are two main factors that limit the max capacity of a communication system. Therefore, broadening the bandwidth of a system could expand the capacity of the system with SNR unchanged. And a wide-band antenna is an essential part for a wide-band communication system. In this chapter, an ultra-wide-band tightly coupled dipole reflectarray (TCDR) antenna with linear polarization is proposed. And the method to suppress the cross-polarization of the TCDR antenna is shown in this chapter as well.

4.2 Design of the TCDR Antenna with Linear Polarization

Reflectarray antennas are a hot research topic nowadays [2]. Compared to parabolic reflector antennas, reflectarray antennas are easier to manufacture and have a compact size and a low mass. Moreover, the feed networks of reflectarray antennas are much simpler than those of conventional phased array antennas.

In this chapter, a novel wideband tightly coupled dipole reflectarray (TCDR) antenna is proposed. The concept of "tightly coupled unit cell" is introduced into the design of the proposed TCDR antenna. This is inspired by tightly coupled array antennas and connected array antennas [201-203]. In tightly coupled arrays and connected arrays, the adjacent cells are placed quite close to enhance the mutual coupling between cells. In connected arrays, even inductors and capacitors are added between adjacent cells to enhance the coupling between cells. As reported in [202, 203], these array antennas have a wide impedance bandwidth. Similarly, the distance between adjacent cells of the TCDR antenna is quite small, which means the coupling between cell elements on the reflectarray surface is strong. So this type of unit cells has a wide impedance bandwidth, which overcomes the first factor limiting the bandwidth of reflectarray antennas.

As tightly coupled cell elements are used to construct the TCDR antenna, this design combines advantages of tightly coupled arrays and those of conventional reflectarray antennas. As a result, the TCDR antenna has a wide bandwidth with a much simpler feed network compared with tightly coupled arrays, connected arrays and other UWB direct radiation arrays [204]. In its operating frequency band, the radiation performance of the TCDR antenna is quite stable with reasonable side lobe levels.

4.2.1 Design of Reflectarray Element

In this part, the concept of equivalent distance delay is introduced to design the required cell elements of the TCDR antenna.

4.2.1.1 Equivalent Distance Delay

For a reflectarray antenna shown in Figure 2-1, $\Phi_r(x_i, y_i)$ varies when the antenna works at different frequencies, even if the beam direction, the positions of the reflectarray elements and the position of the feed antenna unchanged. In order to eliminate the effects of frequency, equation (2-7) is divided by k_0, then

$$\frac{\Phi_r(x_i, y_i)}{k_0} = -(x_i \sin\theta_b \cos\theta_b + y_i \sin\theta_b \sin\varphi_b) + R_i \tag{4-2}$$

Let

$$d(x_i, y_i) = \frac{\Phi_r(x_i, y_i)}{k_0} \tag{4-3}$$

Then

$$d(x_i, y_i) = -(x_i \sin\theta_b \cos\theta_b + y_i \sin\theta_b \sin\varphi_b) + R_i \tag{4-4}$$

Here $d(x_i, y_i)$ is called the required equivalent distance delay of a reflectarray element. From the right part of the equation (4-4), $d(x_i, y_i)$ is only determined by (x_i, y_i), (φ_b, θ_b) and R_i. That is to say the required equivalent distance delay only depends on the beam direction, the positions of the reflectarray elements and the position of the feed antenna. It is independent of the frequency.

If one reflectarray element is able to keep its equivalent distance delay unchanged in a frequency band, it means, the reflectarray element can compensate differential spatial phase delay at different frequency point in the same band, and the reflectarray antenna can form a beam with a fix direction (φ_b, θ_b) in the same band. In the next subsection, one of these types of reflectarray elements is introduced.

4.2.1.2 Design of the Element of the TCDR Antenna

As the bandwidth of elements and differential spatial phase delay result in the bandwidth limitation of reflectarray antennas, two aspects are considered to design the proposed elements of the TCDR antenna. Firstly, tightly coupled dipoles are used to broaden the bandwidth of elements. Secondly, distance delay lines are used to compensate the spatial phase delay.

The reflectarray element consists of a dipole, a delay line, and two metal surfaces. The side and front views of an element are shown in Figure 4-1.The delay line is comprised of a pair of parallel microstrips which are connected to the dipole directly. The first metal surface is placed above the second metal surface. The second metal surface is at the bottom of the reflectarray element. The distance between the top of the element and the first metal surface is h_1, which is critical to the performance of the reflectarray element. It determines the impedance bandwidth. Once the bandwidth of the reflectarray is optimized, the value of h_1 is fixed. However, in some cases, to compensate the spatial phase delay, the required delay line may become very long and the space above the first metal is not enough. In order to accommodate the phase delay lines, a hole is added on the first metal surface. Thus, the delay line can go through the first metal surface via this hole. As the distance between the first metal surface and the second metal surface h_2 is arbitrary, there is no limitation on the length of the delay lines. In this design, h_2 is 20 mm. The diameter of the hole is D. The length of the delay line is l_1.

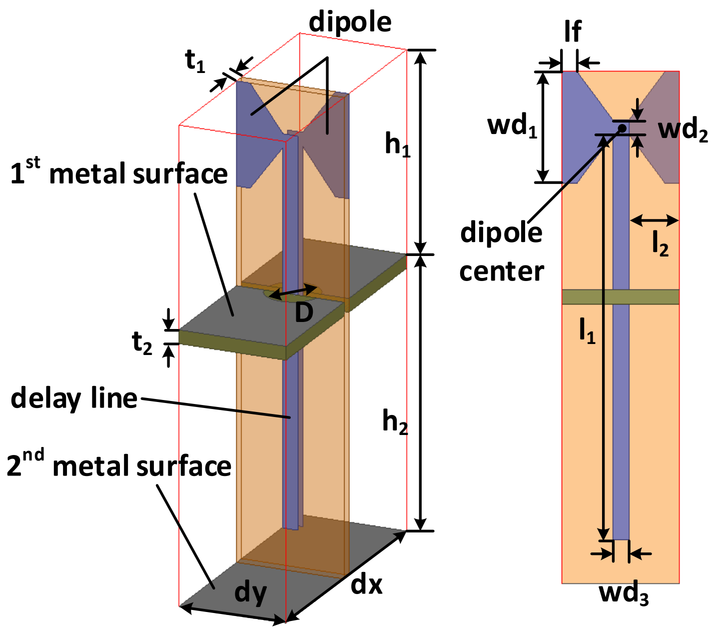

Figure 4-1 Side and front views of the proposed element

The dipole and the delay line are printed on both sides of a substrate (Rogers RO4003C), of which the thickness is t_1. The first metal surface is printed on a substrate (Rogers RO4003C) with the thickness of t_2. By adjusting l_1, the equivalent distance delay of the reflectarray element can be controlled. The parameters of the reflectarray element are shown in Table 4-1. The element is simulated under the periodic boundary.

Table 4-1 Parameters of the Reflectarray Element (unit: mm)

t_1	t_2	h_1	h_2	D	dy
0.813	0.813	14.8	20	4	8
dy	wd_1	wd_2	wd_3	lf	l_2
20	7.6	1	1.1	1	3.45

From the results in Table 4-1, it can be seen the minimum distance between adjacent elements is 8 mm. This distance is less than 1/10 wavelength in free space at 3.4 GHz, which is the lowest working frequency in the design. As the distance between two elements is quite small, the coupling between elements is strong as well. So the element has a very wide impedance bandwidth [201]. It means the element can transfer the energy it receives from the feed antenna to the delay line in a wide band when the reflecting surface is illuminated by the feed antenna, which is shown in Figure 4-2. And the delay line used in the design is a true-time-delay line, so it also has wide-band performance. Thus, the two factors limiting the bandwidth of a reflectarray are overcome.

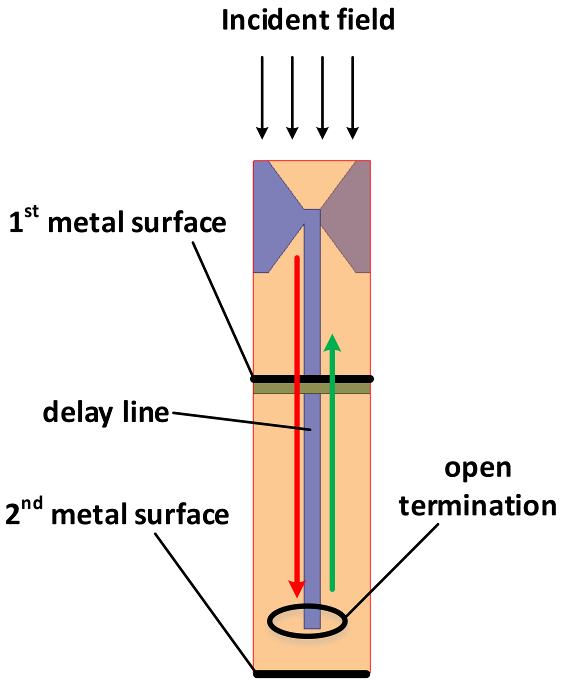

Figure 4-2 Energy flowing in the element

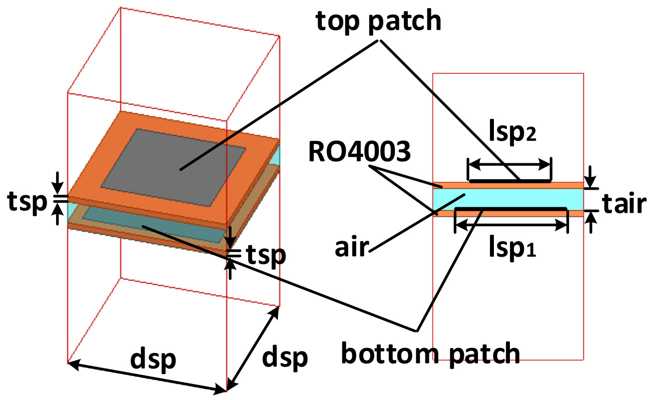

Figure 4-3 Side and front views of the stacked patch

To better demonstrate the performance of the proposed reflectarray element, the equivalent distance delay that a conventional stacked square patch can offer is also given. The configuration of the stacked patch is shown in Figure 4-3. The stacked patch is printed on two substrates (Rogers RO4003C) both with the thickness of tsp. The length of sides of the bottom patch is lsp_1, and that of the top patch is $0.8 \times \mathrm{lsp}_1$. Between the substrates is the air gap, whose thickness is tair. The distance between adjacent cells for stacked patch dsp is set to $0.49\lambda_0$. λ_0 is the free space wavelength at the center frequency, which is 7 GHz here. The parameters of the stacked patch are given in Table 4-2.

Table 4-2 Parameters of the Stacked Patch (unit: mm)

tsp	dsp	lsp_2	tair
0.813	21	$0.8 \times lsp_1$	3.1

The equivalent distance delay that the reflectarray element can offer is shown in Figure 4-4. That of the stacked patch is shown in Figure 4-5. The proposed element and the stacked patch are simulated in periodic boundary in HFSS. The equivalent distance delays in Figure 4-4 and Figure 4-5 are calculated from the simulated phases of reflection coefficients in HFSS and equation (4-3).

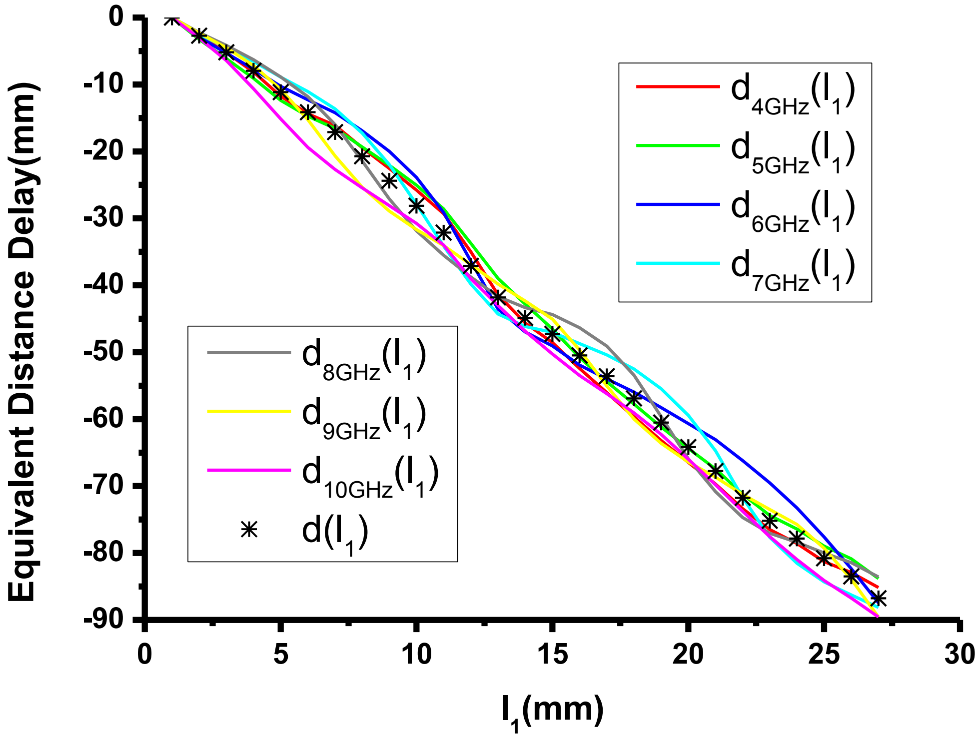

Figure 4-4 Equivalent distance delay of the proposed element

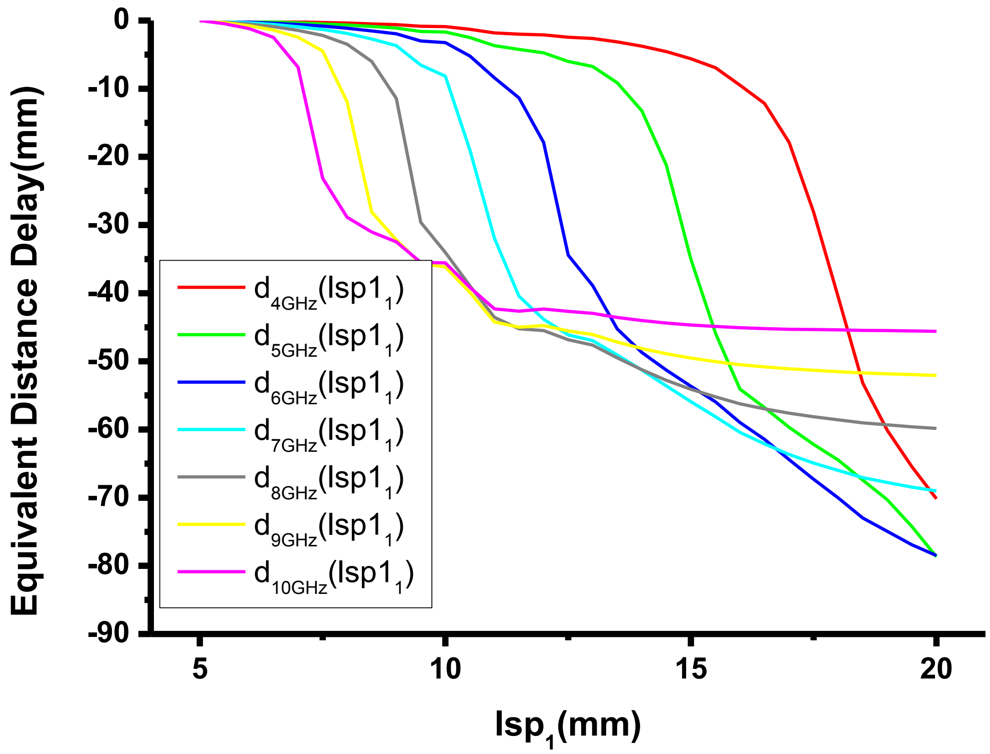

Figure 4-5 Equivalent distance delay of the stacked patch

Let $d_f(l_1)$ denote the curve of the proposed element's equivalent distance delay versus l_1 at frequency *f*, and let $d_f(lsp_1)$ denote the curve of the stacked patch's equivalent distance delay versus lsp_1 at frequency *f*. It can be seen that $d_f(l_1)$ of the proposed element is more converged than $d_f(lsp_1)$ of the stacked patch, which means $d_f(l_1)$ changed much less than $d_f(lsp_1)$ with frequency changing from 4 to 10 GHz. When l_1 is fixed, although the equivalent distance delays of the proposed element for different frequencies are not the same precisely, they have very small deviations. This means the proposed element can approximately satisfy equation (4-4) within a wide frequency band.

Although $d_f(l_1)$ is quite stable when frequency *f* changes, in a certain band, for example from f_1 to f_2, it is desirable to find a function $d(l_1)$ to design the reflectarray, which satisfies the equation (4-5).

$$\sum_{f=f_1}^{f_2} [d(l_1) - d_f(l_1)]^2 = min \tag{4-5}$$

Equation (4-5) means the sum of squared differences between $d(l_1)$ and $d_f(l_1)$ from f_1 to f_2 is minimum. Using $d(l_1)$ to design the reflectarray results in a more reasonable phase error distribution on the reflecting surface for different frequencies.

As the left part of equation (4-5) is minimum, the derivative of it with respect to $d(l_1)$ should be zero. Then,

$$2\sum_{f=f_1}^{f_2}[d(l_1) - d_f(l_1)] = 0 \tag{4-6}$$

Equation (4-6) can be re-written as:

$$d(l_1) = \sum_{f=f_1}^{f_2}\frac{d_f(l_1)}{N} \tag{4-7}$$

where N is the number of frequency points from f_1 to f_2. In this thesis, $f_1 =$ 4 GHz, $f_2 =$ 10 GHz, and N = 7. In Figure 4-4, the curve of $d(l_1)$ versus l_1 is drawn by asterisk. In the design of TCDR antenna, l_1 is used to calculate the length of delay line for each reflectarray element.

4.2.2 Design of the Feed antenna

As the reflectarray operates from 3.4 to 10.6 GHz, a wideband feed antenna is needed. The log-periodic dipole array (LPDA) which consists of dipoles and a pair of parallel microstrips is chosen as the feed antenna [205]. Because LPDA is a low cost antenna, and the radiation patterns of LPDA are easy to control compared with wide-band monopole antennas. The dipoles and microstrips are printed on both sides of a substrate (Rogers RO4003C) with the thickness of 0.813 mm. The LPDA is fed by a coaxial cable, of which the outer conductor is connected to one microstrip, and the inner pin is soldered to the other microstrip. The configuration of LPDA is shown in Figure 4-6. The width of the microstrip is 2.5 mm. $fl_1 = 29.72$ mm. $fw_1 = 3.72$ mm. $\alpha = 21.8$ deg.

$$\frac{fl_1}{fl_2} = \frac{fw_1}{fw_2} = 1.2 \tag{4-8}$$

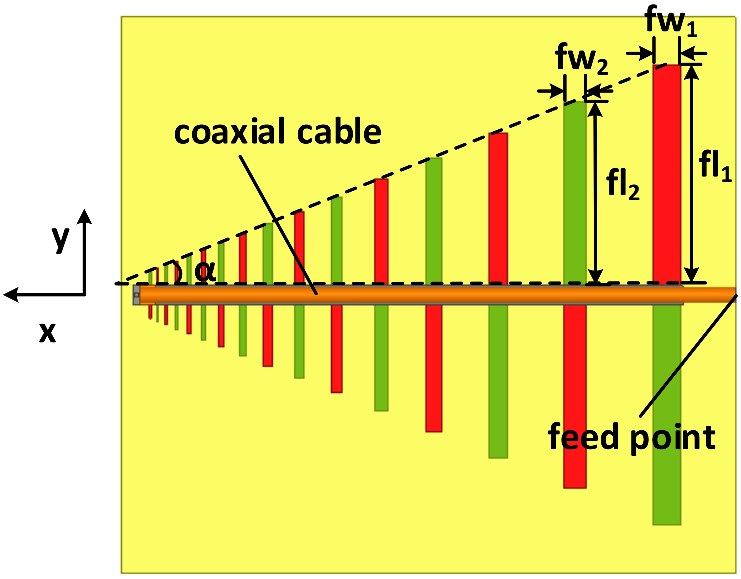

Figure 4-6 Configuration of LPDA

The position of the phase center of the LPDA changes at different frequency points. Let $p_f(x,y)$ denote the position of the phase center at frequency f. The coordinates of the phase center at some frequency points are given in Table 4-3. In this design, the position of the phase center $p(x,y)$, is calculated by using equation (4-9), where N is the number of frequency points from f_1 to f_2.

$$p(x,y) = \sum_{f=f_1}^{f_2} \frac{p_f(x,y)}{N} \tag{4-9}$$

Table 4-3 Coordinates of Phase Center (unit: mm)

Frequency (GHz)	4	5	6	7
$p_f(x,y)$	(-32,0)	(-20,0)	(-11.6,0)	(-7,0)
Frequency (GHz)	8	9	10	
$p_f(x,y)$	(-10.3,0)	(-10.4,0)	(-9.6,0)	

4.2.3 Design of TCDR Antenna

This reflectarray antenna consists of an LPDA as the feed antenna and a reflecting surface. The reflecting surface is composed of 26×11 elements. The dimension of reflecting surface is 210×210×34.8 mm^3. The distance between the top of reflecting surface and feed antenna Rh_1 is 97.6 mm. The distance between the phase center of the LPDA and reflecting surface Rh_2 is 119 mm. The required equivalent distance delay for each reflectarray element is calculated according to equation (4-4) and is shown in Figure 4-7(a). According to the results in Figure 4-7(a), the required length of delay line for each element is calculated via $d(l_1)$ in Figure 4-4 and shown in Figure 4-7(b). The configuration of the whole antenna is shown in Figure 4-8. In this design it should be noted that R_i is the distance between the center of the dipole and the phase center of the LPDA.

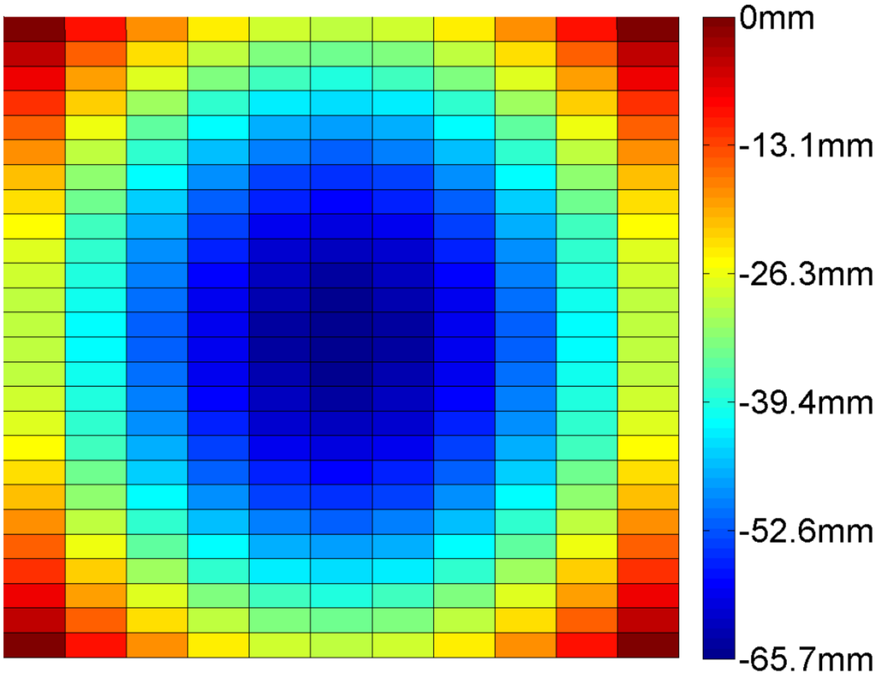

(a)

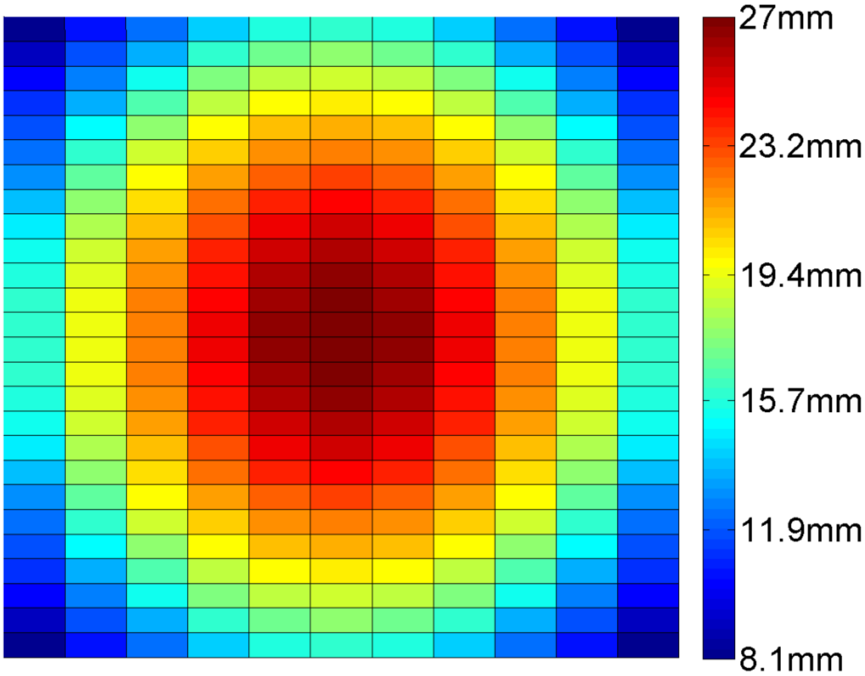

(b)

Figure 4-7 Required (a) equivalent distance delay and (b) length of the delay line for each element on the reflecting surface

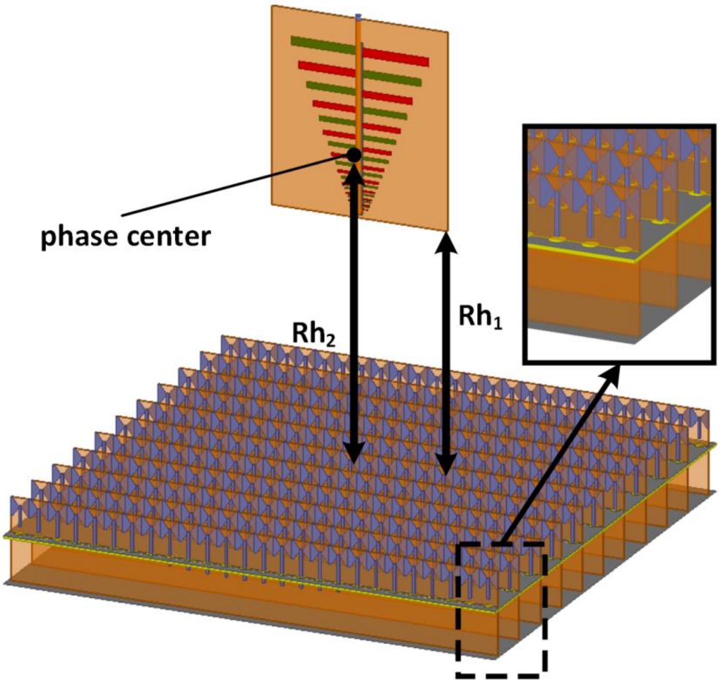

Figure 4-8 Configuration of the TCDR antenna

4.2.3.1 Phase Error Distribution and Its Effects on the SLL of the Reflectarray

Theoretically, to form a focused beam in broadside, the phase on the reflecting surface should be equal after the elements of the reflectarray compensate the spatial phase delay. However, phase errors can exist on the reflecting surface of a reflectarray at some frequency points. As the central frequency of the reflectarray is about 7 GHz, the phase error distribution based on $d(l_1)$ is shown in Figure 4-9, while that based on $d_{7GHz}(l_1)$ is shown in Figure 4-10.

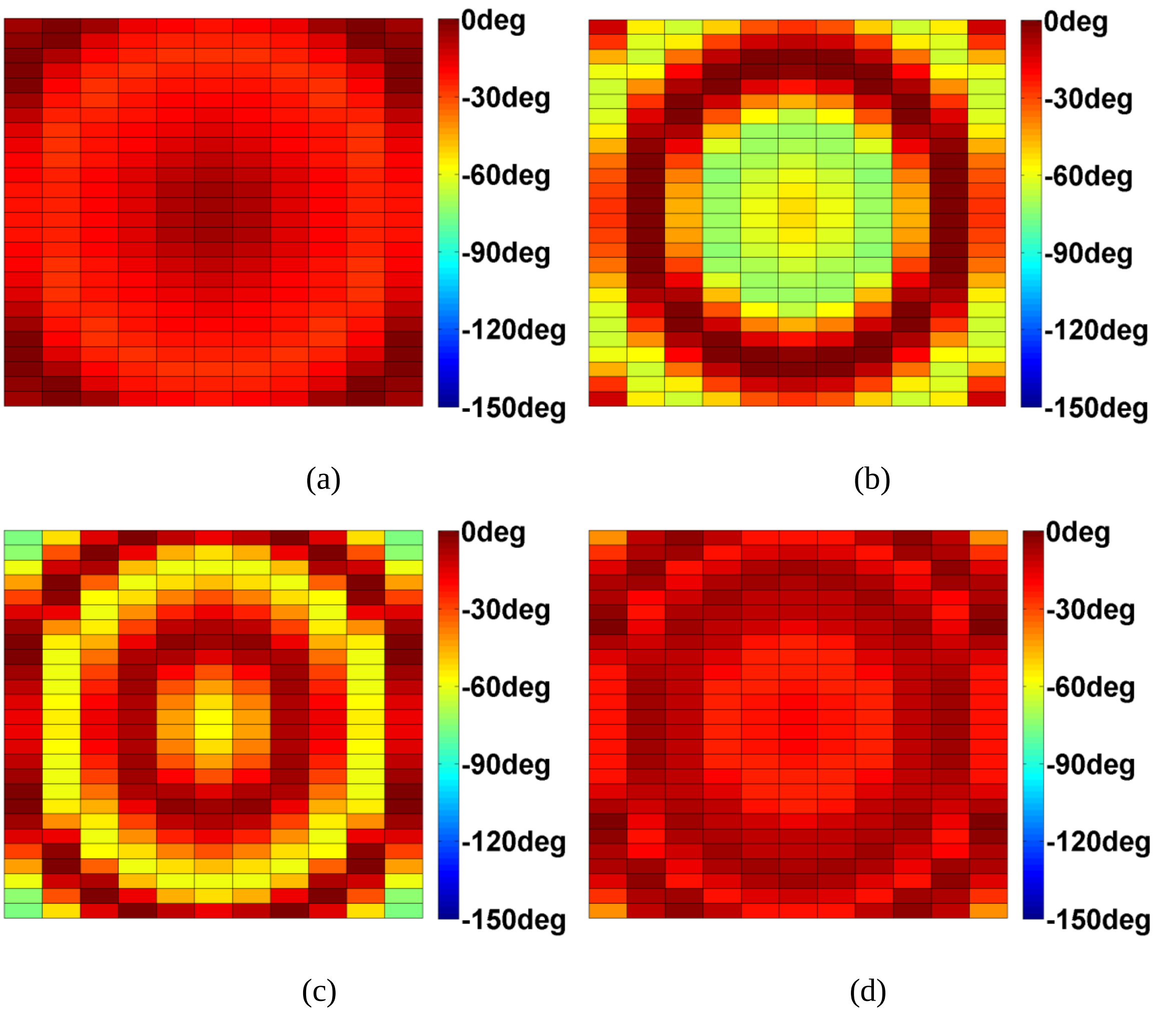

Figure 4-9 Phase error distribution at (a) 4 GHz, (b) 7 GHz, (c) 9 GHz and (d) 10 GHz when $d(l_1)$ is used to design the reflectarray.

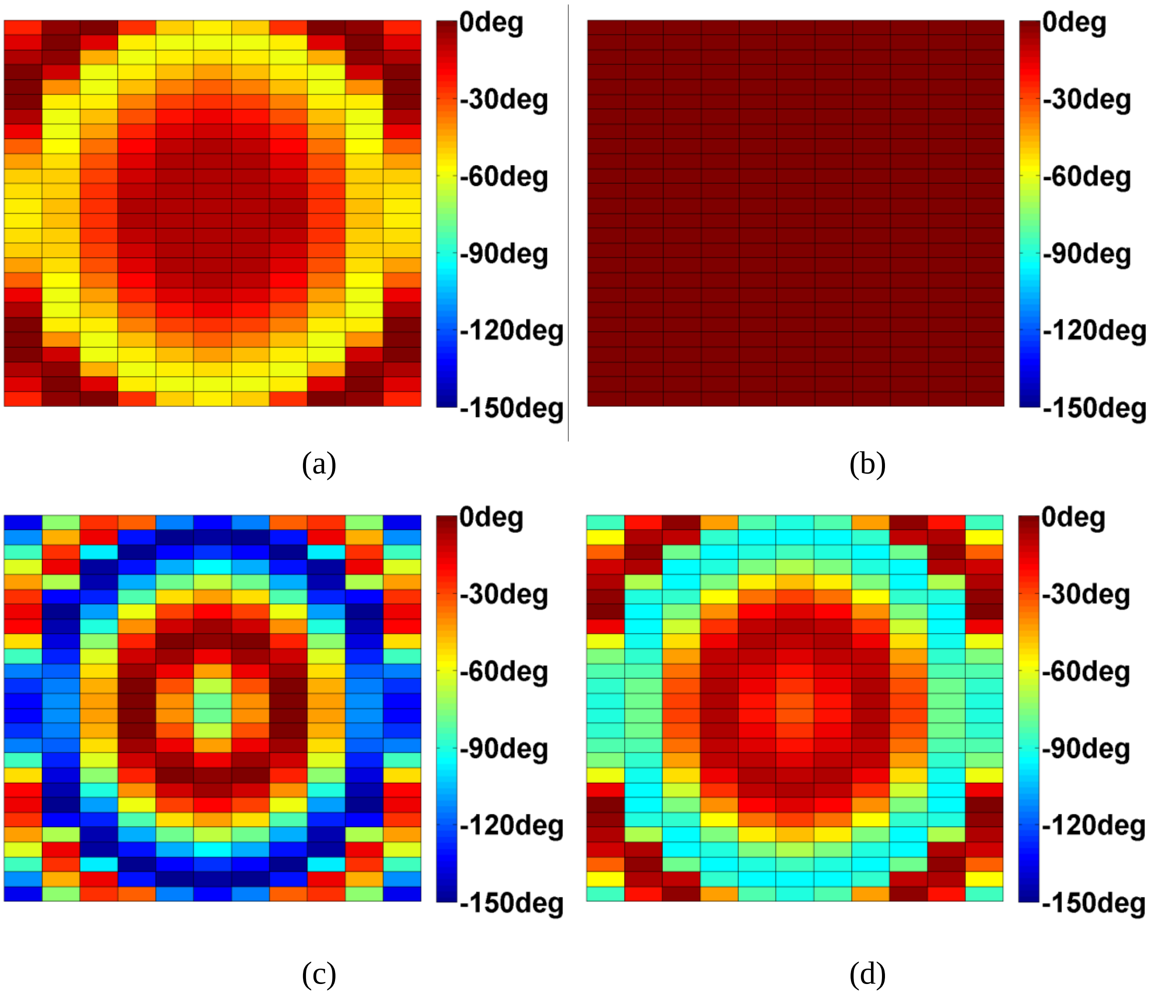

Figure 4-10 Phase error distribution at (a) 4 GHz, (b) 7 GHz, (c) 9 GHz and (d) 10 GHz when $d_{7GHz}(l_1)$ is used to design the reflectarray

In Figure 4-9, it can be seen that the worst phase error distribution appears at 9 GHz when $d(l_1)$ is used to design the reflectarray. At 9 GHz, the largest phase error on the reflecting surface is 76 degree. However, if $d_{7GHz}(l_1)$ is used to design the reflectarray, although no phase error exists on the reflecting surface at 7 GHz, phase error distribution at other frequency points is enlarged. For example, the largest phase error on the reflecting surface at 9 GHz is 150 degree, which is much larger than that based on $d(l_1)$ design. Compared with $d_{7GHz}(l_1)$, using $d(l_1)$ to design the reflectarray minimizes the phase error distribution in a wide frequency range.

As the phase error distribution affects the radiation pattern of the reflectarray, array factors on H-plane at different frequency points are calculated [206] and are shown in Figure 4-11.

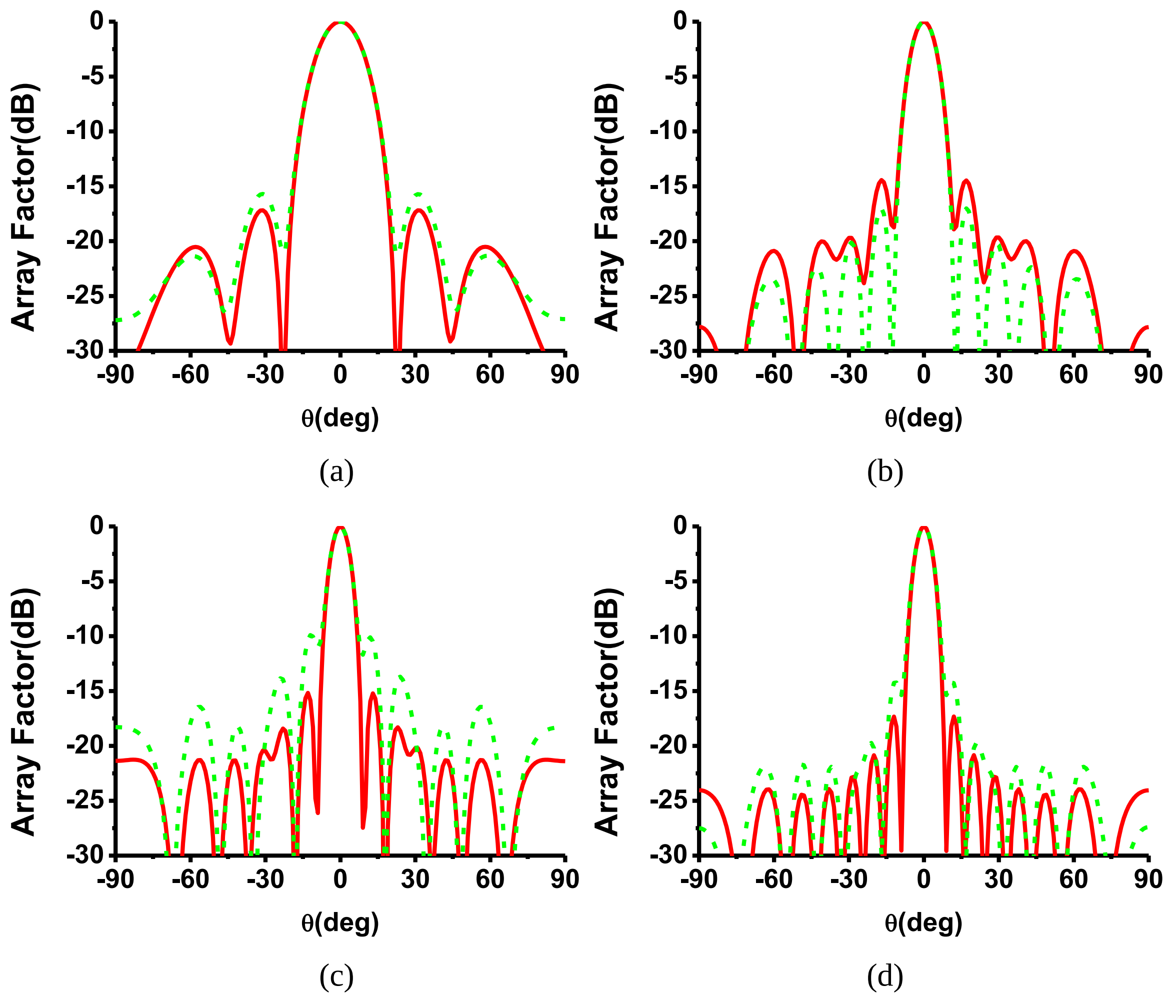

Figure 4-11 Array factors at (a) 4 GHz, (b) 7 GHz, (c) 9 GHz and (d) 10 GHz when $d(l_1)$ and $d_{7GHz}(l_1)$ are used to design the reflectarray respectively. Solid lines are array factors when $d(l_1)$ is used. Dash lines are array factors when $d_{7GHz}(l_1)$ is used.

As shown in Figure 4-11, different phase error distributions on the reflecting surface result in different first side lobe level (SLL1). Compared with $d_{7GHz}(l_1)$, using $d(l_1)$ to design the reflectarray decreases the SLL1 within a wide frequency range except slightly increasing the SLL1 at 7 GHz. Especially at 9 GHz, using $d(l_1)$ decreases the SLL1 by 5 dB.

For the TCDR antenna, its SLL1 is low enough at the central frequency. Compared with SLL1 at the central frequency, TCDR antenna's SLL1 is higher at the lowest and highest operating frequencies. So slightly increasing the SLL1 at the central frequency would not deteriorate the radiation pattern of the TCDR antenna significantly. Decreasing the SLL1 at lowest and highest operating frequencies will expand the working bandwidth, in which the TCDR antenna has relatively low SLL. As a result, using $d(l_1)$ to design the reflectarray can obtain better operating bandwidth than using $d_{7GHz}(l_1)$ to design the reflectarray. Figure 4-12 shows the simulated radiation patterns of the reflectarray in HFSS when $d(l_1)$ and $d_{7GHz}(l_1)$ are used to design the reflectarray respectively. Compared to $d_{7GHz}(l_1)$, $d(l_1)$ can lead to better SLL of the TCDR antenna.

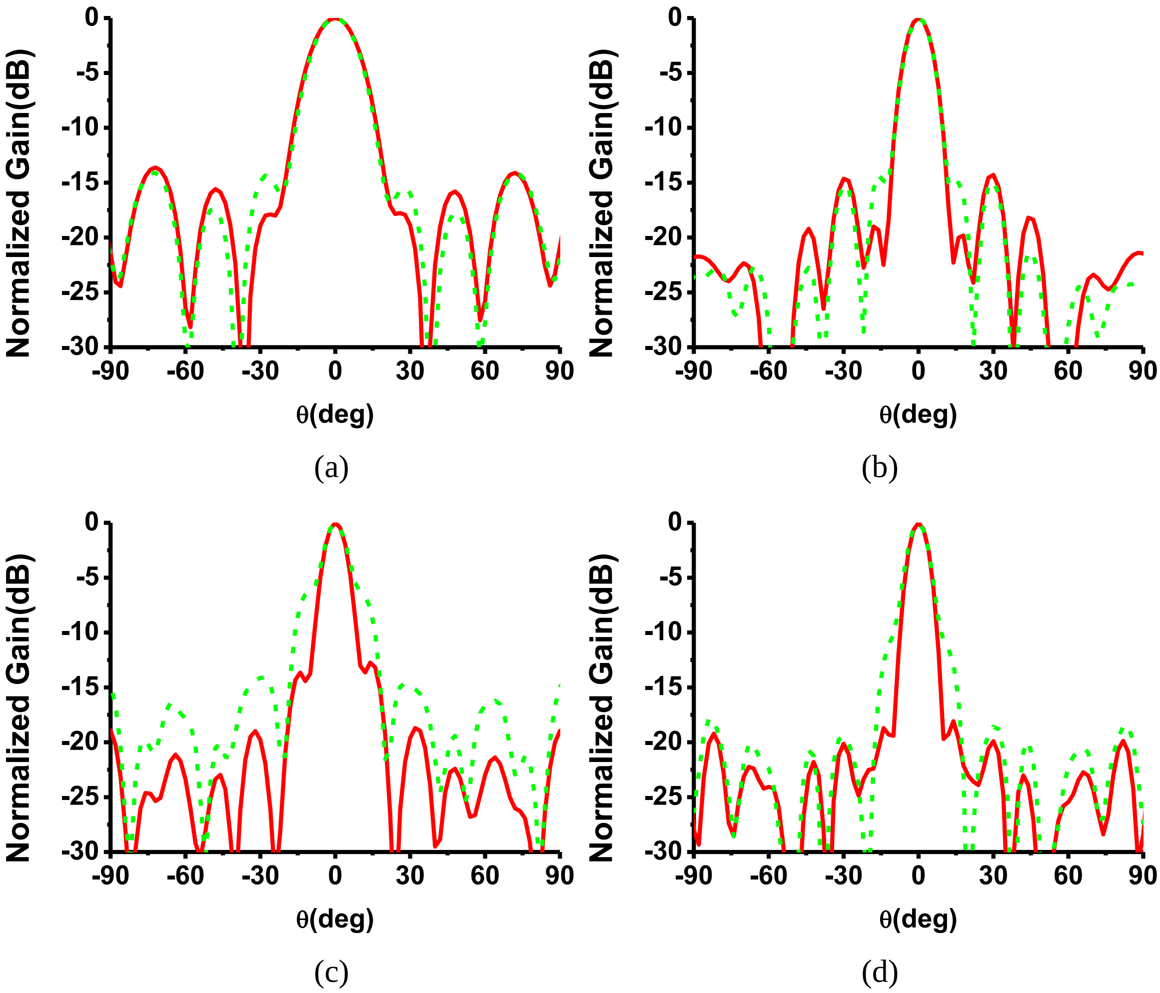

Figure 4-12 Simulated radiation patterns at (a) 4 GHz, (b) 7 GHz, (c) 9 GHz and (d) 10 GHz when $d(l_1)$ and $d_{7GHz}(l_1)$ are used to design the reflectarray respectively. Solid lines are array factors when $d(l_1)$ is used. Dash lines are array factors when $d_{7GHz}(l_1)$ is used.

4.2.4 Simulated and Measured Results

The TCDR antenna is simulated in HFSS. Then, it is fabricated and measured in an anechoic chamber. The photograph of the antenna is shown in Figure 4-13. Simulated and measured results are given in this subsection.

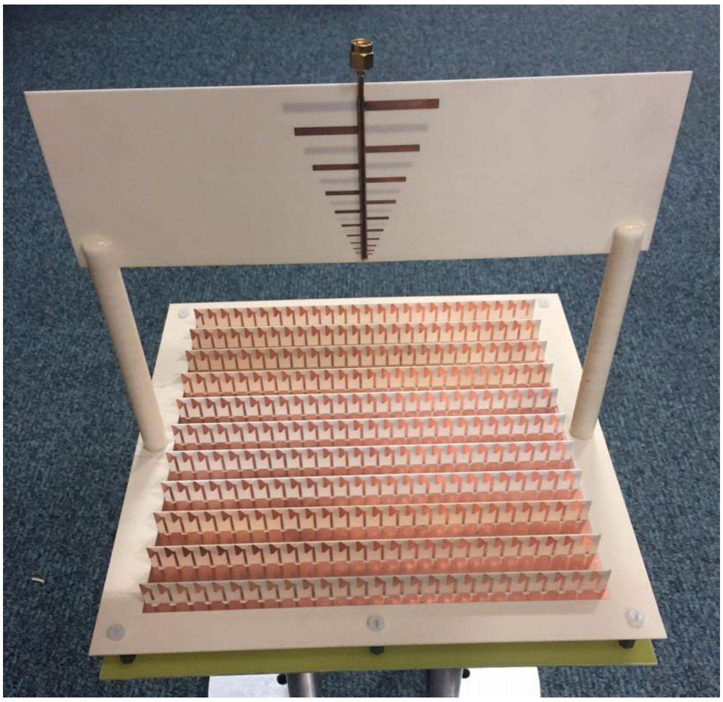

Figure 4-13 Photograph of the TCDR antenna.

4.2.4.1 Radiation Patterns and Reflection Coefficient

As discussed above, the proposed reflectarray element can offer the required equivalent distance delay on the reflecting surface in a wide band. Therefore, one feature of the TCDR antenna is that it can keep its radiation pattern stable in a large frequency range. The simulated and measured radiation patterns are shown in Figure 4-14. Good agreement between the simulated and measured results is observed. From Figure 4-14, it can be seen that the radiation pattern performance keeps stable. The shape of the main beam is not distorted with frequency varying from 3.4 to 10.6 GHz. The highest SLL is about -11.7 dB.

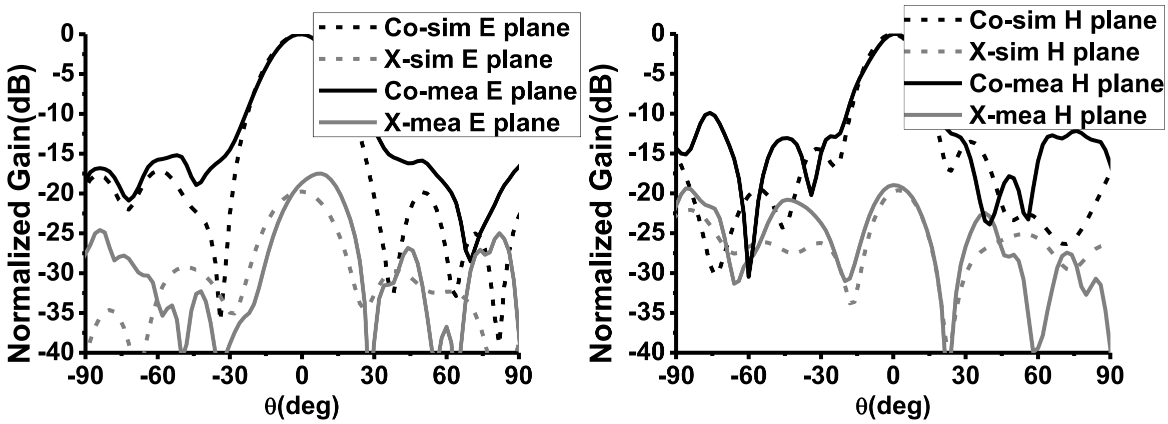

(a) 3.4 GHz

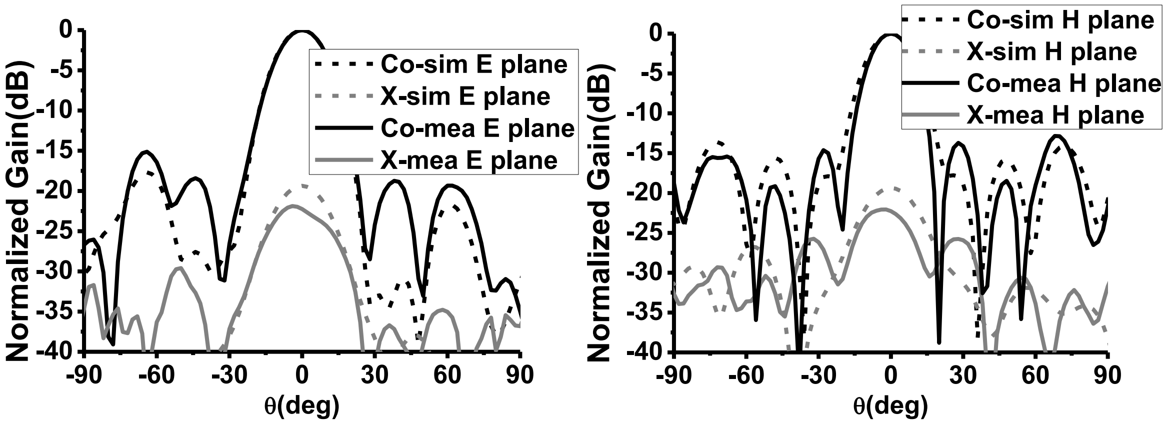

(b) 4 GHz

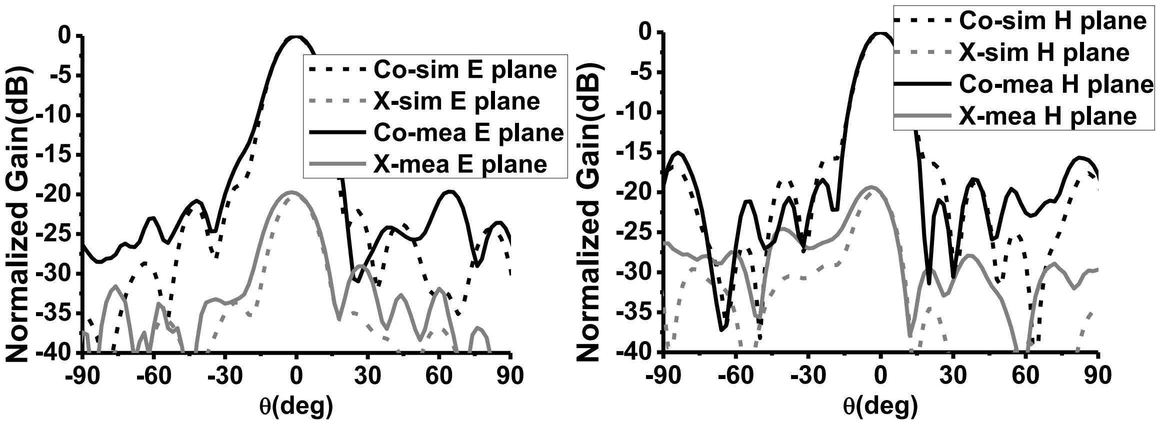

(c) 5 GHz

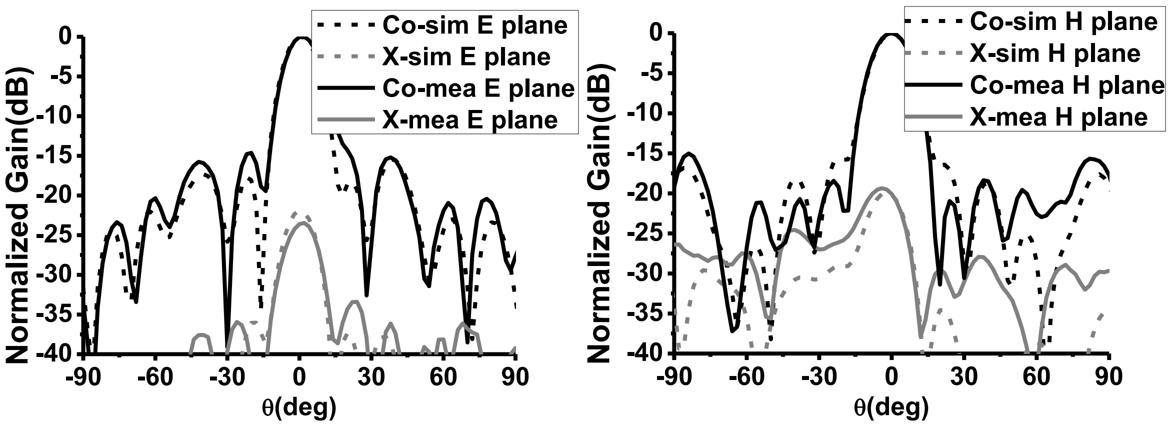

(d) 6 GHz

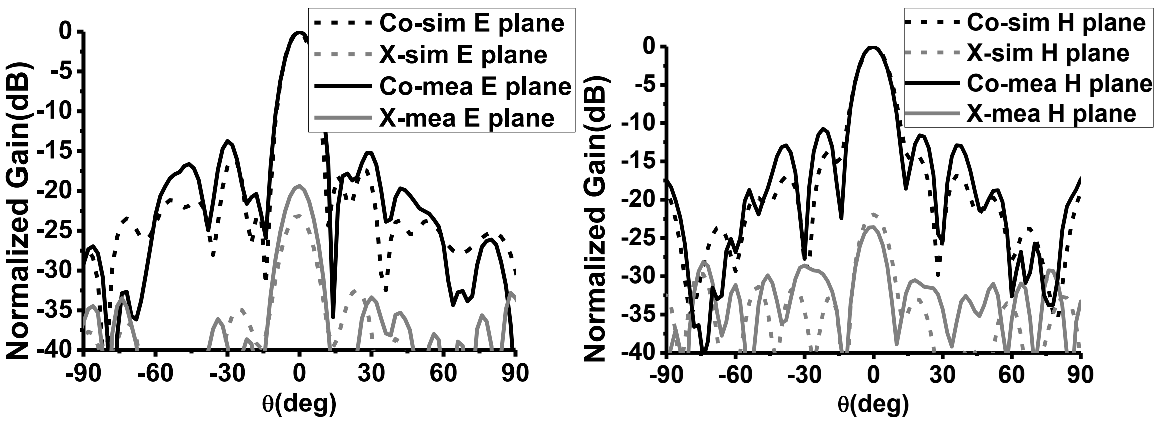

(e) 7 GHz

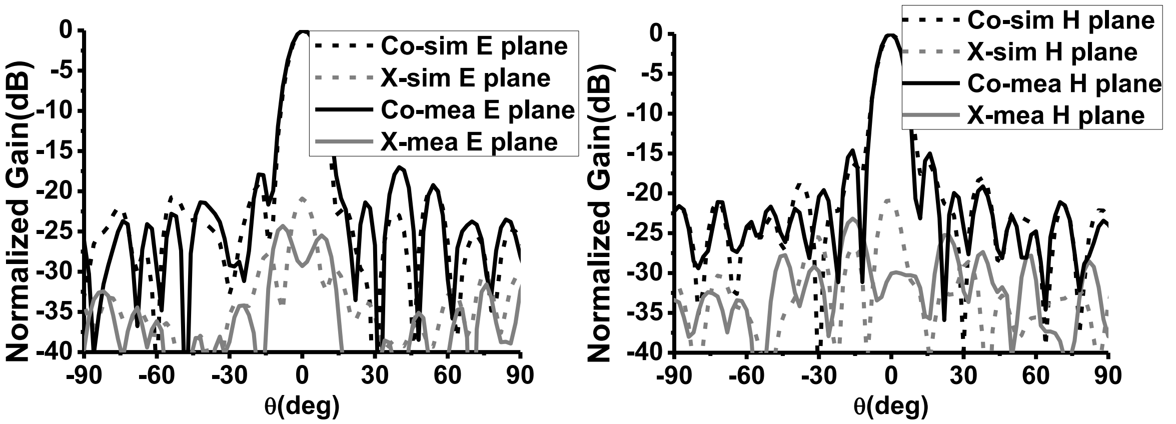

(f) 8 GHz

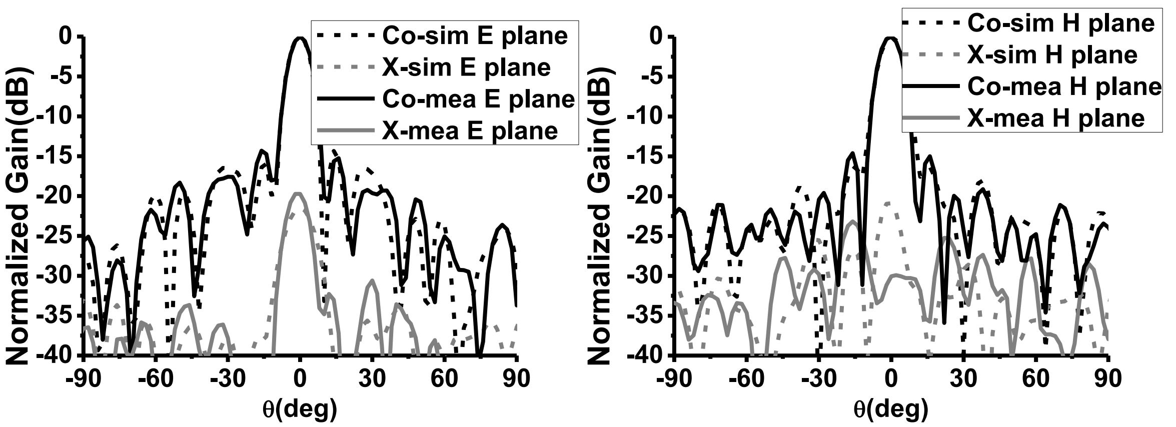

(g) 9 GHz

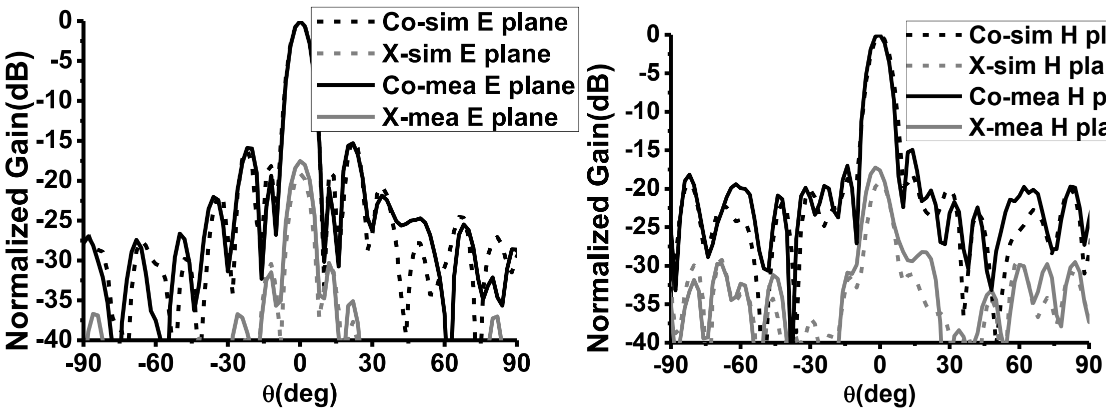

(h) 10 GHz

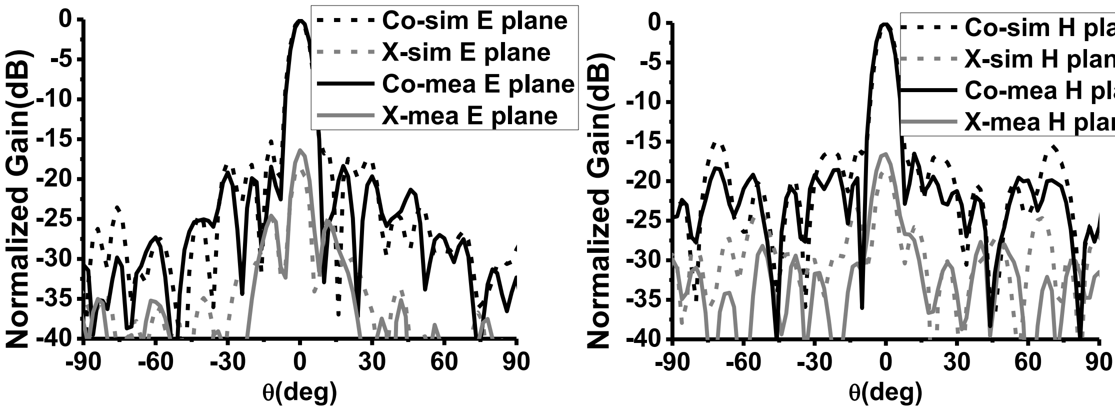

(i) 10.6 GHz

Figure 4-14 Radiation patterns of the TCDR antenna

Some recent wideband reflectarray antennas reported in the literature and the TCDR antenna in this thesis are summarized in Table 4-4. It should be mentioned that the definition of bandwidth used in those works are not exactly the same. In this table, the achieved bandwidths are abstracted by checking whether the antennas have reasonable SLLs (SLL<-10 dB).

Table 4-4 Comparison with Antennas in References

Ref. No.	Bandwidth	Max aperture efficiency	Method to achieve wide bandwidth
[103]	2:1	not given	Using Bessel Filters to design element
[104]	1.45:1	78%	Subwavelength spacing & multi-resonance element
[100]	≤1.5:1	56.5%	Subwavelength element
[90]	≤1.8:1	64.1%	Using parallel dipoles as element

[86]	1.5:1	not given	True-time-delay element
TCDR antenna	3.12:1	38%	Tightly coupled element & true-time-delay

4.2.4.2 Gain and Aperture Efficiency

Figure 4-15 shows the simulated and measured gains of the antenna. The simulated gain varies from 12.7 to 21.9 dBi from 3.4 to 10.6 GHz and peaks at 10 GHz. The measured gain varies from 13.8 to 22.6 dBi and the highest gain appears at 10.6 GHz. The simulated and measured aperture efficiency (AE) of the antenna is also shown in Figure 4-15. The simulated AE of the TCDR is over 20% from 3.4 to 10 GHz, and it is larger than 17.8% from 10 to 10.6 GHz. The measured AE of the TCDR is over 20% from 3.4 to 10.6 GHz.

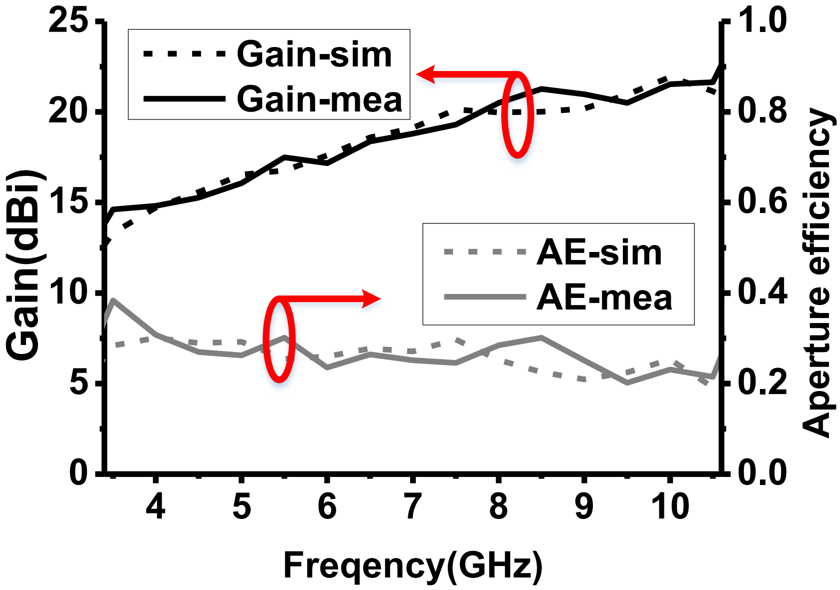

Figure 4-15 Simulated and measured gains and aperture efficiency

4.2.5 Summary

A novel tightly coupled reflectarray element is proposed. Using this element, a wide-band tightly coupled dipole reflectarray antenna is designed and fabricated. The antenna has stable radiation patterns from 3.4 to 10.6 GHz. Over 3:1 frequency range, the main beam of the antenna is not distorted or split with frequency changing. Moreover, the highest side lobe level of the radiation pattern is below -11.7 dB across the band. The antenna is promising for the applications where antennas with wide bandwidth and stable radiation patterns are needed.

4.3 Method of Improving the Polarization Purity of TCDR Antenna

In this subsection, the method to reduce the cross-polarization of TCDR antenna is proposed. By introducing this method, the level of cross-polarization at main beam direction can be decreased by 5 to 10 dB in the working band.

4.3.1 Mechanism of Reducing Cross-polarization

For a unit cell on the reflecting surface, equation (4-10) exists [206].

$$\begin{aligned} E_x^{ref} &= \Gamma_{xx} \cdot E_x^{inc} + \Gamma_{xy} \cdot E_y^{inc} \\ E_y^{ref} &= \Gamma_{yx} \cdot E_x^{inc} + \Gamma_{yy} \cdot E_y^{inc} \end{aligned} \tag{4-10}$$

For a reflectarray antenna with the beam direction along z axis, if the co-polarization is set along y axis and cross-polarization is set along x axis, then equation (4-11) is obtained. E_{xp} is the cross-polarization electronic filed (E field), and E_{cp} represents the co-polarization E field.

$$\begin{aligned} E_{xp}^{ref} &= \Gamma_{xp-xp} \cdot E_{xp}^{inc} + \Gamma_{xp-cp} \cdot E_{cp}^{inc} \\ E_{cp}^{ref} &= \Gamma_{cp-xp} \cdot E_{xp}^{inc} + \Gamma_{cp-cp} \cdot E_{cp}^{inc} \end{aligned} \tag{4-11}$$

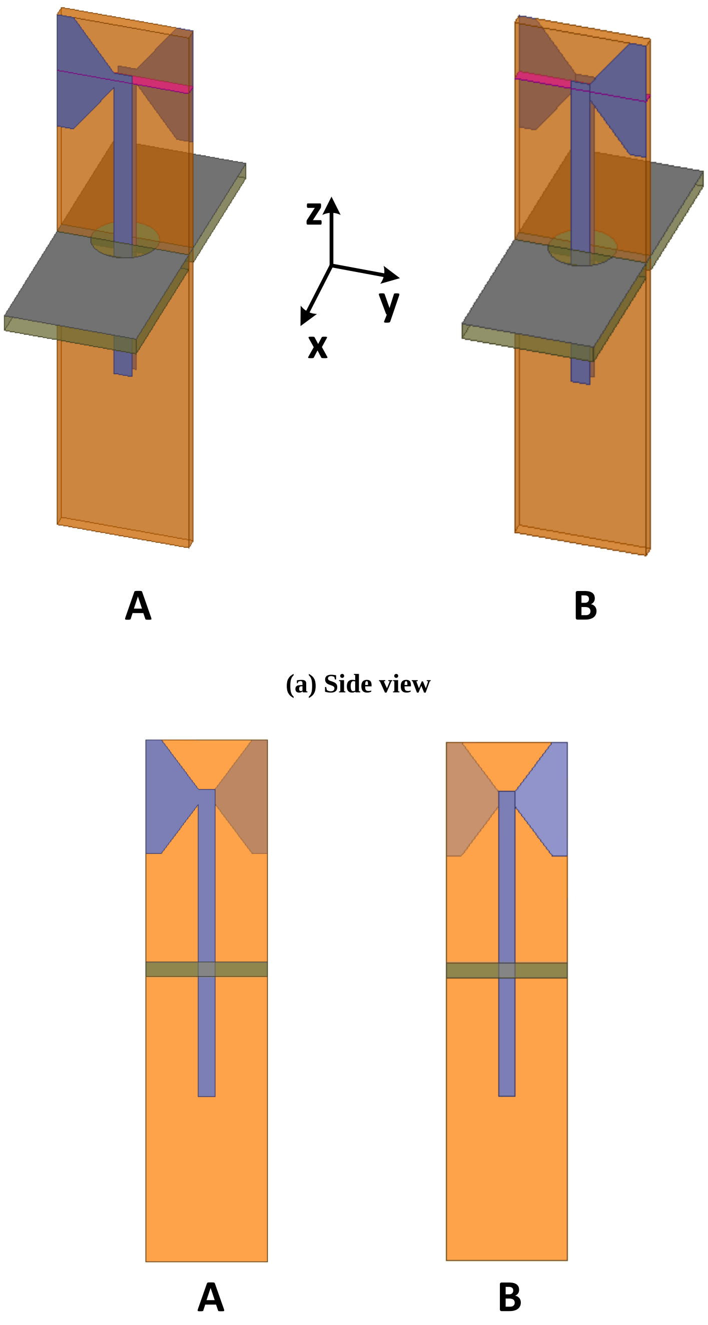

(a) Side view

(b) Front view

Figure 4-16 Unit cell A and unit cell B.

Assume there are two unite cells, type A and type B. Figure 4-16 shows the unit cell A and unit cell B. Let $\Gamma(A)$ and $\Gamma(B)$ denote the S parameters of unit A and B respectively. From Figure 4-16 (b), it can be seen, the structure of unit cell A is mirror-symmetrical with the structure of unit cell B. This symmetry leads to the $\Gamma_{xp-cp}(A)$ has the opposite phase to the $\Gamma_{xp-cp}(B)$. This can be seen intuitively in Figure 4-17. In Figure 4-17 the two unit cells are illuminated by the same incident waves with –y polarization and the incident angle is 0^0. The E filed with x polarization on the pink reference plane is drawn. It is obvious that the E field of element A has an opposite direction with that of element B, which indicates their phases are opposite.

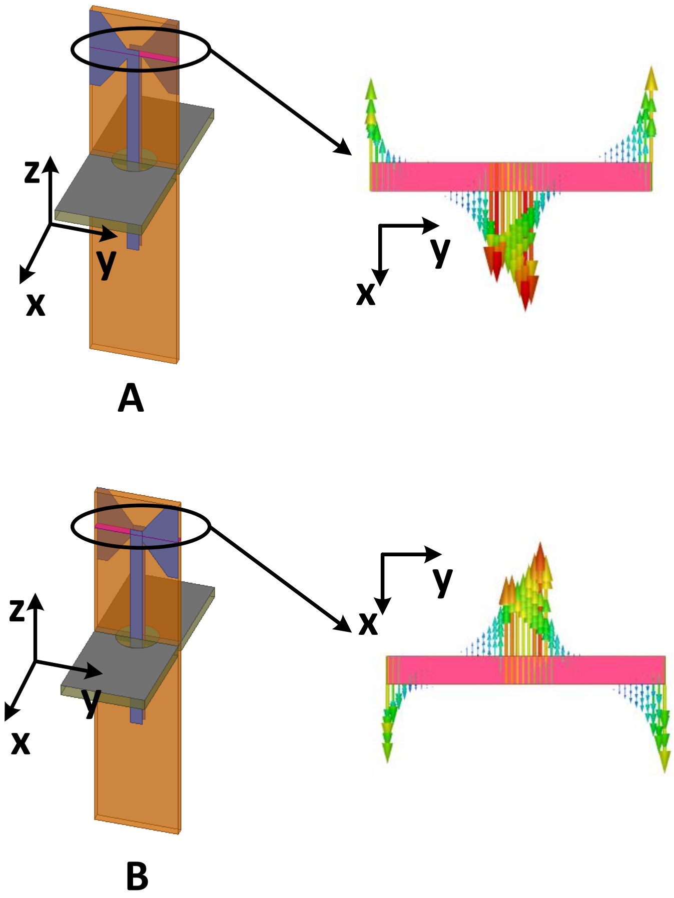

Figure 4-17 Cross-polarization E fields under the same incident waves

Figure 4-18 shows the co-polarization E field of unit A and B. It can be seen they have the same direction, which indicates they have the same phase. From Figure 4-18 and Figure 4-17 , $\Gamma_{xp-cp}(A)$ and $\Gamma_{xp-cp}(B)$ have the opposite phase, and $\Gamma_{cp-cp}(A)$ and $\Gamma_{cp-cp}(B)$ have the same phase intuitively.

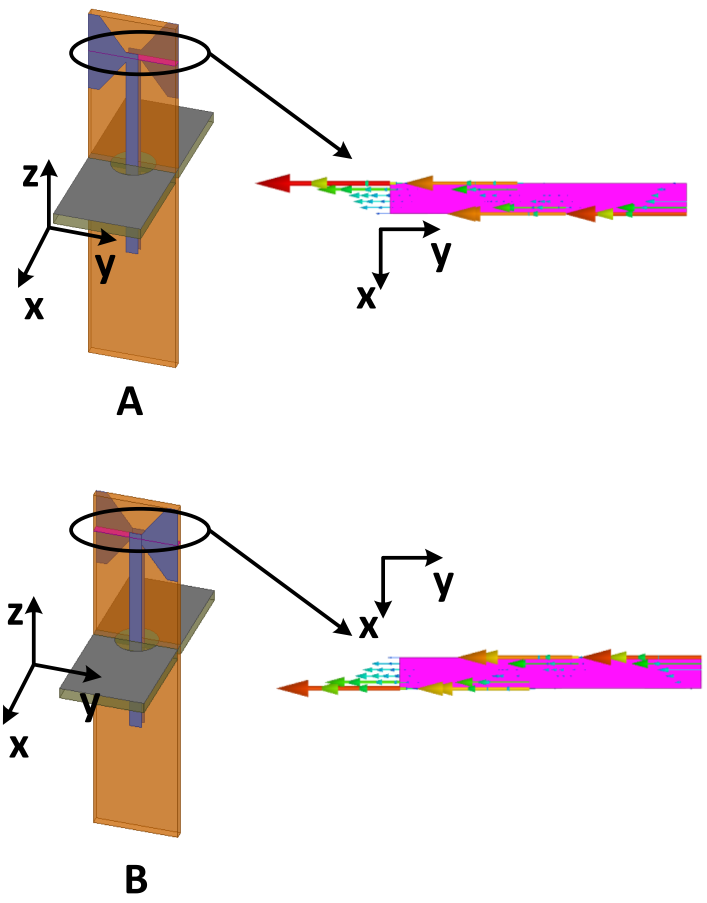

Figure 4-18 Co-polarization E fields under the same incident waves

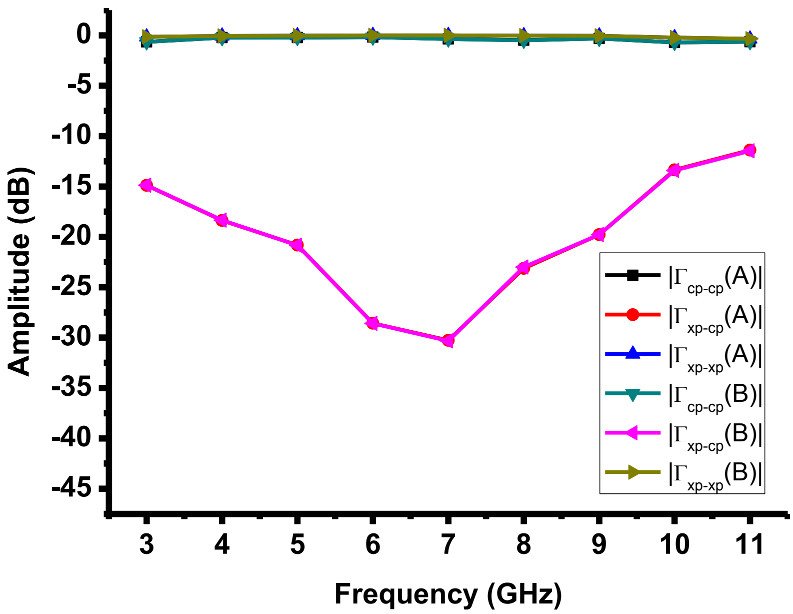

Figure 4-19 Amplitudes of Γ_{xp-cp}, Γ_{cp-cp} and Γ_{xp-xp} for the two unit cells

Figure 4-19 shows the amplitudes of $\Gamma_{xp-cp}(A)$, $\Gamma_{xp-cp}(B)$, $\Gamma_{cp-cp}(A)$, $\Gamma_{cp-cp}(B)$, $\Gamma_{xp-xp}(A)$ and $\Gamma_{xp-xp}(B)$. It can be seen the amplitudes of $\Gamma_{xp-cp}(A)$ and $\Gamma_{xp-cp}(B)$ are equal generally. So are $\Gamma_{cp-cp}(A)$ and $\Gamma_{cp-cp}(B)$. $|\Gamma_{xp-xp}(A)|$ and $|\Gamma_{xp-xp}(B)|$ are almost the same as well.

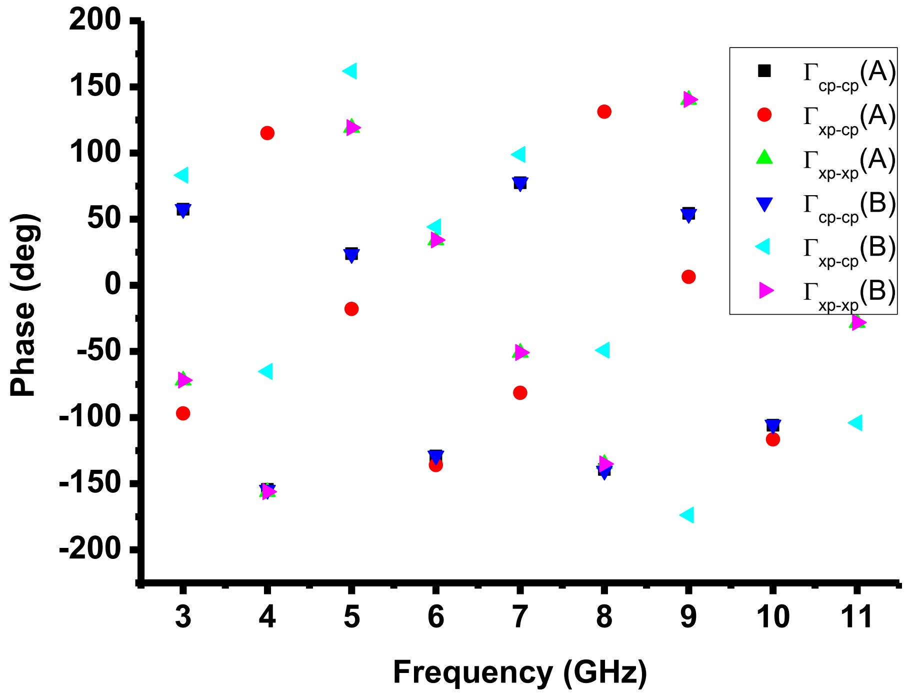

Figure 4-20 Phases of Γ_{xp-cp}, Γ_{cp-cp} and Γ_{xp-xp} for the two unit cells

The phases of $\Gamma_{xp-cp}(A)$, $\Gamma_{xp-cp}(B)$, $\Gamma_{cp-cp}(A)$, $\Gamma_{cp-cp}(B)$, $\Gamma_{xp-xp}(A)$ and $\Gamma_{xp-xp}(B)$ are demonstrated in Figure 4-20. To show their relationships clearly, the differences between the phases of $\Gamma_{xp-cp}(A)$ and $\Gamma_{xp-cp}(B)$ are drawn in Figure 4-22. Those of $\Gamma_{cp-cp}(A)$ and $\Gamma_{cp-cp}(B)$ are shown in Figure 4-21. Figure 4-23 shows the phase differences between $\Gamma_{xp-xp}(A)$ and $\Gamma_{xp-xp}(B)$.

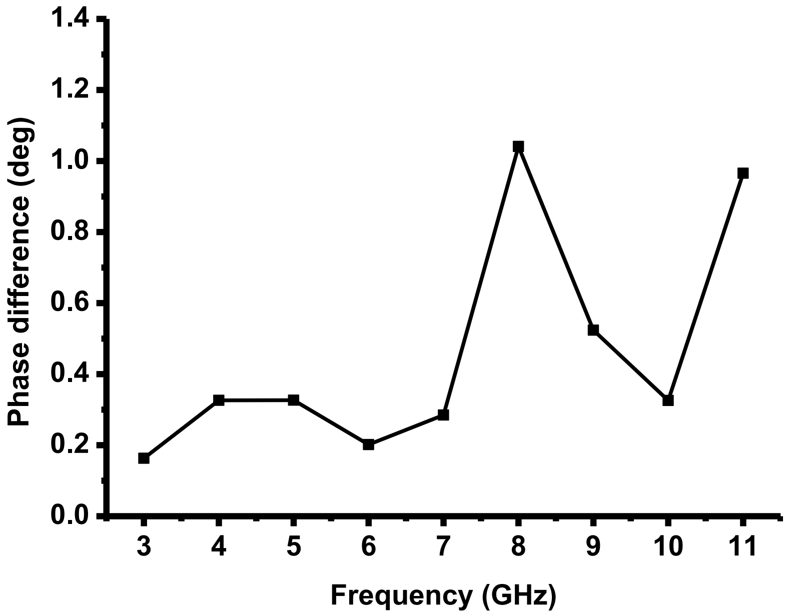

Figure 4-21 Phase differences between $\Gamma_{cp-cp}(A)$ and $\Gamma_{cp-cp}(B)$

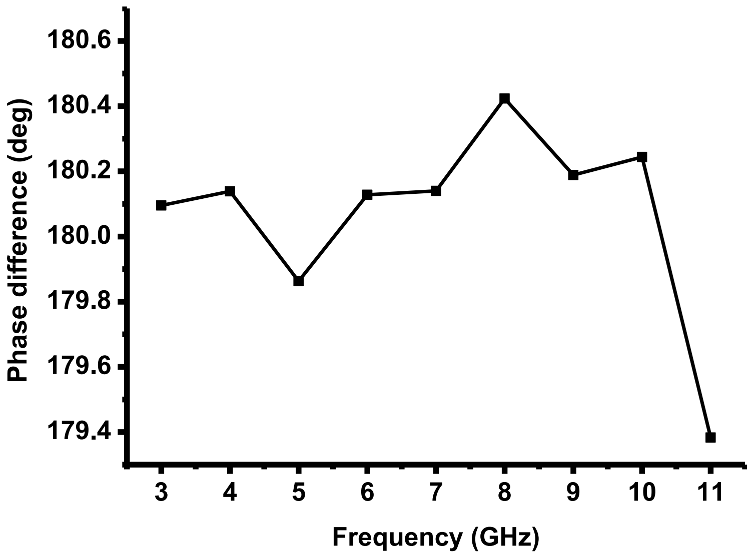

Figure 4-22 Phase differences between $\Gamma_{xp-cp}(A)$ and $\Gamma_{xp-cp}(B)$

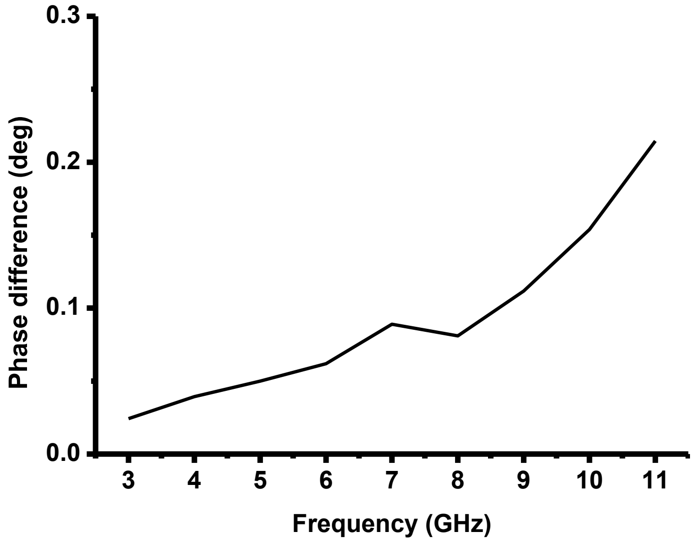

Figure 4-23 Phase differences between $\Gamma_{xp-xp}(A)$ and $\Gamma_{xp-xp}(B)$

The differences between the phases of $\Gamma_{xp-cp}(A)$ and $\Gamma_{xp-cp}(B)$ are from 179.5 to 180.5 degree, which can be seen as 180^0 approximately. Those of $\Gamma_{cp-cp}(A)$ and $\Gamma_{cp-cp}(B)$ is less than 1.1 degree, which is quite near 0^0. So are $\Gamma_{xp-xp}(A)$ and $\Gamma_{xp-xp}(B)$. Therefore, from the results of Figure 4-19, Figure 4-21, Figure 4-22 and Figure 4-23, equation (4-12) can be obtained approximately.

$$|\Gamma_{cp-cp}(A)| = |\Gamma_{cp-cp}(B)|$$
$$|\Gamma_{xp-cp}(A)| = |\Gamma_{xp-cp}(B)|$$
$$|\Gamma_{xp-xp}(A)| = |\Gamma_{xp-xp}(B)|$$
$$phase\left(\Gamma_{cp-cp}(A)\right) = phase\ \left(\Gamma_{cp-cp}(B)\right)$$
$$phase\left(\Gamma_{xp-cp}(A)\right) = -phase\ \left(\Gamma_{xp-cp}(B)\right)$$
$$phase\left(\Gamma_{xp-xp}(A)\right) = phase\ \left(\Gamma_{xp-xp}(B)\right) \quad (4\text{-}12)$$

Equation (4-12) can be rewritten as equation (4-13).

$$\Gamma_{cp-cp}(A) = \Gamma_{cp-cp}(B)$$
$$\Gamma_{xp-cp}(A) = -\Gamma_{xp-cp}(B)$$
$$\Gamma_{xp-xp}(A) = \Gamma_{xp-xp}(B) \quad (4\text{-}13)$$

As unit cell A and B contain no anisotropic materials, they are reciprocal, and equation (4-14) is obtained.

$$\Gamma_{cp-xp}(A) = -\Gamma_{cp-xp}(B) \tag{4-14}$$

Combining equation (4-13) and (4-14) gives equation (4-15).

$$\begin{aligned} \Gamma_{cp-cp}(A) &= \Gamma_{cp-cp}(B) \\ \Gamma_{xp-cp}(A) &= -\Gamma_{xp-cp}(B) \\ \Gamma_{cp-xp}(A) &= -\Gamma_{cp-xp}(B) \\ \Gamma_{xp-xp}(A) &= \Gamma_{xp-xp}(B) \end{aligned} \tag{4-15}$$

Then, rewrite equation (4-11) for unit cell A and B.

$$E_{xp}^{ref}(A) = \Gamma_{xp-xp}(A) \cdot E_{xp}^{inc} + \Gamma_{xp-cp}(A) \cdot E_{cp}^{inc} \tag{4-16}$$

$$E_{cp}^{ref}(A) = \Gamma_{cp-xp}(A) \cdot E_{xp}^{inc} + \Gamma_{cp-cp}(A) \cdot E_{cp}^{inc} \tag{4-17}$$

$$E_{xp}^{ref}(B) = \Gamma_{xp-xp}(B) \cdot E_{xp}^{inc} + \Gamma_{xp-cp}(B) \cdot E_{cp}^{inc} \tag{4-18}$$

$$E_{cp}^{ref}(B) = \Gamma_{cp-xp}(B) \cdot E_{xp}^{inc} + \Gamma_{cp-cp}(B) \cdot E_{cp}^{inc} \tag{4-19}$$

Equation (4-16) plus (4-18) gives equation (4-20).

$$E_{xp}^{ref}(A) + E_{xp}^{ref}(B) = \left[\Gamma_{xp-xp}(A) + \Gamma_{xp-xp}(B)\right] E_{xp}^{inc} + [\Gamma_{xp-cp}(A) + \Gamma_{xp-cp}(B)] \cdot E_{cp}^{inc} \tag{4-20}$$

Substituting (4-15) into (4-20) gives equation (4-21).

$$E_{xp}^{ref}(A) + E_{xp}^{ref}(B) = 2\Gamma_{xp-xp}(A) \cdot E_{xp}^{inc} \tag{4-21}$$

Similarly, equation (4-22) is obtained.

$$E_{cp}^{ref}(A) + E_{cp}^{ref}(B) = 2\Gamma_{cp-xp}(A) \cdot E_{xp}^{inc} + 2\Gamma_{cp-cp}(A) \cdot E_{cp}^{inc} \tag{4-22}$$

Equation (4-16) and (4-17) times two gives equation (4-23) and (4-24).

$$E_{xp}^{ref}(A) + E_{xp}^{ref}(A) = 2\Gamma_{xp-xp}(A) \cdot E_{xp}^{inc} + 2\Gamma_{xp-cp}(A) \cdot E_{cp}^{inc} \quad (4\text{-}23)$$

$$E_{cp}^{ref}(A) + E_{cp}^{ref}(A) = 2\Gamma_{cp-xp}(A) \cdot E_{xp}^{inc} + 2\Gamma_{cp-cp}(A) \cdot E_{cp}^{inc} \quad (4\text{-}24)$$

Comparing (4-21) and (4-23), it is known that $E_{xp}^{ref}(A) + E_{xp}^{ref}(B)$ is less than $E_{xp}^{ref}(A) + E_{xp}^{ref}(A)$ by $2\Gamma_{xp-cp}(A) \cdot E_{cp}^{inc}$, which is the most important part that contributes to the cross-polarization level. Comparing (4-22) and (4-24), it is obvious that $E_{cp}^{ref}(A) + E_{cp}^{ref}(B)$ is equal to $E_{cp}^{ref}(A) + E_{cp}^{ref}(A)$. Therefore, if unit cell A and B are applied in the same reflectarray, the cross-polarization level will be suppressed without reducing the co-polarization level.

4.3.2 Design of the TCDR with Low Cross-polarization

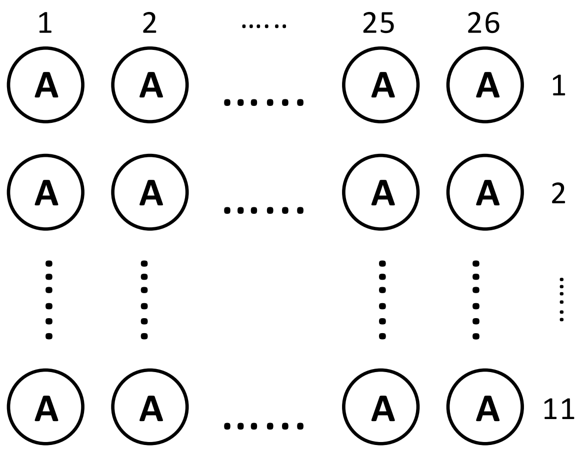

Figure 4-24 Layout of the original TCDR antenna

Figure 4-24 shows the layout of the elements in the TCDR antenna in section 4.2. It can be seen, the TCDR antenna only contains element A.

Based on the results in 4.3.1, other distributions of elements are introduced in this subsection. Figure 4-25 and Figure 4-26 demonstrate the element distributions of array 1 and array 2. The odd rows of array 1 only contain element B while the even rows only contain element A. In array 2, the 5th, 6th and 7th rows consist of element B, and other rows are composed of element A.

Compared with the original TCDR antenna, the array 1 and 2 contain element B. The mixture of element A and B could reduce the cross-polarization of the array 1 and 2.

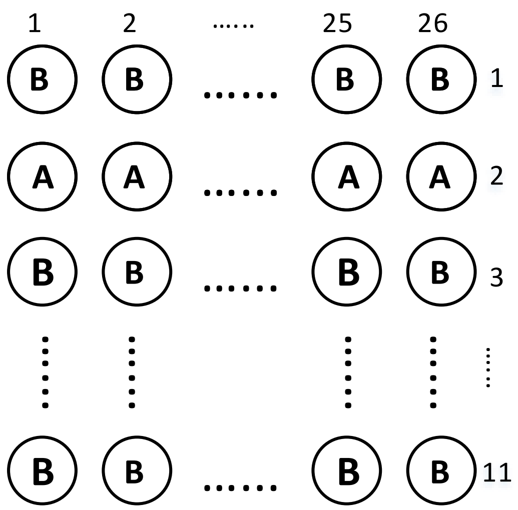

Figure 4-25 Layout of Array 1

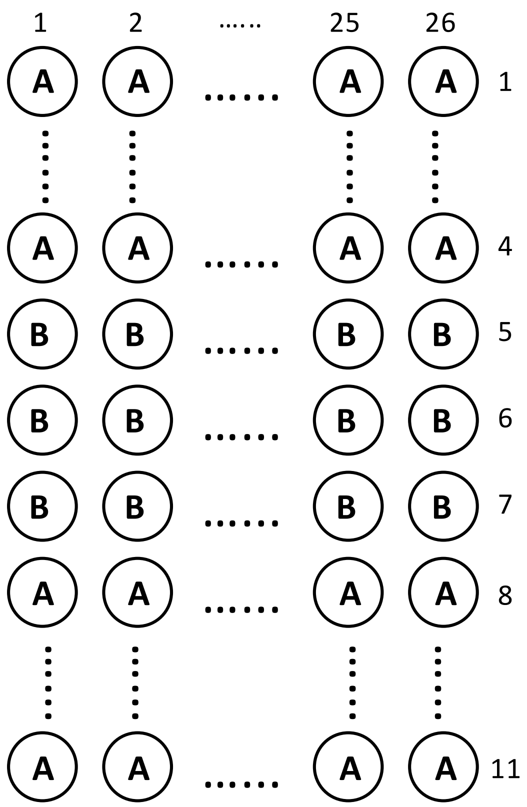

Figure 4-26 Layout of Array 2

4.3.3 Simulated Results

In this subsection, the simulated results of array 1 and 2 are given. Moreover, some results of array 1and 2 are compared with the results of the original TCDR antenna.

Figure 4-27 shows the cross-polarization levels of arrays 1, 2 and the original TCDR antenna at main beam direction. It can be seen the cross-polarization levels of array 1 and

2 are both lower than that of the original TCDR antenna. For array 1, the cross-polarization is decreased by 17 dB at 4GHz, compared with the original TCDR antenna. For array 2, the max cross-polarization reduction is about 11 dB, appearing at 4 and 7 GHz. The comparison proves that the method of reducing the cross-polarization proposed in this chapter is effective. And it has been known that the cross-polarization is reduced by $2\Gamma_{xp-cp}(A) \cdot E_{cp}^{inc}$. $2\Gamma_{xp-cp}(A) \cdot E_{cp}^{inc}$ is obtained under the assumption of normal incident waves. But the elements in Array 1 and 2 are not all illuminated normally. This brings some errors. As the layouts of Array 1 and 2 are different, the errors brought are different for Array 1 and 2 as well. Thus, the cross-polarization reduction of Array 1 is different with that of Array 2.

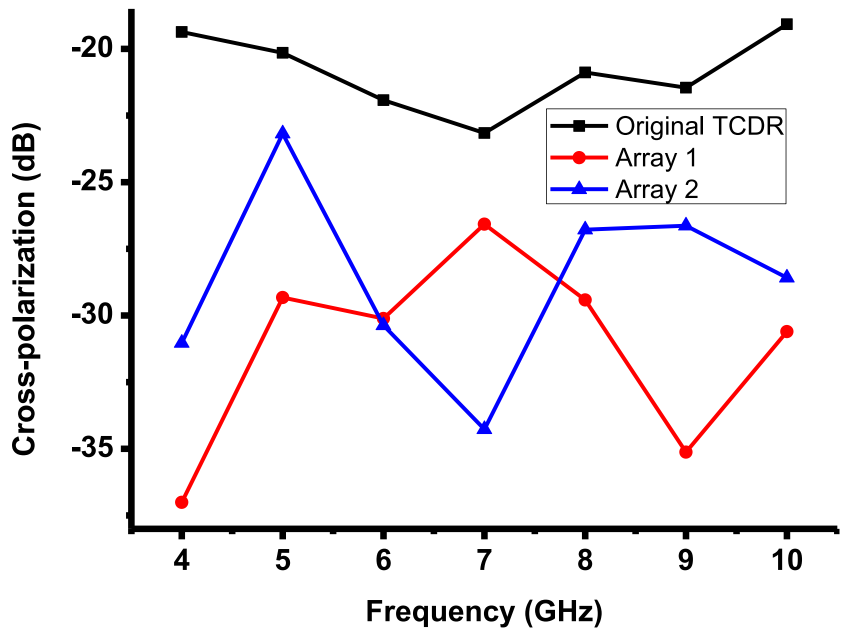

Figure 4-27 Cross-polarization comparison between arrays 1, 2 and TCDR

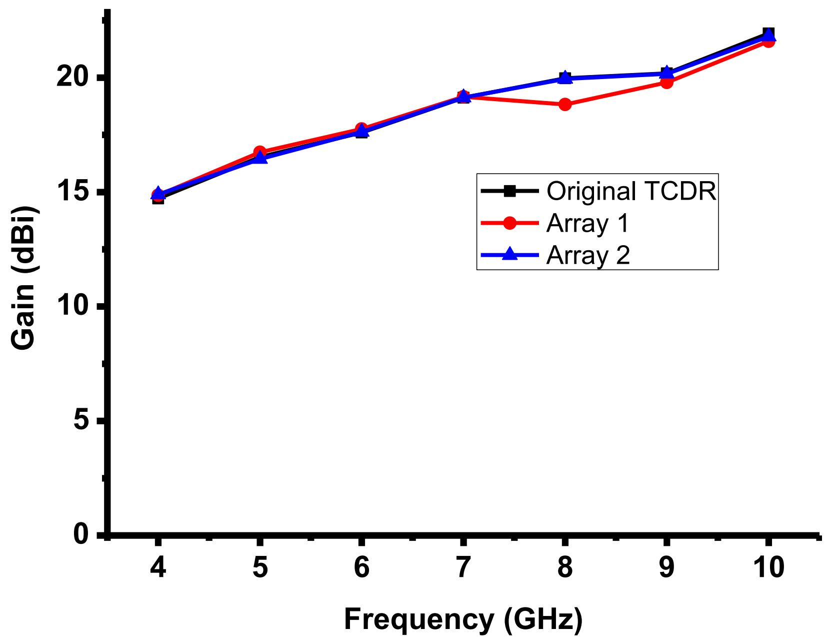

Figure 4-28 Gains of arrays 1, 2 and TCDR

Figure 4-28 shows the gains of arrays 1, 2 and the original TCDR. The gain of array 2 is equal to that of the original TCDR antenna. The gain of array 1 is lower by about 1.1 dB at 8 GHz. This may be resulted from that the Array 1 breaks the original periodic boundary of the TCDR antenna more than Array 2.

4.4 Summary

In this chapter, a novel tightly coupled reflectarray element is introduced firstly. Based on this element, a wide-band TCDR antenna is designed. The TCDR antenna consists of a wide-band feed antenna and a wide-band reflecting surface, which consists of 26×11 unit cells. The feeding antenna is a log-periodic dipole array antenna which has a wide bandwidth. Every unit cell on the reflecting surface is composed of a tightly coupled dipole and a true-time-delay line. The minimum distance between adjacent unit cells is 8 mm, which is about 1/10 wavelength at the lowest working frequency. By combining the advantages of reflectarray antennas and those of tightly coupled array antennas, the TCDR antenna achieves ultra-wide bandwidth with reduced complexity and fabrication cost. A method to minimize the phase errors of the wideband reflectarray is also developed. To verify the design concept, a prototype operating from 3.4 to 10.6 GHz is simulated and fabricated. Good agreement between simulated and measured results is observed. Within the designed frequency band, the radiation pattern of the TCDR antenna is stable and the main beam of the antenna is not distorted or split. The side lobe levels of the radiation patterns are below -11.7 dB in the entire operating band.

Then, a method of reducing the cross-polarization of the TCDR antenna is shown after the introduction of the ultra-wide-band TCDR antenna. In this part, the mechanism of the cross-polarization suppression is explained in detail. Based on this method, two reflectarrays are proposed. These two reflectarrays have the same phase distribution with that of the original TCDR antenna except the unit cell layout. The simulated results show that the new reflectarrays have lower cross-polarization level compared with the original TCDR antenna, proving the method to reduce the cross-polarization is effective.

Chapter 5. Multi-Beam Antennas

5.1 Introduction

Apart from increasing the gain and the bandwidth of antennas, multi-beam antennas could also increase the capacity of a communication system. The multi-beam antennas are antennas forming multiple beams in different directions with the same aperture. These antennas usually have two or more ports, and exciting one port can form one beam. One method to achieve multi-beam antennas is to feed antennas by circuit beam forming networks. These networks mainly include Blass, Butler and Nolen matrix networks. In this section, a novel method of designing the Nolen matrix is introduced. Based on this method, a multi-beam antenna is designed.

5.2 Multi-beam Antenna Fed by Nolen Matrix

In this section, a method to design a Nolen matrix is proposed. Then a 3×3 Nolen matrix is designed step-by-step to show the entire designing process. At last, a multi-beam fed by a 5×5 Nolen matrix is designed.

5.2.1 Method of Design an M×N Nolen Matrix

In [145], the Nolen matrix is introduced for the first time. In [207], a method of design a Nolen matrix was reported. In [208], the authors built a Nolen matrix based on the method reported in [207]. In [209], microstrip ring couplers were used to build a Nolen matrix network. The authors realized a Nolen matrix based on SIW in [210]. The authors of [209, 210] both used an asymptotic method based on [148] to design a Nolen matrix, as the method in [148] are proposed to design a Blass matrix originally.

In this section, a novel method of designing a Nolen matrix is proposed, and relative equations are also given. The method is inspired by the method of designing a Blass matrix reported in [148]. Compared with the designing method introduced in [207], the method proposed in this section is more concise and suitable for programming.

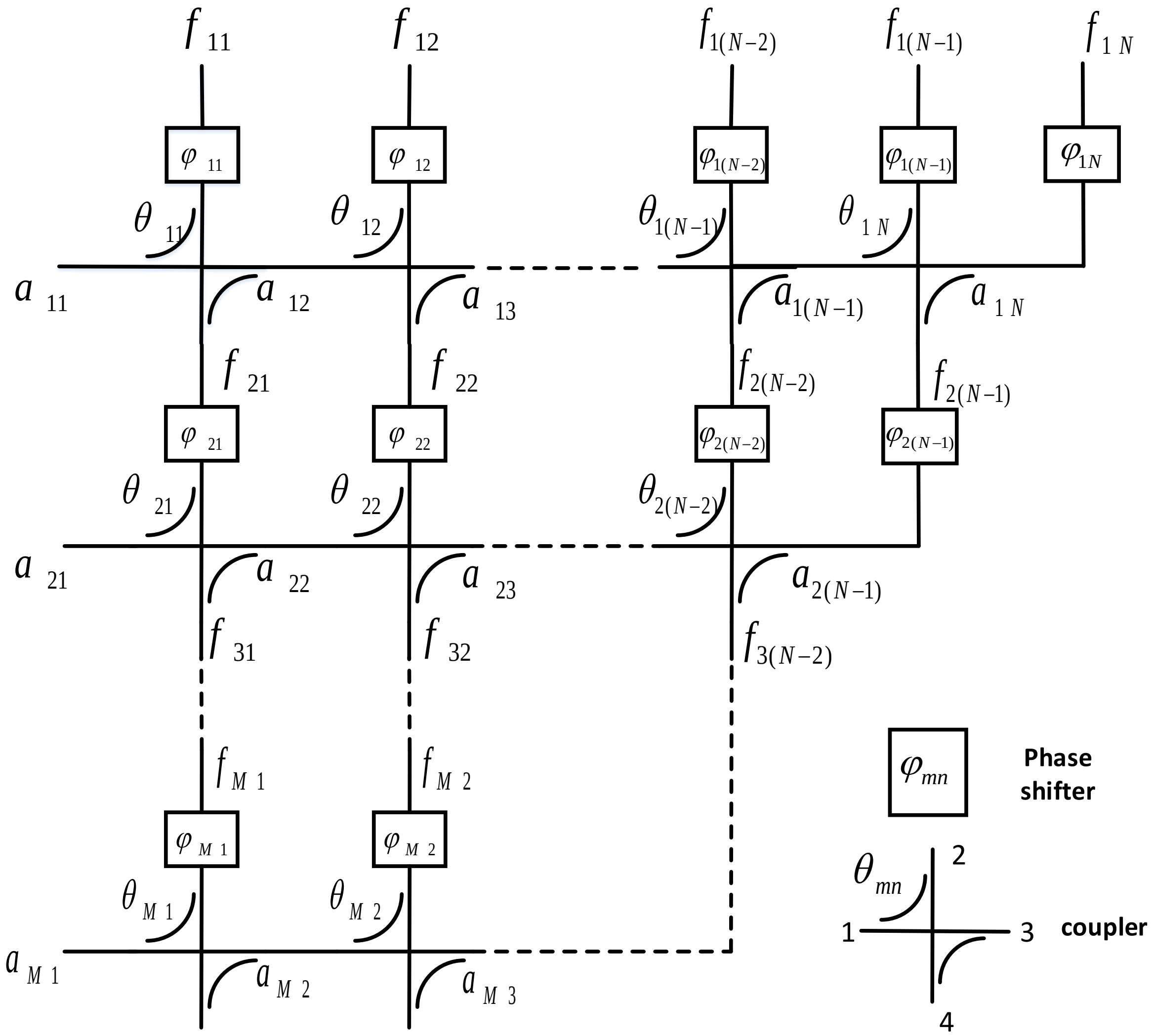

Figure 5-1 Structure of an M×N Nolen matrix

Figure 5-1 shows a structure of an M×N Nolen matrix. The matrix contains several phase shifters and couplers. The value of a phase shifter is φ_{mn}. The coupling value of a coupler is $\sin^2\theta_{mn}$. The scattering matrix of a coupler is [S], which is shown in (5-1). The phase difference between port 1 and 2 is 90^0. The phase difference between port 1 and 3 is 0^0. Port 1 and 4 is isolated. From the [S], it is known that every input port is isolated from other input ports. In the design of a Nolen matrix, the purpose is to calculate the parameters of phase shifters and couplers.

$$[S] = \begin{bmatrix} 0 & j\sin\theta_{mn} & \cos\theta_{mn} & 0 \\ j\sin\theta_{mn} & 0 & 0 & \cos\theta_{mn} \\ \cos\theta_{mn} & 0 & 0 & j\sin\theta_{mn} \\ 0 & \cos\theta_{mn} & j\sin\theta_{mn} & 0 \end{bmatrix} \tag{5-1}$$

The input and output ports are represented by a_1, $a_{2,}$…,a_M and b_1, $b_{2,}$…, b_N. $a_{mn}$and f_{mn} represent the electric field value at each point connecting couplers and phase shifters in the network. a_{mn} represents the electric field value at the point connecting two couplers or that on an input port . f_{mn} represents the electric field value at the point connecting a phase shifter and a coupler or that on an output port. And $\boldsymbol{F_{mn}}$ is defined from equation (5-2). The elements of $\boldsymbol{F_{mn}}$ are the electric field values at the points above the m^{th} row of the phase shifters shown in Figure 5-1.

$$\boldsymbol{F_{mn}} = [f_{m1}\ \ f_{m2}\ \cdots\ f_{mn}]^T \tag{5-2}$$

$\vec{\boldsymbol{a}}$ (of length M) is defined as the input vector, whose elements are the electric field values on input ports. $\vec{\boldsymbol{f}}$ (of length N) is the output vector, of which the elements are the electric field values on output ports.

$$\vec{\boldsymbol{a}} = [a_{11},\ a_{21}, \cdots, a_{M1}]^T \tag{5-3}$$

$$\vec{\boldsymbol{f}} = [f_{11},\ f_{12}, \cdots, f_{1N}]^T \tag{5-4}$$

$\overrightarrow{\boldsymbol{e_m}}$ (of length N) is defined as the excitation vector whose elements are the electric field values on output ports, when one input port a_m is excited with unit power. That is $a_{m1} = 1$.

$$\overrightarrow{\boldsymbol{e_m}} = [e_{m1},\ e_{m2}, \cdots, e_{mN}]^T \tag{5-5}$$

When all the input ports are excited with the input vector $\vec{\boldsymbol{a}}$, the output vector $\vec{\boldsymbol{f}}$ satisfies equation (5-6) due to the isolation between input ports.

$$\vec{\boldsymbol{f}} = \overrightarrow{\boldsymbol{e_1}} \cdot a_{11} + \overrightarrow{\boldsymbol{e_2}} \cdot a_{21} + \cdots + \overrightarrow{\boldsymbol{e_M}} \cdot a_{M1} \tag{5-6}$$

Equation (5-6) is re-written as Equation (5-7).

$$\vec{\boldsymbol{f}} = [\overrightarrow{\boldsymbol{e_1}},\ \overrightarrow{\boldsymbol{e_2}}, \cdots, \overrightarrow{\boldsymbol{e_M}}] \cdot \vec{\boldsymbol{a}} \tag{5-7}$$

For multi-beam networks design, $[\vec{\boldsymbol{e_1}},\ \vec{\boldsymbol{e_2}},\cdots,\vec{\boldsymbol{e_M}}]$ is known. The main working is to obtain the values of φ_{mn} and θ_{mn} where $1 \le m \le M$ and $1 \le n \le N$. The steps of the design are as follows.

(1) Let $i = 1$.

(2) Let $\vec{\boldsymbol{f}} = \vec{\boldsymbol{e_i}}$. This means only the i^{th} input port is excited with unit power ($a_{i1} = 1$), and the output vector is $\vec{\boldsymbol{e_i}}$. According to the definitions of $\vec{\boldsymbol{f}}$ and $\boldsymbol{F_{mn}}$, it can be obtained

$$\vec{\boldsymbol{f}} = \boldsymbol{F_{1N}}$$

Therefore,

$$\boldsymbol{F_{1N}} = \vec{\boldsymbol{e_i}}$$

$$\boldsymbol{F}_{(\boldsymbol{m}+\boldsymbol{1})(\boldsymbol{N}-\boldsymbol{m})} = \boldsymbol{C_m^{-1}} \cdot \boldsymbol{F}_{\boldsymbol{m}(\boldsymbol{N}-\boldsymbol{m})} \tag{5-8}$$

According to equation (5-8), $\boldsymbol{F_{i(N-i+1)}}$ can be obtained in equation (5-9). $\boldsymbol{F_{1(N-1)}}$ is a subset of $\boldsymbol{F_{1N}}$, and $\boldsymbol{F_{1(N-1)}}$ does not contain the last element of $\boldsymbol{F_{1N}}$. The derivation of equation (5-8) and the definition $\boldsymbol{C_m^{-1}}$ are shown in Appendix.

$$\begin{aligned}\boldsymbol{F}_{\boldsymbol{2}(\boldsymbol{N}-\boldsymbol{1})} &= \boldsymbol{C_1^{-1}}\boldsymbol{F}_{\boldsymbol{1}(\boldsymbol{N}-\boldsymbol{1})}\\ \boldsymbol{F}_{\boldsymbol{3}(\boldsymbol{N}-\boldsymbol{2})} &= \boldsymbol{C_2^{-1}}\boldsymbol{F}_{\boldsymbol{2}(\boldsymbol{N}-\boldsymbol{2})}\\ &\vdots\\ \boldsymbol{F}_{\boldsymbol{i}(\boldsymbol{N}-\boldsymbol{i}+\boldsymbol{1})} &= \boldsymbol{C_{i-1}^{-1}}\boldsymbol{F}_{(\boldsymbol{i}-\boldsymbol{1})(\boldsymbol{N}-\boldsymbol{i})}\end{aligned} \tag{5-9}$$

(3) As $\boldsymbol{F_{i(N-i+1)}}$ has been calculated, the values of its elements $f_{i1}\ f_{i2}\ \cdots\ f_{i(N-i+1)}$ are also known. From the [S] of the coupler, port 1 and port 3 are in-phase, and port 2 and port 4 are in-phase. The phase difference between port 1 and 2 is 90 degree. So

$$phase(a_{i1}) = phase(a_{i2}) = \cdots = phase\left(a_{i(N-i+1)}\right). \tag{5-10}$$

And from the structure of the networks, it is known that

When $n = N - i + 1$,

$$f_{in} = a_{in}e^{j\varphi_{in}} \tag{5-11}$$

Then

$$phase(f_{in}) = phase(a_{in}) + \varphi_{in}. \quad (5\text{-}12)$$

When $n < N - i + 1$,

$$phase(f_{in}) = phase(a_{in}) \ + \frac{\pi}{2} + \varphi_{in} \quad (5\text{-}13)$$

It is usually assumed that

$$phase(a_{in}) = 0, (1 \le n \le N - i + 1) \quad (5\text{-}14)$$

Then substituting equation (5-14) into (5-13) and (5-12) , (5-15) is obtained.

$$\varphi_{in} = \begin{cases} angle(f_{in}) - \frac{\pi}{2} & , \quad n = 1,2 \dots N - i \\ angle(f_{in}) & , \quad n = N - i + 1 \end{cases} \quad (5\text{-}15)$$

Thus, φ_{in} $(n = 1,2, \dots, N - i)$ is calculated.

(4) According to the method in [147], the coupling values of couplers in the i^{th} row can be calculated.

$$\sin^2(\theta_{in}) = {f_{in}}^2/({a_{i1}}^2 - \sum_{p=1}^{n-1} {f_{ip}}^2), \quad (n = 1,2, \dots, N - i)$$

(5-16)

Considering $a_{i1} = 1$ in step (2), equation (5-16) is re-written as equation (5-17).

$$\sin^2(\theta_{in}) = {f_{in}}^2/(1 - \sum_{p=1}^{n-1} {f_{ip}}^2), \quad (n = 1,2, \dots, N - i)$$

(5-17)

(5) Let $i = i + 1$ and repeat step (2)-(4) until all the values of the couples and phase shifters are calculated.

When all the five steps are completed, the values of all the phase shifters and couplers are calculated.

5.2.1.1 Excitation Vectors

The excitation vectors mentioned above should be orthonormal, which is proved in Appendix. Therefore, the excitation vector $\overrightarrow{\boldsymbol{e_m}}$ is not arbitrary. For an M×N Nolen matrix network, a series of excitation vector is given in equation (5-18). In equation (5-18), $\Delta\varphi$ is used to adjust the phase difference between elements of $\overrightarrow{\boldsymbol{e_m}}$. It should be noted that $\overrightarrow{\boldsymbol{e_m}}$ is not unique, and equation (5-18) just gives an instance.

$$\overrightarrow{\boldsymbol{e_m}} = \frac{1}{\sqrt{N}}[e^{j(\frac{2\pi(m-1)}{N}+\Delta\varphi)}\ e^{j(\frac{2\pi(m-1)}{N}+\Delta\varphi)\cdot 2}\ \cdots e^{j(\frac{2\pi(m-1)}{N}+\Delta\varphi)\cdot(N-1)}]^T, 1 \le m \le M \le N \tag{5-18}$$

$$\overrightarrow{\boldsymbol{e_p}} \cdot \overrightarrow{\boldsymbol{e_q}} = \frac{1}{N}\left[e^{j\frac{2\pi}{N}(p-q)} + e^{j\frac{2\pi}{N}(p-q)\cdot 2} + \cdots + e^{j\frac{2\pi}{N}(p-q)\cdot N}\right] \tag{5-19}$$

It is noticed that the sum of a geometric sequence is in the square brackets of equation (5-19). The common ratio is $e^{j\frac{2\pi}{N}(p-q)}$.

When $p = q$,

$$\overrightarrow{\boldsymbol{e_p}} \cdot \overrightarrow{\boldsymbol{e_q}} = \frac{1}{N}[1 + 1 + \cdots 1] = 1.$$

When $p \ne q$, as $1 \le p, q \le N$,

$$-(N-1) \le p - q \le N - 1.$$

And

$$p - q \ne 0.$$

So

$$e^{j\frac{2\pi}{N}(p-q)} \ne 1.$$

Therefore,

$$\begin{aligned}\overrightarrow{\boldsymbol{e_p}} \cdot \overrightarrow{\boldsymbol{e_q}} &= \frac{1}{N} \cdot e^{j\frac{2\pi}{N}(p-q)} \cdot \frac{1 - [e^{j\frac{2\pi}{N}(p-q)}]^N}{1 - e^{j\frac{2\pi}{N}(p-q)}} \\ &= \frac{1}{N} \cdot e^{j\frac{2\pi}{N}(p-q)} \cdot \frac{1 - [e^{j2\pi(p-q)}]}{1 - e^{j\frac{2\pi}{N}(p-q)}} \\ &= 0.\end{aligned}$$

In the sum of above,

$$\overrightarrow{\boldsymbol{e_p}} \cdot \overrightarrow{\boldsymbol{e_q}} = \begin{cases} 1\,, p = q \\ 0\,, p \neq q \end{cases}. \tag{5-20}$$

Equation (5-20) proves that the excitation vectors given by equation (5-18) are orthonormal.

With $\overrightarrow{\boldsymbol{e_m}}$, if the distance of the element antenna of the multi-beam antenna is *d*, the beam direction is θ. θ is given below, where λ_0 is the wavelength.

$$\theta = \arcsin\left(\frac{\frac{2\pi(m-1)}{N} + \Delta\varphi}{2\pi \cdot d} \cdot \lambda_0\right)$$

5.2.2 Examples of M×M Nolen matrices

Using the method introduced in 5.2.1, some examples of M×M Nolen matrices are given in this section. A 3×3 Nolen matrix is taken as the example to show how to apply the method.

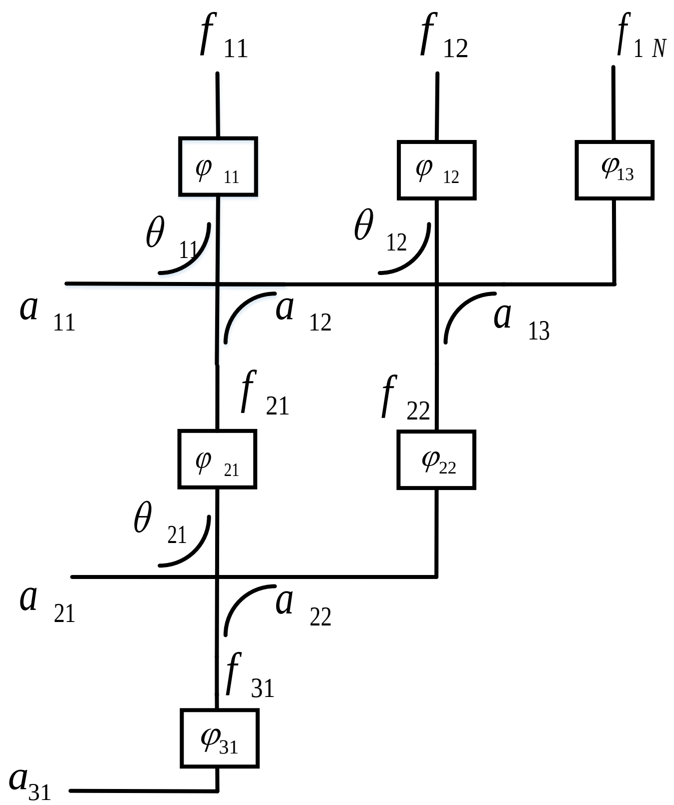

Figure 5-2 Structure of a 3×3 Nolen matrix

First, according to equation (5-18), $\overrightarrow{\boldsymbol{e_1}}$, $\overrightarrow{\boldsymbol{e_2}}$ and $\overrightarrow{\boldsymbol{e_3}}$ are set, which are shown in equation (5-21), and they are orthonormal.

$$\overrightarrow{\boldsymbol{e_1}} = \frac{1}{\sqrt{3}}\begin{bmatrix} e^{j0} \\ e^{j0} \\ e^{j0} \end{bmatrix}, \overrightarrow{\boldsymbol{e_2}} = \frac{1}{\sqrt{3}}\begin{bmatrix} e^{j\frac{2\pi}{3}} \\ e^{j\frac{4\pi}{3}} \\ e^{j2\pi} \end{bmatrix}, \overrightarrow{\boldsymbol{e_3}} = \frac{1}{\sqrt{3}}\begin{bmatrix} e^{j\frac{4\pi}{3}} \\ e^{j\frac{8\pi}{3}} \\ e^{j2\pi} \end{bmatrix} \tag{5-21}$$

Second, let $\vec{\boldsymbol{f}} = \overrightarrow{\boldsymbol{e_1}}$. This means only the input port a_1 is excited and $a_{11} = 1$ when other input ports are not excited. Therefore, according to the definition of $\vec{\boldsymbol{f}}$, f_{11}, f_{12} and f_{13} are obtained.

$$f_{11} = f_{12} = f_{13} = \frac{1}{\sqrt{3}}$$

From (5-15), φ_{11} and φ_{12} are obtained.

$$\varphi_{11} = phase(f_{11}) - \frac{\pi}{2} = -\frac{\pi}{2} = -90deg$$
$$\varphi_{12} = phase(f_{12}) - \frac{\pi}{2} = -\frac{\pi}{2} = -90deg$$
$$\varphi_{12} = phase(f_{13}) = 0$$

From (5-17), $\sin^2(\theta_{11})$ and $\sin^2(\theta_{12})$ are given below.

$$\sin^2(\theta_{11}) = \frac{{f_{11}}^2}{1} = \frac{1}{3}$$
$$\sin^2(\theta_{12}) = \frac{{f_{12}}^2}{1 - {f_{11}}^2} = \frac{1}{2}$$

Thus, φ_{11}, φ_{12}, $\sin^2(\theta_{11})$ and $\sin^2(\theta_{12})$ are calculated.

Third, let $\vec{\boldsymbol{f}} = \overrightarrow{\boldsymbol{e_2}}$. This means only the input port a_2 is excited and $a_{21} = 1$ when other input ports are not excited. From the definition of $\vec{\boldsymbol{f}}$ and $\boldsymbol{F_{mn}}$, $\boldsymbol{F_{13}}$ and $\boldsymbol{F_{12}}$ are obtained.

$$\boldsymbol{F_{13}} = \vec{\boldsymbol{f}} = \overrightarrow{\boldsymbol{e_2}} = \frac{1}{\sqrt{3}}\begin{bmatrix} e^{j\frac{2\pi}{3}} \\ e^{j\frac{4\pi}{3}} \\ e^{j2\pi} \end{bmatrix}$$

$$\boldsymbol{F_{12}} = \frac{1}{\sqrt{3}}\begin{bmatrix} e^{j\frac{2\pi}{3}} \\ e^{j\frac{4\pi}{3}} \end{bmatrix}$$

Then, $\boldsymbol{B_1}$and $\boldsymbol{C_1^{-1}}$ are obtained.

$$\boldsymbol{B_1} = \begin{bmatrix} -0.8165i & 0 \\ 0.4082i & -0.7071i \\ 0.4082i & -0.7071i \end{bmatrix}$$

$$\boldsymbol{C_1^{-1}} = \begin{bmatrix} 1.2247i & 0 \\ 0.7071i & 1.4142i \end{bmatrix}$$

From (5-9), $\boldsymbol{F_{22}}$ is obtained.

$$\boldsymbol{F_{22}} = \boldsymbol{C_1^{-1}}\boldsymbol{F_{12}} = \begin{bmatrix} -0.6124 - 0.3536i \\ 0.3536 - 0.6124i \end{bmatrix}$$

As $\boldsymbol{F_{22}} = [f_{21} \quad f_{22}]^T$, f_{21} and f_{22} are obtained.

$$f_{21} = -0.6124 - 0.3536i$$

$$f_{22} = 0.3536 - 0.6124i$$

Then

$$\varphi_{21} = phase(f_{21}) - \frac{\pi}{2} = 2.0944 = 120deg$$

$$\varphi_{22} = phase(f_{22}) = -1.0472 = -60deg$$

$$\sin^2(\theta_{21}) = \frac{{f_{21}}^2}{1} = \frac{1}{2}$$

Thus, φ_{21} and $\sin^2(\theta_{21})$ are calculated.

Fourth, let $\vec{\boldsymbol{f}} = \overrightarrow{\boldsymbol{e_3}}$. This means only the input port a_3 is excited and $a_{31} = 1$ when other input ports are not excited. From the definition of $\vec{\boldsymbol{f}}$ and $\boldsymbol{F_{mn}}$, $\boldsymbol{F_{13}}$ and $\boldsymbol{F_{12}}$ are obtained.

$$\boldsymbol{F_{13}} = \vec{\boldsymbol{f}} = \overrightarrow{\boldsymbol{e_2}} = \frac{1}{\sqrt{3}}\begin{bmatrix} e^{j\frac{4\pi}{3}} \\ e^{j\frac{8\pi}{3}} \\ e^{j2\pi} \end{bmatrix}$$

$$\boldsymbol{F_{12}} = \frac{1}{\sqrt{3}}\begin{bmatrix} e^{j\frac{4\pi}{3}} \\ e^{j\frac{8\pi}{3}} \end{bmatrix}$$

$\boldsymbol{B_1}$and $\boldsymbol{C_1^{-1}}$ have been obtained in the third step.

$$\boldsymbol{B_1} = \begin{bmatrix} -0.8165i & 0 \\ 0.4082i & -0.7071i \\ 0.4082i & -0.7071i \end{bmatrix}$$

$$\boldsymbol{C_1^{-1}} = \begin{bmatrix} 1.2247i & 0 \\ 0.7071i & 1.4142i \end{bmatrix}$$

Then

$$\boldsymbol{F_{22}} = \boldsymbol{C_1^{-1}}\boldsymbol{F_{12}} = \begin{bmatrix} 0.6124 - 0.3536i \\ -0.3536 - 0.6124i \end{bmatrix}.$$

$$\boldsymbol{F_{21}} = [0.6124 - 0.3536i]$$

Then, $\boldsymbol{B_2}$and $\boldsymbol{C_2^{-1}}$ are obtained.

$$\boldsymbol{B_2} = \begin{bmatrix} -0.3536 + 0.6124i \\ 0.6124 + 0.3536i \end{bmatrix}$$

$$\boldsymbol{C_2^{-1}} = [-0.7071 - 1.2246i]$$

Then

$$\boldsymbol{F_{31}} = \boldsymbol{C_2^{-1}}\boldsymbol{F_{21}} = [-0.8660 - 0.5000i].$$

As $\boldsymbol{F_{31}} = [f_{31}]^T$,

$$f_{31} = -0.8660 - 0.5000i.$$

And

$$\varphi_{31} = phase(f_{31}) = -2.618 = -150deg$$

So far, the values of shifters and couplers composing of a 3×3 Nolen matrix network has been obtained. φ_{mn} and $\sin^2(\boldsymbol{\theta_{mn}})$ are shown in Table 5-1 and Table 5-2.

Table 5-1 $\boldsymbol{\varphi_{mn}}$ in a 3×3 Nolen Matrix Network (unit: degree)

m \ n	1	2	3
1	-90	-90	0

2	120	-60	
3	-150		

Table 5-2 $\sin^2(\theta_{mn})$in a 3×3 Nolen Matrix Network

m \ n	1	2
1	$\frac{1}{3}$	$\frac{1}{2}$
2	$\frac{1}{2}$	

Using the similar method, we can also design Nolen matrices with other sizes. For a 5×5 Nolen matrix network, the excitation vectors are given below, according to equation (5-18).

$$\overrightarrow{\boldsymbol{e_1}} = \frac{1}{\sqrt{5}}[e^{j0}\ e^{j0}\ e^{j0}\ e^{j0}\ e^{j0}]^T$$

$$\overrightarrow{\boldsymbol{e_2}} = \frac{1}{\sqrt{5}}[e^{j\frac{2\pi}{5}}\ e^{j\frac{4\pi}{5}}\ e^{j\frac{6\pi}{5}}\ e^{j\frac{8\pi}{5}}\ e^{j2\pi}]^T$$

$$\overrightarrow{\boldsymbol{e_3}} = \frac{1}{\sqrt{5}}[e^{j\frac{4\pi}{5}}\ e^{j\frac{8\pi}{5}}\ e^{j\frac{2\pi}{5}}\ e^{j\frac{6\pi}{5}}\ e^{j2\pi}]^T$$

$$\overrightarrow{\boldsymbol{e_4}} = \frac{1}{\sqrt{5}}[e^{j\frac{6\pi}{5}}\ e^{j\frac{2\pi}{5}}\ e^{j\frac{8\pi}{5}}\ e^{j\frac{4\pi}{5}}\ e^{j2\pi}]^T$$

$$\overrightarrow{\boldsymbol{e_5}} = \frac{1}{\sqrt{5}}[e^{j\frac{8\pi}{5}}\ e^{j\frac{6\pi}{5}}\ e^{j\frac{4\pi}{5}}\ e^{j\frac{2\pi}{5}}\ e^{j2\pi}]^T$$

φ_{mn} and $\sin^2(\boldsymbol{\theta_{mn}})$ in the 5×5 Nolen matrix network are shown in Table 5-3 and Table 5-4.

Table 5-3 φ_{mn} in a 5×5 Nolen Matrix Network (unit: degree)

m \ n	1	2	3	4	5
1	-90	-90	-90	-90	0
2	-288	-228	-176	-36	
3	-288	-235	-94		
4	-288	-148			
5	-198				

Table 5-4 $\sin^2(\theta_{mn})$ in a 5×5 Nolen Matrix Network

m \ n	1	2	3	4
1	0.2	0.25	0.3333	0.5
2	0.25	0.4327	0.6752	
3	0.3333	0.6752		
4	0.5			

5.2.3 Multi-beam Antenna Fed by a 5×5 Nolen Matrix Network

In this section, a multi-beam antenna based on a 5×5 Nolen matrix network is simulated and fabricated. The antenna works at 5 GHz.

5.2.3.1 5×5 Nolen Matrix Network

As mentioned above, $\sin^2(\theta_{mn})$ of couplers in a 5×5 Nolen matrix network could be 0.2, 0.25, 0.3333, 0.5, 0.4327 and 0.6752. Those correspond to -6.98 dB, -6.02 dB, -4.77 dB, -3 dB, -3.64 dB and -1.71 dB couplers. Circular branch line couplers are applied in this design because they can offer flexible coupling with a fixed size[209]. And it is easy to embed this type of couplers in a Nolen matrix network.

The couplers are printed on the substrate (Arlon AD255A), of which the relative permittivity is 2.55.

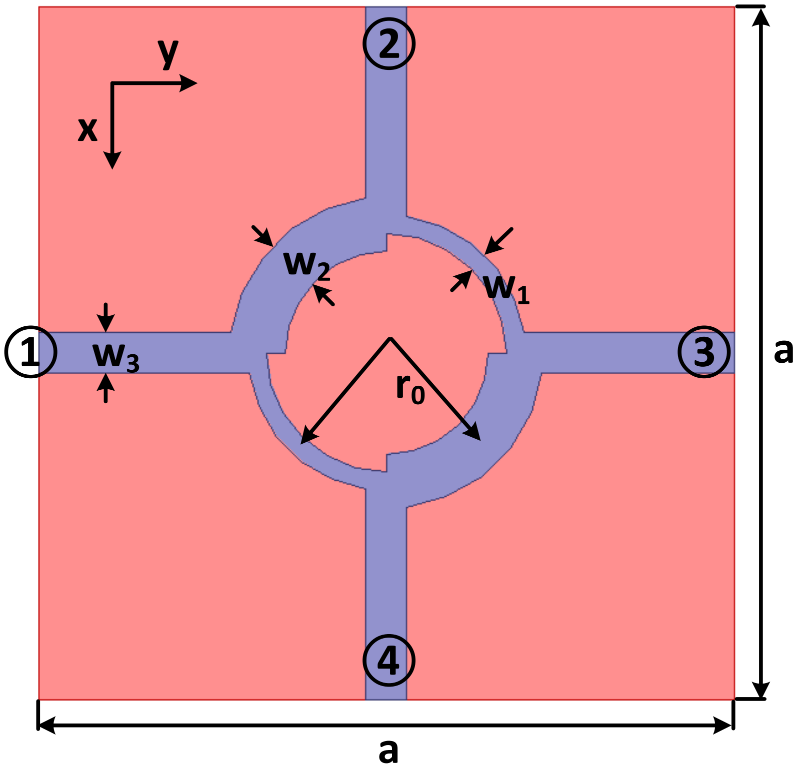

Figure 5-3 Structure of microstrip ring coupler

Figure 5-3 shows the basic structure of the microstrip ring couplers composing of the Nolen matrix network. The ring couplers can be seen as the transformation of a classical branch-line coupler, which is shown in Figure 5-4. Compared with traditional branch-line couplers, some straight microstrip lines are replaced by curved microstrip lines in ring couplers.

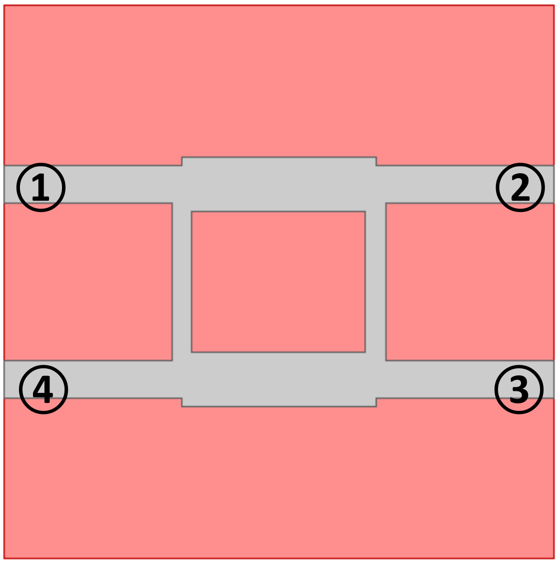

Figure 5-4 Branch-line coupler

In Figure 5-3, the thickness of the substrate is 0.762 mm. To make the characteristic impedance of the microstrip line as 50 Ω, w_3 is set 2.13 mm. In order to build the network conveniently, the dimensions of all required couplers are 31.76×31.76 mm^2. For all couplers, only w_1, w_2 , and r_0 are different. r_0 is the radius of the ring in the couplers. w_1 and w_2 are the widths of the curved microstrip lines.

The simulated S parameters of all couplers are shown below.

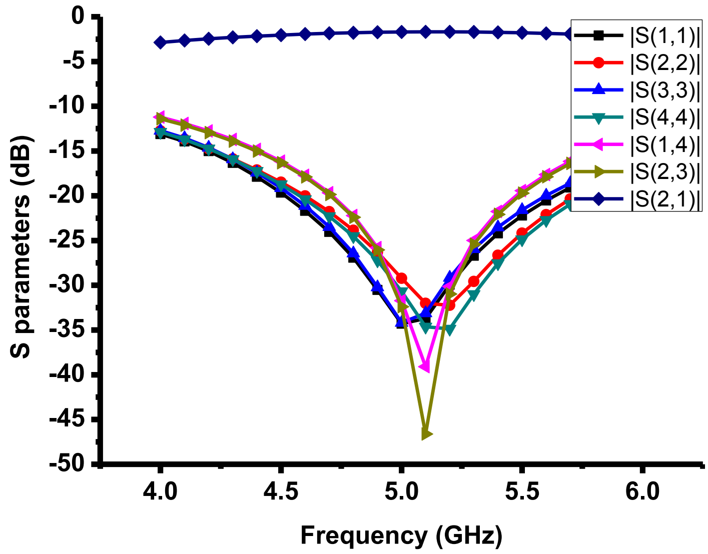

(a) Amplitudes

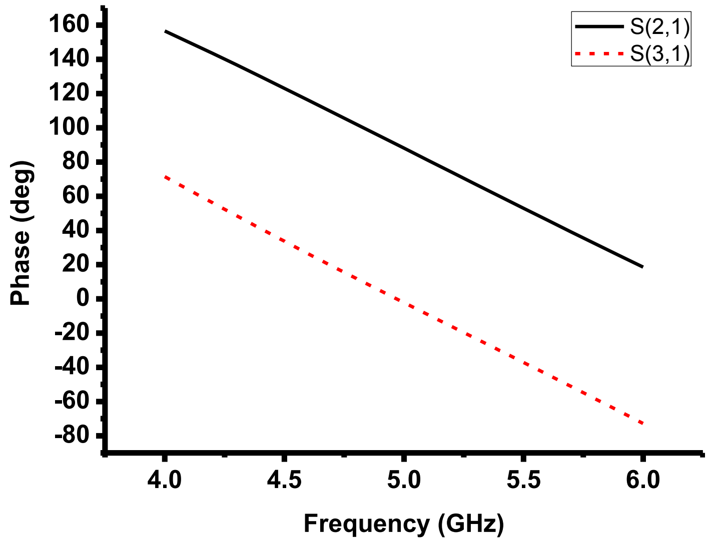

(b) Phases

Figure 5-5 S parameters of -1.71 dB coupler (a) amplitudes and (b) phases

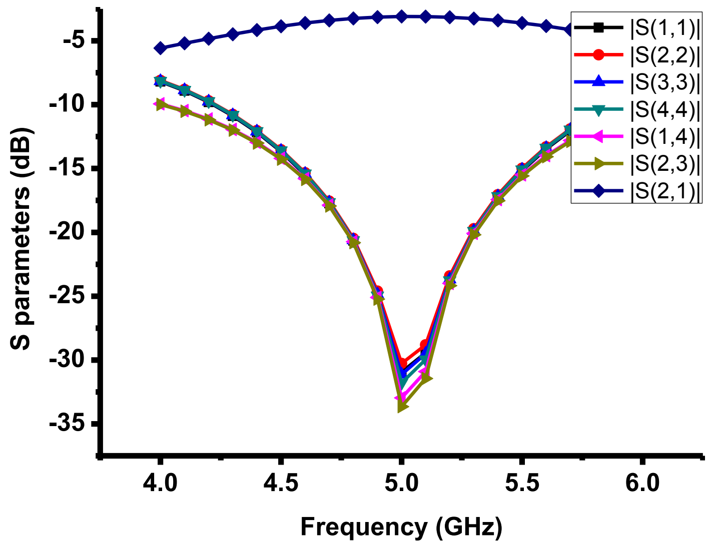

(a) Amplitudes

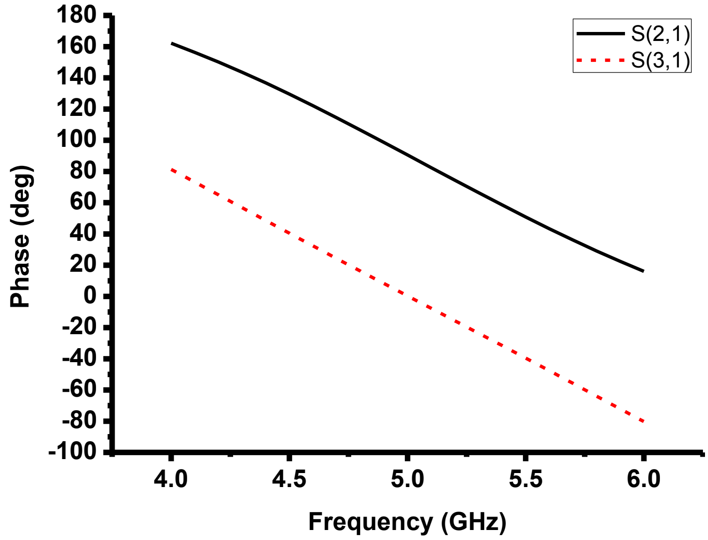

(b) Phases

Figure 5-6 S parameters of -3 dB coupler (a) amplitudes and (b) phases

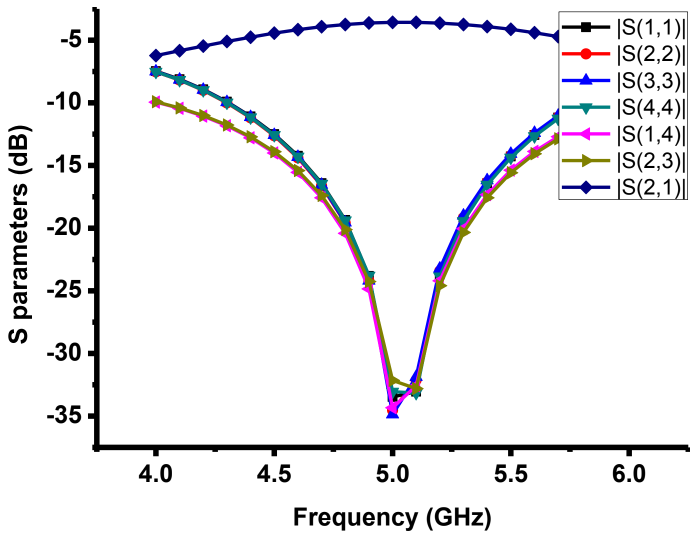

(a) Amplitudes

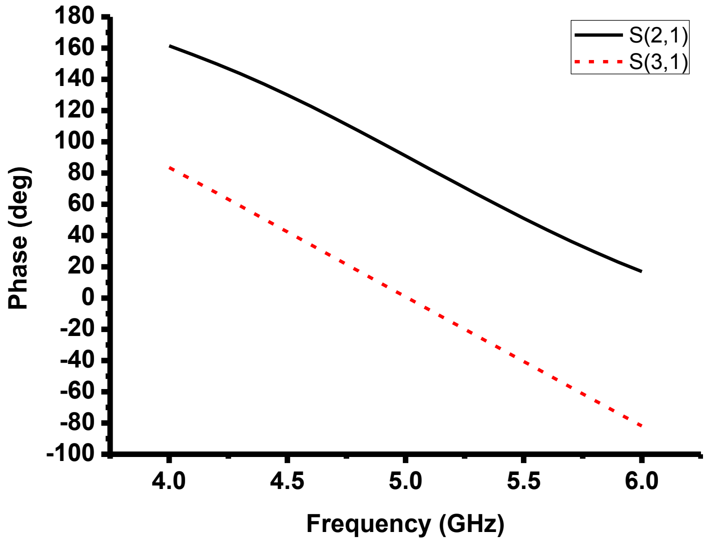

(b) Phases

Figure 5-7 S parameters of -3.64 dB coupler (a) amplitudes and (b) phases

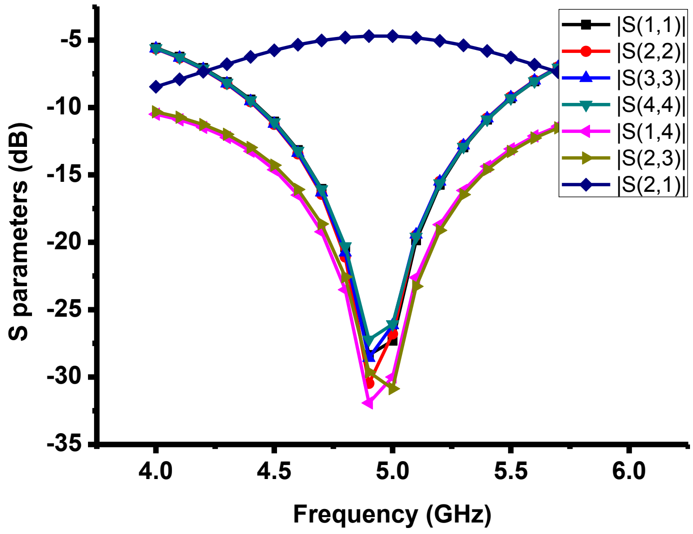

(a) Amplitudes

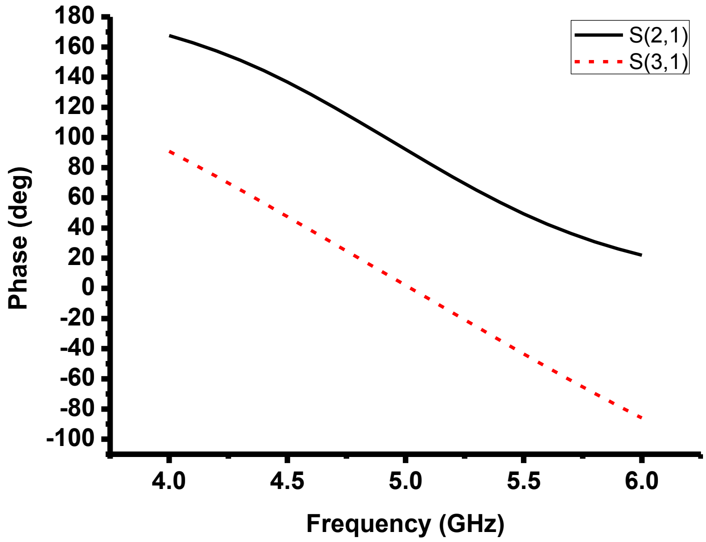

(b) Phases

Figure 5-8 S parameters of -4.77 dB coupler (a) amplitudes and (b) phases

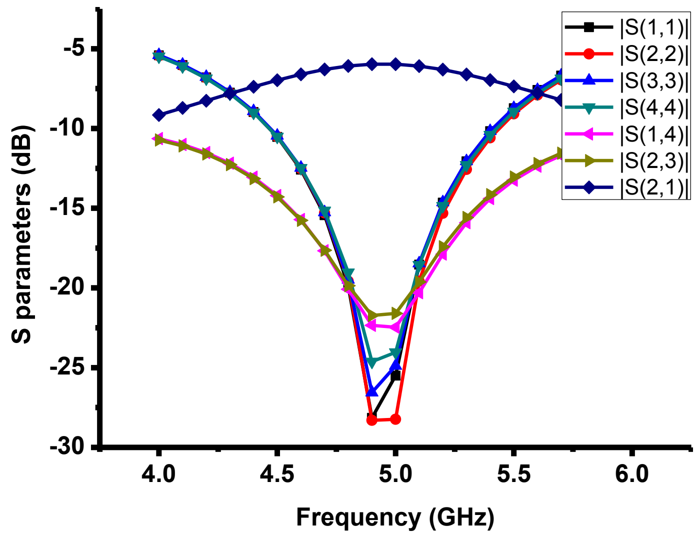

(a) Amplitudes

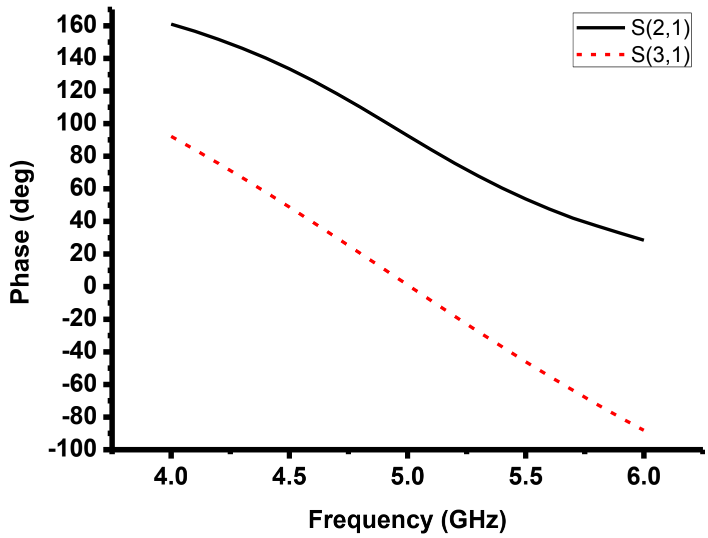

(b) Phases

Figure 5-9 S parameters of -6.02 dB coupler (a) amplitudes and (b) phases

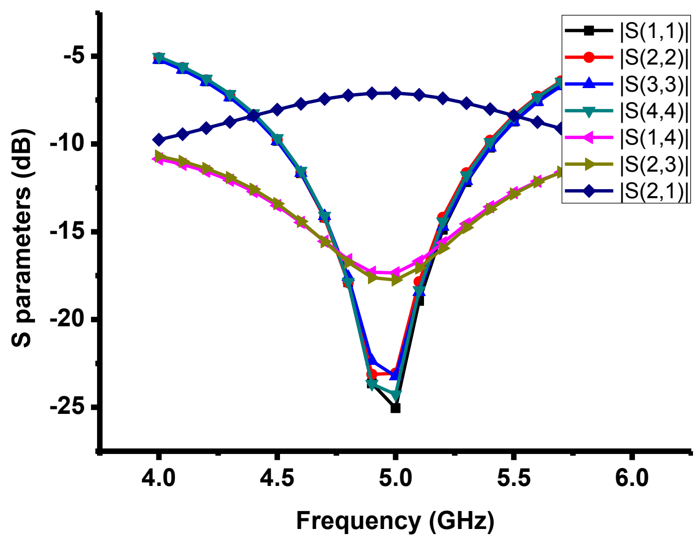

(a) Amplitudes

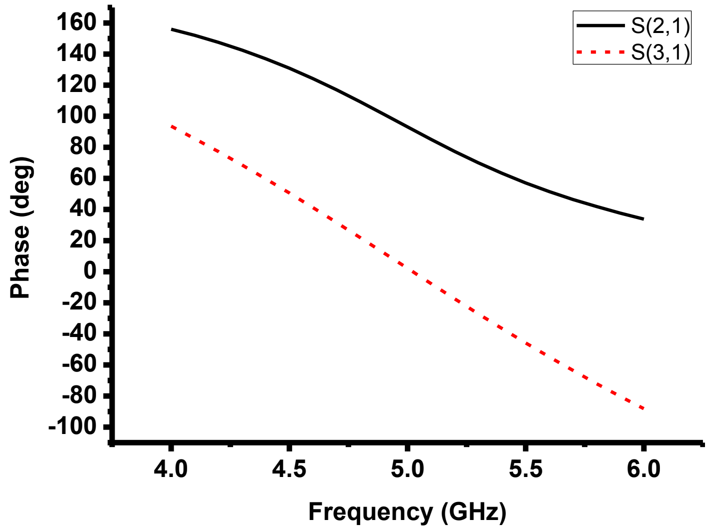

(b) Phases

Figure 5-10 S parameters of -6.98 dB coupler (a) amplitudes and (b) phases

From the simulated results above, it can be seen that the reflection coefficients of all ports are below -20 dB at 5 GHz. The transmission coefficients between port 1 and 4 are below -17 dB for all couplers. The phase of S(2,1) and S(3,1) are also given above. Theoretically, the phase of S(2,1) is 90^0 , and that of S(3,1) is 0^0 at 5 GHz.

Table 5-5 Simulated phases of S(2,1) and S(3,1) at 5 GHz (unit: degree)

	phase(S(2,1))	phase(S(3,1))	phase(S(2,1))- phase(S(3,1))
-1.71 dB coupler	88.1	-2.2	90.3
-3 dB coupler	90.6	0.3	90.3
-3.64 dB coupler	91.0	0.8	90.2
-4.77 dB coupler	92.1	2.0	90.1
-6.02 dB coupler	92.7	1.1	91.6
-6.98 dB coupler	93.1	2.2	91.0

Table 5-5 shows the simulated phases of S(2,1) and S(3,1) at 5 GHz. The max error of the phase of S(2,1) is 3.1^0, which appears in -6.98 dB coupler. For the phase of S(3,1), the largest error is 2.2^0, which exist in -1.71 dB and -6.98 couplers. The differences between the phases of S(2,1) and S(3,1) are also shown in Table 5-5.

Table 5-6 Theoretical and Simulated Coupling Values at 5 GHz

	theoretical coupling value	simulated coupling value	error
-1.71 dB coupler	0.6752	0.67659	2%
-3 dB coupler	0.5	0.48997	2%
-3.64 dB coupler	0.4327	0.43911	1%
-4.77 dB coupler	0.3333	0.33797	1%
-6.02 dB coupler	0.25	0.25288	1%
-6.98 dB coupler	0.2	0.19475	3%

The theoretical and simulated coupling values of couplers at 5 GHz are shown in Table 5-6. The errors between theoretical and simulated values are less than 3%.

Thus, all the needed couplers are obtained. The next goal is to design the phase shifters. In this design, microstrip lines act as phase shifters. First of all, the values of phase shifters in Table 5-3 need to be modified. φ_{mn} represents the original value of a phase shifter and φ'_{mn} represents the modified value of a phase shifter. The relationship between φ_{mn} and φ'_{mn} is shown in equation (5-22).

$$\varphi'_{mn} = \begin{cases} \varphi_{mn} - \varphi_{m1}, m = 1 \\ \varphi_{mn} - \varphi_{m(6-m)} + 8.3^0, m = 2,3,4 \\ \varphi_{mn} - \varphi_{m(6-m)}, m = 5 \end{cases} \tag{5-22}$$

The modification process just changes the absolute values of phase shifters, and in the same row, the phase difference between any two phase shifters is unchanged. Table 5-7 shows the original values of phase shifters while modified values are demonstrated in Table 5-8.

The purpose of the modification is to reduce the complexity of the network. When $m = 1$, four phase shifters are needed originally. After being modified, only 1 phase shifter of 90^0 is needed. When $m = 2,3,4$, $\varphi'_{m(6-m)} = 8.3^0$, which means the phase shifters connecting couplers $\theta_{m(5-m)}$ and $\theta_{(m+1)(5-m)}$ are the same. Thus, the lengths of microstrip lines connecting couplers $\theta_{m(5-m)}$ and $\theta_{(m+1)(5-m)}$ are the same. When $m = 5$, $\varphi'_{m(6-m)} = 0$. Before being modified, the network needs 14 phase shifters in total. After modification, only 10 phase shifters are needed. The network is simplified significantly by modifying the values of phase shifters.

Table 5-7 Original φ_{mn} in the 5×5 Nolen Matrix Network

m \ n	1	2	3	4	5
1	-90	-90	-90	-90	0
2	-288	-228	-176	-36	
3	-288	-235	-94		
4	-288	-148			
5	-198				

Table 5-8 Modified φ'_{mn} in the 5×5 Nolen Matrix Network

m \ n	1	2	3	4	5
1	0	0	0	0	90
2	-243.7	-183.7	-131.7	8.3	
3	- 185.7	-132.7	8.3		
4	- 131.7	8.3			
5	0				

It should be noted that the modification of phase shifters changes the excitation vector $\overrightarrow{\boldsymbol{e}_m}$. The new excitation vector is $\overrightarrow{\boldsymbol{e}_m}'$.

$$
\begin{aligned}
\overrightarrow{\boldsymbol{e}_1}' &= e^{j90^0} \cdot \overrightarrow{\boldsymbol{e}_1} \\
\overrightarrow{\boldsymbol{e}_2}' &= e^{j(90+44.3)^0} \cdot \overrightarrow{\boldsymbol{e}_2} \\
\overrightarrow{\boldsymbol{e}_3}' &= e^{j(90+44.3+102.3)^0} \cdot \overrightarrow{\boldsymbol{e}_3} \\
\overrightarrow{\boldsymbol{e}_4}' &= e^{j(90+44.3+102.3+156.3)^0} \cdot \overrightarrow{\boldsymbol{e}_4} \\
\overrightarrow{\boldsymbol{e}_5}' &= e^{j(90+44.3+102.3+156.3+198)^0} \cdot \overrightarrow{\boldsymbol{e}_5}
\end{aligned}
$$

Thus,

$$\overrightarrow{\boldsymbol{e}_1}' = \frac{1}{\sqrt{5}}[e^{j90^0}\ e^{j90^0}\ e^{j90^0}\ e^{j90^0}\ e^{j90^0}]^T$$

$$\overrightarrow{\boldsymbol{e}_2}' = \frac{1}{\sqrt{5}}[e^{-j153.7^0}\ e^{-j81.7^0}\ e^{-j9.7^0}\ e^{j62.3^0}\ e^{j134.3^0}]^T$$

$$\overrightarrow{\boldsymbol{e}_3}' = \frac{1}{\sqrt{5}}[e^{j20.6^0}\ e^{j164.6^0}\ e^{-j51.4^0}\ e^{j92.6^0}\ e^{-j123.4}]^T$$

$$\overrightarrow{\boldsymbol{e}_4}' = \frac{1}{\sqrt{5}}[e^{-j111.1^0}\ e^{j104.9^0}\ e^{-j39.1^0}\ e^{-j183.1^0}\ e^{j32.9^0}]^T$$

$$\overrightarrow{\boldsymbol{e}_5}' = \frac{1}{\sqrt{5}}[e^{j158.9^0}\ e^{j86.9^0}\ e^{j14.9^0}\ e^{-j57.1^0}\ e^{-j129.1^0}]^T$$

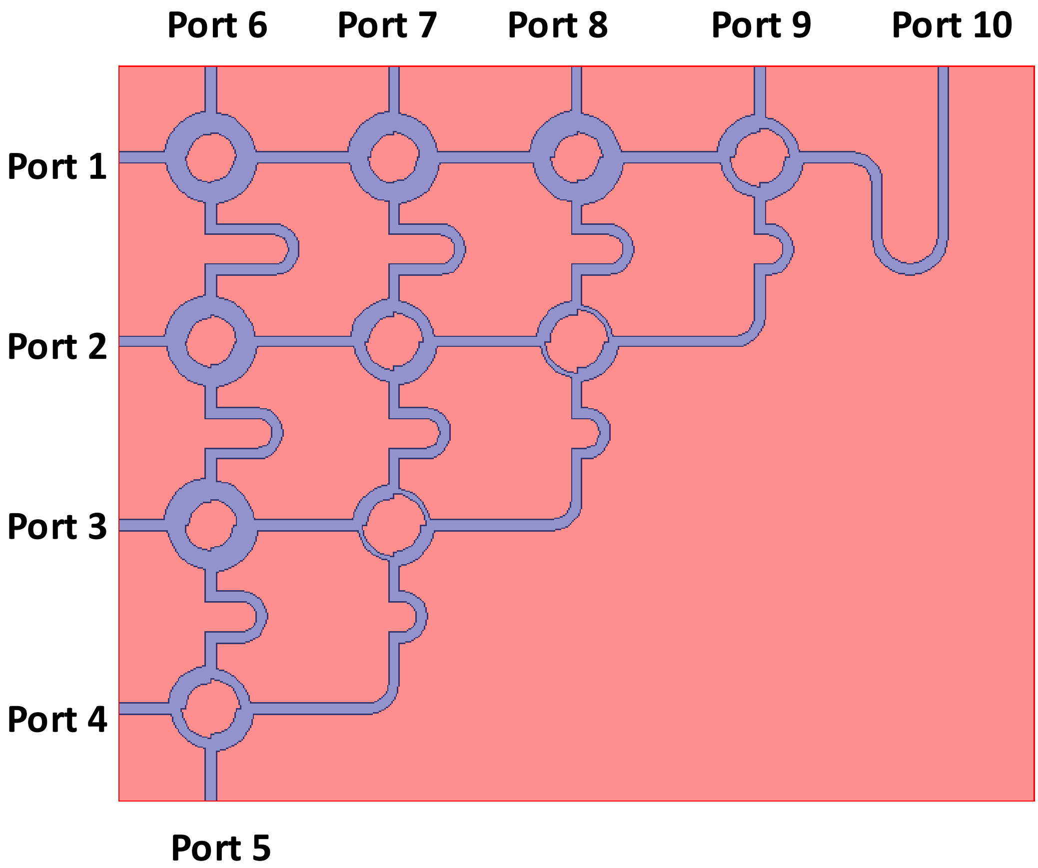

Figure 5-11 Model of the 5×5 Nolen matrix network

Figure 5-11 shows the model of the 5×5 Nolen matrix network in HFSS. Ports 1, 2, 3, 4 and 5 are input ports. Port 6, 7, 8, 9 and 10 are output ports, which are connected to antennas later. Some simulated scattering parameters (S parameters) of the network are shown below. Figure 5-12 shows the reflection coefficients of the five input ports. It can be seen the reflection coefficients are below -15 dB at GHz.

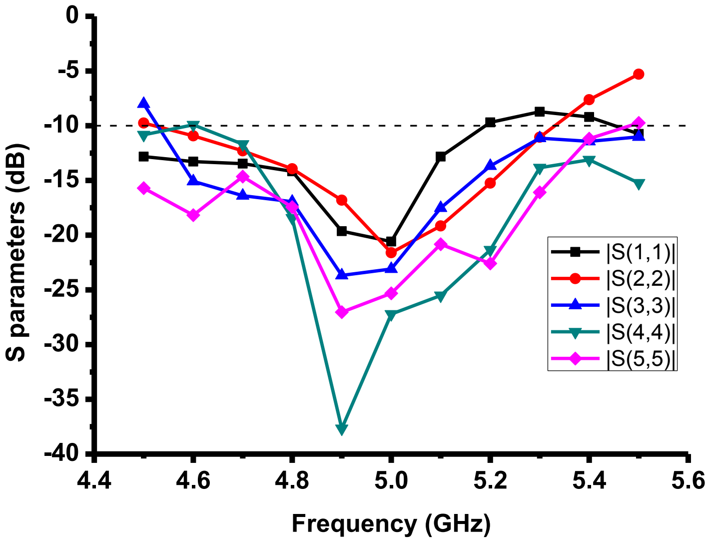

Figure 5-12 Reflection coefficients of input ports

Figure 5-13 shows the amplitudes of scattering parameters from input ports to output ports.

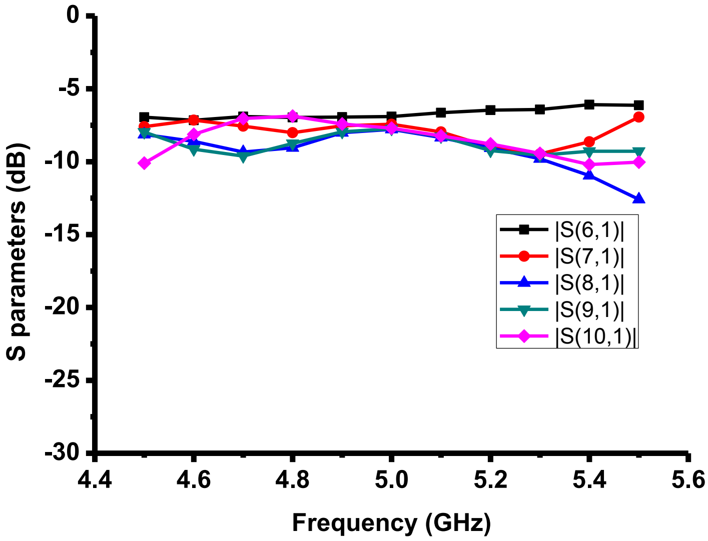

(a) Port 1 to output ports

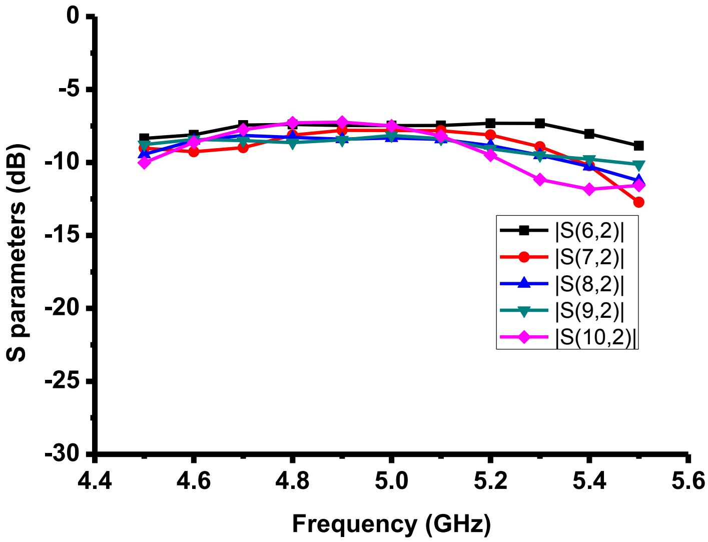

(b) Port 2 to output ports

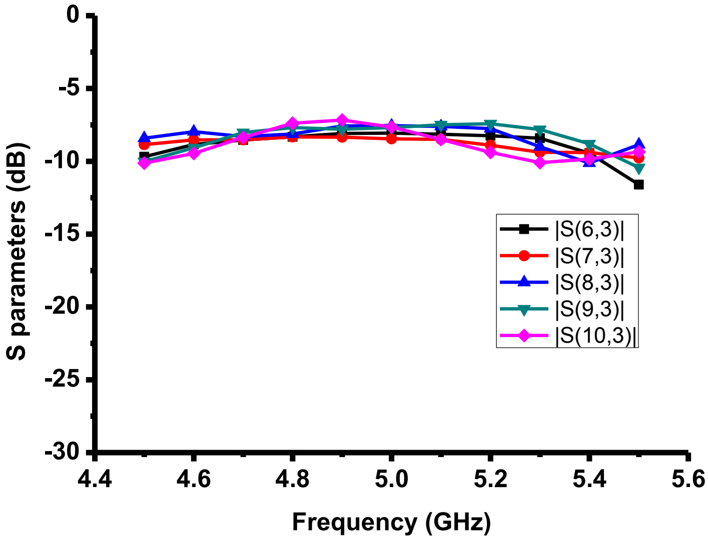

(c) Port 3 to output ports

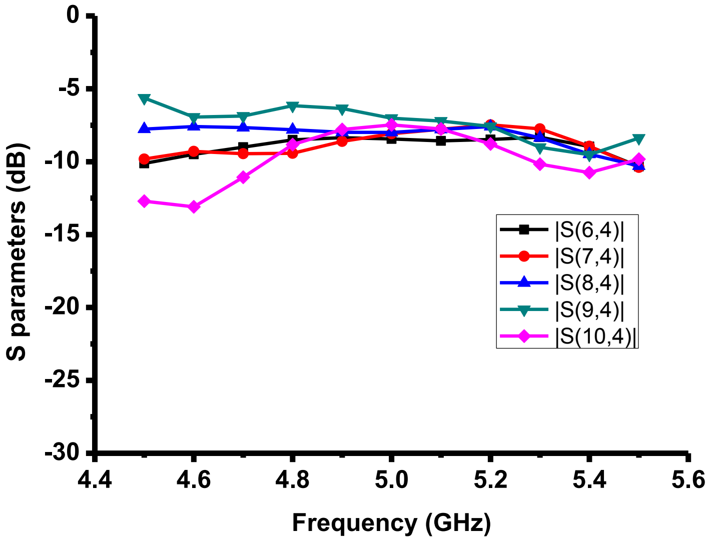

(d) Port 4 to output ports

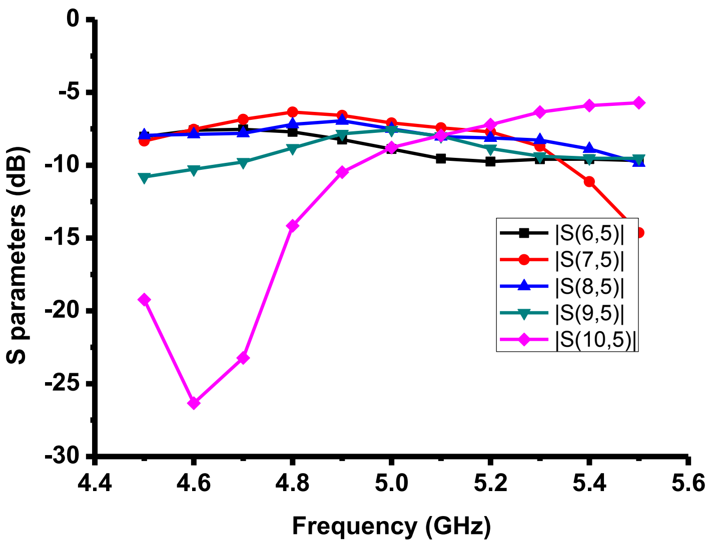

(e) Port 5 to output ports

Figure 5-13 Amplitudes of S parameters from (a) Port 1, (b) Port 2, (c) Port 3, (d) Port 4 and (e) Port 5 to output ports

The amplitudes of the simulated scattering parameters from input ports to output ports at 5 GHz is shown in Table 5-9. Theoretically, the amplitudes of these parameters should be -6.99 dB under the assumption of the lossless network. In practice, the metal and dielectric loss is inevitable in the network. Moreover, the network is based on microstrip lines, and the network itself can radiate energy to free space. Therefore, the network is not strictly lossless, and the amplitudes of simulated scattering parameters in Table 5-9 are not equal to -6.99 dB exactly.

Table 5-9 Amplitudes of Simulated Scattering Parameters at 5 GHz (unit: dB)

|S(6,1)|	|S(7,1)|	|S(8,1)|	|S(9,1)|	|S(10,1)|
-6.9	-7.4	-7.8	-7.7	-7.7
|S(6,2)|	|S(7,2)|	|S(8,2)|	|S(9,2)|	|S(10,2)|
-7.5	-7.8	-8.3	-8.2	-7.5
|S(6,3)|	|S(7,3)|	|S(8,3)|	|S(9,3)|	|S(10,3)|
-7.5	-7.8	-8.3	-8.2	-7.5
|S(6,4)|	|S(7,4)|	|S(8,4)|	|S(9,4)|	|S(10,4)|
-8.4	-8.1	-8.0	-7.0	-7.5

|S(6,5)|	|S(7,5)|	|S(8,5)|	|S(9,5)|	|S(10,5)|
-8.89	-7.1	-7.5	-7.6	-8.8

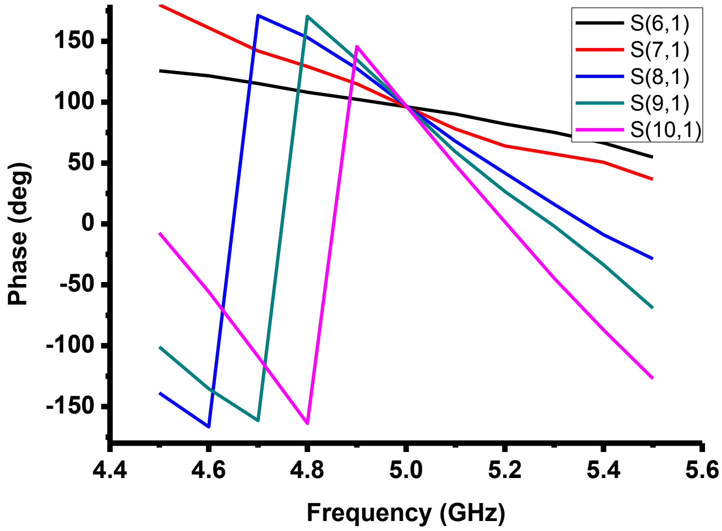

(a) Port 1 to output ports

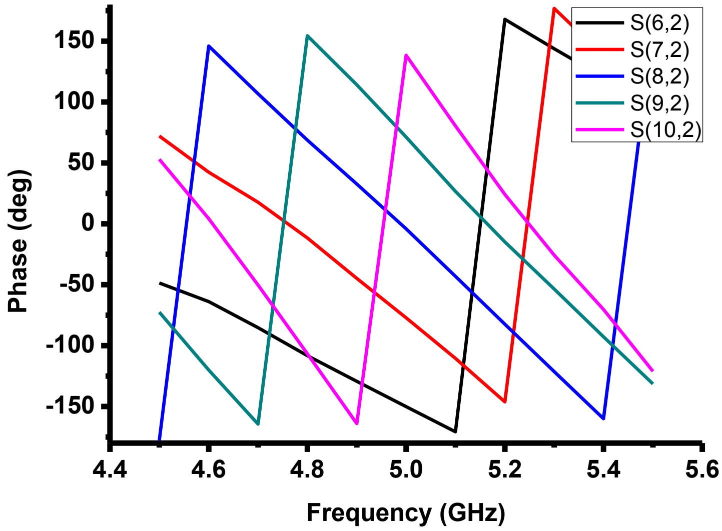

(b) Port 2 to output ports

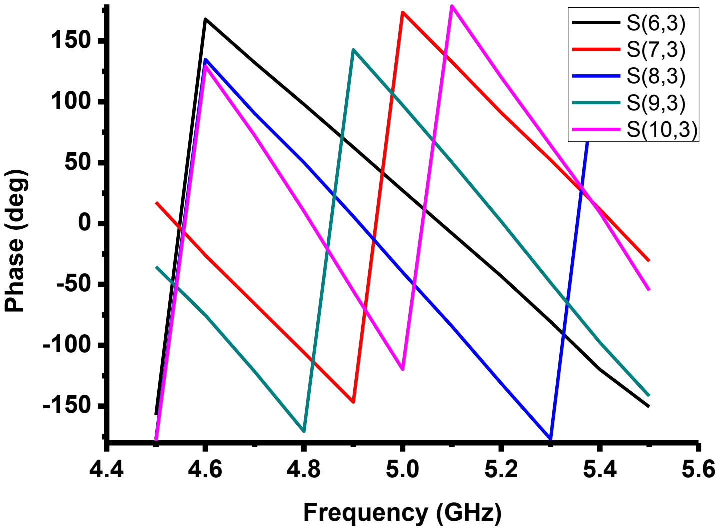

(c) Port 3 to output ports

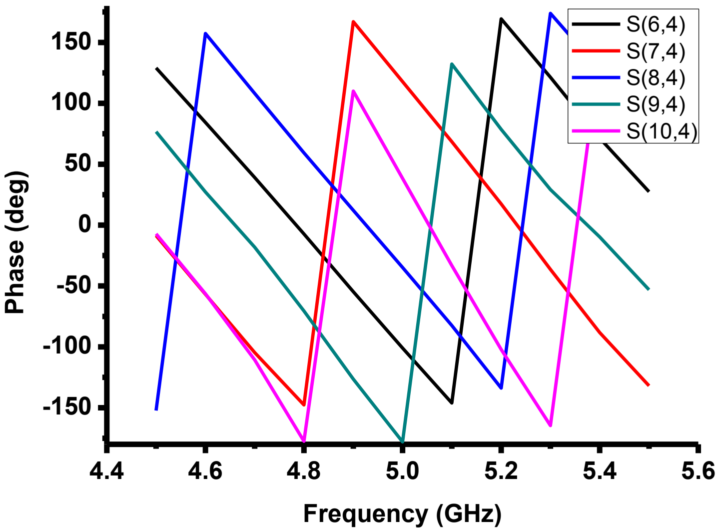

(d) Port 4 to output ports

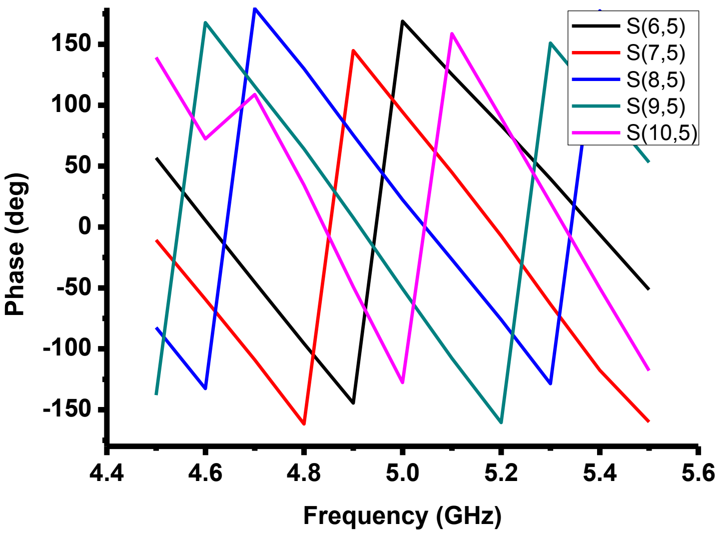

(d) Port 5 to output ports

Figure 5-14 Phases of S Parameters from (a) Port 1, (b) Port 2, (c) Port 3, (d) Port 4 and (e) Port 5 to output ports

Figure 5-14 shows the phases of the simulated S parameters. The theoretical and simulated phases at 5 GHz are compared in Table 5-10. Two factors lead to the differences between the simulated and theoretical values. One is that the network is not strictly lossless, of which the reasons have been explained above. The other factor is that the simulated values of couplers and phase shifters are not precisely equal to the theoretical ones. For example, Table 5-6 shows the differences between the simulated and theoretical values of couplers.

Table 5-10 Phases of Theoretical and Simulated S Parameters at 5 GHz (unit: degree)

S parameter	S(6,1)	S(7,1)	S(8,1)	S(9,1)	S(10,1)
Theoretical phase	90	90	90	90	90
Simulated phase	96.3	96.3	97	97.1	97
S parameter	S(6,2)	S(7,2)	S(8,2)	S(9,2)	S(10,2)
Theoretical phase	-153.7	-81.7	-9.7	62.3	134.3
Simulated phase	-150.1	-77.1	-4.1	71.3	138.4
S parameter	S(6,3)	S(7,3)	S(8,3)	S(9,3)	S(10,3)
Theoretical phase	20.6	164.6	-51.4	92.6	-123.4
Simulated phase	27.2	173.4	-40	97.3	-120
S parameter	S(6,4)	S(7,4)	S(8,4)	S(9,4)	S(10,4)
Theoretical phase	-111.1	104.9	-39.1	-183.1	32.9
Simulated phase	-101	117.8	-34.8	-178	38.4
S parameter	S(6,5)	S(7,5)	S(8,5)	S(9,5)	S(10,5)
Theoretical phase	158.9	86.9	14.9	-57.1	-129.1
Simulated phase	168.9	94.5	22.4	-50.6	-127.6

Figure 5-15 demonstrates the phase differences between adjacent output ports with one input port excited. The simulated results are close to the theoretical ones. When port 1 is excited, the theoretical phase differences between adjacent output ports are 0^0 while the simulated ones are within 0.7^0. When port 2 is fed, the phase differences between adjacent output ports are 72^0 theoretically, and the simulated results are from 67.1^0 to 75.4^0. When port 3 is excited, the phase differences between adjacent output ports should be 144^0 while the simulated ones are from 137.3^0 to 146.6^0. The simulated phase differences between adjacent output ports are from -141.2^0 to -152.6^0 while the theoretical results are -144^0 with port 4 excited. When port 5 is fed, the theoretical phase differences between adjacent output ports are -72^0, and the simulated phase differences are from -72.1^0 to -77^0.

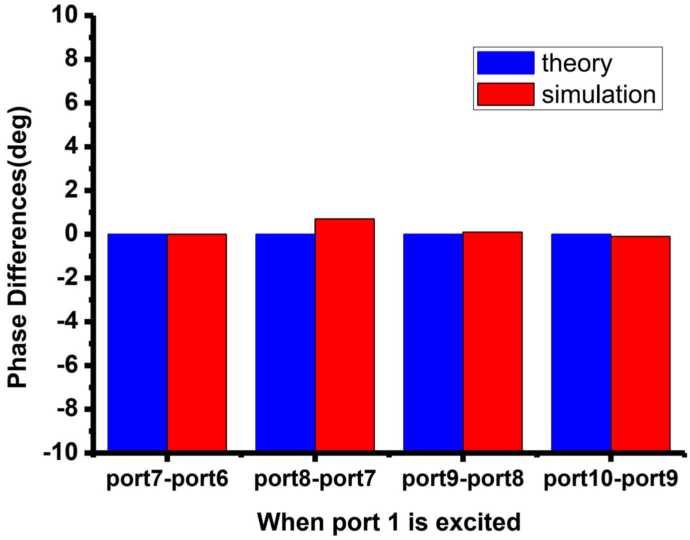

(a)

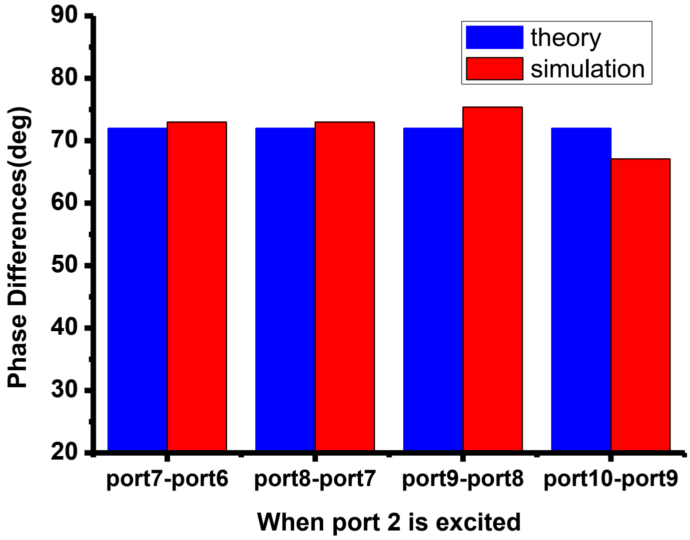

(b)

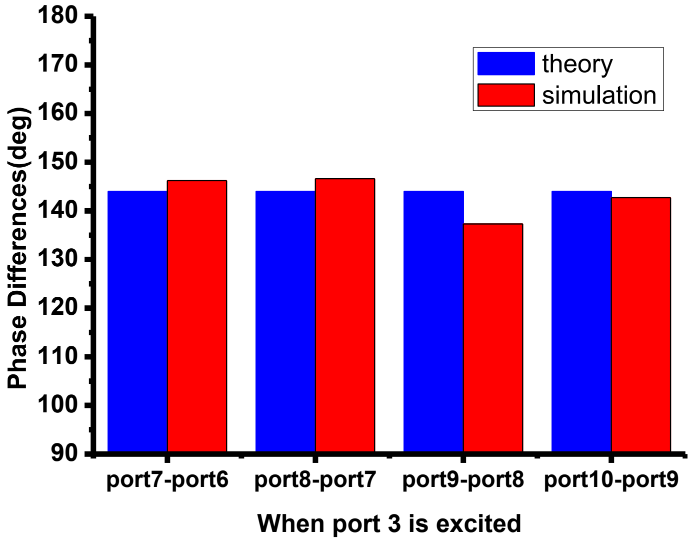
180
170
160
150
140
130
120
110
100
90
Phase Differences(deg)
theory
simulation
port7-port6
port8-port7
port9-port8
port10-port9
When port 3 is excited

(c)

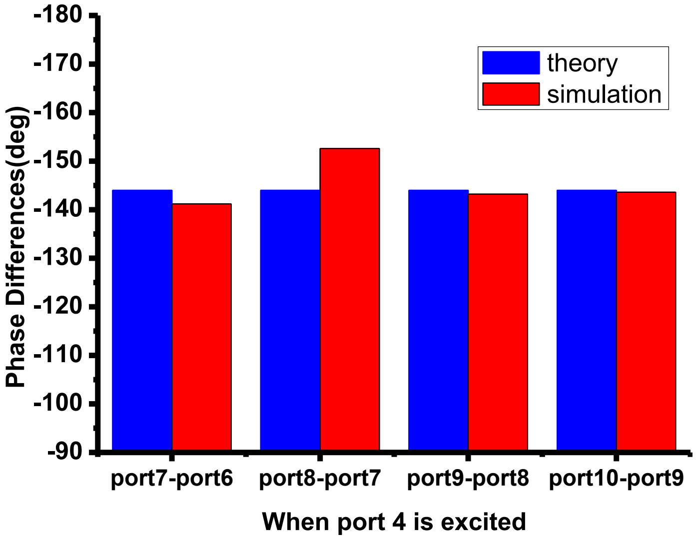
-180
-170
-160
-150
-140
-130
-120
-110
-100
-90
Phase Differences(deg)
theory
simulation
port7-port6
port8-port7
port9-port8
port10-port9
When port 4 is excited

(d)

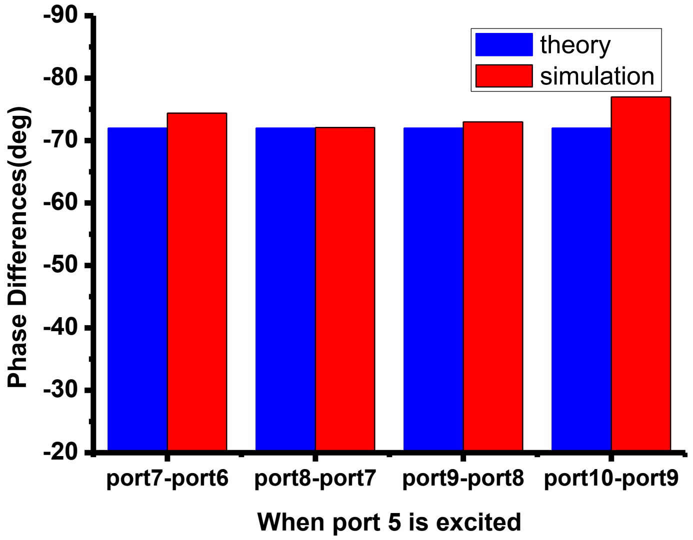
-90
-80
-70
-60
-50
-40
-30
-20
Phase Differences(deg)
theory
simulation
port7-port6
port8-port7
port9-port8
port10-port9
When port 5 is excited

(e)

Figure 5-15 Phase differences between adjacent output ports when (a) Port 1, (b) Port 2, (c) Port 3, (d) Port 4 and (e) Port 5 are excited respectively

5.2.3.2 Multi-beam Antenna with Five beams

In this subsection, a multi-beam antenna fed by a 5×5 Nolen matrix network is designed and simulated in HFSS. Then, a prototype antenna is fabricated. The prototype is measured by a vector network analyzer and in an anechoic chamber. The simulated and measured results agree well.

The element antenna applied here is a square patch antenna which is fed by a recessed microstrip line. For easy simulation and fabrication, the patch antenna and the Nolen matrix network are printed on the same substrate (Arlon AD255A). The configuration of the patch antenna is shown in Figure 5-16, and Table 3-1 shows its parameters.

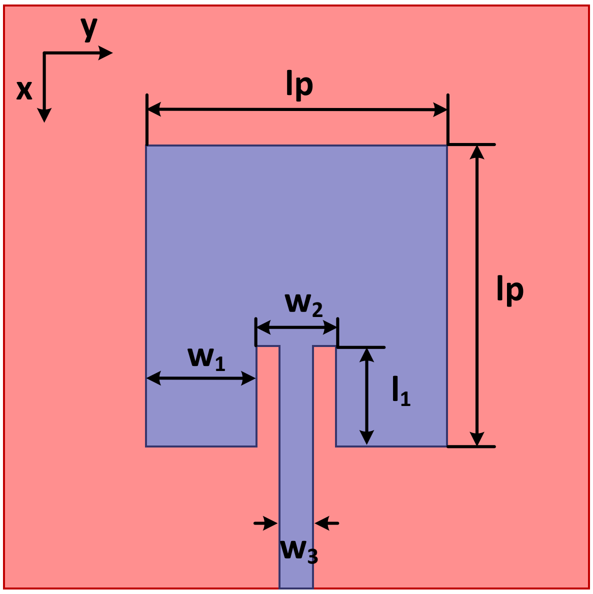

Figure 5-16 Configuration of the patch antenna

Table 5-11 Parameters of the Patch Antenna (unit: mm)

lp	l_1	w_1	w_2	w_3
18.64	6.3	6.82	5	2.13

The simulated |S11| is shown below. It can be seen the patch antenna resonates at 5 GHz.

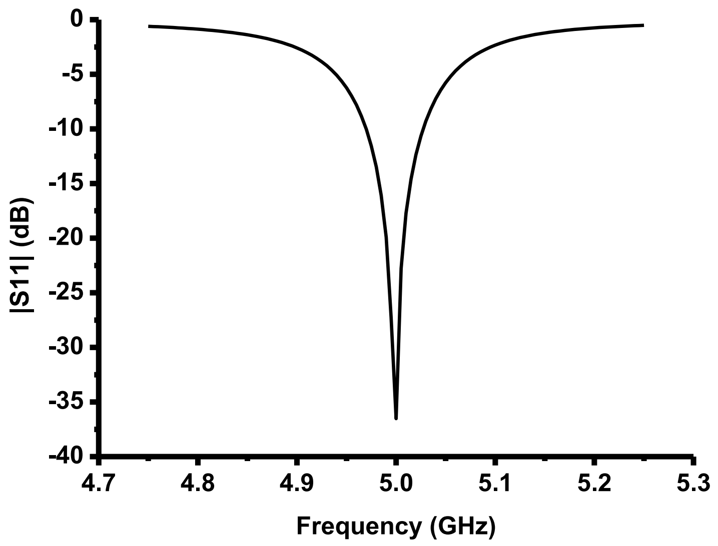

Figure 5-17 Simulated |S11| of the patch antenna

The multi-beam antenna with its feed network is shown in Figure 5-18.

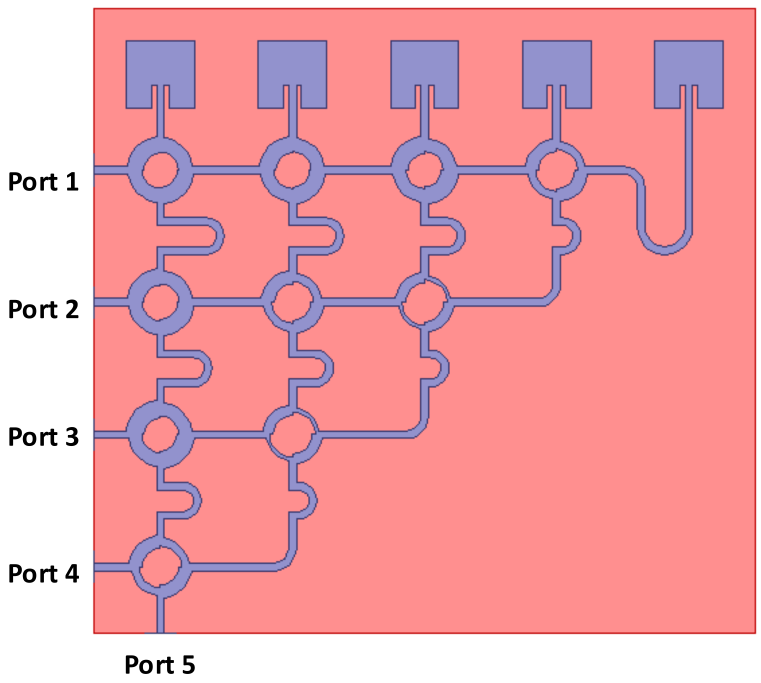

Figure 5-18 Configuration of the multi-beam antenna

The simulated and measured reflection coefficients of all input ports are given in Figure 5-19. The measured reflection coefficients shift to a lower frequency compared with simulated ones. The differences between measured and simulated results may come from the measurement error and the fabrication tolerance.

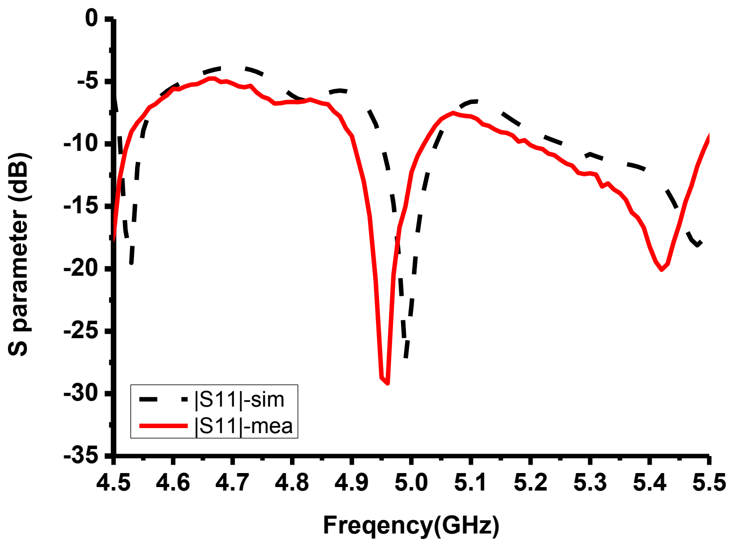

(a) Port 1

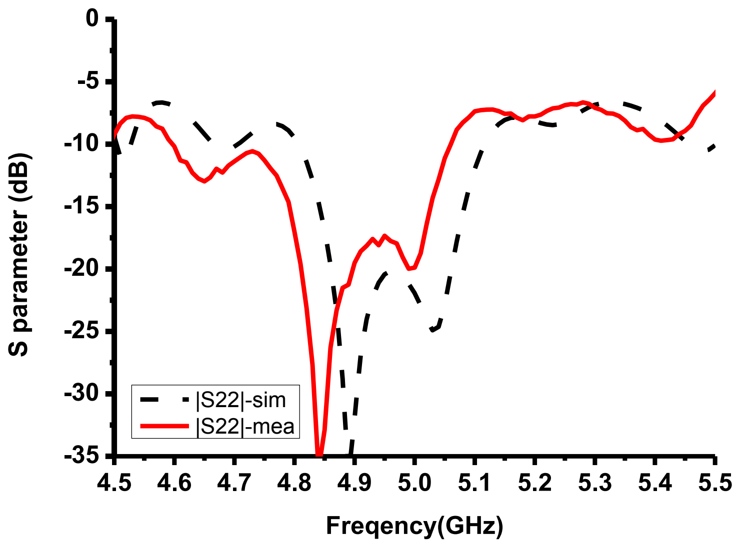

(b) Port 2

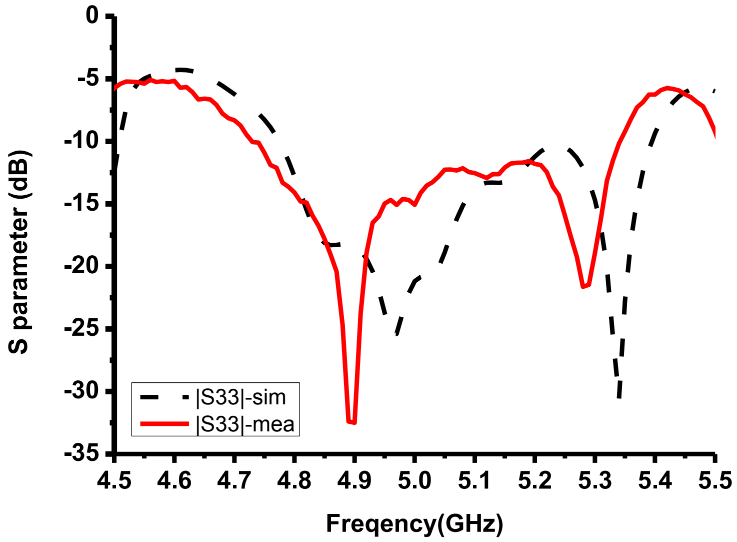

(c) Port 3

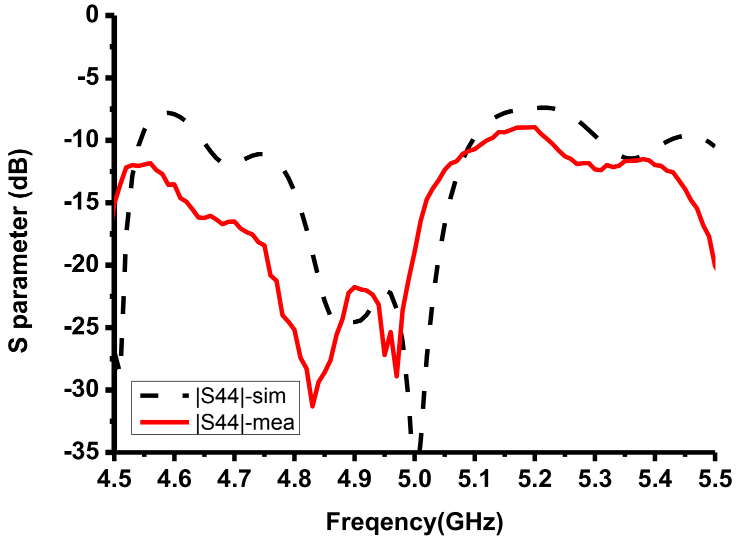

(d) Port 4

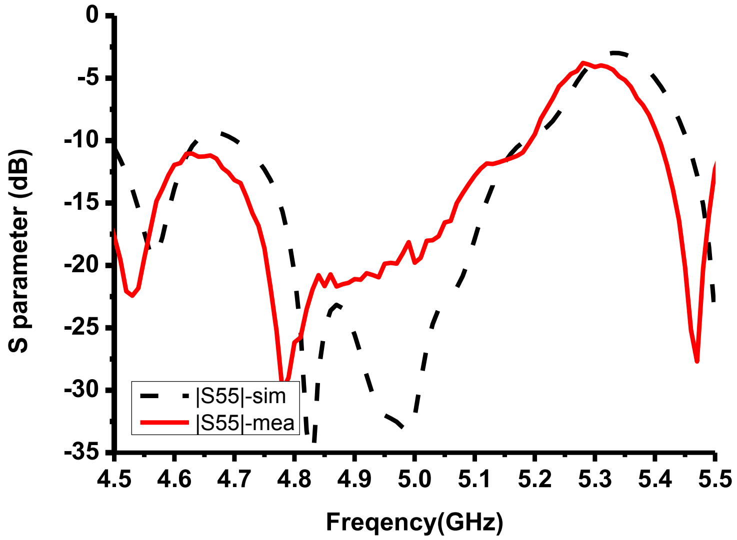

(e) Port 5

Figure 5-19 Reflection coefficients of (a) Port 1, (b) Port 2, (c) Port 3, (d) Port 4 and (e) Port 5

Figure 5-20 shows the simulated and measured radiation patterns when all five input ports are excited respectively. The simulated and measured results agree well. The multi-beam antenna has five beams in total. Each input port corresponds to one beam. The beam directions in simulations and measurements are listed in Table 5-12. For Ports 1, 2 and 5, the measured and simulated beam directions are the same. For Ports 3 and 4, the differences between simulated and measured results are 1 degree.

Table 5-12 Simulated and Measured Beam Directions (unit: degree)

	Port1	Port2	Port3	Port4	Port5
Simulated beam direction	0	-18	-39	39	18
Measured beam direction	0	-18	-38	38	18

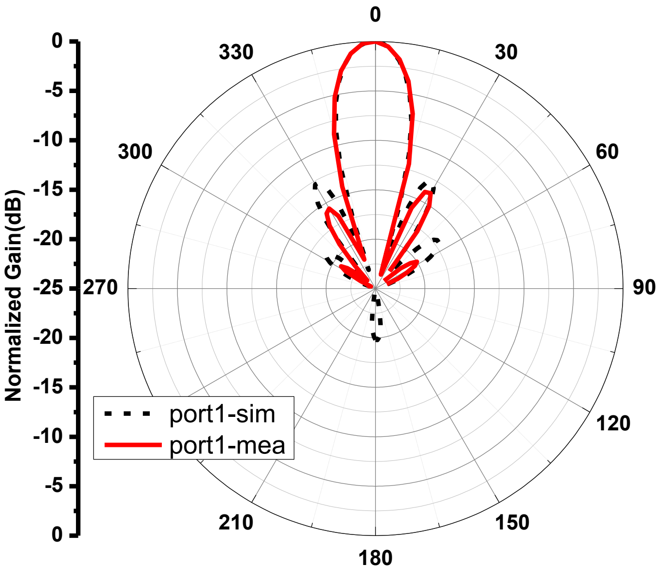

(a) Port 1 is excited

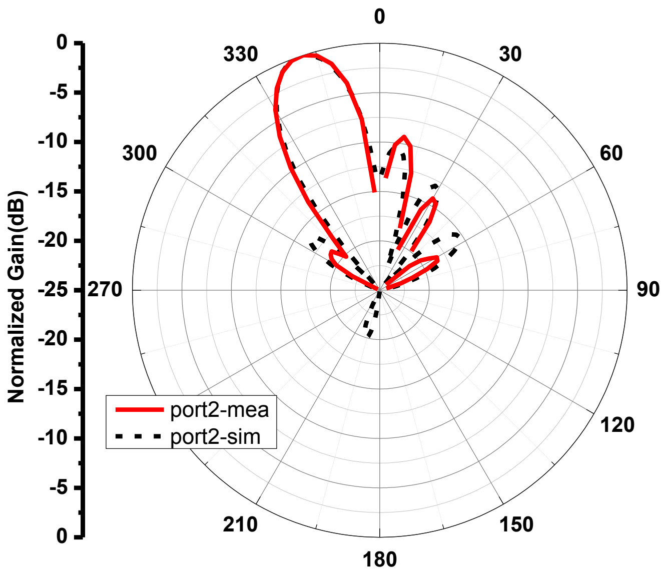

(b) Port 2 is excited

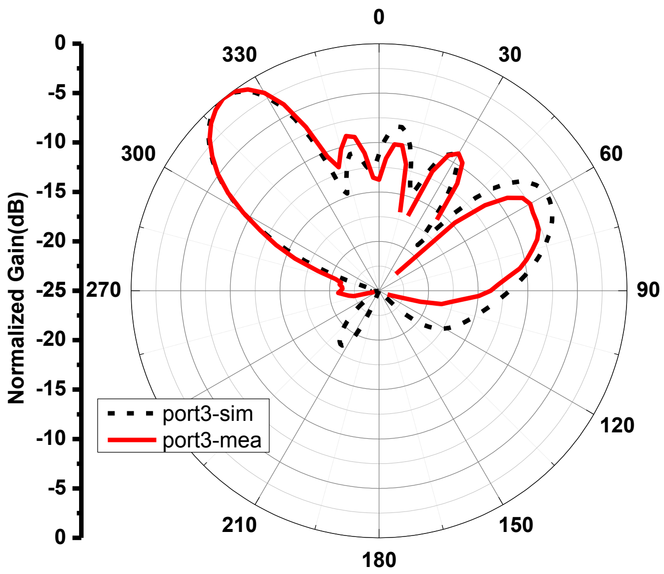

(c) Port 3 is excited

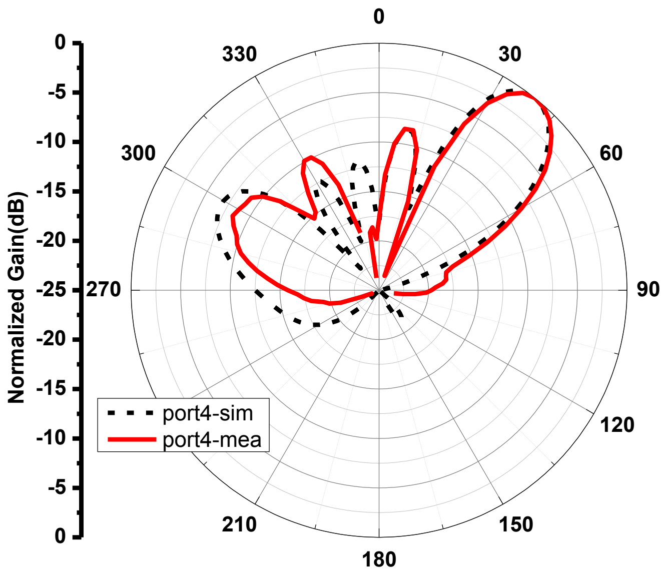

(d) Port 4 is excited

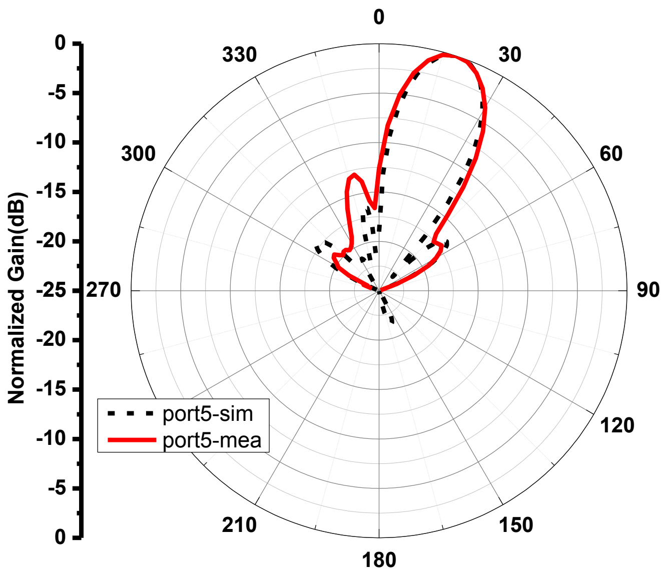

(e) Port 5 is excited

Figure 5-20 Radiation patterns when (a) Port 1, (b) Port 2, (c) Port 3, (d) Port 4 and (e) Port 5 are excited respectively

5.2.4 Summary

In this section, a method of designing a Nolen matrix is introduced. In order to demonstrate the method, a 3×3 Nolen matrix is designed step-by-step. Then, a 5×5 Nolen matrix network is designed by the same method. Based on this network, a multi-beam antenna with 5 beams is proposed and fabricated. The simulated and measured results agree well, which proves that the method introduced is effective.

Chapter 6. Conclusions and Future Work

In this chapter, the thesis is concluded. The main contributions of the thesis are summed up. The possible future work based on the novel designs proposed in this thesis is also shown.

6.1 Conclusions

Array antennas and multi-beam antennas have been developed in the past years. The array antennas usually have relatively high gain, which could increase the capacity of the system by improving the SNR. Multi-beam antennas could be used in MIMO systems, which could also increase the capacity of the communication system. In 5G wireless networks, array antennas and multi-beam antennas are both important parts [1]. The reflectarray has simple feed network compared with a phased array antenna, especially when the number of the unit cell is enormous. Therefore, reflectarray could offer a low-cost solution for some array applications in 5G networks.

In this thesis, previous literature on reflectarray antennas, multi-beam antennas and polarization-reconfigurable CP antennas are reviewed. The novel contributions of the thesis are as below.

- A novel polarization-reconfigurable CP antenna is proposed. This antenna consists of a slot antenna and a polarizer loaded by PIN diodes. The polarizer is able to convert the LP waves from the slot antenna to CP waves. The polarization of the antenna can be electronically switched to LHCP or RHCP by changing the states of PIN diodes on the polarizer. Moreover, it is demonstrated that the antenna is scalable to large-scale array antennas with minor modifications to the DC bias circuit.
- A novel folded CP reflectarray is realized. The antenna consists of a CPSS, a feed antenna and a reflecting surface. The function of the CPSS is similar with that of the polarization grid in folded LP reflectarray antenna. The CPSS is able to reflect LHCP waves, and is transparent for RHCP waves. By introducing the CPSS, the profile of the antenna is reduced from 178 to 95 mm.

- The ultra-wide-band TCDR antenna is proposed. As the concept of "tightly coupled element" is introduced in the design of the unit cell, the bandwidth of the element on the reflecting surface is broadened significantly. The TTD lines are also applied in this design to improve the bandwidth. In this section, phase error distributions of bandwidth reflectarrays are discussed, and a method to suppress phase errors on the reflecting surface in the working band is proposed.
- After introducing the TCDR antenna, the method to reduce the cross-polarization of the TCDR antenna is proposed as well. By applying two types of elements, which have symmetric structures, the cross-polarization of the TCDR antenna is reduced significantly. Two array antennas are proposed according to the method, and the simulated results show the cross-polarization levels are lower than those of the original TCDR antenna, proving that the method is effective.
- A novel method to design an $M\times N$ Nolen matrix is proposed and derived. Following that, a multi-beam antenna fed by a 5×5 Nolen matrix is manufactured and measured. The results prove the effectiveness of the method proposed.

Based on the designs in this thesis, several challenges in the antenna designs are overcome.

- The feed networks of polarization-reconfigurable CP antennas are simplified.
- The profile of CP reflectarrays is reduced significantly.
- The bandwidth of reflectarrays is broadened a lot.
- Nolen matrix networks could be designed more easily.

As the challenges mentioned above are overcome, polarization-reconfigurable CP antennas, reflectarrays and multi-beam antennas fed by Nolen matrix networks could be applied in more systems.

6.2 Future Work

In this thesis, the author proposes some novel designs to solve the problems on array antennas. Some research work could be done in the future.

The polarization-reconfigurable CP antenna is a promising antenna applied in satellite communications and other wireless communication systems. If the ARBW of the polarization-reconfigurable CP antenna is increased, it could be used in more scenarios.

The folded CP reflectarray is a novel design, which reduces profile significantly comparing with the traditional CP reflectarrays. With low profile, the proposed folded CP reflectarray could be used in communication systems on cars, ships and other mobile platforms.

The wide-band TCDR antenna proposed broadens the working bandwidth a lot. With this features, it could be used in scenarios which need wide-band applications, for example ultra-wide-band communication systems. The TCDR antenna is a promising candidate which could attract more researchers to investigate wide-band reflectarray antennas.

The novel method to design a Nolen matrix network gives a concise way to build a Nolen matrix. With this method, it is easy for researchers to design a required Nolen matrix network, which could be used in multi-beam antennas. It is believed that more and more multi-beam antenna designs fed by Nolen matrix networks will be proposed by other researchers.

.

References

[1] G. S. M. A. Intelligence, *Understanding 5G: Perspectives on future technological advancements in mobile*: White paper, 2014.

[2] W. A. Imbriale, S. Gao, and L. Boccia, *Space Antenna Handbook*: John Wiley \& Sons, 2012.

[3] S. Gao, Q. Luo, and F. Zhu, *Circularly polarized antennas*: John Wiley & Sons, 2013.

[4] W. Li, S. Gao, Y. Cai, Q. Luo, M. Sobhy, G. Wei, J. Xu, J. Li, C. Wu, and Z. Cheng, "Polarization-Reconfigurable Circularly Polarized Planar Antenna Using Switchable Polarizer," *IEEE Trans. Antennas Propag.,* vol. 65, pp. 4470-4477, 2017.

[5] W. Li, S. Gao, L. Zhang, Q. Luo, and Y. Cai, "An Ultra-Wide-Band Tightly Coupled Dipole Reflectarray Antenna," *IEEE Trans. Antennas Propag.,* vol. 66, pp. 533-540, 2018.

[6] C. Mao, S. Gao, Q. Luo, T. Rommel, and Q. Chu, "Low-Cost X/Ku/Ka-Band Dual-Polarized Array With Shared Aperture," *IEEE Trans. Antennas Propag.,* vol. 65, pp. 3520-3527, 2017.

[7] W. Li, Q. Jinghui, and S. Ying, "Design and Simulation of Novel Ultra Wideband Planar Reflector Antenna," in *2007 International Conference on Microwave and Millimeter Wave Technology*, 2007, pp. 1-4.

[8] C. Balanis and L. Peters, "Equatorial plane pattern of an axial-TEM slot on a finite size ground plane," *IEEE Trans. Antennas Propag.,* vol. 17, pp. 351-353, 1969.

[9] C. Balanis, "Pattern distortion due to edge diffractions," *IEEE Trans. Antennas Propag.,* vol. 18, pp. 561-563, 1970.

[10] C. Balanis, "Analysis of an array of line sources above a finite ground plane," *IEEE Trans. Antennas Propag.,* vol. 19, pp. 181-185, 1971.

[11] J. D. Kraus, "The Corner-Reflector Antenna," *Proceedings of the IRE,* vol. 28, pp. 513-519, 1940.

[12] H. P. Neff and J. D. Tillman, "The design of the corner-reflector antenna," *Transactions of the American Institute of Electrical Engineers, Part I: Communication and Electronics,* vol. 78, pp. 293-296, 1959.

[13] H. Cottony and A. Wilson, "Gains of finite-size corner-reflector antennas," *IRE Transactions on Antennas and Propagation,* vol. 6, pp. 366-369, 1958.

[14] E. B. Moullin, "Theory and performance of corner reflectors for aerials," *Journal of the Institution of Electrical Engineers - Part I: General,* vol. 92, pp. 326-330, 1945.

[15] O. Woodward, "A circularly-polarized corner reflector antenna," *IRE Transactions on Antennas and Propagation,* vol. 5, pp. 290-297, 1957.

[16] Y. Tanizawa, K. Cho, H. So, and A. Ando, "Radiation characteristics of corner reflector antenna employing frequency selective surface," in *2016 URSI Asia-Pacific Radio Science Conference (URSI AP-RASC)*, 2016, pp. 1-3.

[17] A. Chatterjee and S. K. Parui, "Performance Enhancement of a Dual-Band Monopole Antenna by Using a Frequency-Selective Surface-Based Corner Reflector," *IEEE Trans. Antennas Propag.,* vol. 64, pp. 2165-2171, 2016.

[18] G. Swenson and Y. Lo, "The University of Illinois radio telescope," *IRE Transactions on Antennas and Propagation*, vol. 9, pp. 9-16, 1961.
[19] R. C. Spencer, F. S. Holt, H. M. Johanson, and J. Sampson, "Double parabolic cylinder pencil-beam antenna," *Transactions of the IRE Professional Group on Antennas and Propagation*, vol. 3, pp. 4-8, 1955.
[20] W. Jun, L. Shu, A. Denisov, and L. Lu, "A high gain printed antenna with parabolic metal grid reflector based on SIW technology," in *2017 IEEE International Symposium on Antennas and Propagation & USNC/URSI National Radio Science Meeting*, 2017, pp. 523-524.
[21] D. Zou, R. Wu, P. Chen, and M. Liu, "Enhancement of directivity of source radiation using parabolic cylinder made of left-handed metamaterials," in *2010 International Conference on Microwave and Millimeter Wave Technology*, 2010, pp. 176-179.
[22] D. Jian, L. Qingxia, G. Wei, and Z. Yaoting, "A Sparse Antenna Array with offset Parabolic Cylinder Reflector at Millimeter Wave Band," in *2008 International Conference on Microwave and Millimeter Wave Technology*, 2008, pp. 1667-1670.
[23] A. N. Nechiporenko, L. D. Fesenko, and G. M. Krivosheeva, "An antenna ship RLS with a reflector element as a cutting-out from the parabolic cylinder," in *2007 6th International Conference on Antenna Theory and Techniques*, 2007, pp. 393-395.
[24] Q. Wang, S. Feng, Z. Fang, M. Chen, and M. Jin, "A w-band reflectarray antenna on conformal parabolic cylinder platforms," in *2017 Sixth Asia-Pacific Conference on Antennas and Propagation (APCAP)*, 2017, pp. 1-3.
[25] P. Venkatachalam, N. Gunasekaran, and P. Ramanujam, "A parabolic reflector with asymmetric low sidelobes," *IEEE Trans. Antennas Propag.*, vol. 32, pp. 873-876, 1984.
[26] R. Fante, P. Franchi, N. Kernweis, and L. Dennett, "A parabolic cylinder antenna with very low sidelobes," *IEEE Trans. Antennas Propag.*, vol. 28, pp. 53-59, 1980.
[27] M. S. A. Sanad and L. Shafai, "Performance and design procedure of dual parabolic cylindrical antennas," *IEEE Trans. Antennas Propag.*, vol. 36, pp. 331-338, 1988.
[28] P. Kildal and E. Sorngard, "Circularly polarized feed for cylindrical parabolic reflector antennas," *IEEE Trans. Antennas Propag.*, vol. 28, pp. 210-215, 1980.
[29] R. Zhang, Z. Xie, and Q. Chu, "A New Horn Array Feed for Parabolic Cylindrical Reflector Antenna," in *2007 Asia-Pacific Microwave Conference*, 2007, pp. 1-4.
[30] A. Nesic, Z. Micic, I. Radnovic, and D. Nesic, "Printed antenna arrays with cylindrical parabolic reflector," in *2012 20th Telecommunications Forum (TELFOR)*, 2012, pp. 1201-1204.
[31] A. Mehrabani and L. Shafai, "Compact Dual Circularly Polarized Primary Feeds for Symmetric Parabolic Reflector Antennas," *IEEE Antennas Wireless Propag. Lett.*, vol. 15, pp. 922-925, 2016.
[32] W. Morrow, "Beyond-the-horizon point-to-point UHF radio systems," in *1958 IRE International Convention Record*, 1955, pp. 56-57.
[33] C. C. Cutler, "Parabolic-Antenna Design for Microwaves," *Proceedings of the IRE*, vol. 35, pp. 1284-1294, 1947.
[34] M. Pehlıvan, K. Yeğın, and Y. Aşci, "Design of 1–18 GHz parabolic reflector antenna with LPDA feed," in *2016 24th Telecommunications Forum (TELFOR)*, 2016, pp. 1-3.
[35] M. Nagasaka, S. Nakazawa, and S. Tanaka, "Prototype of a dual-circularly polarized parabolic reflector antenna with microstrip antenna array for 12-GHz

band satellite broadcasting reception," in *2016 10th European Conference on Antennas and Propagation (EuCAP)*, 2016, pp. 1-5.

[36] Y. Asci, E. Curuk, K. Yegin, and C. Ozdemir, "Improved splash-plate feed parabolic reflector antenna for Ka-Band VSAT applications," in *2016 46th European Microwave Conference (EuMC)*, 2016, pp. 1283-1286.

[37] S. M. Ali, M. A. Zakariya, Z. Baharudin, and J. J. Adz, "Parabolic reflector fed by Cylindrical Dielectric Resonator Antenna with high gain," in *2014 5th International Conference on Intelligent and Advanced Systems (ICIAS)*, 2014, pp. 1-6.

[38] Z. Dai, Y. Shang, Y. Liu, X. Xuan, L. Zhang, and F. Yao, "Design of wide-angle scanning parabolic torus reflector antenna realized by rotation of sub-reflector," in *2013 5th IEEE International Symposium on Microwave, Antenna, Propagation and EMC Technologies for Wireless Communications*, 2013, pp. 367-369.

[39] O. Yurduseven and O. Yurduseven, "Compact parabolic reflector antenna design with cosecant-squared radiation pattern," in *2011 MICROWAVES, RADAR AND REMOTE SENSING SYMPOSIUM*, 2011, pp. 382-385.

[40] S. Bo, Q. Jinghui, Y. Caitian, and Z. Lingling, "Effect of design parameters on sidelobe level of short-focus parabolic reflector antenna," in *2008 Asia-Pacific Symposium on Electromagnetic Compatibility and 19th International Zurich Symposium on Electromagnetic Compatibility*, 2008, pp. 851-854.

[41] P. J. B. Clarricoats and G. T. Poulton, "High-efficiency microwave reflector antennas - A review," *P Ieee,* vol. 65, pp. 1470-1504, 1977.

[42] O. Hachenberg, B. H. Grahl, and R. Wielebinski, "The 100-meter radio telescope at Effelsberg," *P Ieee,* vol. 61, pp. 1288-1295, 1973.

[43] B. Peng, C. Jin, Q. Wang, L. Zhu, W. Zhu, H. Zhang, and R. Nan, "Preparatory Study for Constructing FAST, the World's Largest Single Dish," *P Ieee,* vol. 97, pp. 1391-1402, 2009.

[44] D. Berry, R. Malech, and W. Kennedy, "The reflectarray antenna," *IEEE Trans. Antennas Propag.,* vol. 11, pp. 645-651, 1963.

[45] J. Huang, "Microstrip reflectarray," in *Antennas and Propagation Society International Symposium, 1991. AP-S. Digest*, 1991, pp. 612-615 vol.2.

[46] D.-C. Chang and M.-C. Huang, "Multiple-polarization microstrip reflectarray antenna with high efficiency and low cross-polarization," *IEEE Trans. Antennas Propag.,* vol. 43, pp. 829-834, 1995.

[47] R. D. Javor, X.-D. Wu, and K. Chang, "Beam steering of a microstrip flat reflectarray antenna," in *Proceedings of IEEE Antennas and Propagation Society International Symposium and URSI National Radio Science Meeting*, 1994, pp. 956-959 vol.2.

[48] R. D. Javor, X.-D. Wu, and K. Chang, "Design and performance of a microstrip reflectarray antenna," *IEEE Trans. Antennas Propag.,* vol. 43, pp. 932-939, Sep 1995.

[49] D. C. Chang and M. C. Huang, "Microstrip reflectarray antenna with offset feed," *Electron. Lett.,* vol. 28, pp. 1489-1491, 1992.

[50] R. D. Javor, X. D. Wu, and K. Chang, "Offset-fed microstrip reflectarray antenna," *Electron. Lett.,* vol. 30, pp. 1363-1365, 1994.

[51] A. W. Robinson, M. E. Bialkowski, and H. J. Song, "A 137-element active reflect array with dual-feed microstrip patch elements," *Microwave and Optical Technology Letters,* vol. 26, pp. 147-151, 2000/08/05 2000.

[52] E. Carrasco, M. Barba, and J. A. Encinar, "Aperture-coupled reflectarray element with wide range of phase delay," *Electron. Lett.,* vol. 42, pp. 667-668, 2006.

[53] A. Kelkar, "FLAPS: conformal phased reflecting surfaces," in *Proceedings of the 1991 IEEE National Radar Conference*, 1991, pp. 58-62.
[54] D. M. Pozar and S. D. Targonski, "A microstrip reflectarray using crossed dipoles," in *IEEE Antennas and Propagation Society International Symposium. 1998 Digest. Antennas: Gateways to the Global Network. Held in conjunction with: USNC/URSI National Radio Science Meeting (Cat. No.98CH36*, 1998, pp. 1008-1011 vol.2.
[55] Y. Chen, L. Chen, H. Wang, X. T. Gu, and X. W. Shi, "Dual-Band Crossed-Dipole Reflectarray With Dual-Band Frequency Selective Surface," *IEEE Antennas Wireless Propag. Lett.*, vol. 12, pp. 1157-1160, 2013.
[56] D. M. Pozar, S. D. Targonski, and H. D. Syrigos, "Design of millimeter wave microstrip reflectarrays," *IEEE Trans. Antennas Propag.,* vol. 45, pp. 287-296, 1997.
[57] D. M. Pozar and T. A. Metzler, "Analysis of a reflectarray antenna using microstrip patches of variable size," *Electron. Lett.,* vol. 29, pp. 657-658, 1993.
[58] J. A. Encinar, "Design of a dual frequency reflectarray using microstrip stacked patches of variable size," *Electron. Lett.,* vol. 32, pp. 1049-1050, 1996.
[59] D. Cadoret, A. Laisne, R. Gillard, L. L. Coq, and H. Legay, "Design and measurement of new reflectarray antenna using microstrip patches loaded with slot," *Electron. Lett.,* vol. 41, pp. 623-624, 2005.
[60] M. R. Chaharmir, J. Shaker, M. Cubaci, and A. Sebak, "Reflectarray with slots of varying length on ground plane," in *IEEE Antennas and Propagation Society International Symposium (IEEE Cat. No.02CH37313)*, 2002, pp. 144-.
[61] Q. Luo, S. Gao, C. Zhang, D. Zhou, T. Chaloun, W. Menzel, V. Ziegler, and M. Sobhy, "Design and Analysis of a Reflectarray Using Slot Antenna Elements for Ka-band SatCom," *IEEE Trans. Antennas Propag.,* vol. 63, pp. 1365-1374, 2015.
[62] J. Huang and R. J. Pogorzelski, "A Ka-band microstrip reflectarray with elements having variable rotation angles," *IEEE Trans. Antennas Propag.,* vol. 46, pp. 650-656, 1998.
[63] H. Chulmin and C. Kai, "Ka-band reflectarray using ring elements," *Electron. Lett.,* vol. 39, pp. 491-493, 2003.
[64] F. Johansson, "Frequency-scanned reflection gratings consisting of ring patches," *Microwaves, Antennas and Propagation, IEE Proceedings H,* vol. 138, pp. 273-276, 1991.
[65] Y. J. Guo and S. K. Barton, "Phase correcting zonal reflector incorporating rings," *Antennas and Propagation, IEEE Transactions on,* vol. 43, pp. 350-355, 1995.
[66] H. Salti, R. Gillard, R. Loison, and L. L. Coq, "A Reflectarray Antenna Based on Multiscale Phase-Shifting Cell Concept," *IEEE Antennas Wireless Propag. Lett.,* vol. 8, pp. 363-366, 2009.
[67] M. R. Chaharmir, J. Shaker, M. Cuhaci, and A. Sebak, "Circularly polarised reflectarray with cross-slot of varying arms on ground plane," *Electron. Lett.,* vol. 38, pp. 1492-1493, 2002.
[68] J. M. Colin, "Phased array radars in France: present and future," in *Phased Array Systems and Technology, 1996., IEEE International Symposium on*, 1996, pp. 458-462.
[69] R. D. Javor, W. Xiao-Dong, and C. Kai, "Beam steering of a microstrip flat reflectarray antenna," in *Proceedings of IEEE Antennas and Propagation Society International Symposium and URSI National Radio Science Meeting*, 1994, pp. 956-959 vol.2.
[70] A. A. Tolkachev, V. V. Denisenko, A. V. Shishlov, and A. G. Shubov, "High gain antenna systems for millimeter wave radars with combined electronical and

mechanical beam steering," in *Phased Array Systems and Technology, 1996., IEEE International Symposium on*, 1996, pp. 266-271.
[71] O. G. Vendik and M. Parnes, "A phase shifter with one tunable component for a reflectarray antenna," *IEEE Antennas Propag. Mag.*, vol. 50, pp. 53-65, 2008.
[72] S. Ebadi, R. V. Gatti, and R. Sorrentino, "Linear reflectarray antenna design using 1-bit digital phase shifters," in *2009 3rd European Conference on Antennas and Propagation*, 2009, pp. 3729-3732.
[73] S. V. Hum and M. Okoniewski, "An electronically tunable reflectarray using varactor diode-tuned elements," in *Antennas and Propagation Society International Symposium, 2004. IEEE*, 2004, pp. 1827-1830 Vol.2.
[74] L. Boccia, F. Venneri, G. Amendola, and G. Di Massa, "Application of varactor diodes for reflectarray phase control," in *Antennas and Propagation Society International Symposium, 2002. IEEE*, 2002, p. 132.
[75] S. V. Hum and M. Okoniewski, "An electronically tunable reflectarray using varactor diode-tuned elements," in *IEEE Antennas and Propagation Society Symposium, 2004.*, 2004, pp. 1827-1830 Vol.2.
[76] L. Boccia, F. Venneri, G. Amendola, and G. D. Massa, "Application of varactor diodes for reflectarray phase control," in *IEEE Antennas and Propagation Society International Symposium (IEEE Cat. No.02CH37313)*, 2002, p. 132.
[77] S. V. Hum, M. Okoniewski, and R. J. Davies, "Realizing an electronically tunable reflectarray using varactor diode-tuned elements," *IEEE Microwave and Wireless Components Letters*, vol. 15, pp. 422-424, 2005.
[78] S. V. Hum, G. McFeetors, M. Okoniewski, and R. J. Davies, "A Reflectarray Cell Based on a Tunable MEMS Capacitor," presented at the IEEE Antennas and Propagation Society International Symposium, New Mexico, 2006.
[79] H. Legay, B. Pinte, M. Charrier, A. Ziaei, E. Girard, and R. Gillard, "A steerable reflectarray antenna with MEMS controls," in *IEEE International Symposium on Phased Array Systems and Technology, 2003.*, 2003, pp. 494-499.
[80] J. Huang, "Bandwidth study of microstrip reflectarray and a novel phased reflectarray concept," in *Antennas and Propagation Society International Symposium, 1995. AP-S. Digest*, 1995, pp. 582-585 vol.1.
[81] M. R. Chaharmir, J. Shaker, M. Cuhaci, and A. Sebak, "Novel photonically-controlled reflectarray antenna," *Antennas and Propagation, IEEE Transactions on*, vol. 54, pp. 1134-1141, 2006.
[82] M. Al-Tikriti and W. Menzel, "A Folded Reflectarray Antenna with Sidelobe Reduction," in *2002 32nd European Microwave Conference*, 2002, pp. 1-4.
[83] J. A. Zornoza, R. Leberer, J. A. Encinar, and W. Menzel, "Folded multilayer microstrip reflectarray with shaped pattern," *IEEE Trans. Antennas Propag.*, vol. 54, pp. 510-518, 2006.
[84] D. Pilz and W. Menzel, "Folded reflectarray antenna," *Electron. Lett.*, vol. 34, pp. 832-833, 1998.
[85] J. Huang and J. A. Encinar, *Reflectarray Antennas*: Wiley-IEEE Press, 2008.
[86] S. M. A. M. H. Abadi, K. Ghaemi, and N. Behdad, "Ultra-Wideband, True-Time-Delay Reflectarray Antennas Using Ground-Plane-Backed, Miniaturized-Element Frequency Selective Surfaces," *IEEE Trans. Antennas Propag.*, vol. 63, pp. 534-542, Feb 2015.
[87] J. A. Encinar, "Design of two-layer printed reflectarrays using patches of variable size," *IEEE Trans. Antennas Propag.*, vol. 49, pp. 1403-1410, 2001.
[88] J. A. Encinar and J. A. Zornoza, "Broadband design of three-layer printed reflectarrays," *IEEE Trans. Antennas Propag.*, vol. 51, pp. 1662-1664, 2003.

[89] J. A. Encinar, L. S. Datashvili, J. A. Zornoza, M. Arrebola, M. Sierra-Castaner, J. L. Besada-Sanmartin, H. Baier, and H. Legay, "Dual-Polarization Dual-Coverage Reflectarray for Space Applications," *IEEE Trans. Antennas Propag.*, vol. 54, pp. 2827-2837, 2006.

[90] J. H. Yoon, Y. J. Yoon, W. s. Lee, and J. h. So, "Broadband Microstrip Reflectarray With Five Parallel Dipole Elements," *IEEE Antennas Wireless Propag. Lett.*, vol. 14, pp. 1109-1112, 2015.

[91] L. Li, Q. Chen, Q. Yuan, K. Sawaya, T. Maruyama, T. Furuno, and S. Uebayashi, "Novel Broadband Planar Reflectarray With Parasitic Dipoles for Wireless Communication Applications," *IEEE Antennas Wireless Propag. Lett.*, vol. 8, pp. 881-885, 2009.

[92] R. Florencio, J. Encinar, R. R. Boix, and G. Perez-Palomino, "Dual-polarisation reflectarray made of cells with two orthogonal sets of parallel dipoles for bandwidth and cross-polarisation improvement," *IET Microwaves, Antennas Propagation*, vol. 8, pp. 1389-1397, 2014.

[93] E. Carrasco, M. Barba, J. A. Encinar, M. Arrebola, F. Rossi, and A. Freni, "Design, Manufacture and Test of a Low-Cost Shaped-Beam Reflectarray Using a Single Layer of Varying-Sized Printed Dipoles," *IEEE Trans. Antennas Propag.*, vol. 61, pp. 3077-3085, 2013.

[94] M. R. Chaharmir, J. Shaker, M. Cuhaci, and A. Ittipiboon, "A broadband reflectarray antenna with double square rings as the cell elements," in *2006 First European Conference on Antennas and Propagation*, 2006, pp. 1-4.

[95] M. R. Chaharmir, J. Shaker, M. Cuhaci, and A. Ittipiboon, "Broadband reflectarray antenna with double cross loops," *Electron. Lett.*, vol. 42, pp. 65-66, 2006.

[96] M. R. Chaharmir and J. Shaker, "Broadband reflectarray with combination of cross and rectangle loop elements," *Electron. Lett.*, vol. 44, pp. 658-659, 2008.

[97] E. Carrasco, M. Barba, and J. A. Encinar, "Reflectarray Element Based on Aperture-Coupled Patches With Slots and Lines of Variable Length," *IEEE Trans. Antennas Propag.*, vol. 55, pp. 820-825, 2007.

[98] E. Carrasco, J. A. Encinar, and M. Barba, "Bandwidth Improvement in Large Reflectarrays by Using True-Time Delay," *IEEE Trans. Antennas Propag.*, vol. 56, pp. 2496-2503, 2008.

[99] D. M. Pozar, "Wideband reflectarrays using artificial impedance surfaces," *Electron. Lett.*, vol. 43, pp. 148-149, 2007.

[100] P. Y. Qin, Y. J. Guo, and A. R. Weily, "Broadband Reflectarray Antenna Using Subwavelength Elements Based on Double Square Meander-Line Rings," *IEEE Trans. Antennas Propag.*, vol. 64, pp. 378-383, Jan 2016.

[101] P. Nayeri, F. Yang, and A. Z. Elsherbeni, "Broadband Reflectarray Antennas Using Double-Layer Subwavelength Patch Elements," *IEEE Antennas Wireless Propag. Lett.*, vol. 9, pp. 1139-1142, 2010.

[102] P. Nayeri, F. Yang, and A. Z. Elsherbeni, "A broadband microstrip reflectarray using sub-wavelength patch elements," in *2009 IEEE Antennas and Propagation Society International Symposium*, 2009, pp. 1-4.

[103] L. Liang and S. V. Hum, "Design of a UWB Reflectarray as an Impedance Surface Using Bessel Filters," *IEEE Trans. Antennas Propag.*, vol. 64, pp. 4242-4255, Oct 2016.

[104] R. Deng, S. Xu, F. Yang, and M. Li, "A Single-Layer High-Efficiency Wideband Reflectarray Using Hybrid Design Approach," *IEEE Antennas Wireless Propag. Lett.*, vol. 16, pp. 884-887, 2017.

[105] C. Han, C. Rodenbeck, J. Huang, and C. Kai, "A C/ka dual frequency dual Layer circularly polarized reflectarray antenna with microstrip ring elements," *IEEE Trans. Antennas Propag.*, vol. 52, pp. 2871-2876, 2004.

[106] J. Huang, C. Han, and K. Chang, "A Cassegrain Offset-Fed Dual-Band Reflectarray," in *2006 IEEE Antennas and Propagation Society International Symposium*, 2006, pp. 2439-2442.

[107] S. Hsu, C. Han, J. Huang, and K. Chang, "An Offset Linear-Array-Fed Ku/Ka Dual-Band Reflectarray for Planet Cloud/Precipitation Radar," *IEEE Trans. Antennas Propag.*, vol. 55, pp. 3114-3122, 2007.

[108] N. Misran, R. Cahill, and V. F. Fusco, "Design optimisation of ring elements for broadband reflectarray antennas," *IEE Proceedings - Microwaves, Antennas and Propagation*, vol. 150, pp. 440-444, 2003.

[109] M. R. Chaharmir, J. Shaker, and N. Gagnon, "Broadband dual-band linear orthogonal polarisation reflectarray," *Electron. Lett.*, vol. 45, pp. 13-14, 2009.

[110] F. Yang, Y. Kim, A. Yu, J. Huang, and A. Elsherbeni, "A Single Layer Reflectarray Antenna for C/X/Ka Bands Applications," in *2007 International Conference on Electromagnetics in Advanced Applications*, 2007, pp. 1058-1061.

[111] P. S. Hall and S. J. Vetterlein, "Review of radio frequency beamforming techniques for scanned and multiple beam antennas," *IEE Proceedings H - Microwaves, Antennas and Propagation*, vol. 137, pp. 293-303, 1990.

[112] J. Ruze, "Lateral-feed displacement in a paraboloid," *IEEE Trans. Antennas Propag.*, vol. 13, pp. 660-665, 1965.

[113] Y. Lo, "On the beam deviation factor of a parabolic reflector," *IRE Transactions on Antennas and Propagation*, vol. 8, pp. 347-349, 1960.

[114] S. Sandler, "Paraboloidal reflector patterns for off-axis feed," *IRE Transactions on Antennas and Propagation*, vol. 8, pp. 368-379, 1960.

[115] W. Imbriale, P. Ingerson, and W. Wong, "Large lateral feed displacements in a parabolic reflector," *IEEE Trans. Antennas Propag.*, vol. 22, pp. 742-745, 1974.

[116] W. Menzel, M. Al-Tikriti, and R. Leberer, "A 76 GHz multiple-beam planar reflector antenna," in *2002 32nd European Microwave Conference*, 2002, pp. 1-4.

[117] I. Y. Tarn, Y. S. Wang, and S. J. Chung, "A Dual-Mode Millimeter-Wave Folded Microstrip Reflectarray Antenna," *IEEE Trans. Antennas Propag.*, vol. 56, pp. 1510-1517, 2008.

[118] T. V. La, N. T. Nguyen, M. Casaletti, and R. Sauleau, "Design of medium-size dielectric bifocal lenses for wide-angle beam scanning antennas," in *2012 6th European Conference on Antennas and Propagation (EUCAP)*, 2012, pp. 3287-3291.

[119] A. N. Plastikov and B. L. Kogan, "Bifocal reflector antenna design procedure for wide-angle multi-beam applications," in *2013 7th European Conference on Antennas and Propagation (EuCAP)*, 2013, pp. 3349-3353.

[120] E. B. Lima, S. A. Matos, J. R. Costa, C. A. Fernandes, and N. J. G. Fonseca, "Circular Polarization Wide-Angle Beam Steering at Ka-Band by In-Plane Translation of a Plate Lens Antenna," *IEEE Trans. Antennas Propag.*, vol. 63, pp. 5443-5455, 2015.

[121] M. Ettorre, R. Sauleau, and L. L. Coq, "Multi-Beam Multi-Layer Leaky-Wave SIW Pillbox Antenna for Millimeter-Wave Applications," *IEEE Trans. Antennas Propag.*, vol. 59, pp. 1093-1100, 2011.

[122] J. Zhang, W. Wu, and D. g. Fang, "360 degree scanning multi-beam antenna based on homogeneous ellipsoidal lens fed by circular array," *Electron. Lett.*, vol. 47, pp. 298-300, 2011.

[123] C. Wu, M. Feng, and P. Tang, "A multi-beam antenna with 360° beam scanning ability," in *2017 Sixth Asia-Pacific Conference on Antennas and Propagation (APCAP)*, 2017, pp. 1-3.

[124] R. C. Hansen, "Design trades for Rotman lenses," *IEEE Transactions on Antennas and Propagation*, vol. 39, pp. 464-472, Apr 1991.

[125] W. Rotman and R. Turner, "Wide-angle microwave lens for line source applications," *IEEE Trans. Antennas Propag.*, vol. 11, pp. 623-632, 1963.

[126] J. Herd and D. Pozar, "Design of a microstrip antenna array fed by a rotman lens," in *1984 Antennas and Propagation Society International Symposium*, 1984, pp. 729-732.

[127] B. Carlegrim and L. Pettersson, "Rotman Lens in Microstrip Technology," in *1992 22nd European Microwave Conference*, 1992, pp. 882-887.

[128] L. Musa and M. S. Smith, "Microstrip port design and sidewall absorption for printed Rotman lenses," *IEE Proceedings H - Microwaves, Antennas and Propagation*, vol. 136, pp. 53-58, 1989.

[129] L. Musa and M. Smith, "Microstrip rotman lens port design," in *1986 Antennas and Propagation Society International Symposium*, 1986, pp. 899-902.

[130] L. Schulwitz and A. Mortazawi, "A compact dual-polarized multibeam phased-array architecture for millimeter-wave radar," *IEEE Transactions on Microwave Theory and Techniques*, vol. 53, pp. 3588-3594, 2005.

[131] A. Al-Zayed, L. Schulwitz, and A. Mortazawi, "A dual polarized millimetre-wave multibeam phased array," in *2004 IEEE MTT-S International Microwave Symposium Digest (IEEE Cat. No.04CH37535)*, 2004, pp. 87-90 Vol.1.

[132] Y. Liu, H. Yang, Z. Jin, F. Zhao, and J. Zhu, "A Multibeam Cylindrically Conformal Slot Array Antenna Based on a Modified Rotman Lens," *IEEE Trans. Antennas Propag.*, vol. 66, pp. 3441-3452, 2018.

[133] A. Darvazehban, O. Manoochehri, M. A. Salari, P. Dehkhoda, and A. Tavakoli, "Ultra-Wideband Scanning Antenna Array With Rotman Lens," *IEEE Transactions on Microwave Theory and Techniques*, vol. 65, pp. 3435-3442, 2017.

[134] W. Lee, J. Kim, and Y. J. Yoon, "Compact Two-Layer Rotman Lens-Fed Microstrip Antenna Array at 24 GHz," *IEEE Trans. Antennas Propag.*, vol. 59, pp. 460-466, 2011.

[135] K. Sang-Gyu, P. Zepeda, and C. Kai, "Piezoelectric transducer controlled multiple beam phased array using microstrip Rotman lens," *IEEE Microwave and Wireless Components Letters*, vol. 15, pp. 247-249, 2005.

[136] K. Tekkouk, M. Ettorre, and R. Sauleau, "SIW Rotman Lens Antenna With Ridged Delay Lines and Reduced Footprint," *IEEE Transactions on Microwave Theory and Techniques*, vol. 66, pp. 3136-3144, 2018.

[137] Y. J. Cheng, W. Hong, K. Wu, Z. Q. Kuai, C. Yu, J. X. Chen, J. Y. Zhou, and H. J. Tang, "Substrate Integrated Waveguide (SIW) Rotman Lens and Its Ka-Band Multibeam Array Antenna Applications," *IEEE Trans. Antennas Propag.*, vol. 56, pp. 2504-2513, 2008.

[138] K. Tekkouk, M. Ettorre, L. L. Coq, and R. Sauleau, "Multibeam SIW Slotted Waveguide Antenna System Fed by a Compact Dual-Layer Rotman Lens," *IEEE Trans. Antennas Propag.*, vol. 64, pp. 504-514, 2016.

[139] K. Tekkouk, M. Ettorre, and R. Sauleau, "Multilayer SIW Rotman lens antenna in 24 GHz band," in *2016 10th European Conference on Antennas and Propagation (EuCAP)*, 2016, pp. 1-4.

[140] Y. Liu, H. Yang, D. Huang, and J. Zhu, "A low sidelobe multibeam slot array antenna fed by rotman lens," in *2016 Loughborough Antennas & Propagation Conference (LAPC)*, 2016, pp. 1-5.

[141] K. Tekkouk, M. Ettorre, and R. Sauleau, "SIW multilayer Rotman lens antenna in the 24-GHz band," in *2015 European Microwave Conference (EuMC)*, 2015, pp. 1503-1506.

[142] J. Pourahmadazar and T. A. Denidni, "Multi-beam tapered slot antenna array using substrate integrated waveguide Rotman lens," in *2015 European Radar Conference (EuRAD)*, 2015, pp. 425-428.

[143] J. Blass, "Multidirectional antenna - A new approach to stacked beams," in *1958 IRE International Convention Record*, 1960, pp. 48-50.

[144] J. Butler and R. Lowe, "Beamforming matrix simplifies design of electronically scanned antennas," *Elec. Design*, vol. 9, pp. 170-173, 1961.

[145] J. C. Nolan, "Synthesis of Multiple Beam Networks for Arbitzary Illuminations," PHD, John Hopkins University, Baltimore, Maryland, 1965.

[146] M. Fassett, L. Kaplan, and J. Pozgay, "Optimal synthesis of ladder network array antenna feed systems," in *1976 Antennas and Propagation Society International Symposium*, 1976, pp. 58-61.

[147] W. R. Jones and E. C. DuFort, "On the Design of Optimum Dual-Series Feed Networks," *IEEE Trans. Microw. Theory Techn*, vol. 19, pp. 451-458, 1971.

[148] S. Mosca, F. Bilotti, A. Toscano, and L. Vegni, "A novel design method for Blass matrix beam-forming networks," *IEEE Trans. Antennas Propag.*, vol. 50, pp. 225-232, 2002.

[149] S. J. Vetterlein and P. S. Hall, "Novel multiple beam microstrip patch array with integrated beamformer," *Electron. Lett.*, vol. 25, pp. 1149-1150, 1989.

[150] S. J. Vetterlein and P. S. Hall, "Multiple beam microstrip patch array with integrated beamformer," *IEE Proceedings H - Microwaves, Antennas and Propagation*, vol. 138, pp. 176-184, 1991.

[151] W. Y. Lim and K. K. Chan, "Generation of multiple simultaneous beams with a modified Blass matrix," in *2009 Asia Pacific Microwave Conference*, 2009, pp. 1557-1560.

[152] P. Chen, W. Hong, Z. Kuai, and J. Xu, "A Double Layer Substrate Integrated Waveguide Blass Matrix for Beamforming Applications," *IEEE Microwave and Wireless Components Letters*, vol. 19, pp. 374-376, 2009.

[153] M. Bonnedal, I. Karlsson, and K. V. t. Klooster, "A dual beam slotted waveguide array antenna for SAR applications," in *1991 Seventh International Conference on Antennas and Propagation, ICAP 91 (IEE)*, 1991, pp. 559-562 vol.2.

[154] A. B. Constantine and I. I. Panayiotis, *Introduction to Smart Antennas*: Morgan & Claypool, 2007.

[155] M. Koubeissi, C. Decroze, T. Monediere, and B. Jecko, "Switched-beam antenna based on novel design of Butler matrices with broadside beam," *Electron. Lett.*, vol. 41, pp. 1097-1098, 2005.

[156] B. Piovano, L. Accatino, A. Angelucci, T. Jones, P. Capece, and M. Votta, "Design And Breadboarding Of Wideband Nxn Butler Matrices For Multiport Amplifiers," in *SBMO International Microwave Conference/Brazil*, 1993, pp. 175-180.

[157] N. Jastram and D. S. Filipovic, "Wideband multibeam millimeter wave arrays," in *2014 IEEE Antennas and Propagation Society International Symposium (APSURSI)*, 2014, pp. 741-742.

[158] A. A. M. Ali, N. J. G. Fonseca, F. Coccetti, and H. Aubert, "Design and Implementation of Two-Layer Compact Wideband Butler Matrices in SIW

Technology for Ku-Band Applications," *IEEE Trans. Antennas Propag.*, vol. 59, pp. 503-512, 2011.
[159] A. Ali, N. Fonseca, F. Coccetti, and H. Aubert, "Novel two-layer broadband 4 × 4 Butler matrix in SIW technology for Ku-band applications," in *2008 Asia-Pacific Microwave Conference*, 2008, pp. 1-4.
[160] T. Djerafi and K. Wu, "A Low-Cost Wideband 77-GHz Planar Butler Matrix in SIW Technology," *IEEE Trans. Antennas Propag.*, vol. 60, pp. 4949-4954, 2012.
[161] K. Tekkouk, J. Hirokawa, R. Sauleau, M. Ettorre, M. Sano, and M. Ando, "Dual-Layer Ridged Waveguide Slot Array Fed by a Butler Matrix With Sidelobe Control in the 60-GHz Band," *IEEE Trans. Antennas Propag.*, vol. 63, pp. 3857-3867, 2015.
[162] K. Wincza, S. Gruszczynski, and K. Sachse, "Reduced sidelobe four-beam antenna array fed by modified Butler matrix," *Electron. Lett.*, vol. 42, pp. 508-509, 2006.
[163] S. Gruszczynski, K. Wincza, and K. Sachse, "Reduced Sidelobe Four-Beam N-Element Antenna Arrays Fed by $4times N$ Butler Matrices," *IEEE Antennas Wireless Propag. Lett.*, vol. 5, pp. 430-434, 2006.
[164] W. Li, C. Chu, K. Lin, and S. Chang, "Switched-beam antenna based on modified Butler matrix with low sidelobe level," *Electron. Lett.*, vol. 40, pp. 290-292, 2004.
[165] H. Ting, S. Hsu, and T. Wu, "Broadband Eight-Port Forward-Wave Directional Couplers and Four-Way Differential Phase Shifter," *IEEE Transactions on Microwave Theory and Techniques*, vol. 66, pp. 2161-2169, 2018.
[166] J. Lian, Y. Ban, C. Xiao, and Z. Yu, "Compact Substrate-Integrated 4 × 8 Butler Matrix With Sidelobe Suppression for Millimeter-Wave Multibeam Application," *IEEE Antennas Wireless Propag. Lett.*, vol. 17, pp. 928-932, 2018.
[167] K. Uehara, T. Seki, and K. Kagoshima, "A planar sector antenna for indoor high-speed wireless communication terminals," in *IEEE Antennas and Propagation Society International Symposium 1997. Digest*, 1997, pp. 1352-1355 vol.2.
[168] T. H. Jang, H. Y. Kim, and C. S. Park, "A 60 GHz Wideband Switched-Beam Dipole-Array-Fed Hybrid Horn Antenna," *IEEE Antennas Wireless Propag. Lett.*, vol. 17, pp. 1344-1348, 2018.
[169] J. Lian, Y. Ban, Q. Yang, B. Fu, Z. Yu, and L. Sun, "Planar Millimeter-Wave 2-D Beam-Scanning Multibeam Array Antenna Fed by Compact SIW Beam-Forming Network," *IEEE Trans. Antennas Propag.*, vol. 66, pp. 1299-1310, 2018.
[170] G. C. Huang, M. F. Iskander, and Z. Zhang, "Circularly Polarized Beam-Switching Antenna Array Design for Directional Networks," *IEEE Antennas Wireless Propag. Lett.*, vol. 17, pp. 604-607, 2018.
[171] J. T. Bernhard, "Reconfigurable antennas and apertures: state-of-the-art and future outlook," in *SPIE Conf. on Smart Electronics, MEM's, BioMEM's, and Nanotechnology*, 2003.
[172] C. A. Balanis, *Antenna theory: analysis and design,3rd edition*: John Wiley & Sons, 2005.
[173] W.-J. Tseng and S.-J. Chung, "A dual CP slot antenna using a modified Wilkinson power divider configuration," *IEEE Microwave and Guided Wave Letters*, vol. 8, pp. 205-207, 1998.
[174] Y. F. Lin, Y. K. Wang, H. M. Chen, and Z. Z. Yang, "Circularly Polarized Crossed Dipole Antenna With Phase Delay Lines for RFID Handheld Reader," *IEEE Trans. Antennas Propag.*, vol. 60, pp. 1221-1227, 2012.
[175] J. D. Kraus and R. J. Marhefka, *Antennas for all applications, 3rd editon*: McGraw-Hill, 2002.

[176] J. Dyson, "The equiangular spiral antenna," *IRE Transactions on Antennas and Propagation*, vol. 7, pp. 181-187, 1959.

[177] L. Young, L. A. Robinson, and C. Hacking, "Meander-line polarizer," *IEEE Trans. Antennas Propag.*, vol. 21, pp. 376-378, 1973.

[178] H. L. Zhu, S. W. Cheung, C. Kwok Lun, and T. I. Yuk, "Linear-to-Circular Polarization Conversion Using Metasurface," *IEEE Trans. Antennas Propag.*, vol. 61, pp. 4615-4623, 2013.

[179] H. L. Zhu, S. W. Cheung, X. H. Liu, and T. I. Yuk, "Design of Polarization Reconfigurable Antenna Using Metasurface," *IEEE Trans. Antennas Propag.*, vol. 62, pp. 2891-2898, 2014.

[180] R. Orr, G. Goussetis, and V. Fusco, "Design Method for Circularly Polarized Fabry-Perot Cavity Antennas," *IEEE Trans. Antennas Propag.*, vol. 62, pp. 19-26, 2014.

[181] S. Gao, A. Sambell, and S. S. Zhong, "Polarization-agile antennas," *IEEE Antennas Propag. Mag.*, vol. 48, pp. 28-37, 2006.

[182] M. Boti, L. Dussopt, and J. M. Laheurte, "Circularly polarised antenna with switchable polarisation sense," *Electron. Lett.*, vol. 36, pp. 1518-1519, 2000.

[183] H. Aissat, L. Cirio, M. Grzeskowiak, J. M. Laheurte, and O. Picon, "Reconfigurable circularly polarized antenna for short-range communication systems," *IEEE Trans. Microw. Theory Techn*, vol. 54, pp. 2856-2863, 2006.

[184] Y.-F. Wu, C.-H. Wu, D. Y.Lai, and F.-C. Chen, "A Reconfigurable Quadri-Polarization Diversity Aperture-Coupled Patch Antenna," *IEEE Trans. Antennas Propag.*, vol. 55, pp. 1009-1012, 2007.

[185] S. L. S. Yang and K.-M. Luk, "A Wideband L-Probes Fed Circularly-Polarized Reconfigurable Microstrip Patch Antenna," *IEEE Trans. Antennas Propag.*, vol. 56, pp. 581-584, 2008.

[186] K.-F. Tong and J. Huang, "New Proximity Coupled Feeding Method for Reconfigurable Circularly Polarized Microstrip Ring Antennas," *IEEE Trans. Antennas Propag.*, vol. 56, pp. 1860-1866, 2008.

[187] X.-S. Yang, B.-Z. Wang, S. H. Yeung, Q. Xue, and K. F. Man, "Circularly Polarized Reconfigurable Crossed-Yagi Patch Antenna," *IEEE Antennas Propag. Mag.*, vol. 53, pp. 65-80, 2011.

[188] N. Jin, F. Yang, and R.-S. Y., "A novel patch antenna with switchable slot (PASS): dual-frequency operation with reversed circular polarizations," *IEEE Trans. Antennas Propag.*, vol. 54, pp. 1031-1034, 2006.

[189] F. Yang and Y. Rahmat-Samii, "A reconfigurable patch antenna using switchable slots for circular polarization diversity," *IEEE Microw. Compon. Lett.*, vol. 12, pp. 96-98, 2002.

[190] M. K. Fries, M. Grani, and R. Vahldieck, "A reconfigurable slot antenna with switchable polarization," *IEEE Microw. Compon. Lett.*, vol. 13, pp. 490-492, 2003.

[191] Y. J. Sung, T. U. Jang, and Y. S. Kim, "A reconfigurable microstrip antenna for switchable polarization," *IEEE Microw. Compon. Lett.*, vol. 14, pp. 534-536, 2004.

[192] S.-H. Hsu and C. Kai, "A Novel Reconfigurable Microstrip Antenna With Switchable Circular Polarization," *IEEE Antennas Wireless Propag. Lett.*, vol. 6, pp. 160-162, 2007.

[193] W.-S. Yoon, J.-W. Baik, H.-S. Lee, S. Pyo, S.-M. Han, and Y.-S. Kim, "A Reconfigurable Circularly Polarized Microstrip Antenna With a Slotted Ground Plane," *IEEE Antennas Wireless Propag. Lett.*, vol. 9, pp. 1161-1164, 2010.

[194] M. Maqsood, S. Gao, T. W. C. Brown, M. Unwin, R. d. v. V. Steenwijk, and J. D. Xu, "A Compact Multipath Mitigating Ground Plane for Multiband GNSS Antennas," *IEEE Trans. Antennas Propag.*, vol. 61, pp. 2775-2782, 2013.

[195] M. Zhao, G. Zhang, X. Lei, J. Wu, and J. Shang, "Design of New Single-Layer Multiple-Resonance Broadband Circularly Polarized Reflectarrays," *IEEE Antennas Wireless Propag. Lett.*, vol. 12, pp. 356-359, 2013.

[196] S. Mener, R. Gillard, R. Sauleau, A. Bellion, and P. Potier, "Dual Circularly Polarized Reflectarray With Independent Control of Polarizations," *IEEE Trans. Antennas Propag.*, vol. 63, pp. 1877-1881, 2015.

[197] R. Deng, F. Yang, S. Xu, and M. Li, "An FSS-Backed 20/30-GHz Dual-Band Circularly Polarized Reflectarray With Suppressed Mutual Coupling and Enhanced Performance," *IEEE Trans. Antennas Propag.*, vol. 65, pp. 926-931, 2017.

[198] C. Zhang, Y. Wang, F. Zhu, G. Wei, J. Li, C. Wu, S. Gao, and H. Liu, "A Planar Integrated Folded Reflectarray Antenna With Circular Polarization," *IEEE Trans. Antennas Propag.*, vol. 65, pp. 385-390, 2017.

[199] R. Deng, Y. Mao, S. Xu, and F. Yang, "A Single-Layer Dual-Band Circularly Polarized Reflectarray With High Aperture Efficiency," *IEEE Trans. Antennas Propag.,* vol. 63, pp. 3317-3320, 2015.

[200] L. Zhang, S. Gao, Q. Luo, W. Li, Y. He, and Q. Li, "Single-Layer Wideband Circularly Polarized High-Efficiency Reflectarray for Satellite Communications," *IEEE Trans. Antennas Propag.*, vol. 65, pp. 4529-4538, 2017.

[201] B. A. Munk, *Finite antenna arrays and FSS*: John Wiley \& Sons, 2003.

[202] J. P. Doane, K. Sertel, and J. L. Volakis, "A Wideband, Wide Scanning Tightly Coupled Dipole Array With Integrated Balun (TCDA-IB)," *IEEE Trans. Antennas Propag.,* vol. 61, pp. 4538-4548, 2013.

[203] D. Cavallo, A. Neto, G. Gerini, A. Micco, and V. Galdi, "A 3- to 5-GHz Wideband Array of Connected Dipoles With Low Cross Polarization and Wide-Scan Capability," *IEEE Trans. Antennas Propag.*, vol. 61, pp. 1148-1154, 2013.

[204] F. Zhu, S. Gao, A. T. Ho, R. A. Abd-Alhameed, C. H. See, T. W. C. Brown, J. Li, G. Wei, and J. Xu, "Multiple Band-Notched UWB Antenna With Band-Rejected Elements Integrated in the Feed Line," *IEEE Trans. Antennas Propag.,* vol. 61, pp. 3952-3960, Aug 2013.

[205] K. Zhang, J. Li, G. Wei, Y. Fan, J. Xu, and S. Gao, "Design and optimization of broadband single-layer reflectarray," in *2013 Proceedings of the International Symposium on Antennas Propagation*, 2013, pp. 1226-1229.

[206] P. Nayeri, A. Z. Elsherbeni, and F. Yang, "Radiation Analysis Approaches for Reflectarray Antennas [Antenna Designer's Notebook]," *IEEE Antennas Propag. Mag.*, vol. 55, pp. 127-134, Feb 2013.

[207] W. C. Cummings, "Multiple beam forming networks," *MASSACHUSETTS INST OF TECH LEXINGTON LINCOLN LAB,* vol. TN-1978-9, 1978.

[208] F. E. Fanourios and G. A. Kyriacou, "Novel Nolen matrix based beamforming networks for series-fed low SLL multibeam antennas," *Progress In Electromagnetics Research,* vol. 51, pp. 33-64, 2013.

[209] N. J. G. Fonseca, "Printed S-Band 4 times 4 Nolen Matrix for Multiple Beam Antenna Applications," *IEEE Trans. Antennas Propag.,* vol. 57, pp. 1673-1678, 2009.

[210] T. Djerafi, N. J. G. Fonseca, and K. Wu, "Planar Ku Band 4 times 4 Nolen Matrix in SIW Technology," *IEEE Transactions on Microwave Theory and Techniques,* vol. 58, pp. 259-266, 2010.

Appendix

In this section, some equations in Section 5.2.1 are derived and proved.

A. Proof of equation (5-8)

In this subsection, the equation (5-8) is derived. To give a clearer demonstration, the structure of a Nolen matrix is shown in Figure 1. A typical node which contains a phase shifter and a coupler is also given in Figure 1.

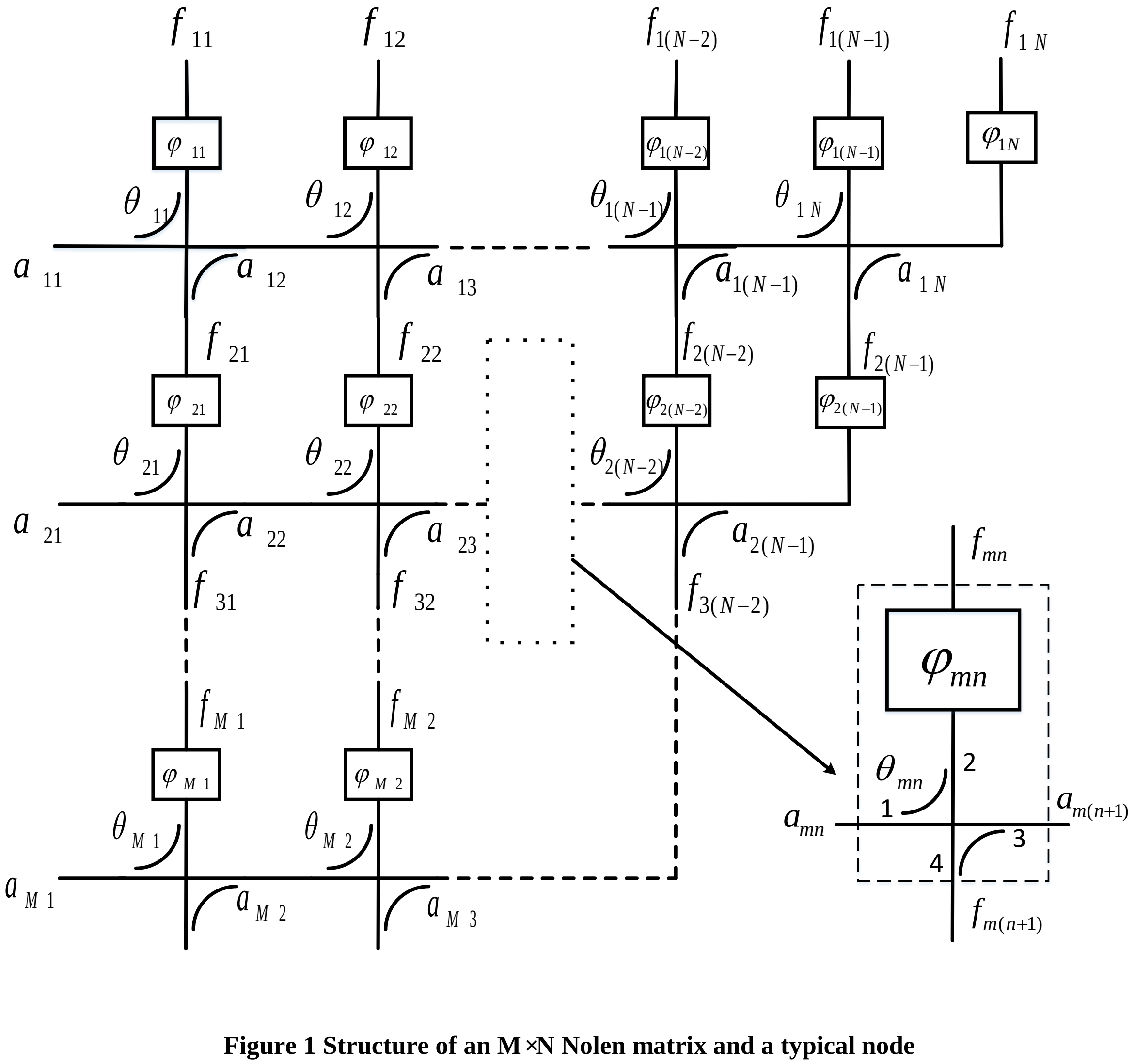

Figure 1 Structure of an M×N Nolen matrix and a typical node

The scattering matrix of the coupler in the typical node is [S].

$$[S]=\begin{bmatrix} 0 & j\sin\theta_{mn} & \cos\theta_{mn} & 0 \\ j\sin\theta_{mn} & 0 & 0 & \cos\theta_{mn} \\ \cos\theta_{mn} & 0 & 0 & j\sin\theta_{mn} \\ 0 & \cos\theta_{mn} & j\sin\theta_{mn} & 0 \end{bmatrix} \quad (1)$$

From the structure of the Nolen matrix and (1), f_{mn} can be obtained. When $n < N - m + 1$, f_{mn} is expressed as the equation (2).

$$f_{mn} = ja_{mn}e^{j\varphi_{mn}}\sin\theta_{mn} + f_{(m+1)n}e^{j\varphi_{mn}}\cos\theta_{mn}\,, (n < N - m + 1) \quad (2)$$

When $n = N - m + 1$, f_{mn} is expressed as the equation (3)

$$f_{mn} = a_{mn}e^{j\varphi_{mn}} \quad (3)$$

Equation (2) and equation (3) are combined as the equation (4).

$$f_{mn} = \begin{cases} ja_{mn}e^{j\varphi_{mn}}\sin\theta_{mn} + f_{(m+1)n}e^{j\varphi_{mn}}\cos\theta_{mn}\,, n < N - m + 1 \\ a_{mn}e^{j\varphi_{mn}}, n = N - m + 1 \end{cases} \quad (4)$$

To clarify the derivation, some matrices and vectors are defined. $\boldsymbol{E}_{(q-1)}$ is an unit matrix of size (q-1).

$$\boldsymbol{\Theta}_{pq}^{s} = \begin{bmatrix} sin\,\theta_{p1} & 0 & \dots & 0 \\ 0 & sin\,\theta_{p2} & \dots & 0 \\ \vdots & \vdots & \ddots & \vdots \\ 0 & 0 & \dots & sin\,\theta_{pq} \end{bmatrix}_{q\times q}$$

$$\boldsymbol{\Theta}_{pq}^{sup} = \begin{bmatrix} sin\,\theta_{p1} & 0 & \dots & 0 \\ \vdots & \ddots & \dots & 0 \\ 0 & 0 & sin\,\theta_{p(q-1)} & \vdots \\ 0 & 0 & \dots & -1\cdot j \end{bmatrix}_{q\times q}$$

Appendix

$$\boldsymbol{\Theta}_{\boldsymbol{pq}}^{\boldsymbol{c}} = \begin{bmatrix} cos\,\theta_{p1} & 0 & \dots & 0 \\ 0 & cos\,\theta_{p2} & \dots & 0 \\ \vdots & \vdots & \ddots & \vdots \\ 0 & 0 & \dots & cos\,\theta_{pq} \end{bmatrix}_{q\times q}$$

$$\boldsymbol{\Phi}_{\boldsymbol{pq}} = \begin{bmatrix} e^{j\varphi_{p1}} & 0 & \dots & 0 \\ 0 & e^{j\varphi_{p2}} & \dots & 0 \\ \vdots & \vdots & \ddots & \vdots \\ 0 & 0 & \dots & e^{j\varphi_{pq}} \end{bmatrix}_{q\times q}$$

$$\boldsymbol{A}_{\boldsymbol{pq}} = [a_{p2} \quad a_{p3} \quad \cdots \quad a_{pq}]^T{}_{(q-1)\times 1}$$

$$\boldsymbol{T}_{\boldsymbol{q}}^{\boldsymbol{f}} = \begin{bmatrix} 1 & 0 & \cdots & 0 & 0 \\ 0 & 1 & \cdots & 0 & 0 \\ \vdots & \vdots & \ddots & \vdots & \vdots \\ 0 & 0 & \cdots & 1 & 0 \\ 0 & 0 & \cdots & 0 & 1 \\ 0 & 0 & \cdots & 0 & 0 \end{bmatrix}_{q\times(q-1)} = \begin{bmatrix} \boldsymbol{E}_{(q-1)} \\ \boldsymbol{0} \end{bmatrix}_{q\times(q-1)}$$

$$\boldsymbol{T}_{\boldsymbol{q}}^{\boldsymbol{a}} = \begin{bmatrix} 0 & 0 & \cdots & 0 & 0 \\ 1 & 0 & \cdots & 0 & 0 \\ 0 & 1 & \cdots & 0 & 0 \\ \vdots & \vdots & \ddots & \vdots & \vdots \\ 0 & 0 & \cdots & 1 & 0 \\ 0 & 0 & \cdots & 0 & 1 \end{bmatrix}_{q\times(q-1)} = \begin{bmatrix} \boldsymbol{0} \\ \boldsymbol{E}_{(q-1)} \end{bmatrix}_{q\times(q-1)}$$

$$\boldsymbol{u}_{\boldsymbol{1q}} = [1 \quad 0 \quad \cdots \quad 0]^T{}_{q\times 1}$$

Equation (4) is rewritten for $n = 1,2, \dots N - m + 1$ and equation (5) is acquired.

$$\begin{bmatrix} f_{m1} \\ f_{m2} \\ \vdots \\ f_{m(N-m+1)} \end{bmatrix} = j \begin{bmatrix} e^{j\varphi_{m1}} & 0 & \dots & 0 \\ 0 & e^{j\varphi_{m2}} & \dots & 0 \\ \vdots & \vdots & \ddots & \vdots \\ 0 & 0 & \dots & e^{j\varphi_{m(N-m+1)}} \end{bmatrix} \cdot \begin{bmatrix} \sin\theta_{m1} & 0 & \dots & 0 \\ 0 & \sin\theta_{m2} & \dots & 0 \\ \vdots & \vdots & \ddots & \vdots \\ 0 & 0 & \dots & -1 \cdot j \end{bmatrix}$$
$$\cdot \begin{bmatrix} a_{m1} \\ a_{m2} \\ \vdots \\ a_{m(N-m+1)} \end{bmatrix} + \begin{bmatrix} e^{j\varphi_{m1}} & 0 & \dots & 0 \\ 0 & e^{j\varphi_{m2}} & \dots & 0 \\ \vdots & \vdots & \ddots & \vdots \\ 0 & 0 & \dots & e^{j\varphi_{m(N-m+1)}} \end{bmatrix}$$
$$\cdot \begin{bmatrix} \cos\theta_{m1} & 0 & \dots & 0 \\ 0 & \cos\theta_{m2} & \dots & 0 \\ \vdots & \vdots & \ddots & \vdots \\ 0 & 0 & \dots & \cos\theta_{m(N-m+1)} \end{bmatrix} \cdot \begin{bmatrix} f_{(m+1)1} \\ f_{(m+1)2} \\ \vdots \\ f_{(m+1)(N-m)} \\ 0 \end{bmatrix} \tag{5}$$

By introducing the matrices defined above and the definition of $\boldsymbol{F_{mn}}$ in equation (5-2), equation (5) is rewritten as equation (6).

$$\boldsymbol{F}_{\boldsymbol{m}(\boldsymbol{N}-\boldsymbol{m}+\boldsymbol{1})} = j\boldsymbol{\Phi}_{\boldsymbol{m}(\boldsymbol{N}-\boldsymbol{m}+\boldsymbol{1})} \cdot \boldsymbol{\Theta}^{\boldsymbol{sup}}_{\boldsymbol{m}(\boldsymbol{N}-\boldsymbol{m}+\boldsymbol{1})} \cdot \left(\begin{bmatrix} a_{m1} \\ \boldsymbol{0} \end{bmatrix} + \begin{bmatrix} 0 \\ \boldsymbol{A}_{\boldsymbol{m}(\boldsymbol{N}-\boldsymbol{m}+\boldsymbol{1})} \end{bmatrix} \right) + \boldsymbol{\Phi}_{\boldsymbol{m}(\boldsymbol{N}-\boldsymbol{m}+\boldsymbol{1})} \cdot \boldsymbol{\Theta}^{\boldsymbol{c}}_{\boldsymbol{m}(\boldsymbol{N}-\boldsymbol{m}+\boldsymbol{1})} \cdot \begin{bmatrix} \boldsymbol{F}_{(\boldsymbol{m}+\boldsymbol{1})(\boldsymbol{N}-\boldsymbol{m})} \\ \boldsymbol{0} \end{bmatrix} \tag{6}$$

It is also known that equation (7), (8) and (9) exist.

$$\begin{bmatrix} a_{m1} \\ \boldsymbol{0} \end{bmatrix} = a_{m1}\boldsymbol{u}_{\boldsymbol{1}(\boldsymbol{N}-\boldsymbol{m}+\boldsymbol{1})} \tag{7}$$

$$\begin{bmatrix} 0 \\ \boldsymbol{A}_{\boldsymbol{m}(\boldsymbol{N}-\boldsymbol{m}+\boldsymbol{1})} \end{bmatrix} = \boldsymbol{T}^{\boldsymbol{a}}_{(\boldsymbol{N}-\boldsymbol{m}+\boldsymbol{1})} \cdot \boldsymbol{A}_{\boldsymbol{m}(\boldsymbol{N}-\boldsymbol{m}+\boldsymbol{1})} \tag{8}$$

$$\begin{bmatrix} \boldsymbol{F}_{(\boldsymbol{m}+\boldsymbol{1})(\boldsymbol{N}-\boldsymbol{m})} \\ 0 \end{bmatrix} = \boldsymbol{T}^{\boldsymbol{f}}_{(\boldsymbol{N}-\boldsymbol{m}+\boldsymbol{1})} \cdot \boldsymbol{F}_{(\boldsymbol{m}+\boldsymbol{1})(\boldsymbol{N}-\boldsymbol{m})} \tag{9}$$

Substituting equation (7), (8) and (9) into equation (6), equation (10) is obtained.

Appendix

$$\boldsymbol{F}_{\boldsymbol{m}(\boldsymbol{N}-\boldsymbol{m}+\mathbf{1})} = \boldsymbol{\Phi}_{\boldsymbol{m}(\boldsymbol{N}-\boldsymbol{m}+\mathbf{1})} \cdot [j\boldsymbol{\Theta}^{\boldsymbol{sup}}_{\boldsymbol{m}(\boldsymbol{N}-\boldsymbol{m}+\mathbf{1})} \cdot (a_{m1}\mathbf{u}_{\mathbf{1}(\boldsymbol{N}-\boldsymbol{m}+\mathbf{1})} + \mathbf{T}^{\boldsymbol{a}}_{(\boldsymbol{N}-\boldsymbol{m}+\mathbf{1})} \cdot \mathbf{A}_{\boldsymbol{m}(\boldsymbol{N}-\boldsymbol{m}+\mathbf{1})}) + \boldsymbol{\Theta}^{\boldsymbol{c}}_{\boldsymbol{m}(\boldsymbol{N}-\boldsymbol{m}+\mathbf{1})} \cdot \mathbf{T}^{\boldsymbol{f}}_{(\boldsymbol{N}-\boldsymbol{m}+\mathbf{1})} \cdot \mathbf{F}_{(\boldsymbol{m}+\mathbf{1})(\boldsymbol{N}-\boldsymbol{m})}] \tag{10}$$

From the structure of the Nolen matrix and (1), $a_{m(n+1)}$ can be obtained as well.

$$a_{m(n+1)} = jf_{(m+1)n} \sin\theta_{mn} + a_{mn}\cos\theta_{mn}\,, (n < N - m + 1) \tag{11}$$

Equation (11) is rewritten as equation (12).

$$-a_{mn}\cos\theta_{mn} + a_{m(n+1)} = jf_{(m+1)n}\sin\theta_{mn}\,, (n < N - m + 1) \tag{12}$$

Equation (12) is rewritten for $n = 1,2, \dots N - m$ and equation (13) is derived.

$$\begin{bmatrix} -\cos\theta_{m1} & 1 & 0 & \cdots & 0 & 0 \\ 0 & -\cos\theta_{m2} & 1 & \cdots & 0 & 0 \\ 0 & 0 & -\cos\theta_{m3} & \ddots & \vdots & \vdots \\ \vdots & \vdots & \vdots & \ddots & 1 & 0 \\ 0 & 0 & 0 & 0 & -\cos\theta_{m(N-m)} & 1 \end{bmatrix} \cdot \begin{bmatrix} a_{m1} \\ a_{m2} \\ \vdots \\ a_{m(N-m+1)} \end{bmatrix} = j \begin{bmatrix} \sin\theta_{m1} & 0 & \dots & 0 \\ 0 & \sin\theta_{m2} & \dots & 0 \\ \vdots & \vdots & \ddots & \vdots \\ 0 & 0 & \dots & \sin\theta_{m(N-m)} \end{bmatrix} \cdot \begin{bmatrix} f_{(m+1)1} \\ f_{(m+1)2} \\ \vdots \\ f_{(m+1)(N-m)} \end{bmatrix} \tag{13}$$

Equation (13) is rewritten as equation (14), in which $\boldsymbol{A_d}$ is defined in equation (15).

$$[-\cos\theta_{m1}\,\boldsymbol{u}_{\mathbf{1}(\boldsymbol{N}-\boldsymbol{m}+\mathbf{1})} \quad \boldsymbol{A_d}] \cdot \left(\begin{bmatrix} a_{m1} \\ \mathbf{0} \end{bmatrix} + \begin{bmatrix} 0 \\ \boldsymbol{A}_{\boldsymbol{m}(\boldsymbol{N}-\boldsymbol{m}+\mathbf{1})} \end{bmatrix}\right) = j\boldsymbol{\Theta}^{\boldsymbol{s}}_{\boldsymbol{m}(\boldsymbol{N}-\boldsymbol{m})} \cdot \boldsymbol{F}_{(\boldsymbol{m}+\mathbf{1})(\boldsymbol{N}-\boldsymbol{m})} \tag{14}$$

$$\boldsymbol{A_d} = \begin{bmatrix} 1 & 0 & \cdots & 0 & 0 \\ -\cos\theta_{m2} & 1 & \cdots & 0 & 0 \\ 0 & -\cos\theta_{m3} & \ddots & \vdots & \vdots \\ \vdots & \vdots & \ddots & 1 & 0 \\ 0 & 0 & 0 & -\cos\theta_{m(N-m)} & 1 \end{bmatrix}_{(N-m)\times(N-m)}$$

(15)

From equation (14), equation (16) is gained.

$$-\cos\theta_{m1}\, a_{m1}\boldsymbol{u}_{\mathbf{1}(\boldsymbol{N}-\boldsymbol{m}+\mathbf{1})} + \boldsymbol{A_d} \cdot \boldsymbol{A}_{\boldsymbol{m}(\boldsymbol{N}-\boldsymbol{m}+\mathbf{1})} = j\boldsymbol{\Theta}^{\boldsymbol{s}}_{\boldsymbol{m}(\boldsymbol{N}-\boldsymbol{m})} \cdot \boldsymbol{F}_{(\boldsymbol{m}+\mathbf{1})(\boldsymbol{N}-\boldsymbol{m})} \tag{16}$$

When the i^{th} input port is excited only, $a_{p1} = 0$ if $p \neq i$. As $m + 1 \leq i$, $m \neq i$. Therefore, $a_{m1} = 0$, and equation (16) is simplified as equation (17).

$$\boldsymbol{A_d} \cdot \boldsymbol{A}_{\boldsymbol{m}(\boldsymbol{N}-\boldsymbol{m}+\mathbf{1})} = j\boldsymbol{\Theta}^{\boldsymbol{s}}_{\boldsymbol{m}(\boldsymbol{N}-\boldsymbol{m})} \cdot \boldsymbol{F}_{(\boldsymbol{m}+\mathbf{1})(\boldsymbol{N}-\boldsymbol{m})} \tag{17}$$

For $n = 2, \ldots N - m$, equation (18) exists.

$$|\cos\theta_{mn}| < 1. \tag{18}$$

From equation (18), it is known that $\boldsymbol{A_d}$ is a strictly diagonally dominant matrix, which means $\boldsymbol{A_d}$ is invertible. That is $\boldsymbol{A_d^{-1}}$ exists. From equation (17), the expression of $\mathbf{A}_{\boldsymbol{m}(\boldsymbol{N}-\boldsymbol{m}+\mathbf{1})}$ is obtained in equation (19).

$$\boldsymbol{A}_{\boldsymbol{m}(\boldsymbol{N}-\boldsymbol{m}+\mathbf{1})} = j\boldsymbol{A_d^{-1}} \cdot \boldsymbol{\Theta}^{\boldsymbol{s}}_{\boldsymbol{m}(\boldsymbol{N}-\boldsymbol{m})} \cdot \boldsymbol{F}_{(\boldsymbol{m}+\mathbf{1})(\boldsymbol{N}-\boldsymbol{m})} \tag{19}$$

Substituting equation (19) and $a_{m1} = 0$ into equation (10), equation (20) is acquired.

$$\begin{aligned}
\boldsymbol{F}_{\boldsymbol{m}(\boldsymbol{N}-\boldsymbol{m}+\mathbf{1})} &= j\boldsymbol{\Phi}_{\boldsymbol{m}(\boldsymbol{N}-\boldsymbol{m}+\mathbf{1})} \cdot \boldsymbol{\Theta}^{\boldsymbol{sup}}_{\boldsymbol{m}(\boldsymbol{N}-\boldsymbol{m}+\mathbf{1})} \cdot \left(\boldsymbol{T}^{\boldsymbol{a}}_{(\boldsymbol{N}-\boldsymbol{m}+\mathbf{1})} \cdot j\boldsymbol{A_d^{-1}} \cdot \boldsymbol{\Theta}^{\boldsymbol{s}}_{\boldsymbol{m}(\boldsymbol{N}-\boldsymbol{m})} \cdot \boldsymbol{F}_{(\boldsymbol{m}+\mathbf{1})(\boldsymbol{N}-\boldsymbol{m})}\right) \\
&\quad + \boldsymbol{\Phi}_{\boldsymbol{m}(\boldsymbol{N}-\boldsymbol{m}+\mathbf{1})} \cdot \boldsymbol{\Theta}^{\boldsymbol{c}}_{\boldsymbol{m}(\boldsymbol{N}-\boldsymbol{m}+\mathbf{1})} \cdot \left[\boldsymbol{T}^{\boldsymbol{f}}_{(\boldsymbol{N}-\boldsymbol{m}+\mathbf{1})} \cdot \boldsymbol{F}_{(\boldsymbol{m}+\mathbf{1})(\boldsymbol{N}-\boldsymbol{m})}\right] \\
&= \boldsymbol{\Phi}_{\boldsymbol{m}(\boldsymbol{N}-\boldsymbol{m}+\mathbf{1})} \\
&\quad \cdot \left[-\boldsymbol{\Theta}^{\boldsymbol{sup}}_{\boldsymbol{m}(\boldsymbol{N}-\boldsymbol{m}+\mathbf{1})} \cdot \boldsymbol{T}^{\boldsymbol{a}}_{(\boldsymbol{N}-\boldsymbol{m}+\mathbf{1})} \cdot \boldsymbol{A_d^{-1}} \cdot \boldsymbol{\Theta}^{\boldsymbol{s}}_{\boldsymbol{m}(\boldsymbol{N}-\boldsymbol{m})} + \boldsymbol{\Theta}^{\boldsymbol{c}}_{\boldsymbol{m}(\boldsymbol{N}-\boldsymbol{m}+\mathbf{1})} \cdot \boldsymbol{T}^{\boldsymbol{f}}_{(\boldsymbol{N}-\boldsymbol{m}+\mathbf{1})}\right] \\
&\quad \cdot \boldsymbol{F}_{(\boldsymbol{m}+\mathbf{1})(\boldsymbol{N}-\boldsymbol{m})}
\end{aligned} \tag{20}$$

$\boldsymbol{B_m}$ is defined in equation (21). If equation (21) is substituted into equation (20), equation (22) is obtained. It is should be noticed that $\boldsymbol{B_m}$ is a $(N-m+1)\times\ (N-m)$ matrix and $\boldsymbol{B_m}$ cannot be inverted directly.

$$\boldsymbol{B_m} = \boldsymbol{\Phi_{m(N-m+1)}} \cdot \left[-\boldsymbol{\Theta^s_{m(N-m+1)}} \cdot \boldsymbol{T^a_{(N-m+1)}} \cdot \boldsymbol{A_d^{-1}} \cdot \boldsymbol{\Theta^s_{m(N-m)}} + \boldsymbol{\Theta^c_{m(N-m+1)}} \cdot \boldsymbol{T^f_{(N-m+1)}}\right] \tag{21}$$

$$\boldsymbol{F_{m(N-m+1)}} = \boldsymbol{B_m} \cdot \boldsymbol{F_{(m+1)(N-m)}} \tag{22}$$

Then, $\mathbf{T}^{\boldsymbol{b}}_{\boldsymbol{q}}$ and $\boldsymbol{C_m}$ are defined below. $\boldsymbol{C_m}$ is a square matrix.

$$\boldsymbol{T^b_q} = \begin{bmatrix} 1 & 0 & \cdots & 0 & 0 \\ 0 & 1 & \cdots & 0 & 0 \\ \vdots & \vdots & \ddots & \vdots & \vdots \\ 0 & 0 & \cdots & 1 & 0 \end{bmatrix}_{(q-1)\times q} = [\boldsymbol{E_{(q-1)}} \quad \mathbf{0}] \tag{23}$$

$$\boldsymbol{C_m} = \boldsymbol{T^b_{N-m+1}} \cdot \boldsymbol{B_m} \tag{24}$$

Equation (22) times $\boldsymbol{T^b_{N-m+1}}$, and equation (25) is obtained.

$$\boldsymbol{T^b_{N-m+1}} \cdot \boldsymbol{F_{m(N-m+1)}} = \boldsymbol{T^b_{N-m+1}} \cdot \boldsymbol{B_m} \cdot \boldsymbol{F_{(m+1)(N-m)}} \tag{25}$$

Due to equation (26), equation (25) is rewritten as equation (27).

$$\mathbf{F}_{\boldsymbol{m(N-m)}} = \boldsymbol{T^b_{N-m+1}} \cdot \boldsymbol{F_{m(N-m+1)}} \tag{26}$$

$$\boldsymbol{F_{m(N-m)}} = \boldsymbol{C_m} \cdot \boldsymbol{F_{(m+1)(N-m)}} \tag{27}$$

Thus, equation (28) is obtained.

$$\boldsymbol{F_{(m+1)(N-m)}} = \boldsymbol{C_m^{-1}} \cdot \boldsymbol{F_{m(N-m)}} \tag{28}$$

Equation (28) is the required equation (5-8), and the proof is completed.

B. Limitation on Excitation Vectors

An M×N Nolen matrix has M input ports and N output ports. As defined in 5.2.1, the input and output ports are represented by a_1, a_2,…,a_M and b_1, b_2,…, b_N. The electric field values on input and output ports are $\vec{\boldsymbol{a}}$ and $\vec{\boldsymbol{f}}$.

From (5-7), equation (29) is obtained.

$$\begin{bmatrix} f_{11} \\ f_{12} \\ \vdots \\ f_{1N} \end{bmatrix} = \begin{bmatrix} e_{11} & e_{21} & \cdots & e_{M1} \\ e_{12} & e_{22} & \cdots & e_{M2} \\ \vdots & \vdots & \ddots & \vdots \\ e_{1N} & e_{2N} & \cdots & e_{MN} \end{bmatrix} \cdot \begin{bmatrix} a_{11} \\ a_{12} \\ \vdots \\ a_{1M} \end{bmatrix} \tag{29}$$

Therefore, the relationship between input ports and output ports is shown from (30).

$$\begin{bmatrix} b_1 \\ b_2 \\ \vdots \\ b_N \end{bmatrix} = \begin{bmatrix} e_{11} & e_{21} & \cdots & e_{M1} \\ e_{12} & e_{22} & \cdots & e_{M2} \\ \vdots & \vdots & \ddots & \vdots \\ e_{1N} & e_{2N} & \cdots & e_{MN} \end{bmatrix} \cdot \begin{bmatrix} a_1 \\ a_2 \\ \vdots \\ a_M \end{bmatrix} \tag{30}$$

The scattering matrix of an M×N Nolen matrix $[\boldsymbol{SN}]$ is shown in equation (31).

$$[\boldsymbol{SN}] = \begin{bmatrix} s_{a_1,a_1} & s_{a_1,a_2} & \cdots & s_{a_1,a_M} & s_{a_1,b_1} & s_{a_1,b_2} & \cdots & s_{a_1,b_{1N}} \\ s_{a_2,a_1} & s_{a_2,a_2} & \cdots & s_{a_2,a_M} & s_{a_2,b_1} & s_{a_2,b_2} & \cdots & s_{a_2,b_{1N}} \\ \vdots & \vdots & \ddots & \vdots & \vdots & \vdots & \ddots & \vdots \\ s_{a_M,a_1} & s_{a_M,a_2} & \cdots & s_{a_M,a_M} & s_{a_M,b_1} & s_{a_M,b_2} & \cdots & s_{a_M,b_{1N}} \\ s_{b_1,a_1} & s_{b_1,a_2} & \cdots & s_{b_1,a_M} & s_{b_1,b_1} & s_{b_1,b_2} & \cdots & s_{b_1,b_{1N}} \\ s_{b_2,a_1} & s_{b_2,a_2} & \cdots & s_{b_2,a_M} & s_{b_2,b_1} & s_{b_2,b_2} & \cdots & s_{b_2,b_{1N}} \\ \vdots & \vdots & \ddots & \vdots & \vdots & \vdots & \ddots & \vdots \\ s_{b_N,a_1} & s_{b_N,a_2} & \cdots & s_{b_N,a_M} & s_{b_N,b_1} & s_{b_N,b_2} & \cdots & s_{b_N,b_{1N}} \end{bmatrix} \tag{31}$$

From the equation (30), it is known that $s_{b_n,a_m} = e_{mn}(1 \le n \le N, 1 \le m \le M)$. As each input port is matched and isolated from other input ports, $s_{a_p,a_q} = 0, (1 \le p, q \le m)$. Therefore, equation (31) is rewritten as equation (32).

$$[\boldsymbol{SN}] = \begin{bmatrix} 0 & 0 & \cdots & 0 & s_{a_1,b_1} & s_{a_1,b_2} & \cdots & s_{a_1,b_{1N}} \\ 0 & 0 & \cdots & 0 & s_{a_2,b_1} & s_{a_2,b_2} & \cdots & s_{a_2,b_{1N}} \\ \vdots & \vdots & \ddots & \vdots & \vdots & \vdots & \ddots & \vdots \\ 0 & 0 & \cdots & 0 & s_{a_M,b_1} & s_{a_M,b_2} & \cdots & s_{a_M,b_{1N}} \\ e_{11} & e_{21} & \cdots & e_{M1} & s_{b_1,b_1} & s_{b_1,b_2} & \cdots & s_{b_1,b_{1N}} \\ e_{12} & e_{22} & \cdots & e_{M2} & s_{b_2,b_1} & s_{b_2,b_2} & \cdots & s_{b_2,b_{1N}} \\ \vdots & \vdots & \ddots & \vdots & \vdots & \vdots & \ddots & \vdots \\ e_{1N} & e_{2N} & \cdots & e_{MN} & s_{b_N,b_1} & s_{b_N,b_2} & \cdots & s_{b_N,b_{1N}} \end{bmatrix}$$

(32)

Under the assumption that the phase shifters and couplers are lossless, the Nolen matrix is a lossless network as well. As a result, $[\boldsymbol{SN}]$ is a unitary matrix, which satisfies equation (33).

$$[\boldsymbol{SN}]^{\boldsymbol{T}} = ([\boldsymbol{SN}]^*)^{-\boldsymbol{1}} \quad (33)$$

Equation (33) is written in summation form as equation (34) .

$$\sum_{k=1}^{M+N} \boldsymbol{SN_{ki}} \cdot \boldsymbol{SN_{kj}^*} = \begin{cases} 1, i = j \\ 0, i \neq j \end{cases}$$

(34)

Equation (34) states that any column of $[\boldsymbol{SN}]$ doing the dot product with the conjugate of the same column gives one, and gives zero if it does the dot product with the conjugate of a different column. This means the columns of $[\boldsymbol{SN}]$ are orthonormal.

Considering the definition in (5-5), the first M columns of $[\boldsymbol{SN}]$ can be written as equation (35).

$$\begin{bmatrix} \boldsymbol{0} & \boldsymbol{0} & \cdots & \boldsymbol{0} \\ \overrightarrow{\boldsymbol{e_1}} & \overrightarrow{\boldsymbol{e_2}} & \cdots & \overrightarrow{\boldsymbol{e_M}} \end{bmatrix} \quad (35)$$

As these M columns of $[\boldsymbol{SN}]$ are orthonormal, $\overrightarrow{\boldsymbol{e_1}}, \overrightarrow{\boldsymbol{e_2}}, \cdots, \overrightarrow{\boldsymbol{e_M}}$ are orthonormal. This is the limitation on not only Nolen matrix networks, but also other lossless networks.